INFN ISTITUTO NAZIONALE DI FISICA NUCLEARE
Laboratori Nazionali di Frascati

FRASCATI PHYSICS SERIES

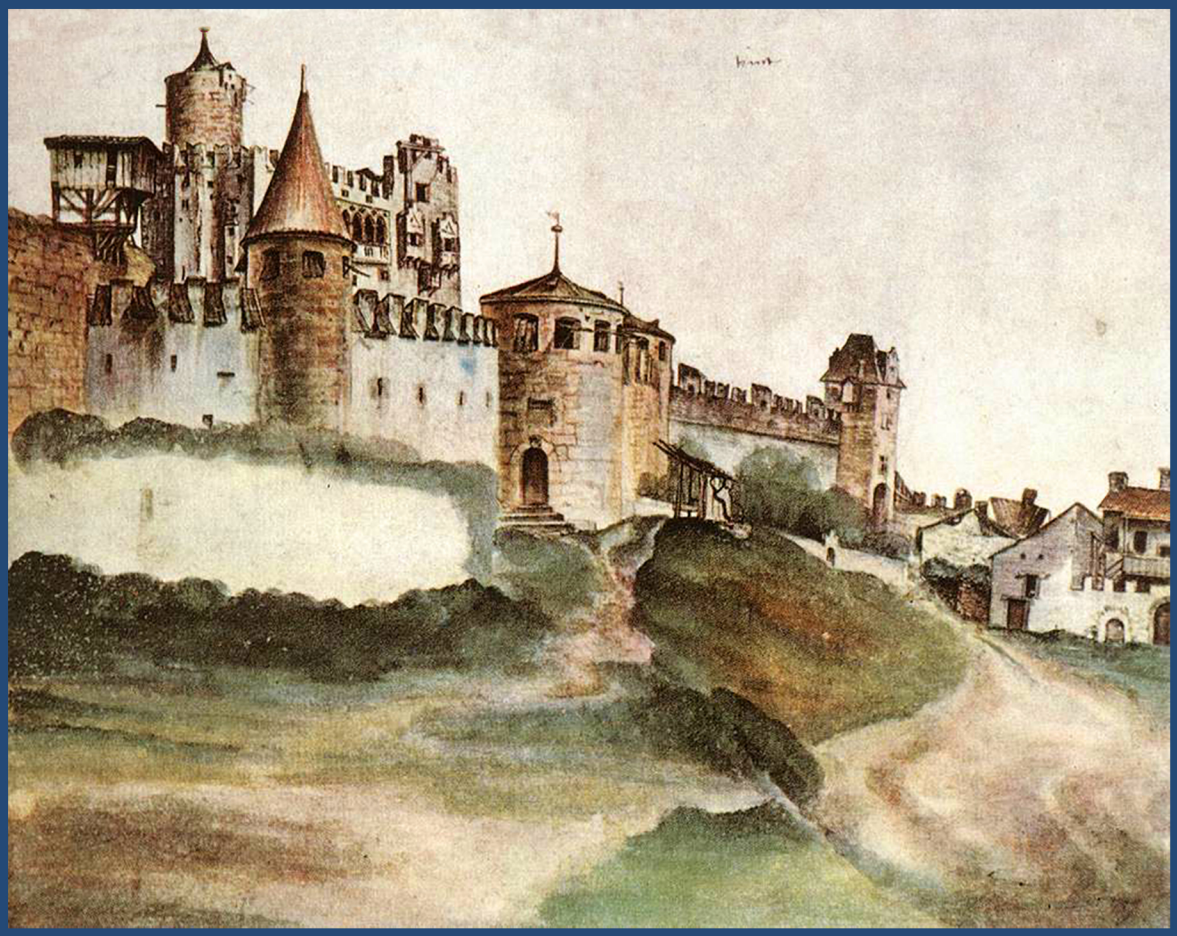

LFC17: Old and New Strong Interactions from LHC to Future Colliders

ECT*, Trento, Italy, September 11 - 15, 2017

Editors:

Gennaro Corcella, Stefania De Curtis, Stefano Moretti,
Giulia Pancheri, Roberto Tenchini, Marcel Vos

FRASCATI PHYSICS SERIES

Series Editor
Paola Gianotti

Technical Editor
Lia Sabatini

Cover by Claudio Federici

Volume LXV

Istituto Nazionale di Fisica Nucleare – Laboratori Nazionali di Frascati
Divisione Ricerca
Ufficio Biblioteca e Pubblicazioni
P.O. Box 13, I-00044 Frascati Roma Italy
email: library@lists.lnf.infn.it

ISBN 978-88-86409-88-9-61-2

LFC17:
Physics prospects for Linear and other Future Colliders after the discovery of the Higgs 2017

CONTENTS

Frascati Physics Series Vol. 65 (2017)
LFC17: Old and New Strong Interactions from LHC to Future Colliders
11 - 15 September, 2017

PREFACE

The workshop 'LFC17: Old and New Strong Interactions from LHC to Future Colliders' was held at the European Center for Theoretical Physics (ECT*), Villazzano (TN), Italy, on September 11-15, 2017. It has been the eighth edition of a series which in the beginning was mostly devoted to the physics of high-energy electron-positron Linear Colliders, while it has now become a regular appointment to discuss all projects for future accelerators, both linear and circular, as well as lepton and hadron colliders. Such meetings have been taking place in Italy, gathering both Italian and international scientists active in experiments, theory and phenomenology of future colliders. The location has been ECT* in 2011, 2013 and 2015, whereas the previous editions were held in Florence (2007), Perugia (2009) and Frascati National Laboratories (2008 and 2010).

As for the structure of the workshop, the first day has always been devoted to general presentations on the phenomenology and the experiments at present and future colliders, while the following days we had topical sessions and specific talks on perturbative and non-perturbative Quantum Chromody-namics, heavy ions, leptonic gyromagnetic moment, top-quark physics, electroweak interactions, Higgs phenomenology, physics beyond the Standard Model (BSM) and Dark Matter (DM).

The 2017 edition was focused on the role played by strong interactions, in perturbative and non-perturbative regimes, both within and beyond the SM. The introductive session dealt with general issues on strong interactions at present and future colliders. In particular, the main experimental projects at the future energy frontier, from both viewpoints of physics and accelerators, were reviewed. Moreover, we had an overview of LHC QCD results, discussing the experimental and theoretical perspectives, and of heavy-ion phenomenology at LHC, RHIC and future colliders. The prospects for strongly-interacting physics at future accelerators were presented as well; furthermore, regarding BSM physics, we focused on models based on strong dynamics and their predictions for the LHC and for experiments at higher energy and luminosity, in both pp and e^+e^- regimes.

The main results presented in the perturbative QCD session concerned recent experimental measurements and novel theoretical developments in hard QCD processes. Results on high-p_T reactions at the Large Hadron Collider were highlighted, showing, in particular, recent measurements on vector-boson production in association with QCD jets, diboson, single and double Higgs-boson production. It was pre-

sented an algorithm to calculate jet cross sections up to next-to-next-to-leading order (NNLO) QCD in lepton and hadron collisions, along with new quantitative results based on the CoLorFulNNLO subtraction method. A novel technique for higher-order calculations was discussed: such a method is based on the duality relation between loops and phase-space integrals and an explicit calculation of the total Higgs boson decay rate at NLO was presented. New results on azimuthal correlations among particles in hard QCD scattering were shown, underlying that fixed-order computations can lead to divergences which can be removed by means of a proper all-order resummation procedure. An infrared QCD model, describing the energy dependence of the total cross section at very high energies and the non-diffractive soft and semi-hard collisions in hadronic processes, was also debated.

The 'Non Perturbative QCD and Heavy Ions' session was introduced by a general talk, giving a broad overview of the main items touched more deeply in the specific contributions. A talk was devoted to nuclear parton distribution functions (nPDF's), showing how a wide set of observables in eA, νA and pA collisions can be accommodated within a picture based on collinear factorization. Initial-state effects were also addressed, paying special attention to gluon saturation. The picture, initially developed to describe the low-x evolution of the gluon density and to provide an interpretation of peculiar features of HERA DIS data, was later employed to get a first-principle description of the initial state in high-energy pA and AA collisions. Relativistic hydrodynamics was addressed as well: the major surprise in the field came from the recent discovery of collective effects, suggesting a hydrodynamic interpretation in small systems, like the ones produced in high-multiplicity pp and pA collisions. It was also conveyed the message that the same physics is at work in producing the quenching of jets in AA collisions and in making the initial system thermalize. One of the most important issues to understand in the forthcoming heavy-ion runs of the LHC is the absence of jet-quenching in small systems (pA collisions), which, on the other hand, display signatures of collective flow. Finally, heavy-flavour observables were debated too, given the fact that one has the potential to get access, in particular through bottom-quark measurements, to the transport coefficients of the plasma.

The 'Top Quark Physics' session began with an overview of top-quark phenomenology at the LHC and was concluded by a companion presentation debating the perpectives at future lepton and hadron colliders. Furthermore, recent progress in the POWHEG program for top physics was explored: the latest version of this NLO Monte Carlo generator contains NLO corrections to top decays, width effects, interference between production and decay phases, as well as non-resonant contributions. The top-quark mass extraction was also investigated, taking particular care about the relation between the reconstructed mass and the pole mass; recent NNLO computations of the total $t\bar{t}$ cross section were presented, paying attention to the comparison of analytical and numerical approaches.

The 'Higgs and BSM' session aimed at investigating the role played by strong interactions in physics at the TeV scale and above. The main topics covered were the following: strongly-interacting theories of the Higgs boson and their short-distance realization; strongly-interacting DM; signals at colliders from composite states, emerging as bound states of the new-physics strong interactions; relations between strongly-coupled theories of electroweak symmetry breaking, their apparent fine tuning in parameter space and symmetry-breaking patterns observed in real-world condensed matter systems.

The anomalous magnetic moment of the muon, namely $a_\mu = (g_\mu - 2)/2$ is one of the best known quantities in particle physics, from both experimental and theoretical sides: intriguingly, there is a long-standing discrepancy between the current experimental measurements and the best theoretical predictions within the SM, of the order of $3 - 4$ standard deviations. In the '$g - 2$' session we had an overview of the experimental techniques and results from past experiments, as well as updates on the status of the

future Fermilab (USA) and J-PARC (KEK, Japan) facilities. The theory status of the a_μ calculation was briefly summarized, focusing on a new proposed experiment to measure the hadronic contribution to the running of the electromagnetic coupling constant in the space-like region, via the scattering process $\mu e \to \mu e$. This high-precision measurement will allow to estimate the leading-order hadronic contribution to a_μ, which currently yields the largest theoretical error. An improved analysis of the available data was then presented: the current theoretical error on a_μ may be reduced by 30% and thus induce a discrepancy of 3.9σ between the SM prediction and the current experimental value.

The 'Exotics and Dark Matter' session was opened by a presentation on exotic quarks of charge 5/3, predicted in composite models with higher-isospin multiplets: recasting the present experimental analyses, it is possible to set exclusion bounds on the exotic-quark masses. Moreover, we investigated DM searches at the LHC, with most of the attention devoted to weakly-interacting models, since they are within the experimental reach. In particular, we emphasized the importance of the so-called 'Simplified Models' that are characterized only by the presence of a DM candidate and a mediator with the SM sector. Searches for vector-like top-quark partners at the LHC were motivated and explored: direct searches and indirect constraints from electroweak precision data can play a complementary role in probing the existence of new vector-like quarks. From the experimental viewpoint, we had a summary of the present status of vector-like top-partner searches at the LHC and a presentation discussing the relation between B-decay anomalies and DM in strong-dynamics scenarios. In fact, the recent B-decay anomalies observed by LHCb could be explained in the context of a simple model with strong dynamics, containing a vector-like quark partner, a right-handed neutrino partner and an inert Higgs doublet. As for DM searches at the LHC, we focused on a class of theories in which the DM candidate is a pseudo Nambu–Goldstone boson arising from a strongly-interacting sector: in these models, the experimental results can be re-interpreted in terms of effective field theory approaches.

Most of the oral contributions at the LFC17 workshop are summarized in these proceedings, which are therefore a useful collection, reviewing the state of the art of particle physics in the era of the LHC Run II as well as a number of astrophysics observations, and exploring the prospects for future hadron and lepton colliders. More details and the slides of the talks can be found at:
`http://www.ectstar.eu/node/2228`;
`https://agenda.infn.it/conferenceDisplay.py?confId=13162`.

Before concluding, we wish to warmly thank the conveners, whose names are listed below, for their remarkable effort to invite the speakers and chair the sessions, in such a way to achieve a fruitful workshop and release the present volume. We also acknowledge the INFN 'Commissione IV' and the ECT* for financial support; we are especially grateful to Christian Fossi for his invaluable help with the organization of the logistics.

Conveners:

Andrea Beraudo, INFN Turin (Non Perturbative QCD and Heavy Ions)
Carlo Carloni Calame, INFN Pavia ($g-2$)
Aldo Deandrea, IPN Lyon (Higgs Physics)
Giancarlo Ferrera, University of Milan (Perturbative QCD)
Roberto Franceschini, University of Rome 3 (Beyond the Standard Model)
Orlando Panella, INFN Perugia (Exotics)
Francesco Tramontano, University of Naples (Top Quark Physics)
Alfredo Urbano, CERN (Dark Matter)

LFC17: Old and New Strong Interactions from LHC to Future Colliders

Chaired by

Gennaro Corcella, Marcel Vos, Stefania De Curtis, Stefano Moretti,
Roberto Tenchini, Giulia Pancheri

from Monday, 11 September 2017 at 14:30 to Friday, 15 September 2017 at 14:00

at ECT*, Villa Tambosi, Villazzano (Trento)

Aim of the workshop

The proposed workshop will highlight current problems posed by strong interactions in perturbative and non-perturbative regimes and discuss how future colliders beyond the LHC can shed light on them. In particular, our meeting will deal with the following issues: state of the art of perturbative and non-perturbative QCD, non-perturbative uncertainties and interpretation of the top-quark mass, strong interactions as the binding force of new fermions in composite Higgs models, role played by QCD in new physics searches at the LHC, hadronic contribution to the leptonic gyromagnetic moment.

The program will be organized with introductory talks on strong interactions at present and future colliders and the following topical working groups:

Perturbative QCD (Convener G. Ferrera)
Non-perturbative QCD and heavy ions (Convener A. Beraudo)
Top-quark physics (Convener F. Tramontano)
Leptonic g-2 (Convener C. Calame Carloni)
Higgs physics (Conveners A. Deandrea and R. Franceschini)
Exotics and Dark Matter (Conveners A. Urbano and O. Panella)

Organizers:

Gennaro Corcella (INFN LNF, chairman)
Stefania De Curtis (INFN Florence)
Stefano Moretti (University of Southampton)
Giulia Pancheri (INFN LNF)
Roberto Tenchini (INFN Pisa)
Marcel Vos (Universidad de Valencia)

Monday, 11 September 2017

Introduction to strong interactions at present and future colliders (Chairs: G. Corcella and R. Tenchini)

14:30 Accelerators and experiments for the future energy frontier 30'
Speaker: Brian Foster

15:00 QCD measurements at the LHC 30'
Speaker: Ulla Blumenschein

15:30 Strong-interaction physics at future energy-frontier colliders 30'
Speaker: Frank Simon

16:00 Coffee Break 30'

16:30 The QCD challenge for precision at colliders 30'
Speaker: Pier Francesco Monni

17:00 Beyond the Standard Model with strong dynamics 30'
Speaker: Roberto Contino

17:30 State of the art and open issues in heavy-ion physics at present and future colliders 30'
Speaker: Gunther Roland

18:00 Discussion 30'

Tuesday, 12 September 2017

Perturbative QCD (Chair: G. Ferrera)

9:30 Highlights on high pT measurements at the LHC 30'
Speaker: Andrea Rizzi

10:00 Jets cross sections in NNLO QCD in lepton and hadron collisions 30'
Speaker: Gabor Somogyi

10:30 Coffee Break 30'

11:00 New techniques for higher-order calculations in lepton and hadron collisions 30'
Speaker: German Sborlini

11:30 Azimuthal asymmetries in QCD hard scattering: IR safe but divergent 30'
Speaker: Massimiliano Grazzini

12:00 Discussion 30'

12:30 Lunch Break

Non-perturbative QCD and heavy ions (Chairs: A. Beraudo and G. Roland)

14;30 A democratic resummation procedure for infrared gluons: an application to survival probabilities 30'
Speaker: Giulia Pancheri

15:00 Nuclear parton distribution functions 30'
Speaker: Petja Paakkinen

15:30 Initial state and gluon saturation 30'
Speaker: Guillaume Beuf

16:00 Coffee Break 30'

16:30 Mapping of longitudinal correlations through collective expansion 30'
Speaker: Piotr Bozek

17:00 Jet quenching and fluid dynamics 30'
Speaker: Urs Wiedemann

17:30 Heavy flavours in high-energy nuclear collisions: overview of transport calculations 30'
Speaker: Andrea Beraudo

18:00 Discussion 30'

Wednesday, 13 September 2017

Top-quark phenomenology (Chair: F. Tramontano)

9:30 Overview of top phenomenology 30'
Speaker: Alberto Orso Maria Iorio

10:00 Top-quark pair production with resonance-aware methods 30'
Speaker: Paolo Nason

10:30 Top-quark mass determination 30'
Speaker: Peter Uwer

11:00 Coffee Break 30'

11:30 t-tbar production at hadron colliders 30'
Speaker: Roberto Bonciani

12:00 Top physics at future hadron and lepton colliders 30'
Speaker: Marcel Vos

12:30 Discussion 30'

13:00 Lunch Break

Excursion to Lake Tovel, with an introduction to the lake by Dr. Giovanna Flaim (Edmund Mach Foundation)

Thursday, 14 September 2017

g-2 (Chair: C.M. Carloni Calame)

9:30 Past and future muon g-2 experiments 30'
Speaker: Anna Driutti

10:00 Muon-electron scattering: measuring the leading hadronic contribution to the muon g-2 30'
Speaker: Massimo Passera

10:30 The hadronic vacuum polarisation contribution to the muon g-2 30'
Speaker: Alex Keshavarzi

11:00 Discussion 30'

11:30 Coffee Break 30'

BSM in Higgs and Dark Matter physics (Chair: A. Deandrea)

12:00 Lattice field theory results on new strong dynamics 30'
Speaker: Enrico Rinaldi

12:30 Strong dynamics and the hierarchy problem 30'
Speaker: Alex Pomarol

13:00 Lunch Break 1h30'

14:30 Baryonic Dark Matter 30’
Speaker: MIchere Redi

15:00 Composite Higgs and Dark Matter 30'
Speaker: Giacomo Cacciapaglia

15:30 Measuring quark polarizations at ATLAS and CMS 30'
Speaker: Yevgeny Kats

16:00 Coffee Break 30'

BSM in Higgs and Dark Matter physics (Chair: A.L. Urbano)

16:30 Exotic quarks of charge 5/3 from composite models 30'
Speaker: Roberto Leonardi

17:00 Dark matter searches at the LHC in the context of strongly coupled theories 30'

Speaker: Daniele Barducci

17:30 Discussion 30'

Friday, 15 September 2017

Exotic BSM (Chairs: O. Panella and R. Franceschini)

09:30 Vector-like top-quark partners 30'
Speaker: Elisabetta Furlan

10:00 Experimental review on top-partner searches 30'
Speaker: Meenakshi Narain

10:30 B-decay anomalies and dark matter from strong dynamics 30'
Speaker: James Cline

11:00 Coffee Break 30'

11:30 Visibility of the Higgs Mode In Condensed Matter 30'
Speaker: Assa Auerbach

12:00 Strongly Interacting Light Dark Matter 30'
Speaker: Alfredo Leonardo Urbano

12:30 Discussion 30'

13:00 Lunch

LFC17: Old and New Strong Interactions from LHC to Future Colliders

Participants

Agugliero	Alessandro	Università Firenze / INFN	Italy
Auerbach	Assa	Technion	Israel
Barducci	Daniele	SISSA	Italy
Becattini	Francesco	Università di Firenze	Italy
Beraudo	Andrea	INFN	Italy
Beuf	Guillaume	ECT*	Italy
Blumenschein	Ulla	QMUL	UK
Bonciani	Roberto	La Sapienza Universita' di Roma	Italy
Bozek	Piotr	AGH University of Science and Technology	Poland
Cacciapaglia	Giacomo	CNRS/IPNL	France
Carloni Calame	Carlo	INFN	Italy
Cline	James	McGill University	Canada
Contino	Roberto	Scuola Normale Superiore, Pisa	Italy
Corcella	Gennaro	INFN - LNF	Italy
De Curtis	Stefania	INFN	Italy
Deandrea	Aldo	University Lyon 1	France
Driutti	Anna	INFN - Sezione di Trieste	Italy
Ferrari	Ruggero	INFN Milano via Celoria	Italia
Ferrera	Giancarlo	Milan University	Italy
Foster	Brian	DESY	Germany
Franceschini	Roberto	Rome 3 University	Italy
Furlan	Elisabetta	ETH Zurich	Switzerland
Grazzini	Massimiliano	University of Zurich	Switzerland
Iorio	Alberto Orso Maria	Università degli Studi di Napoli Federico II	Italy
Kats	Yevgeny	CERN	Switzerland
Keshavarzi	Alex	University of Liverpool	United Kingdom
Leonardi	Roberto	INFN	Italy
Monni	Pier	CERN	Switzerland
Moretti	Stefano	University of Southampton	UK
Narain	Meenakshi	Brown university	USA
Nason	Paolo	INFN, sez. di MIlano Bicocca	Italy
Paakkinen	Petja	University of Jyväskylä	Finland
Pancheri	Giulia	INFN Frascati	Italy
Panella	Orlando	INFN	ITALY
Passera	Massimo	INFN Padova	Italy
Pomarol	Alex	Universitat Autonoma de Barcelona	(Barcelona)
Redi	Michele	INFN	Italy
Rinaldi	Enrico	RIKEN BNL Research Center	United States
Rizzi	Andrea	Università di Pisa	italy
Roland	Gunther	MIT	USA
Sborlini	German	Università degli Studi di Milano	Italy
Simon	Frank	Max-Planck-Insitute for Physics	Germany
Somogyi	Gabor	University of Debrecen	Hungary
Tenchini	Roberto	INFN Sezione di Pisa	Italy
Tramontano	Francesco	University of Naples Federico II	Italy
Uwer	Peter	Humboldt-Universität zu Berlin	Germany
Vos	Marcel	IFIC (UVEG/CSIC)	Spain
Wiedemann	Urs Achim	CERN	Switzerland

Frascati Physics Series Vol. 65 (2017)
LFC17: Old and New Strong Interactions from LHC to Future Colliders
11 - 15 September, 2017

BEYOND THE STANDARD MODEL WITH STRONG DYNAMICS

Roberto Contino*, Andrea Mitridate, Alessandro Podo
Scuola Normale Superiore and INFN, Pisa, Italy
**Corresponding author*

Abstract

Field theoretical extensions of the Standard Model which retain its successful structural features and simplicity are analyzed and characterized. A general classification is provided, in particular, for theories with new strong dynamics where the Dark Matter candidate is an accidentally stable bound state.

1 The Standard Model paradigm

The Standard Model (SM) of particle physics is able to explain a vast amount of experimental data with remarkable precision, yet it is believed to be an effective description of a more fundamental theory. There are two main experimental facts which justify and in fact impose this attitude: the existence of Dark Matter (DM), and the impossibility to explain Baryogenesis in the context of the Standard Model. The existence of a Landau pole for hypercharge, and possibly the inclusion of gravity at the quantum level, represent, on the other hand, internal obstructions to consider the SM as a complete theory valid at all scales. Finally, there are hints which are also suggestive of a deeper theoretical layer, though they do not point to any internal inconsistency: *i)* the fact that SM fermions fill GUT multiplets, together with approximate gauge coupling unification; and *ii)* the observation that we seem to live in a very special point of the SM parameter space, away from which our universe would not have the rich chemistry that we observe and nuclei, including the proton, would be unstable. [1)]

The success of the SM as an Effective Field Theory by and large follows from two ingredients. First, its conservation laws and selection rules (such as baryon and lepton number conservation and approximate flavor and custodial invariance) naturally arise as the consequence of accidental symmetries emerging in the infrared, provided the cutoff scale is sufficiently high. The same indication for a large cutoff scale also comes from gauge coupling unification. Second, fermions come in complex (i.e. chiral) representations of

the gauge group, so that their masses are explained dynamically in terms of couplings. It is extremely suggestive that no fermion has been observed which could have a bare mass prior to symmetry breaking.

A known unsatisfactory feature of the SM is that the electroweak (EW) scale is not predicted but rather derived from an input parameter. Moreover, reproducing the experimentally observed value requires a delicate tuning in light of quantum corrections. Finding an explanation of the EW scale within a natural extension of the SM has driven most of the efforts of the high-energy community in the last forty years. As a matter of fact, all the theories of this kind constructed so far lack the simplicity of the SM. Although they are able –by construction– to explain naturally the weak scale, they require additional assumptions to agree with other experimental observations. It is possible, on the other hand, that naturalness is not the right principle to follow to explain the electroweak scale, and that other mechanisms (such as anthropics [2)], criticality [3)], or cosmological relaxation [4)]) are at work.

With this in mind, it is reasonable to ask if minimal extensions of the SM exist which retain its virtues and simplicity and where the stability of the Dark Matter candidate follows as the result of an accidental symmetry.[1] Taking seriously the hint of gauge couplings unification, one could also ask the new theory to explain it in terms of a grand unified phase at high energies. The prototype of such class of models is one where the SM is extended by new gauge dynamics and new fermion fields in complex representations ("dark" sector).[2] In the following we will focus on the case in which the dark gauge group (or part of it) gets strong in the infrared and confines, so that the DM candidate arises as a bound state. Although it is conceivable that the new fermions couple to the SM sector only through gravitational interactions, here we will consider the possibility that they are charged under the SM gauge group. This choice in general implies easier experimental signatures from the dark sector, but can lead at the same time to strong constraints from electroweak precision tests if the dark dynamics breaks spontaneously the SM gauge symmetry. It is thus interesting to investigate under which conditions the new dynamics preserves the SM gauge group.

2 New dynamics and new symmetries

The new dark dynamics can be broadly characterized depending on whether it generates dynamically its mass scales and whether it preserves the SM gauge symmetry.

Consider a theory defined in terms of a set of left-handed Weyl fermions Ψ transforming under the gauge group G as the direct sum of irreducible, finite-dimensional, unitary representations, $\Psi = \oplus_k \psi^{(r_k)}$. It follows:

Theorem 1 (mass term):

[1] Stability of the DM as a consequence of an accidental symmetry was considered by many authors and appeared, for example, in the early work on technibaryon dark matter of Ref. [5)]. It was recently emphasized and its consequences were thoroughly spelled out in Ref. [6)].

[2] Additional fundamental scalars are also an option but one should make sure that they do not reintroduce hierarchy problems which cannot be addressed by the same mechanisms at work for the Higgs field. One could also envisage even more economical scenarios with only new dynamics or only new matter. In the case with only new dynamics where the DM candidate is a dark glueball, the relic density can be correctly reproduced if the dark and SM sectors are decoupled throughout their thermal histories [7, 8)]. The case with only new matter is realized by theories of Minimal Dark Matter [9)]. The new matter must come in real or pseudo-real representations of the SM gauge group and have a sufficiently large bare mass. Such DM scale is not determined dynamically by the theory, but it could be so by extending the latter to a more fundamental description at high energy where matter fields fill complex representations.

A mass term $\psi^{(r_j)}\psi^{(r_i)}$ is allowed in the Lagrangian if:

(A) $r_j \sim \bar{r}_i$

and (only for $r_i = r_j$)

(B) *$\psi^{(r_j)}\psi^{(r_i)}$ is overall symmetric in gauge and flavor space.*

Condition *(A)* requires that r_j be unitary equivalent to the conjugate representation $\bar{r}_i$, i.e. that there exists a unitary matrix S such that:

$$S^{-1}U(r_j)S = U^*(r_i)\,, \qquad SS^\dagger = 1\,. \tag{1}$$

In order for this to hold, of course, r_i and r_j must have the same dimension. It is a simple result of group theory that the product $r_i \times r_j$ contains a singlet of G, as required in order to write a mass term, if and only if *(A)* is verified. It is also easy to show that, for irreducible r_i and r_j, the matrix S is unique up to an overall phase [10].

For $r_i = r_j$, condition *(B)* ensures that a bilinear $\psi^{(r_j)}\psi^{(r_i)}$ singlet under the Lorentz group is overall antisymmetric under the exchange of the two fermion fields, as required for a mass term. In this case it follows that $SS^t = \pm 1$ and one distinguishes between two possibilities: [10]

for $S = S^t$	r_i is called real-positive, or real. There exists a unitary transformation R which makes the generators of $U(r_i)$ purely imaginary and antisymmetric, with $RR^t = S$;
for $S = -S^t$	r_i is called real-negative, or pseudo-real.

A second useful result which holds true is the following:

Theorem 2 (condensate):
A scalar condensate $\langle\psi^{(r_j)}\psi^{(r_i)}\rangle$ can be a singlet of the gauge symmetry group, and can thus preserve it, only if conditions (A) and (B) are satisfied.

Energy considerations suggest that if a scalar fermion condensate is allowed which is a singlet of the confining gauge group G_{strong}, it will dominate over other possible condensates and align the vacuum along a G_{strong}-preserving direction [11]. The fate of the remaining gauge symmetry, G_{weak}, in this case depends on whether $\langle\psi\psi\rangle$ can be a singlet of the whole group $G = G_{strong} \times G_{weak}$. If conditions *(A)* or *(B)* are not satisfied, then G_{weak} is necessarily broken by the condensate, as a consequence of Theorem 2. Identifing G_{strong} with the whole dark dynamics and G_{weak} with the SM gauge group, G_{SM}, implies that the dark dynamics breaks spontaneously the SM gauge symmetry. One thus obtains a Technicolor (TC) theory. In original constructions of this kind [12] there exists no elementary Higgs field and the strong dynamics is entirely responsible for the EW symmetry breaking. Variants of the TC idea have also been proposed where instead the strong (dark) dynamics induces a vev for an elementary Higgs field besides contributing to the EW scale (see for example 'Bosonic Technicolor' [13] and 'Superconformal Technicolor' [14]). It is worth mentioning that while in all the above theories it is condition *(A)* which is violated, i.e. the fermion representations are complex, it is possible to construct models where Theorem 2 fails because *(B)* does not hold. Consider for example a theory with gauge group $G = SU(N_{DC}) \times SU(2)_L$, with $N_{DC} \geq 3$, and a single Weyl fermion field ψ transforming as $(adj, 4)$ of G. We assume that the dark

color group $SU(N_{DC})$ confines at a scale Λ above the EW scale, and ask whether the SM electroweak group $SU(2)_L$ is spontaneously broken by the condensate $\langle\psi\psi\rangle$. In this case ψ is a pseudo-real representation r of G, since it is possible to find a unitary transformation $S = -S^t$ so that $r \sim \bar{r}$. Consequently, $\psi\psi$ can be a singlet of G, but this turns out to be antisymmetric under the exchange of the two fermions fields. Hence condition *(B)* is violated and the dark-color preserving condensate breaks $SU(2)_L$. Notice that this theory is free of global anomalies [15].[3] In general, it is possible to show that for a pseudo-real ψ, the singlet $\psi\psi$ is always antisymmetric in the corresponding gauge indices (conversely, $\psi\psi$ is always symmetric for ψ real). Technicolor theories can thus be constructed with pseudo-real representations provided there is no global symmetry group.

The above discussion suggests that if one wants to build a model where no bare masses are allowed and where the condensate does not break the SM gauge group, there are two possible routes. The first is to consider fermion representations which are real (or pseudo-real) under G_{SM} but violate *(A)* because they are complex under G_{strong}. In this case, however, a scalar fermion condensate cannot be a singlet of G_{strong} and it is common belief that the strong dynamics is spontaneously broken, i.e. Higgsed, in the infrared (IR). Arguments based on the Most Attractive Channel criterion, for example, suggest that the theory may tumble to another one with smaller gauge group [16], and that this process continues until one of the following situations is realized: the gauge symmetry is completely Higgsed; the theory confines; the theory flows to an Abelian phase. While the above behavior is plausible, there is currently no rigorous way to define strongly-coupled chiral theories (i.e. theories with complex representations under the strong group) in a non-perturbative way and thus determine their IR phase. Progress in our understanding of quantum field theory is thus needed before one can construct sensible phenomenological models of this kind. The second route to forbid bare masses consists in taking G_{weak} larger than the SM group and let the new fermions transform as real (or pseudo-real) representations under G_{SM} and G_{strong}, but as complex representations under G_{weak}. In this case the fermion condensate aligns along a G_{strong}-preserving direction and breaks G_{weak}. Whether it breaks G_{SM} or just the remaining part of G_{weak} is a dynamical issue, i.e. depends on the vacuum alignment. If one considers the strong dynamics in isolation, there is a degenerate surface of differently oriented vacua. The degeneracy is lifted when interactions weaker than G_{strong}, in particular those of G_{weak}, are included.

As an example, consider a theory [17] defined in terms of left-handed Weyl fermions charged under a dark $SU(N_{DC}) \times U(1)_{DC}$, with $N_{DC} \geq 3$, and the SM electroweak $SU(2)_L$ as follows:

	$SU(N_{DC})$	$U(1)_{DC}$	$SU(2)_L$
ψ_1	$\square$	1	$\square$
ψ_2	$\square$	-1	$\square$
$\bar{\psi}_1$	$\bar{\square}$	$-a$	$\bar{\square}$
$\bar{\psi}_2$	$\bar{\square}$	a	$\bar{\square}$

The charge a is an arbitrary number between 1 and -1. This is a simple extension of the chiral model proposed in [18] where the new fermions are charged under the SM group. Overall the fermion representations are complex, but they are vector-like with respect to $SU(N_{DC})$ and $SU(2)_L$. We will assume that the subgroup $SU(N_{DC})$ gets strong above the EW scale and confines. The pattern of dynamical symmetry breaking is then determined by the Vafa-Witten theorem [19], similarly to the QCD case: The $SU(4) \times SU(4)$ global symmetry acting on the ψ_i and $\bar{\psi}_i^*$ is spontaneously broken to the diagonal $SU(4)_d$.

[3] If ψ tranformed as $(adj, 2)$ of $SU(N_{DC}) \times SU(2)_L$, i.e. as a spin 1/2 instead of spin 3/2 of $SU(2)_L$, the theory would have a global anomaly.

For $a > 0$, $SU(2)_L$ is contained in $SU(4)_d$ and is thus preserved, while $U(1)_{DC}$ is non-linearly realized. The phenomenology of this model, including aspects related to the DM composition and relic density, will be discussed elsewhere [17].

An important class of theories where the condensate instead aligns along a G_{SM}-breaking direction is that of Composite Higgs (CH) models [20, 21, 22]. In these constructions one requires that the set of Nambu-Goldstone bosons (NGBs) which arise from the global symmetry breaking induced by the strong dynamics includes an $SU(2)_L$ doublet. The latter plays the role of the composite Higgs field. Electroweak symmetry breaking thus follows dynamically from vacuum misalignment, but it can be also described conveniently as a two-step process: first, at some scale f the strong dynamics confines generating the NGBs; these then acquire a potential from weaker radiative corrections and trigger EWSB at a scale $v < f$. As an example consider the model by Dugan, Georgi and Kaplan [20] defined in terms of a gauge group $G_{strong} \times U(1)_A \times SU(2)_L \times U(1)_Y$ and five Weyl fermions transforming as

	G_{strong}	$U(1)_A$	$SU(2)_L$	$U(1)_Y$
ψ	r	$1/\sqrt{20}$	2	$1/2$
$\tilde{\psi}$	r	$1/\sqrt{20}$	2	$-1/2$
ψ_s	r	$-4/\sqrt{20}$	1	0

Here r is some real representation of G_{strong}, and the dark group includes an Abelian factor $U(1)_A$. The representations are overall complex though (pseudo-)real under G_{strong} and $SU(2)_L \times U(1)_Y$. The vacuum alignment can be determined by studying the effective potential of the composite Higgs doublet $H \sim (\psi\psi_s)$. For $5g_A^2 > 3g^2 + g'^2$ the condensate is forced to align in an $U(1)_A$-preserving direction and thus breaks $SU(2)_L \times U(1)_Y$. More in general, other CH theories have been constructed were vacuum misalignment is induced by fermion couplings, in particular interactions involving the top quark (see for example [23, 24]).

In order to get a complete classification of possibilities, it is worth analyzing also theories where the premises of Theorem 1 are fullfilled. In such case bare mass terms are allowed for the dark fermions, which thus introduce arbitrary new scales into the theory. Although constructions of this kind seem to go beyond the paradigm of minimality of the SM, they can still be relevant for our discussion if they are considered as effective theoretical layers valid up to some cutoff energy where they are embedded into a more fundamental description with complex representations. In this way, the mass scales introduced in the effective theory can be derived in terms of couplings of the UV description. Interestingly, the same situation is realized within the SM: below the EW scale the matter content forms vector-like representations of the unbroken $SU(3)_c \times U(1)_{em}$ gauge group, and quarks and leptons have a spectrum of bare masses. Above the EW scale, on the other hand, the theory has complex representations and the value of each mass is explained in terms of the corresponding Yukawa coupling.

If Theorem 1 implies the existence of bare mass terms, then from Theorem 2 it follows that the condensate can preserve the SM gauge symmetry. Whether this actually occurs or not is again a dynamical issue and depends on the vacuum alignment. The same considerations made above apply to this case as well, and one can for example construct CH models where misalignment occurs because of fermion interactions. Interesting alternative scenarios in this case are theories where vacuum misalignment originates from the mixing of the composite Higgs with an elementary one [20, 25, 26]. This is possible if Yukawa couplings are allowed between the dark fermions and the elementary Higgs. The lighter physical Higgs scalar in the spectrum is a mixture of the elementary and the composite fields and for this reason such scenario has been dubbed Partial Higgs Compositeness. See the talk by Michele Redi at this conference for more details on these theories.

Consider finally a situation in which no vacuum misalignment is generated, for example because no additional gauge interactions exist and Yukawa couplings are not allowed. In this case the dark dynamics does not play a direct role in EWSB and consequently such theories are less constrained by EW precision tests. Since bare mass terms for fermions are allowed, the scale at which new physics states first appear is arbitrary. If some of the new particles are within the reach of the LHC or future colliders, these theories can lead to interesting phenomenology and experimental signatures. For a recent study of theories with vector-like dark fermions, a scenario dubbed 'Vectorlike Confinement', see for example Ref. [27]. While the dark dynamics has no impact on EWSB, it may however play a role in explaining the observed DM abundance. If this is the case, then the value of the new physics scale can be fixed or significantly constrained. Most interesting for our discussion are the so-called scenarios of Accidental Composite Dark Matter, where the DM candidate is a composite state of the dark dynamics and its stability is a consequence of accidental symmetries. Ref. [6] performed a systematic classification of such theories focusing on $SU(N)_D$ and $SO(N)_D$ gauge groups with vector-like fermions in the fundamental representation. A robust and viable candidate of DM is given by dark baryons. For example, if the dark quarks are ligher than the confinement scale Λ, then the observed relic density is correctly reproduced for Λ of order 100 TeV. A smaller scale is instead obtained if the quark masses are heavier than Λ [28], because in this case the dark baryons are perturbative bound states and their annihilation cross section decreases. Experimental signatures of these scenarios in general come from direct detection experiments, through the relatively large electric dipole moment predicted for the dark baryons, and from the production of the lighter dark mesons at the LHC or at future colliders.

While dark baryons are a motivated possibility, other bound states of the strong dynamics can play the role of DM candidate. For example, dark mesons can be stable because of accidental species number or G-parity [6]. As a more exotic possibility, consider bound states made of one dark quark Q plus dark glue, in the case in which Q is a Weyl fermion in the adjoint of a dark $SU(N)_{DC}$. Dark Matter candidates of this kind were considered in the context of SUSY theories and dubbed 'glueballinos', as they are the partners of the glueballs [7]. Here we want to briefly discuss the case in which dark quarks have non-trivial quantum numbers also under the SM electroweak group, and will denote the corresponding bound state as the 'gluequark' [29]. The accidental symmetry which makes gluequarks stable is a Z_2 parity under which Q is odd. The spectrum thus divides into even states (glueballs, QQ mesons, etc.) and odd states (gluequarks, QQQ fermions, etc). Requiring to have an EM neutral gluequark in the spectrum, to play the role of DM, and restricting to real or vector-like representations under the SM selects a few viable quantum number assignments. The most minimal non-trivial model consists of three Weyl fermions in the adjoint of $SU(N)_{DC}$ transforming as a triplet of $SU(2)_L$ with zero hypercharge. The lowest-dimensional operator violating the accidental Z_2 in this case is $H\sigma^i\ell\sigma^{\mu\nu}Q^iG_{\mu\nu}$, with dimension 6. The spectrum includes a gluequark V^i triplet of $SU(2)_L$, whose neutral component V^0 is the DM candidate. The thermal history of the universe and the phenomenology at low energies have some distinctive features compared to models with baryonic DM. For example, gluequark DM is expected to have very small electric dipole moment, since its constituents are electrically neutral. This makes it elusive at direct detection experiments. Furthermore, in the limit of large quark masses, the gluequark is a heavy but sizable bound state: its mass is of order M_Q while its size is $\sim 1/\Lambda >> 1/M_Q$. This is to be constrasted with dark baryons, which are small –hence perturbative– bound states of radius $\sim 1/M_Q$. Non-perturbative annihilation processes have thus a much larger cross section in the case of the gluequark and can boost the value of M_Q which reproduces the DM relic density. A detailed analysis of the thermal history of the universe in this model will be presented in a forthcoming publication [29]. In general, models with

gluequark DM tend to reproduce the observed relic density for larger bound state masses, and are more difficult to be discovered. In particular, in the $M_Q > \Lambda$ limit detection may come from indirect DM searches or even gravity wave signals produced during a first-order dark phase transition, rather than from collider signatures. For $M_Q < \Lambda$ the relic density is reproduced for $\Lambda \sim 50\,\text{TeV}$ and discovery may come first from the production of dark mesons at colliders, similarly to the case of baryonic DM with light quarks.

3 Acknowledgements

We are glad to acknowledge Michele Redi for collaboration on some of the topics discussed in this contribution and for many useful discussions.

References

1. For a review, see for example: J. F. Donoghue, Ann. Rev. Nucl. Part. Sci. **66** (2016) 1 [arXiv:1601.05136 [hep-ph]].
2. J. D. Barrow and F. J. Tipler, "The Anthropic Cosmological Principle", Oxford Univ. Press (1988).
3. G. F. Giudice, In *Kane, Gordon (ed.), Pierce, Aaron (ed.): Perspectives on LHC physics* 155-178 [arXiv:0801.2562 [hep-ph]].
4. P. W. Graham, D. E. Kaplan and S. Rajendran, Phys. Rev. Lett. **115** (2015) no.22, 221801 [arXiv:1504.07551 [hep-ph]].
5. S. M. Barr, R. S. Chivukula and E. Farhi, Phys. Lett. B **241** (1990) 387.
6. O. Antipin, M. Redi, A. Strumia and E. Vigiani, JHEP **1507** (2015) 039 [arXiv:1503.08749 [hep-ph]].
7. K. K. Boddy, J. L. Feng, M. Kaplinghat and T. M. P. Tait, Phys. Rev. D **89** (2014) no.11, 115017 [arXiv:1402.3629 [hep-ph]].
8. L. Forestell, D. E. Morrissey and K. Sigurdson, Phys. Rev. D **95** (2017) no.1, 015032 [arXiv:1605.08048 [hep-ph]].
9. M. Cirelli, N. Fornengo and A. Strumia, Nucl. Phys. B **753** (2006) 178 [hep-ph/0512090].
10. See for example: H. Georgi, "Lie algebras in particle physics," Front. Phys. **54** (1999) 1.
11. M. E. Peskin, Lectures presented at the 1982 Les Houches Summer School, SLAC-PUB-3021.
12. S. Weinberg, Phys. Rev. D **13** (1976) 974 Addendum: [Phys. Rev. D **19** (1979) 1277]. L. Susskind, Phys. Rev. D **20** (1979) 2619.
13. S. Samuel, Nucl. Phys. B **347** (1990) 625. M. Dine, A. Kagan and S. Samuel, Phys. Lett. B **243** (1990) 250.
14. A. Azatov, J. Galloway and M. A. Luty, Phys. Rev. Lett. **108** (2012) 041802 [arXiv:1106.3346 [hep-ph]].
15. E. Witten, Phys. Lett. **117B** (1982) 324.

16. S. Raby, S. Dimopoulos and L. Susskind, Nucl. Phys. B **169** (1980) 373.

17. R. Contino, A. Podo and F. Revello, work in progress.

18. K. Harigaya and Y. Nomura, Phys. Rev. D **94** (2016) no.3, 035013 [arXiv:1603.03430 [hep-ph]]; R. T. Co, K. Harigaya and Y. Nomura, Phys. Rev. Lett. **118** (2017) no.10, 101801 [arXiv:1610.03848 [hep-ph]].

19. C. Vafa and E. Witten, Nucl. Phys. B **234** (1984) 173.

20. D. B. Kaplan and H. Georgi, Phys. Lett. **136B** (1984) 183.

21. D. B. Kaplan, H. Georgi and S. Dimopoulos, Phys. Lett. **136B** (1984) 187. doi:10.1016/0370-2693(84)91178-X

22. M. J. Dugan, H. Georgi and D. B. Kaplan, Nucl. Phys. B **254** (1985) 299.

23. K. Agashe, R. Contino and A. Pomarol, Nucl. Phys. B **719** (2005) 165 [hep-ph/0412089].

24. J. Galloway, J. A. Evans, M. A. Luty and R. A. Tacchi, JHEP **1010** (2010) 086 [arXiv:1001.1361 [hep-ph]].

25. O. Antipin and M. Redi, JHEP **1512** (2015) 031 [arXiv:1508.01112 [hep-ph]]; A. Agugliaro, O. Antipin, D. Becciolini, S. De Curtis and M. Redi, Phys. Rev. D **95** (2017) no.3, 035019 [arXiv:1609.07122 [hep-ph]].

26. J. Galloway, A. L. Kagan and A. Martin, Phys. Rev. D **95** (2017) no.3, 035038 [arXiv:1609.05883 [hep-ph]].

27. C. Kilic, T. Okui and R. Sundrum, JHEP **1002** (2010) 018 [arXiv:0906.0577 [hep-ph]].

28. A. Mitridate, M. Redi, J. Smirnov and A. Strumia, JHEP **1710** (2017) 210 [arXiv:1707.05380 [hep-ph]].

29. R. Contino, A. Mitridate, A. Podo, M. Redi, work in progress.

Frascati Physics Series Vol. 65 (2017)
LFC17: Old and New Strong Interactions from LHC to Future Colliders
11 - 15 September, 2017

JET CROSS SECTIONS IN NNLO QCD IN LEPTON AND HADRON COLLISIONS

Gábor Somogyi
MTA-DE Particle Physics Research Group, 4010 Debrecen, PO Box 105, Hungary

Abstract

We present an overview of the main conceptual issues which arise when computing next-to-next-to-leading order perturbative corrections to jet cross sections in QCD. In particular we focus on the issue of infrared singularities that arise in intermediate steps of the calculation and outline the various methods which have been proposed to treat these divergences. We then give a brief overview of the state of the art of the field, concentrating on computations which deal strictly with the production of jets without additional electroweak or Higgs particles.

1 Introduction

The study of the production of hadronic jets in particle collisions played a crucial role in establishing QCD as the correct theory of strong interactions. Today, jet related studies continue to be important for improving our understanding of QCD. Indeed, jet rates and event shapes measured in three jet production in electron-positron annihilation are still among some of the most precise tools used for the extraction of the main parameter of the theory, the strong coupling $\alpha_{\rm s}$. Jet production at hadron colliders such the Tevatron and LHC can provide valuable information on the non-perturbative Parton Distribution Functions (PDF). Although the quark PDFs are significantly constrained by data from lepton-hadron Deep Inelastic Scattering (DIS) experiments such as HERA, the electrical neutrality of the gluon means that in DIS the gluon PDF can only be probed through specific final states (e.g., heavy quarks or jets) or indirectly through DGLAP evolution. In contrast, jet production at a hadron collider is directly sensitive to the gluon PDF, with LHC measurements already providing important constraints, in particular in the large-x region.

In addition to their role in determining Standard Model parameters, jets have also become essential analysis tools in searches for beyond the Standard Model physics. For example, "bump hunting" in the

dijet mass spectrum or testing the QCD running coupling at very large momentum transfer constitute powerful probes of BSM physics.

However, in order to fully exploit the physics potential of the wealth of available data, we must be able to calculate precise and reliable theoretical predictions for jet observables. Since the computation of physical quantities measured at particle colliders relies on the use of perturbation theory, one particular aspect of theoretical precision concerns the evaluation of exact higher-order corrections in perturbative QCD. As the numerical value of the strong coupling is not particularly small even at LHC energies, leading order (LO) results in QCD can only give an order of magnitude estimate of production rates and rough information on the shape of distributions. Furthermore, perturbative predictions depend on the non-physical renormalisation and factorisation scales and this dependence is usually quite sizeable at LO. Hence at least next-to-leading order (NLO) corrections must be evaluated. Nevertheless, in several situations, typically when NLO corrections are large, it is desirable to go even further in the perturbative expansion and include next-to-next-to-leading order (NNLO) corrections in our predictions.

In this contribution, we describe briefly the main conceptual difficulties in computing radiative corrections at NNLO accuracy in perturbative QCD as well as some approaches which have been proposed to overcome them. Then, we give a concise summary of the results available in the literature specifically for the production of jets at lepton and hadron colliders at NNLO accuracy.

2 Jet cross sections in NNLO QCD

At a hadron collider, the cross section for a given final state can be computed using the factorisation theorem,

$$\mathrm{d}\sigma = \sum_{a,b} \int \mathrm{d}x_a \int \mathrm{d}x_b \, f_a(x_a,\mu_F^2) f_b(x_b,\mu_F^2) \mathrm{d}\hat{\sigma}_{ab}(x_a,x_b,Q^2,\alpha_\mathrm{s}(\mu_R^2)) + \mathcal{O}((\Lambda_\mathrm{QCD}/Q)^m)\,, \tag{1}$$

i.e., by convoluting the partonic cross section, $\mathrm{d}\hat{\sigma}_{ab}$ with the PDFs f_a and f_b. (In lepton collisions, the PDFs are essentially Dirac delta functions, hence the convolution is trivial.) The PDFs are non-perturbative and must be extracted from data, however the partonic cross section can be evaluated in perturbation theory and we will focus on this aspect of the computation here. Since the basic issues that arise when computing the partonic cross section at higher orders are already present for the case of lepton collisions, we will present formulae appropriate to this simpler case in the following.

When computing QCD corrections to some specific partonic cross section, two conceptually separate issues must be addressed. The first concerns the evaluation of the matrix elements relevant to the process under study. At NNLO accuracy, we must consider up to two-loop corrections to the Born matrix element, one-loop matrix elements with one extra parton emission and tree level matrix elements with up to two extra parton emissions as compared to the Born process. These days the calculation of tree level matrix elements is essentially trivial and they can be computed in a completely automated way. Due to enormous progress in the past several years, by now also the evaluation of one-loop matrix elements has essentially been automated. While it should be said that the requirements on the numerical stability of one-loop amplitudes is more stringent in an NNLO calculation than an NLO one, this issue is being addressed by the newest generation of automated one-loop computations. Finally as regards the two-loop matrix elements, we recall that these have been available for some time for all $2 \to 2$ processes at the LHC (including the production of a vector boson pair, computed more recently) as well as for the production of three partons from a colourless initial state, relevant for electron-positron colliders. There is also a huge ongoing effort to move beyond these multiplicities and compute complete two-loop amplitudes relevant

for the production of three jets at the LHC or four jets at a lepton collider. (See e.g., [1, 2] for some very recent examples.) While a great deal of progress has been made in this direction, the evaluation of two-loop amplitudes at high multiplicities currently remains a bottleneck.

Second, even if the relevant matrix elements are available, the computation of physical cross sections is not straightforward due to the presence of infrared and collinear singularities in intermediate stages of the calculation. In particular the finite NLO correction to some generic m-jet observable J is the sum of two terms, the real emission and virtual ones (J_n denotes the value of the observable J evaluated on an n-parton final state),

$$\sigma^{\mathrm{NLO}} = \sigma^{\mathrm{R}}_{m+1} + \sigma^{\mathrm{V}}_{m} = \int_{m+1} \mathrm{d}\sigma^{\mathrm{R}}_{m+1} J_{m+1} + \int_{m} \mathrm{d}\sigma^{\mathrm{V}}_{m} J_{m} \,. \tag{2}$$

Both terms appearing above are separately divergent in $d = 4$ spacetime dimensions due to the presence of explicit ϵ poles from loop integrals (we use dimensional regularisation in $d = 4 - 2\epsilon$ dimensions) or phase space singularities associated with the emission of an unresolved parton. At NNLO accuracy we find that the complete NNLO correction is composed of three terms, the double-real, real-virtual and double-virtual ones,

$$\sigma^{\mathrm{NNLO}} = \sigma^{\mathrm{RR}}_{m+2} + \sigma^{\mathrm{RV}}_{m+1} + \sigma^{\mathrm{VV}}_{m} = \int_{m+2} \mathrm{d}\sigma^{\mathrm{RR}}_{m+2} J_{m+2} + \int_{m+1} \mathrm{d}\sigma^{\mathrm{RV}}_{m+1} J_{m+1} + \int_{m} \mathrm{d}\sigma^{\mathrm{VV}}_{m} J_{m} \,. \tag{3}$$

Again, the three pieces appearing above are all separately divergent in $d = 4$ dimensions due to the presence of explicit ϵ poles and/or phase space singularities which emerge in kinematic limits when one or two partons become unresolved. Although these divergences cancel for sufficiently inclusive (infrared and collinear safe) observables in the sum, in order to perform a numerical computation, this cancellation must be made explicit.

In broad terms, there have been two approaches to dealing with infrared and collinear singularities at NNLO: phase space slicing and the subtraction method. The slicing method relies on regularising the real emission phase space singularities with an explicit cut-off. With this cut-off in place, the real emission contribution is finite and can thus be computed numerically. On the other hand, the combination of the virtual contribution with the piece of the real contribution which has been discarded by the cut can be obtained from an appropriate resummation framework. This combination is also finite and can again be computed numerically. This procedure then regularises both real emission and virtual pieces, however an explicit cut-off parameter, δ, is introduced into the calculation. Since the rearrangement of terms in the slicing method is only exact for $\delta \to 0$, one must be careful to check that the results are independent (within numerical uncertainties) of the value of δ chosen. This can be challenging, since using a smaller value of δ generates a larger numerical cancellation between the regularised real and virtual contributions.

In practice, two types of such slicing methods have been employed to compute physical observables at NNLO accuracy, q_{T} slicing [3] and N-jettiness slicing [4, 5]. These methods use either the transverse momentum of the produced system, q_{T}, or the N-jettiness variable, τ_N, to disentangle "pure" NNLO regions in phase space, which are treated as explained above, while NLO type singularities are handled with some NLO subtraction method (see below).

On the other hand, the subtraction method makes use of approximate cross sections in order to perform an exact rearrangement of singular terms between the real and virtual contributions. At NLO accuracy one such approximate cross section is sufficient

$$\sigma^{\mathrm{NLO}} = \int_{m+1} \mathrm{d}\sigma^{\mathrm{R}}_{m+1} J_{m+1} + \int_{m} \mathrm{d}\sigma^{\mathrm{V}}_{m} J_{m} = \int_{m+1} \left[\mathrm{d}\sigma^{\mathrm{R}}_{m+1} J_{m+1} - \mathrm{d}\sigma^{\mathrm{R,A}_1}_{m+1} J_{m} \right]_{d=4} + \int_{m} \left[\mathrm{d}\sigma^{\mathrm{V}}_{m} J_{m} + \int_{1} \mathrm{d}\sigma^{\mathrm{R,A}_1}_{m+1} J_{m} \right]_{d=4} . \tag{4}$$

The approximate cross section $\mathrm{d}\sigma_{m+1}^{\mathrm{R,A_1}}$ is constructed such that it has the same kinematic singularity structure (in d dimensions) as $\mathrm{d}\sigma_{m+1}^{\mathrm{R}}$ itself, hence the difference is free of non-integrable kinematic singularities and can be computed numerically with standard Monte Carlo methods. The poles of the virtual contribution, $\mathrm{d}\sigma_m^{\mathrm{V}}$, are then exactly cancelled by adding back the approximate cross section after integrating over the momentum and summing over the quantum numbers (colour, flavour) of the unresolved particle (these operations are all denoted by $\int_1$). Several explicit constructions are available in the literature for the approximate cross section $\mathrm{d}\sigma_{m+1}^{\mathrm{R,A_1}}$ [6].

At NNLO accuracy this rearrangement is more involved due to the more elaborate structure of singularities. Since the double-real contribution has both single and double unresolved kinematic singularities, we write

$$\sigma_{m+2}^{\mathrm{NNLO}} = \int_{m+2} \left\{ \mathrm{d}\sigma_{m+2}^{\mathrm{RR}} J_{m+2} - \mathrm{d}\sigma_{m+2}^{\mathrm{RR,A_2}} J_m - \left[\mathrm{d}\sigma_{m+2}^{\mathrm{RR,A_1}} J_{m+1} - \mathrm{d}\sigma_{m+2}^{\mathrm{RR,A_{12}}} J_m \right] \right\}_{d=4}, \tag{5}$$

where $\mathrm{d}\sigma_{m+2}^{\mathrm{RR,A_2}}$ regularises double unresolved singularities, while $\mathrm{d}\sigma_{m+2}^{\mathrm{RR,A_1}}$ serves as a counterterm in single unresolved limits. The last term, $\mathrm{d}\sigma_{m+2}^{\mathrm{RR,A_{12}}}$, is introduced to remove both the single unresolved singularities of $\mathrm{d}\sigma_{m+2}^{\mathrm{RR,A_2}}$, as well as the double unresolved ones of $\mathrm{d}\sigma_{m+2}^{\mathrm{RR,A_1}}$. Then, Eq. (5) is free of non-integrable singularities and can be computed with standard numerical methods.

The real-virtual contribution has both explicit ϵ-poles from one-loop amplitudes, as well as kinematic singularities associated with the emission of one extra parton as compared to the Born process. Thus we write

$$\sigma_{m+1}^{\mathrm{NNLO}} = \int_{m+1} \left\{ \left[\mathrm{d}\sigma_{m+1}^{\mathrm{RV}} + \int_1 \mathrm{d}\sigma_{m+2}^{\mathrm{RR,A_1}} \right] J_{m+1} - \left[\mathrm{d}\sigma_{m+1}^{\mathrm{RV,A_1}} + \left(\int_1 \mathrm{d}\sigma_{m+2}^{\mathrm{RR,A_1}} \right)^{\mathrm{A_1}} \right] J_m \right\}_{d=4}. \tag{6}$$

The integrated form of the single unresolved subtraction from the double-real contribution, $\int_1 \mathrm{d}\sigma_{m+2}^{\mathrm{RR,A_1}}$, precisely cancels the ϵ-poles of $\mathrm{d}\sigma_{m+1}^{\mathrm{RV}}$, however both terms are still singular in regions of phase space where one parton becomes unresolved. The task of the last two terms, $\mathrm{d}\sigma_{m+1}^{\mathrm{RV,A_1}}$ and $\left(\int_1 \mathrm{d}\sigma_{m+2}^{\mathrm{RR,A_1}} \right)^{\mathrm{A_1}}$ is precisely the regularisation of these kinematic singularities. Hence, Eq. (6) is free of both ϵ-poles and non-integrable singularities and may be evaluated numerically.

Finally, the ϵ-poles of the double-virtual contribution are exactly cancelled by the sum of integrated counterterms which we have not yet added back,

$$\sigma_m^{\mathrm{NNLO}} = \int_m \left\{ \mathrm{d}\sigma_m^{\mathrm{VV}} + \int_2 \left[\mathrm{d}\sigma_{m+2}^{\mathrm{RR,A_2}} - \mathrm{d}\sigma_{m+2}^{\mathrm{RR,A_{12}}} \right] + \int_1 \left[\mathrm{d}\sigma_{m+1}^{\mathrm{RV,A_1}} + \left(\int_1 \mathrm{d}\sigma_{m+2}^{\mathrm{RR,A_1}} \right)^{\mathrm{A_1}} \right] \right\}_{d=4} J_m, \tag{7}$$

hence Eq. (7) is finite as guaranteed by the Kinoshita–Lee–Nauenber theorem and one can compute it numerically.

The construction of the approximate cross sections is not unique and indeed, several approaches exist in the literature for defining them such as iterated sector decomposition [7], antenna subtraction [8], sector improved residue subtraction [9], nested soft-collinear subtractions [10], the projection to Born technique [11] and the CoLoRFulNNLO scheme [12, 13, 14, 15].

3 Jet production at lepton colliders

As mentioned in the Introduction, the analysis of hadronic event shapes and jet rates at lepton colliders still provides one of the most precise ways to determine the value of the strong coupling α_s. Accordingly, these observables have been extensively measured in the past. In addition, the study of jet production in

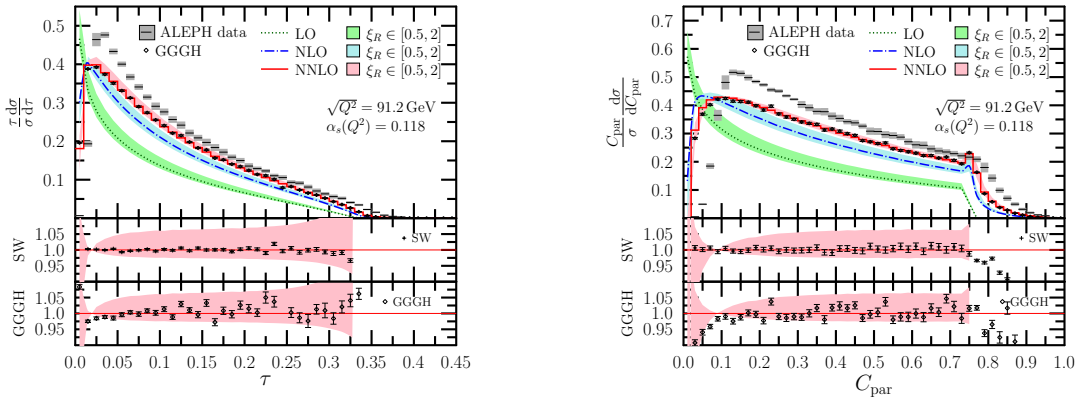

Figure 1: *Physical predictions for thrust ($\tau = 1 - T$) (left) and C-parameter (right) at LO, NLO and NNLO accuracy. The bands represent scale uncertainty. Data measured by the ALEPH collaboration is also shown. The lower panels show the ratio of predictions of* [19] *(SW) and* `EERAD3` [20] *(GGGH) to CoLorFulNNLO.*

lepton collisions also serves as an ideal testing ground for developing tools and techniques fo higher-order calculations in QCD.

Currently, the state of the art includes NLO predictions for the production of up to five jets [16] (up to seven jets [17] in the leading colour approximation) and NNLO predictions for the production of three jets [14, 15, 18, 19]. In particular, the six standard event shapes measured in three jet production in electron-positron annihilation (thrust, heavy jet mass, total and wide jet broadening, C-parameter and the two-to-three jet transition variable y_{23} in the Durham jet clustering algorithm) have been computed at NNLO accuracy using both the antenna subtraction method [18, 19] and the CoLoRFulNNLO subtraction scheme [15]. By way of illustration, we present in Fig. 1 physical predictions for the distributions of thrust (T) and C-parameter up to NNLO accuracy at the LEP2 energy of $\sqrt{s} = 91.2$ GeV, computed in the CoLoRFulNNLO framework. The figures also show the comparison of these results to the predictions obtained with `EERAD3` [20] (denoted as GGGH[1]) as well with those of reference [19] (denoted as SW[2]), both obtained with the antenna subtraction method. We observe a quite good agreement between the predictions of SW and CoLorFulNNLO and a reasonably good agreement between GGGH and CoLorFulNNLO. We note also the very good numerical convergence of the CoLorFulNNLO method at NNLO.

Predictions for jet rates and event shapes computed at NNLO accuracy and supplemented with resummation, have been used to extract the strong coupling α_s from data (see [21] for a review).

4 Jet production at hadron colliders

The computation of jet production at the LHC at NNLO accuracy, also in association with an electroweak or Higgs boson, is also of significant interest as discussed in the Introduction. Here we limit ourselves

[1] We are grateful to G. Heinrich for providing the predictions of `EERAD3` for us.

[2] In these comparisons we use updated (with respect to those published in [19]) but unpublished predictions provided to us by S. Weinzierl. We are grateful to S. Weinzierl for providing these updated results for us.

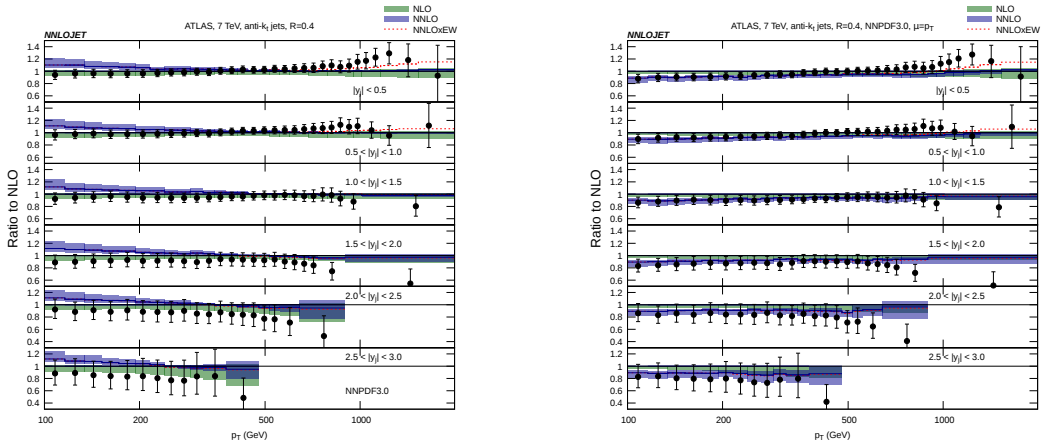

Figure 2: *Double-differential inclusive jet cross sections as a function of jet p_{T} in slices of rapidity form* [23] *(left) and* [24] *(right). The central scales are set to the transverse momentum of the leading jet, p_{T_1} (left) or the individual jet p_{T} (right). The bands represent scale uncertainty.*

to discussing only those results which pertain strictly to the production of jets, without additional electroweak or Higgs particles. In this regard, the state of the art computations include NLO predictions for up to five jets in hadronic collisions [22], as well as the very recent NNLO predictions for single jet inclusive production [23, 24] and dijet production [25]. The NNLO computations have so far been obtained in the leading colour approximation, however they do include all partonic subprocesses. In each case, they have been computed within the antenna subtraction framework.

As an illustration, we present in Fig. 2 double-differential results for the jet p_{T} in rapidity bins in single inclusive jet production at the 7 TeV LHC from references [23] and [24], together with data measured by the ATLAS collaboration. The jets in these computations are defined using the anti-k_{t} algorithm with a radius of $R = 0.4$. The left and right panels present predictions with two different choices of renormalisation and factorisation scales. On the left, the scales are set to the transverse momentum of the leading jet, p_{T_1}, while on the right, they are set equal to the individual jet p_{T}. The bands represent the effects of varying $\mu = \mu_R = \mu_F$ by factors of 0.5 and 2 around the central value. We observe that overall the NNLO corrections are moderate and the two different scale choices are equivalent at large transverse momentum. However, at low transverse momentum, differences between the predictions emerge that are outside the scale band. Evidently the calculation based on the individual jet p_{T} provides a better description of data, however the fact that the two predictions deviate in excess of the scale band implies that further studies of scale setting are required.

We note that the first qualitative comparisons of these NNLO predictions with LHC data have already appeared in the literature [26].

5 Conclusions

In this contribution we discussed the state of the art with regards to computing QCD radiative corrections to jet cross sections in lepton and hadron collisions. These days, it is possible to compute these corrections at NNLO accuracy in QCD perturbation theory for the production of up to three jets in electron-positron annihilation and up to two jets in hadron collisions. After discussing the main conceptual issues that

must be addressed when going to NNLO, we gave brief illustrative examples of results obtained for event shape variables measured at LEP2 as well as for single inclusive jet production at the LHC.

6 Acknowledgements

The author is grateful to A. Kardos for useful discussions. This work was supported by grant K 125105 of the National Research, Development and Innovation Office in Hungary.

References

1. S. Badger, C. Brønnum-Hansen, H. B. Hartanto and T. Peraro, arXiv:1712.02229 [hep-ph].
2. D. Chicherin, J. Henn and V. Mitev, arXiv:1712.09610 [hep-th].
3. S. Catani and M. Grazzini, Phys. Rev. Lett. **98**, 222002 (2007)
4. J. Gaunt, M. Stahlhofen, F. J. Tackmann and J. R. Walsh, JHEP **1509**, 058 (2015)
5. R. Boughezal, C. Focke, X. Liu and F. Petriello, Phys. Rev. Lett. **115**, no. 6, 062002 (2015)
6. S. Frixione, Z. Kunszt and A. Signer, Nucl. Phys. B **467**, 399 (1996), S. Catani and M. H. Seymour, Nucl. Phys. B **485**, 291 (1997) Erratum: [Nucl. Phys. B **510**, 503 (1998)], G. Somogyi, JHEP **0905**, 016 (2009), C. H. Chung and T. Robens, Phys. Rev. D **87**, 074032 (2013)
7. T. Binoth and G. Heinrich, Nucl. Phys. B **585**, 741 (2000)
8. A. Gehrmann-De Ridder, T. Gehrmann and E. W. N. Glover, JHEP **0509**, 056 (2005)
9. M. Czakon, Phys. Lett. B **693**, 259 (2010)
10. F. Caola, K. Melnikov and R. Rntsch, Eur. Phys. J. C **77**, no. 4, 248 (2017)
11. M. Cacciari, F. A. Dreyer, A. Karlberg, G. P. Salam and G. Zanderighi, Phys. Rev. Lett. **115**, no. 8, 082002 (2015)
12. G. Somogyi, Z. Trócsányi and V. Del Duca, JHEP **0701**, 070 (2007)
13. G. Somogyi and Z. Trócsányi, JHEP **0701**, 052 (2007)
14. V. Del Duca, C. Duhr, A. Kardos, G. Somogyi and Z. Trcsnyi, Phys. Rev. Lett. **117**, no. 15, 152004 (2016)
15. V. Del Duca, C. Duhr, A. Kardos, G. Somogyi, Z. Szőr, Z. Trócsányi and Z. Tulipánt, Phys. Rev. D **94**, no. 7, 074019 (2016)
16. R. Frederix, S. Frixione, K. Melnikov and G. Zanderighi, JHEP **1011**, 050 (2010)
17. S. Becker, D. Goetz, C. Reuschle, C. Schwan and S. Weinzierl, Phys. Rev. Lett. **108**, 032005 (2012)
18. A. Gehrmann-De Ridder, T. Gehrmann, E. W. N. Glover and G. Heinrich, JHEP **0712**, 094 (2007)
19. S. Weinzierl, JHEP **0906**, 041 (2009)

20. A. Gehrmann-De Ridder, T. Gehrmann, E. W. N. Glover and G. Heinrich, Comput. Phys. Commun. **185**, 3331 (2014)

21. C. Patrignani *et al.* [Particle Data Group], Chin. Phys. C **40**, no. 10, 100001 (2016).

22. Z. Bern *et al.*, Phys. Rev. Lett. **109**, 042001 (2012), S. Badger, B. Biedermann, P. Uwer and V. Yundin, Phys. Lett. B **718**, 965 (2013), S. Badger, B. Biedermann, P. Uwer and V. Yundin, Phys. Rev. D **89**, no. 3, 034019 (2014)

23. J. Currie, E. W. N. Glover and J. Pires, Phys. Rev. Lett. **118**, no. 7, 072002 (2017)

24. J. Currie, E. W. N. Glover, T. Gehrmann, A. Gehrmann-De Ridder, A. Huss and J. Pires, Acta Phys. Polon. B **48**, 955 (2017)

25. J. Currie, A. Gehrmann-De Ridder, T. Gehrmann, E. W. N. Glover, A. Huss and J. Pires, Phys. Rev. Lett. **119**, no. 15, 152001 (2017)

26. M. Aaboud *et al.* [ATLAS Collaboration], arXiv:1711.02692 [hep-ex].

Frascati Physics Series Vol. 65 (2017)
LFC17: Old and New Strong Interactions from LHC to Future Colliders
11 - 15 September, 2017

NEW TECHNIQUES FOR HIGHER-ORDER CALCULATIONS IN LEPTON AND HADRON COLLISIONS

Germán F. R. Sborlini,
Dipartimento di Fisica, Università di Milano and INFN Sezione di Milano, I-20133 Milan, Italy.

Félix Driencourt-Mangin and Germán Rodrigo
Instituto de Física Corpuscular, UVEG – CSIC, Parc Científic, E-46980 Paterna, Valencia, Spain.

Abstract

In this talk, we describe a novel framework to perform perturbative computations. The four-dimensional unsubtraction (FDU) approach, based on the loop-tree duality (LTD) theorem, aims for an efficient numerical implementation through a fully local cancellation of both infrared and ultraviolet singularities. Due to the application of LTD, the virtual amplitudes are written in terms of phase-space integrals that closely resembles the real-emission contributions. Then, a suitable momentum mapping is introduced to express the real corrections using the same integration variables appearing in the dual contributions. In this way, the mapped real terms and the dual contributions are combined at integrand level, leading to a smooth cancellation of singularities. We provide some physical examples at next-to-leading order and briefly discuss possible extensions to deal with next-to-next-to-leading order calculations.

1 Introduction

The presence of ill-defined expressions in intermediate steps of quantum field theory (QFT) computations requires the introduction of regularization methods to render them convergent and unambiguously defined. In many cases, these problems arise as a consequence of physical singularities, such as infrared (IR) or ultraviolet (UV) ones. Within the community of high-energy physics, one of the most accepted methods is Dimensional Regularization (DREG). Roughly speaking, DREG assumes that the number of space-time dimensions is extended from $d = 4$ to $d = 4 - 2\epsilon$; thus, the convergence issues manifest as ϵ-poles.

On the other hand, we know that any physically relevant observable must be independent of the regularization technique applied. In particular, this means that infrared-safe observables in QCD (and calculated within DREG) have to be finite in the limit $\epsilon \to 0$. However, these kind of computations require to consider both virtual (i.e. loop diagrams) and real (i.e. diagrams with additional physical particles being radiated) contributions. Provided that the loop contributions have been properly renormalized,

then only IR singularities will survive in the virtual component: the Kinoshita-Lee-Nauenberg (KLN) theorem [1, 2] establishes that these IR singularities can be canceled by adding those present in the real contributions. Thus, the combination of real and virtual components must be free of IR singularities, which translates into the absence of ϵ-poles after integrating them within the DREG approach. This is the main reason behind the development of the subtraction methods [3, 4, 5, 6], which introduce proper counter-terms in the real and virtual terms in order to cancel separately the IR-singularities: i.e. these counter-terms exactly reproduce the IR-singular behaviour of the real matrix elements, and their integrated form must cancel the IR poles present in the virtual components. There are several variations of the subtraction framework, that provide alternative paths to build the counter-terms. In any case, the cancellation of singularities in the virtual component takes place *after* integration, even if the counter-terms render the real contribution locally integrable.

In this work, we explain how to directly use the real-emission amplitude as a counter-term for the renormalized virtual contribution: this constitutes the central idea of the four-dimensional unsubtraction (FDU) approach [7, 8, 9, 10, 11, 12, 13]. Within this framework, the introduction of IR counter-terms is avoided and a fully local cancellation of singularities is achieved. In consequence, the limit $\epsilon \to 0$ can be safely considered at integrand level and a complete four-dimensional numerical implementation becomes feasible.

2 Description of the FDU framework

The four-dimensional unsubtraction (FDU) approach is a fully-local, four-dimensional regularization framework to implement higher-order computations in any quantum field theory. It relies on the loop-tree duality (LTD) theorem [14, 15, 16], which establishes the possibility of decomposing any loop amplitude into tree-level objects by *cutting* (i.e. *putting on-shell*) internal lines circulating the loops. As an example, let's consider a generic one-loop scalar Feynman integral with N external legs, whose momenta are denoted $\{p_i\}_{i=1\dots N}$; the application of the LTD decomposition leads to

$$\int_\ell \prod_{i=1}^{N} \frac{1}{q_i^2 - m_i^2 + \imath 0} = -\sum_{i=1}^{N} \int_\ell \tilde{\delta}\left(q_i\right) \prod_{j\neq i, j=1}^{N} \frac{1}{q_j^2 - m_j^2 - \imath 0\, \eta\cdot\left(q_j - q_i\right)}\,, \tag{1}$$

with m_i the mass associated to the internal line with momenta $q_i = \ell + k_i$ ($k_i = p_1 + \ldots + p_i$) and η an arbitrary future-like vector (i.e. $\eta^2 \geq 0$). It is important to notice that the usual Feynman prescription in the l.h.s. of Eq. (1) is converted into a *modified* prescription inside the dual propagators in the r.h.s., which depends on the momenta carried by the cut line and the propagating particle. Also, the loop measure is transformed into a phase-space measure by inserting the factor $\tilde{\delta}\left(q_i\right) = 2\pi\,\imath\,\theta(q_{i,0})\delta(q_i^2 - m_i^2)$, that forces the momenta q_i to represent a physical on-shell state with positive energy.

Beyond one loop, the LTD theorem establishes that the number of cuts required to formulate the dual representation equals the number of loops involved [14, 16]. This is particularly important since N^{n}LO computations involve adding together all the possible $(n-l)$-loop amplitudes with l radiated particles, where $l = 0, \ldots, n$. So, after the iterative application of the LTD, any N^{n}LO calculation is reduced to a set of tree-level objects containing n additional on-shell positive-energy momenta [12].

In the following sections, we will explain how to unveil the IR structure of the virtual amplitudes by using the LTD. Moreover, by exploiting this knowledge, we will define a set of kinematical transformations that allows to map the IR singular points of the dual and real contributions to the same points in the integration domain.

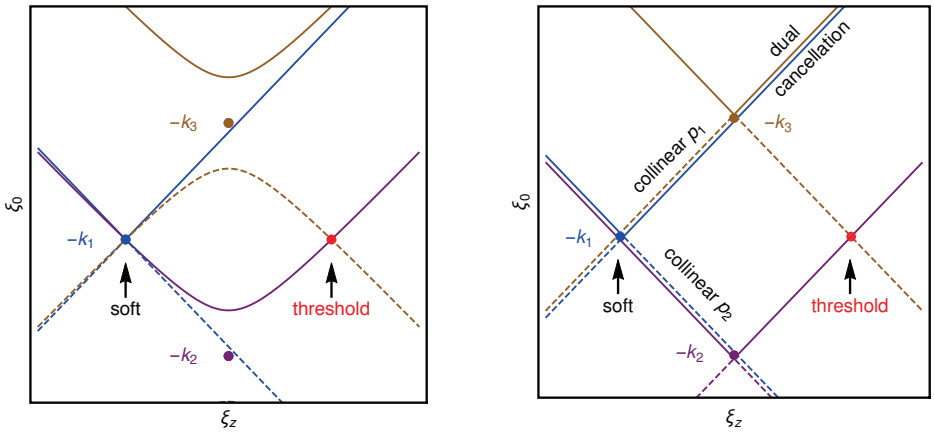

Figure 1: Integration region in the (ξ_0, ξ_z)-plane for the dual contributions associated with a triangle with two massive lines (left) and with only massless particles (right). The solid (dashed) lines represent the forward (backward) regions, i.e. the positive (negative) energy solutions of the on-shell conditions. Intersection among these lines are related with multiple propagators becoming singular; in particular, forward-backward intersections lead to the IR poles of the Feynman integral.

2.1 Location of IR singularities

After the application of the LTD, we get a set of *dual* amplitudes which include a factor $\tilde{\delta}\,(q_i)$ inside the integration measure. This means that we must restrict the integration to the solutions of the on-shell conditions, i.e.

$$G_F^{-1}(q_i) = q_i^2 - m_i^2 + \imath 0 = 0\,, \quad q_{i,0}^{(+)} = \sqrt{\vec{q}_i^{\,2} + m_i^2 - \imath 0}\,, \tag{2}$$

where we choose the positive energy solutions. In Fig. 1, we consider the integration domains associated to a Feynman integral with three propagators. In the left panel, the integral under consideration contains two internal lines with mass $m_i = M$ and a massless one, which translates into the presence of two hyperboloids for the massive particles and a light-cone associated to the massless line. When the limit $M \to 0$ is considered, the hyperboloids degenerate into light-cones, as shown in the right panel. In both cases, the solid (dashed) lines represent the forward (backward) regions, i.e. the positive (negative) energy solutions of the on-shell conditions. The crucial fact is that the intersection of the on-shell hyperboloids is related with the presence of IR and threshold singularities. Essentially, this is due to multiple particles satisfying the on-shell condition, and, thus, more than one propagator becoming singular in the integration domain. However, as explained in Refs. [17, 20], forward-forward intersections cancel among dual contributions but forward-backward intersections originate the physical IR and threshold singularities. The last ones are integrable but might introduce some numerical instabilities.

We can appreciate in the right panel of Fig. 1 that the region responsible of the IR singularities of the virtual contribution is contained in a compact domain. This is the most remarkable property that allows to infer how to combine the real and virtual contributions to achieve a local cancellation of IR singularities, as we carefully explained in Refs. [7, 10, 12]. Since the IR structure of the virtual component matches the one in the real part, and the real-emission phase-space (PS) is finite, then regularizing the combined real-virtual contribution is equivalent to properly mapping the singular points in two compact spaces.

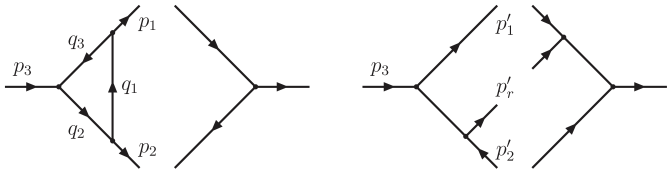

Figure 2: Topological correspondence among one-loop (left) and real-emission amplitudes (right). When we cut the line q_1 and consider the limit $q_1 \parallel p_1$, the virtual diagram factorizes in the same way that the real contribution does in the limit $p_r^{'} \parallel p_1^{'}$. This information is used to split the real-phase space and build the proper momentum mapping in each partition.

2.2 Real-virtual mapping

In order to motivate the construction of the real-virtual momentum mapping, let's consider that the Born process contains m external momenta. Then, the NLO corrections are given by one-loop virtual amplitudes with m on-shell momenta and a free loop-momentum, and real-emission amplitudes with $m+1$ on-shell momenta. Once LTD is applied to the virtual part, we obtain m dual components, which are described in terms of the external m momenta and a free *on-shell* momentum with *positive* energy. Thus, the number of kinematical variables in both contributions exactly matches and we can propose a transformation to map them. We denote the Born level momenta as $\{p_i^\mu\}_{i=1\dots m}$, $\vec{q_j}$ is the spatial part of the dual momentum and $\{p_i'^\mu\}_{i=1\dots m+1}$ are the momenta entering in the real-emission process.

In order to simplify the development of the mapping, we introduce a partition of the real phase-space to isolate the collinear configurations [4]. Explicitly, we define $\mathcal{R}_i = \{{y'}_{ir} < \min {y'}_{jk}\}$, where ${y'}_{ij} = 2\,p_i' \cdot p_j'/Q^2$, r is the label associated to the radiated parton from parton i, and Q is the typical hard scale of the scattering process. Of course, we have m regions and the constraint $\sum_{i=1}^m \mathcal{R}_i = 1$ to cover the whole phase-space. With this definition, the only allowed collinear/soft configurations in $\mathcal{R}_i$ are $i \parallel r$ or $p_r'^\mu \to 0$.

The next step consists in mapping the dual contributions and the real-emission components inside an specific partition. Motivated by the factorization picture shown in Fig. 2, we look for the diagrams which originate the same kind of topologies when their internal lines are set on-shell: the cut-line in the dual amplitude must be interpreted as the extra-radiated particle in the real contribution. This means that if we identify $q_i \leftrightarrow p_r'$, then the have to look for the real-emission diagrams that become singular in the limit $i \parallel r$, and restrict the integration to the region $\mathcal{R}_i$.

After the previous explanations, let's present the explicit mapping. Using the language of the dipole formalism [5, 6], if i is the *emitter* and r is the *radiated* particle, the transformation that generates the kinematics inside the partition $\mathcal{R}_i$ with the kinematics of the i-th dual component is given by

$$
\begin{aligned}
p_r'^\mu &= q_i^\mu \;, & p_j'^\mu &= (1-\alpha_i)\, p_j^\mu \;, \\
p_i'^\mu &= p_i^\mu - q_i^\mu + \alpha_i\, p_j^\mu \;, & \alpha_i &= \frac{(q_i - p_i)^2}{2 p_j \cdot (q_i - p_i)} \;,
\end{aligned}
\tag{3}
$$

where the particle j is the *spectator*. Notice that, by construction, the generated momenta fulfill $p_k'^2 = 0$ (in the massless case) and $\sum_l {p'}_l = 0$. On the other hand, it is important to mention that the mapping does not change the initial-state momenta (p_a and p_b) neither p_k' with $k \neq i, j$, and that the global momentum conservation is respected.

3 Application examples at NLO

We use the FDU approach to recompute the decay processes $H \to q\bar{q}$ and $Z, \gamma^* \to q\bar{q}$ at NLO in QCD with massive quarks [12]. In both cases, we apply the techniques mentioned in the previous sections to obtain a combined real-virtual integrand with a regular behavior, i.e. numerically integrable in four dimensions. The results are compared with the known expressions computed within the DREG framework. In Fig. 3, the solid lines denote the analytical results computed in DREG as a function of $m = M/\sqrt{(Q^2)}$ (where M is the quark mass), whilst the colored dots are the values obtained through the FDU implementation.

In first place, the agreement between both approaches is excellent. We notice that the massless transition is smooth in both cases, which is a non-trivial result. In fact, when dealing with the analytical expressions with $m > 0$, we find some logarithmic-enhanced terms in the real and virtual contributions, separately. Within DREG, these logarithms transforms into ϵ-poles when considering the limit $m \to 0$; thus, a naive implementation of the calculation could lead to huge numerical instabilities. It is a remarkable property of the FDU approach that this transition is completely stable numerically, as a consequence of the local regularization of the integrand and the smoothness of the real-virtual mapping in the massless limit.

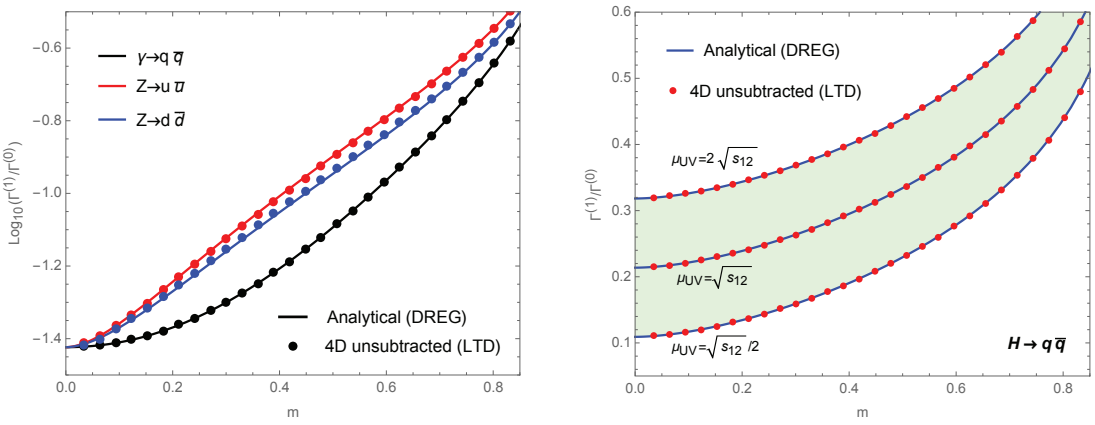

Figure 3: NLO QCD corrections to the decay rates $Z, \gamma^* \to q\bar{q}$ (left) and $H \to q\bar{q}$ (right), as a function of the mass m of the quarks. The solid lines represent the results obtained within the DREG approach, which are known in a closed analytical form. The colored dots were computed numerically thorough the application of the FDU technique. We can appreciate the agreement between these approaches, and in particular the smoothness of the massless limit. Moreover, the scale dependence for the Higgs decay is exactly reproduced, thanks to the introduction of local UV counter-terms.

Also, we should mention that UV singularities are hidden inside the renormalization factors and the self-energy corrections [18], as well as in the *usual* virtual diagrams. In the processes under consideration here, there is a partial cancellation of UV divergences between the vertex corrections and the self-energy contributions (which also contains some IR-singular pieces). To achieve integrability in four-dimensions, we define local UV counter-terms and apply the LTD to obtain the corresponding dual expressions. The presence of higher-powers of the propagators inside these counter-terms is tackled with an extended version of the LTD, as discussed in Refs. [10, 12, 19]. These dual UV counter-terms are added to the remaining dualized virtual contributions, rendering the total sum finite in the high-energy limit. In fact, as we can appreciate from the right panel of Fig. 3, the renormalization scale dependence is successfully

reproduced with this four-dimensional framework.

4 Towards a full NNLO implementation

The core ideas behind FDU at one-loop can be extended to deal with NNLO computations. Within the usual framework, the total NNLO cross-section consists of three contributions,

$$\sigma^{\rm NNLO} = \int_m d\sigma^{(2)}_{\rm VV} + \int_{m+1} d\sigma^{(2)}_{\rm VR} + \int_{m+2} d\sigma^{(2)}_{\rm RR} \ , \tag{4}$$

where the double virtual cross-section $d\sigma^{(2)}_{\rm VV}$ contains the interference of the two-loop with the Born scattering amplitudes and the square of the one-loop scattering amplitude with m final-state particles; the virtual-real cross-section $d\sigma^{(2)}_{\rm VR}$ includes the contributions from the interference of one-loop and tree-level scattering amplitudes with one extra external particle; and the double real cross-section $d\sigma^{(2)}_{\rm RR}$ are tree-level contributions with emission of two extra particles.

The LTD representation of the two-loop scattering amplitude is obtained by setting two internal lines on-shell [16], and it leads to the two-loop dual components $\langle \mathcal{M}^{(0)}_N | \mathcal{M}^{(2)}_N(\tilde{\delta}(q_i, q_j)) \rangle$. The two-loop momenta of the squared one-loop amplitude are independent and generate the dual contributions $\langle \mathcal{M}^{(1)}_N(\tilde{\delta}(q_i)) | \mathcal{M}^{(1)}_N(\tilde{\delta}(q_j)) \rangle$. It is important to notice that, in both cases, there are two independent loop three-momenta and m final-state momenta. On the other hand, the dual representation of the real-virtual contribution $d\sigma^{(2)}_{\rm VR}$ is obtained by setting only one internal line on-shell. Thus, they include an additional external momenta and a free loop three-momentum, i.e. two independent integration variables. Analogously, the double-real terms are associated with the presence of two additional real-particles in the final state. So, through the definition of a proper momentum mapping, the three contributions could be merged at integrand level, and define an integrable function in four space-time dimensions. More details about the explicit implementation of a two-loop computation inside this framework will be provided in a forthcoming publication.

5 Conclusions and outlook

In this article, we present some features of the four-dimensional unsubtraction (FDU) approach. This method is intended to implement higher-order computations of physical observables in any QFT, and is based on the loop-tree duality (LTD) theorem. The dual decomposition of finite Feynman integrals was proven to be very efficient for numerical calculations in four-dimensions [20], including complicated tensorial structures and thus its application to physical observables.

The presence of IR and UV singularities forces to introduce regularization methods and counter-terms. In the usual subtraction framework, these counter-terms cancel locally the IR divergences of the real components, but analytical manipulations are required for the virtual part (as well as the renormalization). Recently, there were many developments to by-pass DREG with alternative regularization techniques, leading to integrable expressions in four-dimensions [21]. It is worth appreciating that regularization might be required even when the final result is finite, since intermediate steps could contain ill-defined expressions [22, 23].

In conclusion, the FDU approach allows to combine all the ingredients required to perform higher-order computations into a single numerically-integrable expression. Moreover, since this approach is completely process-independent, it could be used to develop fully-automated numerical implementations for any physical observable, without dealing with complicated analytical formulae in intermediate steps.

6 Acknowledgements

This work is supported by the Spanish Government and ERDF funds from European Commission (Grants No. FPA2014-53631-C2-1-P and SEV-2014- 0398), by Generalitat Valenciana (Grant No. PROMETEO/2017/057), and by Consejo Superior de Investigaciones Científicas (Grant No. PIE-201750E021). FDM acknowledges support from Generalitat Valenciana (GRISOLIA/2015/035) and GS from Fondazione Cariplo under the Grant No. 2015-0761.

References

1. T. Kinoshita, J. Math. Phys. **3** (1962) 650.
2. T. D. Lee and M. Nauenberg, Phys. Rev. **133** (1964) B1549.
3. Z. Kunszt and D. E. Soper, Phys. Rev. D **46** (1992) 192.
4. S. Frixione, Z. Kunszt and A. Signer, Nucl. Phys. B **467** (1996) 399.
5. S. Catani and M. H. Seymour, Phys. Lett. B **378** (1996) 287.
6. S. Catani and M. H. Seymour, Nucl. Phys. B **485** (1997) 291. Erratum: [Nucl. Phys. B **510** (1998) 503].
7. R. J. Hernández-Pinto, G. F. R. Sborlini and G. Rodrigo, JHEP **1602** (2016) 044.
8. G. F. R. Sborlini, R. Hernández-Pinto and G. Rodrigo, PoS **EPS-HEP2015** (2015) 479.
9. G. F. R. Sborlini, PoS RADCOR **2015** (2016) 082.
10. G. F. R. Sborlini, F. Driencourt-Mangin, R. J. Hernández-Pinto and G. Rodrigo, JHEP **1608** (2016) 160; PoS ICHEP **2016** (2016) 353.
11. G. Rodrigo, F. Driencourt-Mangin, G. F. R. Sborlini and R. J. Hernández-Pinto, PoS LL **2016** (2016) 037.
12. G. F. R. Sborlini, F. Driencourt-Mangin and G. Rodrigo, JHEP **1610** (2016) 162.
13. R. J. Hernández-Pinto, F. Driencourt-Mangin, G. Rodrigo and G. F. R. Sborlini, J. Phys. Conf. Ser. **761** (2016) no.1, 012021.
14. S. Catani, T. Gleisberg, F. Krauss, G. Rodrigo and J. C. Winter, JHEP **0809** (2008) 065.
15. G. Rodrigo, S. Catani, T. Gleisberg, F. Krauss and J. C. Winter, Nucl. Phys. Proc. Suppl. **183** (2008) 262.
16. I. Bierenbaum, S. Catani, P. Draggiotis and G. Rodrigo, JHEP **1010** (2010) 073.
17. S. Buchta, G. Chachamis, P. Draggiotis, I. Malamos and G. Rodrigo, JHEP **1411** (2014) 014.
18. N. Selomit Ramírez-Uribe, R. J. Hernández-Pinto and G. Rodrigo, J. Phys. Conf. Ser. **912** (2017) no.1, 012013 [arXiv:1709.07802 [hep-ph]].
19. I. Bierenbaum, S. Buchta, P. Draggiotis, I. Malamos and G. Rodrigo, JHEP **1303** (2013) 025.

20. S. Buchta, G. Chachamis, P. Draggiotis and G. Rodrigo, Eur. Phys. J. C **77** (2017) no.5, 274.

21. C. Gnendiger *et al.*, Eur. Phys. J. C **77** (2017) no.7, 471.

22. F. Driencourt-Mangin, G. Rodrigo and G. F. R. Sborlini, arXiv:1702.07581 [hep-ph].

23. G. F. R. Sborlini, F. Driencourt-Mangin and G. Rodrigo, PoS(EPS-HEP2017)767. arXiv:1709.09860 [hep-ph].

Frascati Physics Series Vol. 65 (2017)
LFC17: Old and New Strong Interactions from LHC to Future Colliders
11 - 15 September, 2017

A DEMOCRATIC RESUMMATION PROCEDURE OF SOFT GLUON EMISSION FOR HADRONIC INELASTIC CROSS-SECTIONS AND SURVIVAL PROBABILITIES *

Giulia Pancheri
INFN Frascati National Laboratories, Via E. Fermi 40, Frascati, 00044 Italy
Yogendra N. Srivastava
Physics Department of Physics & Geology, University of Perugia, Via A. Pascoli, Perugia, 00123, Italy

Abstract

We discuss a model for soft gluon re-summation based on a statistical description of independent emissions during inelastic collisions. The model is applied to estimate Survival Probabilities at the LHC. A comparison with other models and experimental data is presented.

1 Introduction

Survival probabilities at LHC energies are of special interest when looking for hard scattering events which need to be selected from the large hadronic background accompanying them. The concept was introduced in [1], later defined and discussed in [2]. We recently presented our estimates and discussed them in comparison with other models in [3]. In this contribution, we shall summarize our findings and the particulars of the model we use for calculating the total and the inelastic cross-sections.

As discussed in [3], the probability to find events devoid of hadronic background in the central region can be obtained in its simplest form as:

$$\mathcal{S}^2(s) = \int d^2\mathbf{b} A(b,s) P^{ND}_{no-hadr-bckg}(b,s) \tag{1}$$

where $P^{ND}_{no-hadr-bckground}(b,s)$ represents the probability of events without activity in the central rapidity region, which can be approximated as the non-diffractive (ND) region of phase space. This is clearly an approximation. However, our aim, as it was in [3], is to give an order of magnitude estimate of the Survival probabilities, and compare it with other existing predictions. The quantity $A(b,s)$ refers to the normalized distribution of such events in impact parameter space, and the problem is to calculate the function $A(b,s)$ appropriate to those events excluded by $P^{ND}_{no-hadr-bckg}(b,s)$.

In the sections to follow, we shall describe our model for these two quantities and present our phenomenological analysis for $\mathcal{S}^2(s)$. To estimate survival probabilities following [2] we shall use the model for the total cross-section we developed in [4, 5]. This model is based on i) single channel eikonal formalism, ii) QCD mini-jets to drive the rise of the total cross-section, iii) soft gluon emission to tame the rise that leads to a high energy behaviour consistent with the Froissart bound.

2 Mini-jets vs total cross-sections

Our suggestion is to extract the quantities, $A(b,s)$ and $P^{ND}_{no-hadr-bckg}(b,s)$, from single channel mini-jet models [6]. We start with the following expressions for the tototal cross-section:

$$\sigma_{total} = 2\int d^2\mathbf{b}\Im mF_{el}(b,s) = 2\int d^2\mathbf{b}[1-exp(-\chi_I(b,s))] = \int d^2\mathbf{b}[1-exp(-\bar{n}(b,s)/2)] \qquad (2)$$

where the imaginary part of the eikonal function is obtained from the average number of inelastic hadronic collisions. In this approximation, the inelastic total cross-section obtains as

$$\sigma_{inel} = \int d^2\mathbf{b}[1-exp(-\bar{n}(b,s))] = \int d^2\mathbf{b}[1-exp(-A_{FF}(b,s)\sigma_{soft}(s) - A_{mini-jets}(b,s)\sigma_{mini-jets}(s))] \qquad (3)$$

with $\sigma_{soft}(s)$ either a constant or a slowly decreasing function of energy, and $\sigma_{mini-jets}(s)$ is calculated from perturbative QCD, i.e. using Parton Distribution Functions (PDFs) DGLAP evolved and folded with parton-parton cross-sections. Our mini-jet calculation uses the asymptotic freedom expression for the strong coupling constant and thus implies using a lower cut-off for outgoing partons, p_{tmin}, which effectively separates perturbative and non-perturbative collisions. We show in the left panel of Fig. 1 the behaviour of $\sigma_{mini-jets}(s)$ when calculated for different LO PDFs, and different values of p_{tmin}. The comparison with the total cross-section shown in the same figure, indicates that a mechanism to slow down the excessive growth of the mini-jet cross-section at high energy must be present. In our model, such taming of the mini-jet cross-section is obtained through the average parton distribution function in impact parameter space $A_{mini-jets}(b,s)$, for which a distinctive choice based on soft gluon emission processes is made, as we shall describe in the next section. As for the b-distribution of non-mini-jet events $A_{FF}(b)$, the present version of the model is obtained from the Fourier transform of the proton e.m. form factor.

3 Soft Gluon Re-summation : a democratic pathway through confinement

In the right hand panel of Fig. 1 we show the mechanism which we propose to be responsible for the taming of the mini-jet effect, soft gluon re-summation (SRG). To tackle SRG, we proceed with the following guiding ideas:

- if the total cross-section has to follow the limitations of the Froissart bound, hadronic interactions must exhibit a large distance cut-off,
- the large distance behaviour (Froissart bound) is controlled by contributions from very low momentum gluons, i.e. gluons with momentum lower than the pQCD cut-off Λ_{QCD},
- since very soft emitted gluons are not individually counted, only missing energy-momentum is the observed quantity, and the development of a formalism for infrared gluons requires energy momentum balance to be enforced on the soft gluon sea.

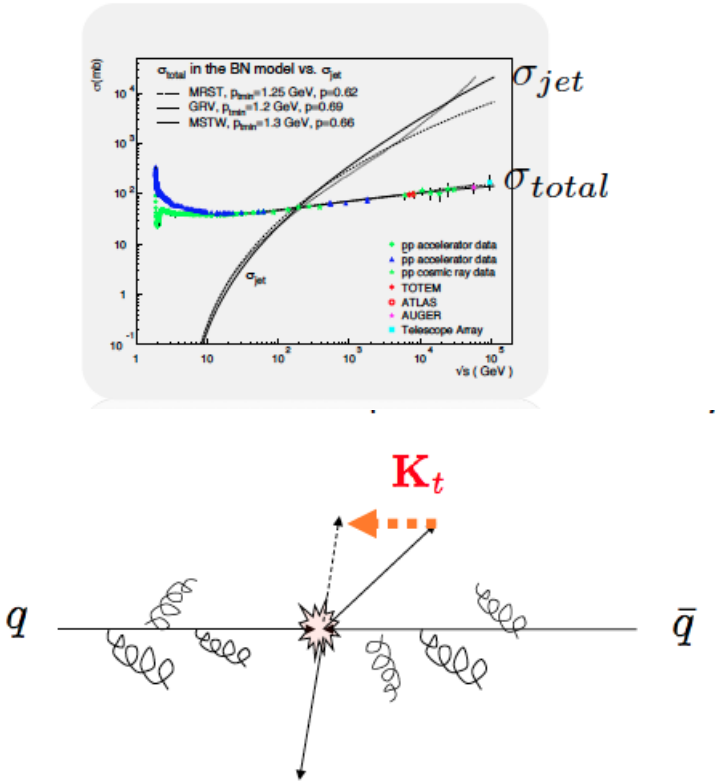

Figure 1: *a) The mini-jet proton-proton cross section for inelastic events compared with the total cross-section as a function of c.m. energy b) the soft gluon emission mechanism proposed to tame the fast mini-jet rise.*

We propose to use a semiclassical re-summation procedure, inspired by what was originally proposed in [8] for soft photons. This approach is based on a *democratic* treatment, a term we shall render more explicit below, and which is represented graphically on the left-hand side in Fig. 2. Let us start with a discrete description of the process of emission. Additional details about the soft-gluon re-summation model can be found in our review [7].

Let $n_{\mathbf{k}}$ be the number of gluons emitted with a given momentum value $\mathbf{k}$. If these gluons are *soft*, they are by definition indistinguishable, and independent from the source. Hence, the first assumption: these $n_{\mathbf{k}}$ gluons, all having exactly the same momentum $k < \Lambda_{QCD}$, are all emitted independently from each other (and from the source). In analogy to what Bloch and Nordsieck demonstrated [9] for the case of QED, for each value of the momentum k the number of soft gluons $n_{\mathbf{k}}$ is taken as being distributed according to a Poisson distribution around an average value $\bar{n}_{\mathbf{k}}$. The next step in the derivation of the expression we propose, is to consider all possible values of the soft gluon momentum $\mathbf{k}$, each contributing equally to the final energy momentum imbalance. Thus we obtain an overall probability for emission as the product over $\mathbf{k}$ of the individual Poisson distributions, i.e.

$$P(\{n_{\mathbf{k}}\}) = \Pi_{\mathbf{k}} \frac{[\bar{n}_{\mathbf{k}}]^{n_{\mathbf{k}}}}{n_{\mathbf{k}}!} e^{-\bar{n}_{\mathbf{k}}} \tag{4}$$

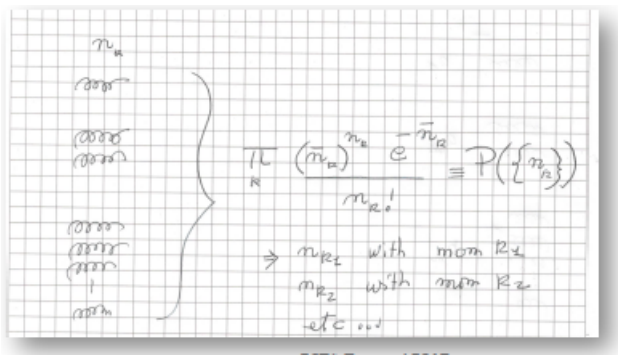

Figure 2: *Democratic emission of $n_{\mathbf{k}}$ soft gluons of given momentum $\mathbf{k}$ is shown at left side, with, at right, the overall probability described by the product of Poisson distributions.*

The next three steps are:
1: for each possible number of gluons, $n_{\mathbf{k}}$, impose energy-momentum conservation, i.e. $K_\mu = \sum_{\mathbf{k}} n_{\mathbf{k}} k_\mu$,
2: considering the distribution in transverse momentum, sum on all the distributions giving the observed missing transverse momentum $\mathbf{K}_t$,
3: exchange the product with the sum,
4: take the continuum limit.
Explicitly, from

$$d^2P(\mathbf{K}_t) = \sum_{n_{\mathbf{k}}} P(\{n_{\mathbf{k}}\}) d^2\mathbf{K}_t \delta^2(\mathbf{K}_t - \sum_{\mathbf{k}} \mathbf{k}_t n_{\mathbf{k}}) = \sum_{n_k} \Pi_{\mathbf{k}} \frac{[\bar{n}_{\mathbf{k}}]^{n_{\mathbf{k}}}}{n_{\mathbf{k}}!} e^{-\bar{n}_{\mathbf{k}}} d^2\mathbf{K}_t \delta^2(\mathbf{K}_t - \sum_{\mathbf{k}} \mathbf{k}_t n_{\mathbf{k}}) \quad (5)$$

and using the integral representation of the delta-function, one exchanges the sum with the product obtaining

$$d^2P(\mathbf{K}_t) = \frac{d^2\mathbf{K}_t}{(2\pi)^2} \int d^2\mathbf{b} e^{-i\mathbf{K}_t\cdot\mathbf{b}} exp\{-\sum_{\mathbf{k}} \bar{n}_{\mathbf{k}}[1 - e^{i\mathbf{k}_t\cdot\mathbf{b}}]\} \quad (6)$$

Going to the continuum, brings

$$d^2P(\mathbf{K}_t) = \frac{d^2\mathbf{K}_t}{(2\pi)^2} \int d^2\mathbf{b} e^{-i\mathbf{K}_t\cdot\mathbf{b}} exp\{-\int d^3\bar{n}_{\mathbf{k}}[1 - e^{i\mathbf{k}_t\cdot\mathbf{b}}]\} \quad (7)$$

Taking then the Fourier transform of Eq. (7), we obtain the impact parameter distribution as an input into the eikonal formalism for the inelastic hadronic cross-section, namely

$$A_{mini-jets} \equiv A_{BN}(b,s) = \mathcal{N}(s) e^{-h(b,s)} \quad (8)$$

with $\mathcal{N}(s)$ the normalisation factor, required for dimensional reasons. Following derivations in our previous publications, we have [5)]

$$h(b,s) = \frac{8}{3\pi^2} \int_0^{qmax(s)} d^2k_t [1 - e^{i\mathbf{k}_t\cdot\mathbf{b}}] \alpha_s(k_t^2) \frac{\ln(2q_{max}/k_t)}{k_t^2} \quad (9)$$

Of notice are the two limits of integration, the upper limit which is chosen from the kinematics of single gluon emission, and the lower limit, which, in our model, we put to zero. Thus, a specification for the coupling of soft gluons to their source is needed, since the asymptotic freedom expression of pQCD cannot

be used for $k_t \leq \Lambda_{QCD}$. For such k_t values, we propose a phenomenological ansatz of a singular but integrable behaviour, namely $\alpha_s(k_t^2) \to (\Lambda_{QCD}/k_t)^{2p}$, with the condition $1/2 < p < 1$. Then the integral in Eq. (9) is finite, and the total cross-section is found to behave asymptotically as $\sigma_{tot} \simeq (\ln s)^{1/p}$ [10].

Because our model for re-summation was inspired by the Bloch and Nordsieck theorem, we refer to it as the *BN model*.

4 The inelastic cross-section and survival probabilities

We now apply the above model to describe proton data for the total and inelastic hadronic cross-section in the available energy c.m. range. Applying Eqs. (2) and (3), we obtain the curves shown in Fig. 3, with the blue band indicating the uncertainty arising, at very high energies, from the different low-x-behaviour of the proton PDFs used in the mini-jet calculation. Fig. 3 summarises the results obtained

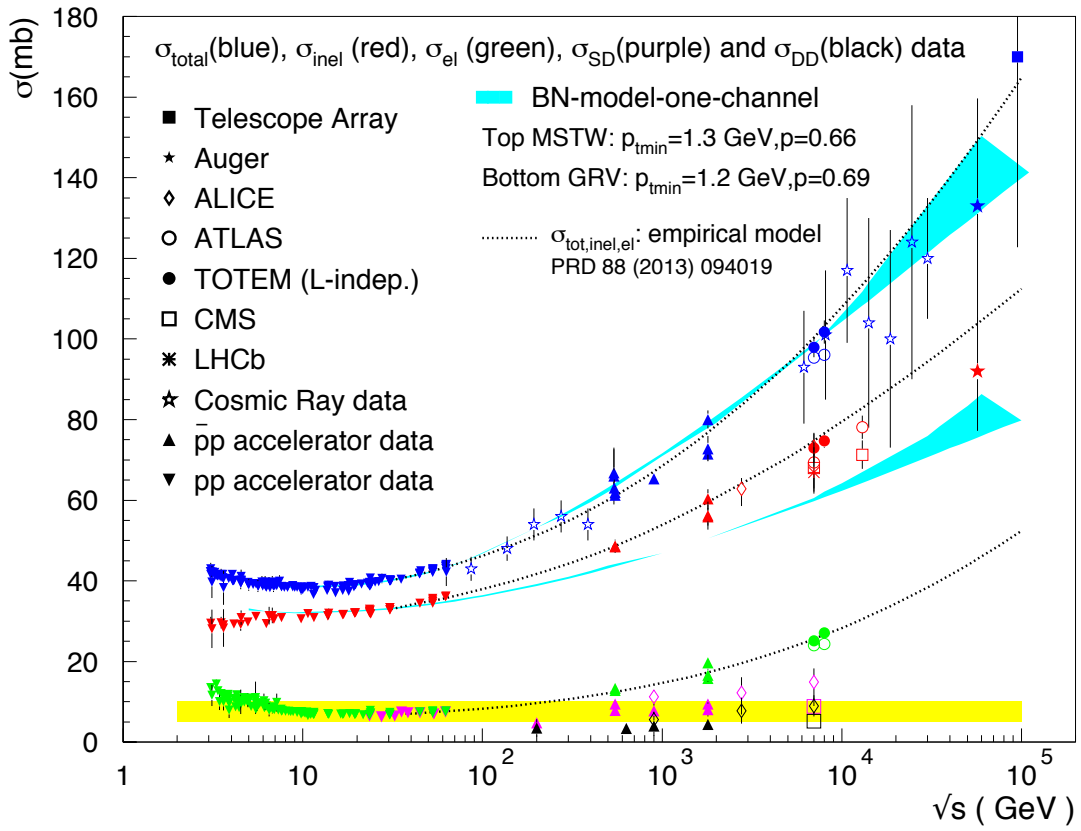

Figure 3: *Proton-proton total cross sections, with blue bands corresponding to the BN model expectations, and dotted lines are fits through an empirical parametrisation* [11].

with the mini-jet model described in the previous sections, and compares them with results from an empirical model, which was fashioned after [12], and which provides a fit to the total, the elastic and, by

subtraction, to the inelastic cross-section. The empirical model is shown by the dotted lines, which are obtained using an elastic scattering amplitude parametrised as [11]

$$\mathcal{A}(s,t) = i[F_p^2(t)\sqrt{A(s)}e^{B(s)t/2} + e^{i\phi(s)}\sqrt{C(s)}e^{D(s)t/2}] \tag{10}$$

with $F_p(t)$ the e.m. proton form factor.

Comparing the fit with the blue band, confirms that the mini-jet model used here for σ_{inel} does non include diffractive events. This was discussed in our previous publications [3] where we also noted that Single Diffractive (SD) events constitute about 10% of the full inelastic cross-section (approximately indicated by the yellow band in Fig. 3). Their origin can be connected to hadronic products from single hard QCD bremsstrahlung from the quarks in one of colliding protons, but are not described by a single-channel eikonal model, with only two components in the eikonal, a non perturbative one, and one from mini-jets, calculable from semi-hard gluon-gluon scattering. However, the model we have presented can be used in the calculation of the survival probability when searching for events unaccompanied by hadronic semi-hard activity in the central region.

In Fig. 4 we show results for the survival probability, estimated using two different models. For the curves shown at left, we use Eq. (1), with the probability of events with no hadronic background in the central region given as $P^{ND}_{no-hadr-bckg}(b,s) = exp\{-\bar{n}(b,s)\}$, with the $\bar{n}(b,s)$ function determined through our description of the inelastic cross-section, as described in the previous section. As for the impact parameter distribution, we have used $A(b) = A_{FF}(b)$, namely the Fourier transform of the electromagnetic form factor. This follows previous estimates, from Bloch, Durand, Ha and Halzen [13] and our BN model as well (BN-2008 model) [14]. Our improved proposal [3] is shown in panel b) of Fig. 4, where dotted and full curves correspond to different PDFs in the mini-jet calculation. These curves are obtained using the results of the previously described BN model into an expression for the survival probability, where soft and a mini-jet contributions are estimated according to their overall weight, as follows:

$$\bar{\mathcal{S}}^2(s) = \bar{\mathcal{S}}^2_{soft}(s) + \bar{\mathcal{S}}^2_{mini-jets}(s) \equiv w_{soft}(s) < |S(b)|^2 >_{soft} + w_{mini-jets}(s) < |S(b)|^2 >_{mini-jets} \tag{11}$$

with

$$< |S(b)|^2 >_{soft} = \int d^2\mathbf{b} A_{FF}(b,s) e^{-\bar{n}_{soft}(b,s)} \tag{12}$$

$$< |S(b)|^2 >_{mini-jets} = \int d^2\mathbf{b} A_{BN}(b,s) e^{-\bar{n}_{mini-jets}(b,s)} \tag{13}$$

$$\bar{n}_{soft}(b,s) = A_{FF}(b)\sigma_{soft}(s), \qquad \bar{n}_{mini-jets}(b,s) = A_{BN}(b,s)\sigma_{mini-jets}(s) \tag{14}$$

$$w_{soft/mini-jets}(s) \equiv \frac{\sigma_{soft/mini-jets}(s)}{\sigma_{soft}(s) + \sigma_{mini-jets(s)}} \tag{15}$$

Our proposed additive model is compared in panel b) of Fig. 4 with other model predictions [13, 16, 15], as well as with CMS data for the survival probability associated to diffractive jet production at LHC [17].

Comparing results between the two panels and within each figure, we see very large differences, of almost one order of magnitude, and also large uncertainties, between the various estimates. Following our present picture of how mini-jet events populate the central region, we propose Eq. (11) as an adequate way to develop a realistic approximation of survival probabilities in the central region.

This contribution is based on recent joint work with our collaborators, Agnes Grau, Daniel A. Fagundes and Olga Shekhovotsova. YS would like to thank the Department of Physics & Geology at the University of Perugia for their hospitality.

References

1. Y. L. Dokshitzer, V. A. Khoze, and T. Sjostrand, Phys. Lett. **B274**, 116 (1992).
2. J. D. Bjorken, Phys. Rev. **D47**, 101 (1993).
3. D. Fagundes, A. Grau, G. Pancheri, O. Shekhovtsova and Y.N. Srivastava, Phys. Rev. **D96**, 054010 (2017).
4. A. Corsetti, A. Grau, G. Pancheri, and Y. N. Srivastava, Phys. Lett. **B382**, 282 (1996).
5. R. M. Godbole, A. Grau, G. Pancheri, and Y. N. Srivastava, Phys. Rev. **D72**, 076001 (2005).
6. L. Durand and H. Pi, Phys. Rev. **D40**, 1436 (1989).
7. G. Pancheri and Y. Srivastava, Eur. Phys. J., **C77** (2017) no. 3, 150 arXiv:hep-ph/1610.10038.
8. E. Etim, G. Pancheri and B. Touschek, Nuovo Cimento **51B**, 276 (1967).
9. F. Bloch and A. Nordsieck, Phys. Rev. **52**, 54 (1937).
10. A. Grau, R. M. Godbole, G. Pancheri, and Y. N. Srivastava, Phys. Lett. **B682**, 55 (2009).
11. D. A. Fagundes, A. Grau, S. Pacetti, G. Pancheri, and Y. N. Srivastava, Phys. Rev. **D88**, 094019 (2013).
12. R. Phillips and V. D. Barger, Phys.Lett. **B46**, 412 (1973).
13. M. M. Block, L. Durand, P. Ha, and F. Halzen, Phys. Rev. **D92**, 014030 (2015).
14. A. Achilli, R. Hegde, R. M. Godbole, A. Grau, G. Pancheri, and Y. Srivastava, Phys. Lett. **B659**, 137 (2008).
15. V. A. Khoze, A. D. Martin, and M. G. Ryskin, Eur. Phys. J. **C73**, 2503 (2013).
16. E. Gotsman, E. Levin, and U. Maor, Eur. Phys. J. **C76**, 177 (2016).
17. S. Chatrchyan et al. (CMS), Phys. Rev. **D87**, 012006 (2013).
18. G. Aad et al. (ATLAS), Phys. Lett. **B754**, 214 (2016).

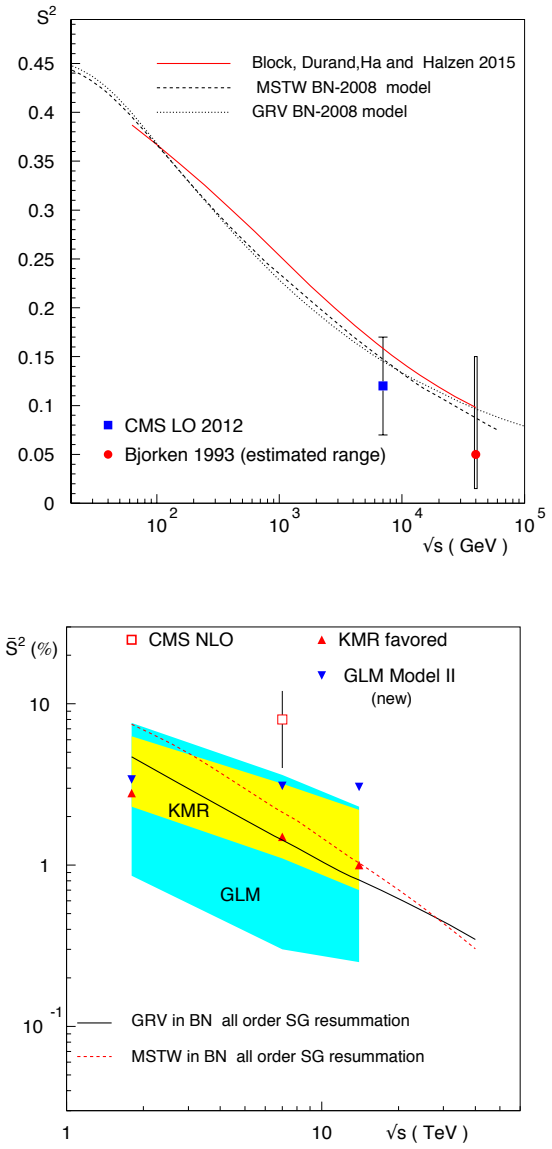

Figure 4: *Our results for the survival probability, when selecting hard events without accompanying hadronic activity in the central region, are compared with other estimates: a) when the impact parameter distribution is modelled after the proton e.m. form factor, dotted and dashed lines, vs. estimates by Bjorken* [2] *and Block, Durand, Ha and Halzen* [13] *(the full red line), b) when an additive model, described in the text, is used, compared with results from Khoze, Martin and Ryskin* [15]*, Gotsman, Levin and Maor from* [16]*. CMS data are from* [17]*, similar results have also been presented by ATLAS* [18]*.*

Frascati Physics Series Vol. 65 (2017)
LFC17: Old and New Strong Interactions from LHC to Future Colliders
11 - 15 September, 2017

NUCLEAR PARTON DISTRIBUTION FUNCTIONS

Petja Paakkinen
University of Jyvaskyla, Department of Physics, P.O. Box 35, FI-40014 University of Jyvaskyla, Finland

Abstract

I review recent developments in the extraction of nuclear parton distribution functions. First describing the global analysis framework, I then present a comparison of the latest analyses in terms of included data and theoretical details, pointing out a few general trends.

1 Introduction: Collinear factorization and nuclear PDFs

Parton distribution functions (PDFs) are defined in the context of collinear factorization theorem, which states that when a hard scale Q^2 is involved, the hard-process cross section for the colliding hadrons A, B to produce a final state k (in association with anything else) can be factorized in terms of a sum over the involved partons i, j as

$$\mathrm{d}\sigma^{AB\to k+X} \overset{Q\gg\Lambda_{\mathrm{QCD}}}{=} \sum_{i,j,X'} f_i^A(Q^2)\otimes \mathrm{d}\hat{\sigma}^{ij\to k+X'}(Q^2)\otimes f_j^B(Q^2) \;+\; \mathcal{O}(1/Q^2) \tag{1}$$

up to power corrections in the reciprocal of the hard scale [1]. By virtue of the asymptotic freedom of QCD, the coefficient functions $\mathrm{d}\hat{\sigma}^{ij\to k+X'}$ are perturbatively calculable but the PDFs f_i^A, f_j^B contain long-range physics and cannot be obtained by perturbative means. However, the PDFs are universal, process independent, and obey the DGLAP equations

$$Q^2\frac{\partial f_i}{\partial Q^2} = \sum_j P_{ij}\otimes f_j \tag{2}$$

with splitting functions P_{ij} governing the scale evolution [2].

For a nucleus A with Z protons and $N = A - Z$ neutrons, it is convenient to write

$$f_i^A(x, Q^2) = \frac{Z}{A} f_i^{\mathrm{p}/A}(x, Q^2) + \frac{N}{A} f_i^{\mathrm{n}/A}(x, Q^2), \tag{3}$$

where $f_i^{\mathrm{p}/A}$ are the PDFs of a bound proton and the neutron contents $f_i^{\mathrm{n}/A}$ are obtained from $f_i^{\mathrm{p}/A}$ via isospin symmetry. As revealed by deep inelastic scattering (DIS) experiments, the bound nucleon PDFs are not the same as those of a free proton, but are modified in a nontrivial way. This observation has led to global analyses of nuclear parton distribution functions (nPDFs); for earlier reviews, see Refs. [3, 4, 5]. The first such fit was EKS98 [6] also including Drell–Yan (DY) dilepton data, followed by HKM [7] providing the first error analysis. Both of these were done in leading order (LO) perturbative QCD; the first next-to-leading order (NLO) analysis was provided by nDS [8]. The EPS08 analysis [9] was the first to include RHIC dAu hadron-production data.

The relation of the bound-proton PDFs with respect to free-proton PDFs f_i^{p} is often expressed in terms of the nuclear modification factors

$$R_i^A(x, Q^2) = \frac{f_i^{\mathrm{p}/A}(x, Q^2)}{f_i^{\mathrm{p}}(x, Q^2)}. \tag{4}$$

A typical form of such modifications is shown in the left panel of Fig. 1: small-x shadowing followed by antishadowing, EMC-effect, and Fermi motion at large x. The global-analysis procedure is the same as in free-proton fits (see Ref. [10] for a review), but there is a further complication since not enough data are available to fit each nucleus independently, and instead one needs to parametrize also the mass number dependence. Also the kinematic reach of the available data is more restricted than in corresponding free proton fits; see the right panel of Fig. 1 for an illustration of the data used in the most recent EPPS16 analysis [11].

2 Global analysis

The PDF global analysis aims at finding the best possible parameter values such that a large set of experimental data from various hard processes are optimally described. In practice this is done by minimizing the figure-of-merit function

$$\chi^2_{\mathrm{global}} = \sum_{i,j} \left[T_i(\{a\}) - D_i\right] C_{ij}^{-1} \left[T_j(\{a\}) - D_j\right] \tag{5}$$

with respect to a set of parameters $\{a\}$. Fig. 2 summarizes the various steps and inputs needed in the minimization process. One begins by parameterizing the PDFs at some initial scale Q_0^2 and sets initial values for the parameters. The PDFs are then evolved to higher scales by solving the DGLAP equations and then convoluted with the coefficient functions to obtain theory predictions T_i. These are then compared to experimental values D_i with covariances C_{ij} using Eq. (5). If the minimum attainable χ^2 was reached, one declares that the best fit was found and proceeds to uncertainty analysis. If not, one alters the parameter values and computes the observables again. Since this loop has to be traversed multiple times, fast methods for both solving the DGLAP equations and computing the observables are needed so that neither of these becomes a bottleneck in the analysis.

It is worth to note that all of the inputs in Fig. 2 are possible sources of uncertainty. However, the theoretical uncertainties related to the choice of the parametrization form or neglecting higher order corrections in the splitting and coefficient functions are hard to quantify. Thus one usually restricts oneself to asking how the experimental uncertainties translate to uncertainties in the parameter values.

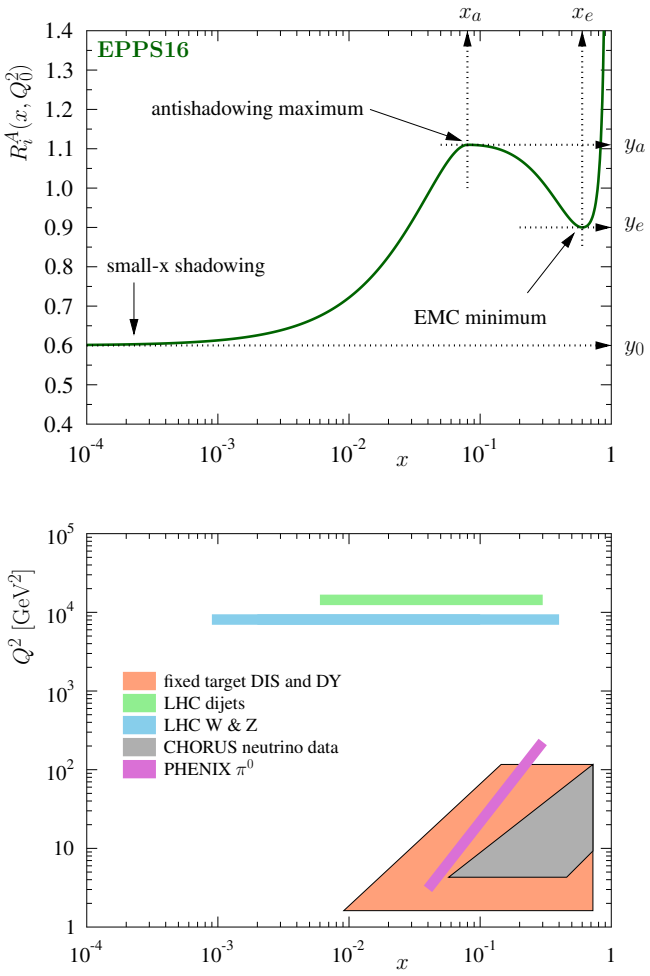

Figure 1: *Left: Typical form of PDF modifications in a nucleus. Right: Kinematic reach of the data used in nPDF global analyses. Figures from Ref.* [11].

The Hessian method for uncertainty extraction [12] relies on the quadratic approximation of the χ^2 function

$$\chi^2_{\text{global}} \approx \chi^2_0 + \sum_{i,j} (a_i - a_i^0)\, H_{ij}\, (a_j - a_j^0) = \chi^2_0 + \sum_i z_i^2, \tag{6}$$

where χ^2_0 is the minimum of χ^2 at parameter values a_i^0, and the latter expression is written in terms of new parameters z_i such that they are linear combinations of the original parameters and uncorrelated in the quadratic approximation. In these new parameters, one then finds the maximal upward and downward deviations $\delta z_i^{\pm}$ corresponding to a fixed increase $\Delta\chi^2$ in the χ^2_{global} function.

To enable a general user to calculate PDF related uncertainties, global analyses provide "error sets", PDFs evaluated with the parameter deviations $\delta z_i^{\pm}$ corresponding to the tolerance $\Delta\chi^2$. The uncertainty of any PDF related quantity X can then be obtained separately for the upward and downward directions

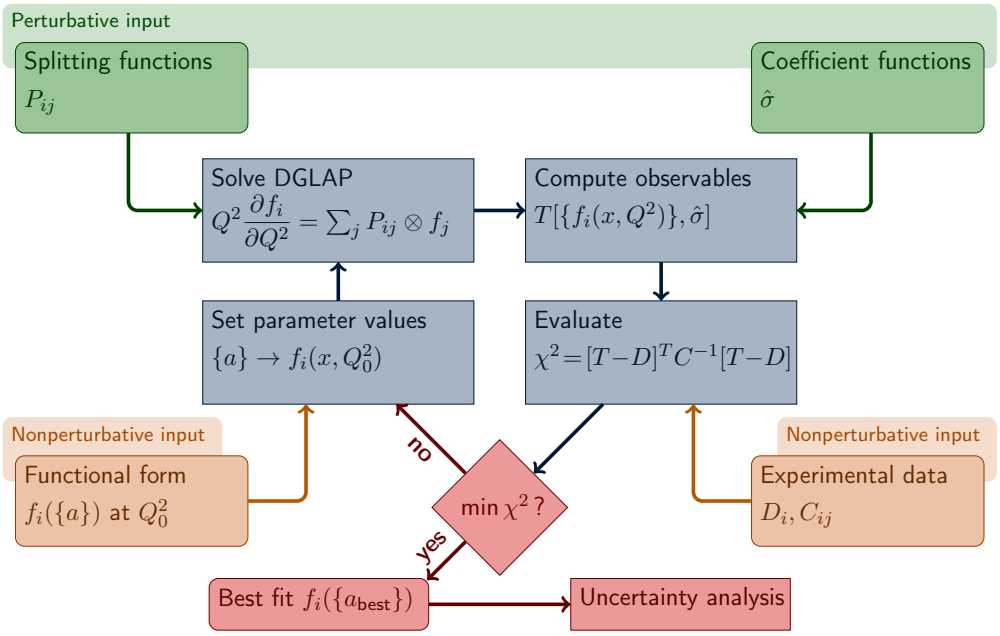

Figure 2: *Flowchart for PDF global analysis.*

with

$$\left(\delta X^{\pm}\right)^2 = \sum_i \left[{}^{\max}_{\min}\left\{X\left(\delta z_i^+\right) - X_0, X\left(\delta z_i^-\right) - X_0, 0\right\}\right]^2, \tag{7}$$

where X_0 is the value obtained using PDFs with best fit parameters, the "central set", and $X\left(\delta z_i^{\pm}\right)$ are calculated with the error sets. The allowed error tolerance $\Delta\chi^2$ varies from analysis to analysis, as do the details of how to extract this value. A common practice is to use a "90% confidence criterion", where $\Delta\chi^2$ is taken to be the average of changes in χ^2 corresponding to a maximal shifts in each of the new parameters z_i such that all data sets remain within their 90% confidence ranges. For a more detailed discussion, see Ref. [11].

3 Nuclear PDF comparison

Now that we are familiar with the global analysis framework, it is time to compare results of different analyses. Table 1 summarizes the details of the latest global nPDF analyses, including EPS09 [13], DSSZ [14], KA15 [15], nCTEQ15 [16] and EPPS16 [11]. Most of these are NLO QCD analyses. While the KA15 analysis was performed at next-to-NLO (NNLO), they only included DIS and DY data, thus lacking a direct constraint for gluons, and are not at the same global footing as other (NLO) analyses which also include inclusive pion production data from RHIC. DSSZ were the first to include neutrino–nucleus DIS, but the full potential of these data was not fully unleashed due to an assumption of flavour symmetric valence and sea quark nuclear modifications. Independent valence distributions were first allowed in nCTEQ15, but with very limited constraints since no νA data were included. Most recently, EPPS16 provided the first analysis with parametric freedom for all flavours and constraints not only from νA DIS, but also πA DY and LHC pPb W and Z production. Due to lack of sufficient statistics, the

Table 1: *Selection of global nPDF analyses. Table adapted from Ref.* [5].

	EPS09 [13]	DSSZ [14]	KA15 [15]	nCTEQ15 [16]	EPPS16 [11]
Order in α_s	LO & NLO	NLO	NNLO	NLO	NLO
NC DIS lA/ld	✓	✓	✓	✓	✓
DY pA/pd	✓	✓	✓	✓	✓
RHIC pions dAu/pp	✓	✓		✓	✓
νA DIS		✓			✓
πA DY					✓
LHC pPb W, Z					✓
LHC pPb jets					✓
Q cut in DIS	1.3 GeV	1 GeV	1 GeV	2 GeV	1.3 GeV
datapoints	929	1579	1479	708	1811
free parameters	15	25	16	16	20
error analysis	Hessian	Hessian	Hessian	Hessian	Hessian
error tolerance $\Delta\chi^2$	50	30	not given	35	52
Free proton PDFs	CTEQ6.1	MSTW2008	JR09	CTEQ6M-like	CT14
HQ treatment	ZM-VFNS	GM-VFNS	ZM-VFNS	GM-VFNS	GM-VFNS
Flavour separation	no	no	no	valence	full
Weight data in χ^2	yes	no	no	no	no

latter observables however are not able to give as stringent constraints as νA DIS. Also new in EPPS16, more constraints for gluon nuclear modifications were obtained from the inclusion of LHC pPb dijet data. This has enabled EPPS16 to lift the data weight which was used in the EPS09 analysis to emphasize the impact of RHIC pion data in the absence of other gluon constraints. An important development is the employment of the general-mass variable-flavor-number scheme (GM-VFNS), see Ref. [17] and the references therein, for heavy-quark treatment in DSSZ, nCTEQ15 and EPPS16 as opposed to the zero-mass scheme (ZM-VFNS) used in EPS09 and KA15.

Fig. 3 shows the nuclear modifications of partons in lead nucleus from EPPS16 and nCTEQ15 analyses. The two are compatible as the error bands always overlap, but there are certain differences which need to be addressed. First, the central predictions for valence-quark modifications obtained by the two analyses appear quite different. While in EPPS16 the u and d valence quark modifications are very similar, in nCTEQ15 these differ significantly with u quark exhibiting a large EMC suppression whereas d quark obtains an enhancement in the same kinematic region. This is possibly due to nCTEQ15 using isospin-symmetric DIS data and having no νA DIS in their fit. As pointed out also in Ref. [16], such differences become more dilute when we construct the PDFs of the full nucleus according to Eq. (3). This is also the reason why EPPS16 valence uncertainties are so large: while the average valence quark distribution is well under control (cf. Fig. 4 left panel), we would need high-precision data on non-isoscalar nuclei to constrain the difference in u and d modifications. Second, the EPPS16 sea-quark uncertainties are much larger than those of nCTEQ15. This is simply due to nCTEQ15 having less freedom in their parametrization: in nCTEQ15 there are only 2 free parameters for all sea quarks with no flavour dependence, whereas EPPS16 has altogether 9 free sea-quark parameters, of which only 3 are common to all flavours. Third, the nCTEQ15 gluon uncertainties at high x are larger than those of EPPS16 resulting from nCTEQ15 having a harder Q^2 cut in DIS data and not including LHC jet data.

Comparing EPPS16 with EPS09 and DSSZ in Fig. 4, since the latter have no flavour freedom, we

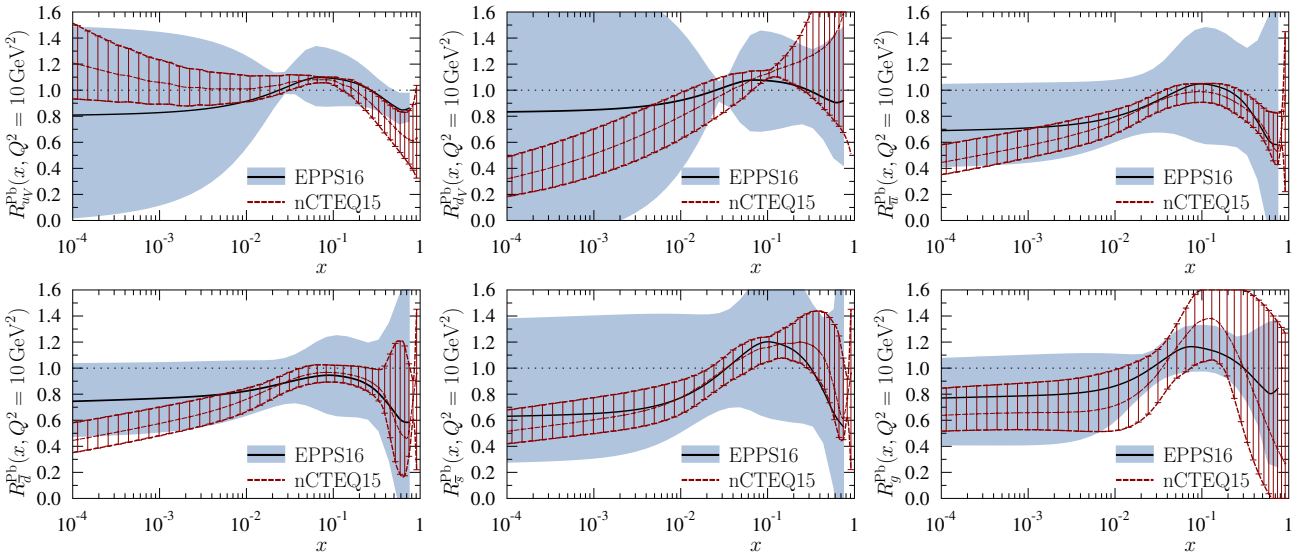

Figure 3: *Comparison of the EPPS16 and nCTEQ15 nuclear PDFs. Figure from Ref.* [11].

find it sensible only to compare the averages

$$R_{\mathrm{V}}^{\mathrm{Pb}} \equiv \frac{u_{\mathrm{V}}^{\mathrm{p/Pb}} + d_{\mathrm{V}}^{\mathrm{p/Pb}}}{u_{\mathrm{V}}^{\mathrm{p}} + d_{\mathrm{V}}^{\mathrm{p}}}, \qquad R_{\mathrm{S}}^{\mathrm{Pb}} \equiv \frac{\overline{u}^{\mathrm{p/Pb}} + \overline{d}^{\mathrm{p/Pb}} + \overline{s}^{\mathrm{p/Pb}}}{\overline{u}^{\mathrm{p}} + \overline{d}^{\mathrm{p}} + \overline{s}^{\mathrm{p}}}. \tag{8}$$

The valence-quark modifications of these three analyses are very similar to each other, except in the EMC region, where DSSZ is close to unity. This has been identified with a misinterpretation of the isospin corrections in the DSSZ analysis [4]. The EPPS16 sea-quark uncertainty is larger than in EPS09 and DSSZ due to additional parametric freedom from allowing flavour separation, but the shapes of the obtained modifications match very well. Regarding the gluon modifications, we find EPS09 and EPPS16 to give similar results. The EPS09 uncertainties however are artificially small because the additional weight for RHIC data was used. DSSZ gives a rather different behavior, as it contains virtually no gluon modifications at all. This follows from the choice in DSSZ to use nuclear fragmentation functions (nFFs), the gluonic component of which was constrained with the very same pion production data as used in the DSSZ analysis. Hence, by necessity, they arrived with similar small gluon modifications as in nDS which was used in the nFF extraction [3].

4 Conclusions

I have reviewed the recent nuclear-PDF analyses and the developments therein. A major step forward is the inclusion of LHC pPb data. Especially the gluon-PDF extraction is benefiting from the new constraints coming from the dijet measurements. For electroweak pPb data to give stringent constraints, we need to wait until measurements with better statistics are published. Apart from including more and more data, we can see a few general trends which can be expected to continue also in the future. Most prominently, we are experiencing a shift towards parameterizing the full flavour dependence of nPDFs, as opposed to using simplifying assumptions. While this tends to make flavour by flavour uncertainties larger

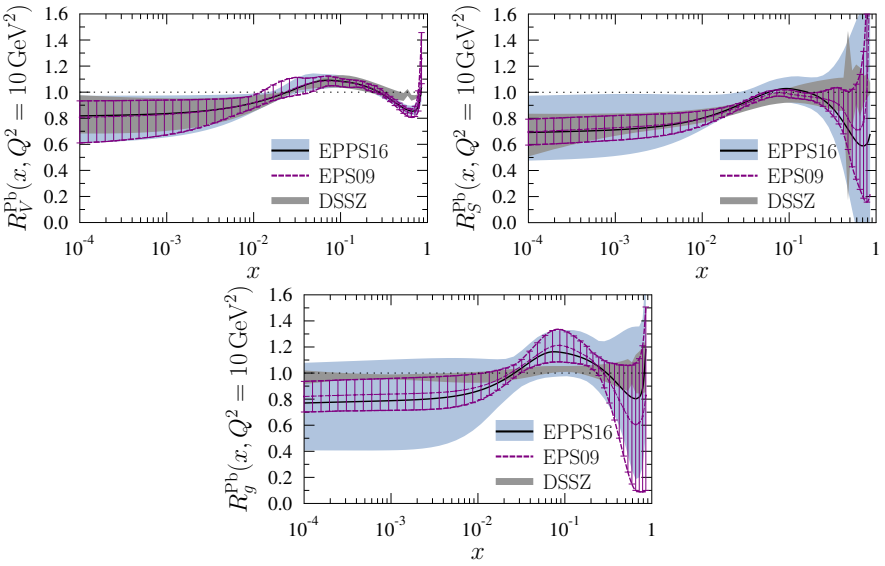

Figure 4: *Comparison of the EPPS16, EPS09 and DSSZ nuclear PDFs. Figure from Ref.* [11].

at first, it renders the global analysis more data driven and thus less biased. Also, the treatment of heavy-quark mass effects with GM-VFNS is becoming a well established practice. An emerging development seems to be the inclusion of NNLO corrections; the pace at which these will be implemented in the future analyses remains to be seen.

5 Acknowledgements

I thank K. J. Eskola and H. Paukkunen for comments. Financial support from the Magnus Ehrnrooth Foundation and the Academy of Finland, Project 297058, is acknowledged.

References

1. J. C. Collins, D. E. Soper and G. F. Sterman, Adv. Ser. Direct. High Energy Phys. **5**, 1 (1989) [hep-ph/0409313].

2. Y. L. Dokshitzer, Sov. Phys. JETP **46**, 641 (1977); V. N. Gribov and L. N. Lipatov, Sov. J. Nucl. Phys. **15**, 438 (1972); V. N. Gribov and L. N. Lipatov, Sov. J. Nucl. Phys. **15**, 675 (1972); G. Altarelli and G. Parisi, Nucl. Phys. B **126**, 298 (1977).

3. K. J. Eskola, Nucl. Phys. A **910-911**, 163 (2013), arXiv:1209.1546 [hep-ph].

4. H. Paukkunen, Nucl. Phys. A **926**, 24 (2014), arXiv:1401.2345 [hep-ph].

5. H. Paukkunen, Nucl. Phys. A **967**, 241 (2017), arXiv:1704.04036 [hep-ph].

6. K. J. Eskola, V. J. Kolhinen and P. V. Ruuskanen, Nucl. Phys. B **535**, 351 (1998) [hep-ph/9802350]; K. J. Eskola, V. J. Kolhinen and C. A. Salgado, Eur. Phys. J. C **9**, 61 (1999) [hep-ph/9807297].

7. M. Hirai, S. Kumano and M. Miyama, Phys. Rev. D **64**, 034003 (2001) [hep-ph/0103208].

8. D. de Florian and R. Sassot, Phys. Rev. D **69**, 074028 (2004) [hep-ph/0311227].

9. K. J. Eskola, H. Paukkunen and C. A. Salgado, JHEP **0807**, 102 (2008), arXiv:0802.0139 [hep-ph].

10. J. Gao, L. Harland-Lang and J. Rojo, arXiv:1709.04922 [hep-ph].

11. K. J. Eskola, P. Paakkinen, H. Paukkunen and C. A. Salgado, Eur. Phys. J. C **77** no.3, 163 (2017), arXiv:1612.05741 [hep-ph].

12. J. Pumplin, D. Stump, R. Brock, D. Casey, J. Huston, J. Kalk, H. L. Lai and W. K. Tung, Phys. Rev. D **65**, 014013 (2001) [hep-ph/0101032].

13. K. J. Eskola, H. Paukkunen and C. A. Salgado, JHEP **0904**, 065 (2009), arXiv:0902.4154 [hep-ph].

14. D. de Florian, R. Sassot, P. Zurita and M. Stratmann, Phys. Rev. D **85**, 074028 (2012), arXiv:1112.6324 [hep-ph].

15. H. Khanpour and S. Atashbar Tehrani, Phys. Rev. D **93** no.1, 014026 (2016), arXiv:1601.00939 [hep-ph].

16. K. Kovarik *et al.*, Phys. Rev. D **93** no.8, 085037 (2016), arXiv:1509.00792 [hep-ph].

17. R. S. Thorne and W. K. Tung, arXiv:0809.0714 [hep-ph].

Frascati Physics Series Vol. 65 (2017)
LFC17: Old and New Strong Interactions from LHC to Future Colliders
11 - 15 September, 2017

HEAVY FLAVOUR IN HIGH-ENERGY NUCLEAR COLLISIONS: THEORY OVERVIEW OF TRANSPORT CALCULATIONS

Andrea Beraudo
INFN - Sezione di Torino

Abstract

Transport calculations are the tool to study medium modifications of heavy-flavour particle distributions in high-energy nuclear collisions. We give a brief overview on their state-of-the art, on the information one can extract, on the questions remaining open and on further analysis to carry out in the near future.

1 Introduction

The description of heavy-flavour (HF) observables in relativistic heavy-ion collisions requires to develop an involved multi-step setup. One has to simulate the initial $Q\overline{Q}$ production in a hard process and for this automated QCD event generators – to validate against proton-proton data – are available, possibly supplemented with initial-state effects, like nuclear Parton Distribution Functions. One has then to rely on a description of the background medium, provided by hydrodynamic calculations tuned to reproduce soft-hadron data. One needs then to model the interaction of the heavy quarks with the medium, summarized in a few transport coefficients in principle derived from QCD, but for which we are still far from a definite answer for the experimentally relevant conditions. One can then describe the heavy-quark dynamics in the medium: under well-defined kinematic conditions this can be done rigorously through transport equations, which however require the above transport coefficients as an input. The heavy quarks, once they reach a fluid-cell below the deconfinement temperature, undergo hadronization; one can expect that, at variance with the case of elementary collisions, some sort of recombination with the abundant nearby partons is at work. This represents an item of interest in itself, but at the same time the related theoretical uncertainties affect the predictions for the final hadronic observables, preventing one from getting an unambiguous information on the partonic stage. Finally, D and B mesons can still rescatter with the surrounding hadrons before reaching kinetic freeze-out: also this possible effect deserves some

study. In the following we will discuss the above items in a more quantitative way, eventually considering how the above setup can be applied to perform more refined analysis of the final HF particle distributions and extended to the study of HF production in small systems, like high-multiplicity proton-proton/nucleus collisions.

2 Transport calculations: theoretical setup

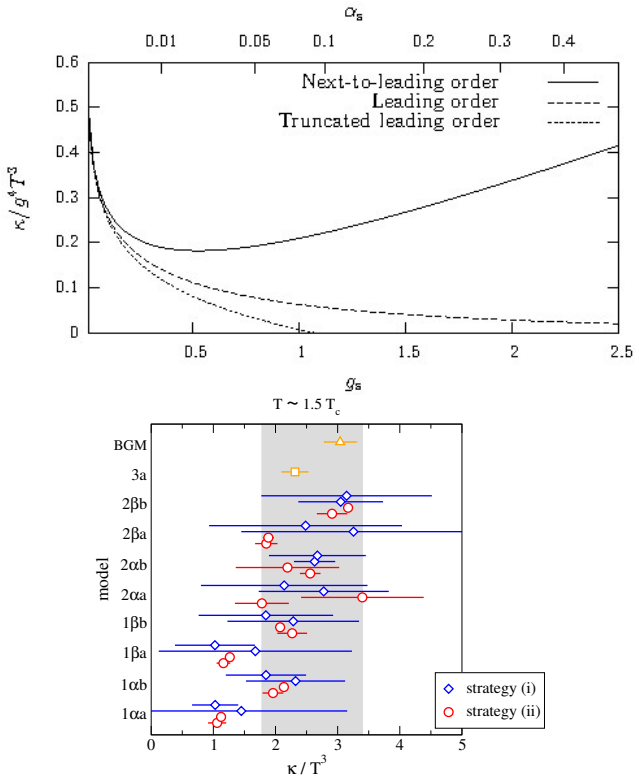

Figure 1: Momentum-diffusion coefficient k. Left panel: result of a NLO weak-coupling calculation [1]. Right panel: continuum-extrapolated lattice-QCD results for a gluon plasma [2].

Transport calculations for c and b quarks in heavy-ion collisions are usually formulated in terms of the relativistic Langevin equation [3, 4, 5]

$$\Delta\vec{p}/\Delta t = -\eta_D(p)\vec{p} + \vec{\xi}(t). \tag{1}$$

In the time-step Δt the heavy-quark momentum changes due to a deterministic friction force (quantified by the coefficient η_D) and a random noise term $\vec{\xi}$ fixed by its temporal correlator

$$\langle \xi^i(\vec{p}_t)\xi^j(\vec{p}_{t'})\rangle = b^{ij}(\vec{p}_t)\delta_{tt'}/\Delta t, \quad \text{with} \quad b^{ij}(\vec{p}) \equiv \kappa_\parallel(p)\hat{p}^i\hat{p}^j + \kappa_\perp(p)(\delta^{ij} - \hat{p}^i\hat{p}^j). \tag{2}$$

In the above the transport coefficients $\kappa_\parallel(p)$ and $\kappa_\perp(p)$ describe the longitudinal and transverse momentum broadening acquired by the heavy quark while propagating through the medium. In the non-relativistic limit one can ignore the dependence on the heavy-quark momentum and simply set

$\kappa_\parallel(p) = \kappa_\perp(p) \equiv \kappa$. In such a limit, from the large-time behaviour of the average squared displacement, one can identify the spatial diffusion coefficient D_s:

$$\langle \vec{x}^2(t) \rangle \underset{t\to\infty}{\sim} 6 D_s t \quad \text{with} \quad D_S = \frac{2T^2}{\kappa}. \tag{3}$$

The latter is often used to quantify the strength of the coupling with the medium.

First principle theoretical results are available for κ in the static $M \to \infty$ limit, arising both from analytic weak-coupling calculations [1)] and from lattice-QCD simulations [2)]. In the left panel of Fig. 1 one can see how, for realistic values of α_s, the weak-coupling calculation for κ receives large NLO corrections, arising mainly from overlapping scattering processes with the light partons from the medium. In the case of lattice-QCD calculations, on the other hand, the right panel of Fig. 1 shows that the final result is affected by large systematic theoretical uncertainties arising from the extraction of real-time information from simulations performed in an Euclidean spacetime. Taking into account the large systematic uncertainties, the two calculations provide results in rough agreement.

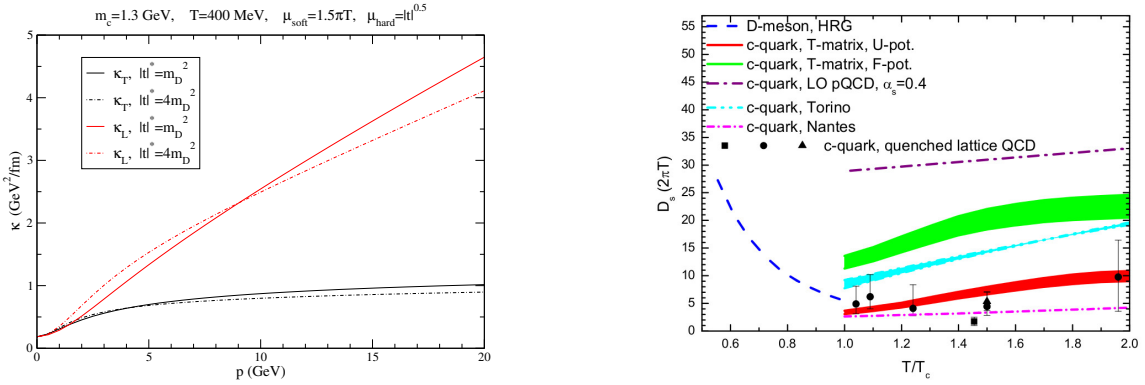

Figure 2: Left panel: charm momentum-broadening coefficients from the weak-coupling calculation in [6)]. Right panel: charm spatial diffusion coefficient provided by different theoretical models [7)].

Unfortunately, experimentally, the accessible kinematic range for heavy-flavour hadron detection covers mainly relativistic momenta. Hence, transport simulations require a theoretical input going beyond the result of the above static calculations and one needs to consider the full momentum dependence of the coefficients. This was done for instance in [6)] with a weak-coupling calculation with Hard-Thermal-Loop (HTL) resummation of medium effects: results for $\kappa_\parallel(p)$ and $\kappa_\perp(p)$ are displayed in the left panel of Fig. 2. Although the figure clearly shows that the dependence on the particle momentum is relevant and very different for the transverse and the longitudinal coefficients, in comparing the results of different transport calculations one very often simply employs the spatial diffusion coefficient D_s defined in Eq. (3) to enlighten the differences of the various models; a collection of results for D_s obtained under different theoretical frameworks is shown in the right panel of Fig. 2 [7)].

3 Heavy-flavour production in nucleus-nucleus collisions

Eq. (1), once interfaced with a realistic model for the evolution of the background medium, allows one to study the propagation of the heavy quarks throughout the fireball produced in high-energy nuclear collisions until they reach a fluid cell below the critical deconfinement temperature, where they are

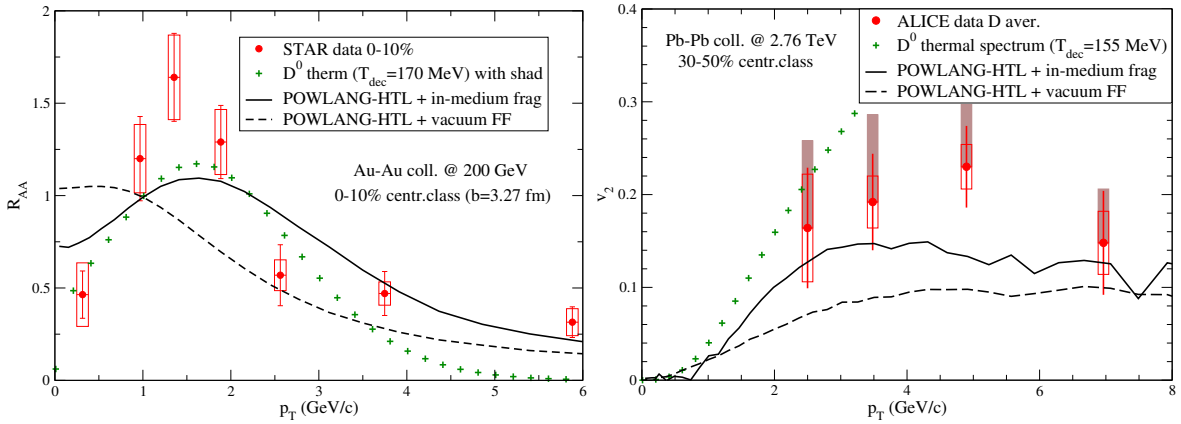

Figure 3: Results for the D-meson $R_{\rm AA}$ and v_2 in nucleus-nucleus collisions [8] arising from the heavy quark transport (dashed curves) and transport + in-medium hadronization (continuous curves) compared to experimental data [9, 10]. Green crosses refer to the kinetic-equilibrium limit.

forced to hadronize. One can then study the modification of the HF hadron distributions introduced by the medium. This is usually done via the nuclear modification factor $R_{\rm AA}$, i.e. the ratio of the spectra in A+A and p+p collisions (rescaled by the number of binary nucleon-nucleon collisions), and the $v_n \equiv \langle \cos[n(\phi - \psi_n)] \rangle$ coefficients, quantifying the asymmetry of the azimuthal particle distributions. One usually focus on the elliptic-flow coefficient v_2, arising mainly from the finite impact parameter of the A+A collision: the initial geometric deformation is converted by the pressure gradients into an anisotropic flow of the matter. The interaction of the heavy quarks with the medium, depending on its strength, leads to a quenching of the HF hadron spectra at high p_T – due to parton energy-loss – to a possible enhancement in the intermediate p_T region – partly due to the radial flow inherited from the fireball and partly due to the conservation of the number of charm/beauty quarks – and to an asymmetry in the azimuthal distribution of HF particles, reflecting the anisotropic geometry and flow of the background medium. Concerning the effect of hadronization, while the latter in the vacuum is usually described in terms of fragmentation functions and leads to an energy degradation of the parent parton, there is evidence that in nuclear collisions recombination with the nearby partons from the medium plays a major role. The process was modeled in several ways in the literature [13, 14, 8], leading however to similar effects in the particle distributions. In Fig. 3 we display some results of the POWLANG model [8], in which hadronization is modeled via fragmentation of color-singlet string/clusters formed through the recombination of a heavy quark with a light thermal anti-quark from the same fluid-cell. It turns out that the light parton from the medium transfers part of its collective (radial and elliptic) flow to the final D-meson, leading to a bump at moderate p_T in the $R_{\rm AA}$ and to an enhancement of the v_2 and moving theory predictions closer to the experimental data [9, 10].

Besides the initial elliptic deformation of the fireball – arising mainly from the finite impact parameter of the collision of the two nuclei – event-by-event fluctuations in the nucleon positions and, possibly, of sub-nucleonic degrees of freedom represent a further source of azimuthal asymmetry, giving rises to higher flow harmonics, absent in the case of smooth initial conditions. At this regard, in Fig. 4 we display the predictions of the POWLANG model for the triangular flow v_3 of D mesons in Pb-Pb collisions at $\sqrt{s_{NN}}$=5.02 TeV [11] compared to preliminary CMS data [12].

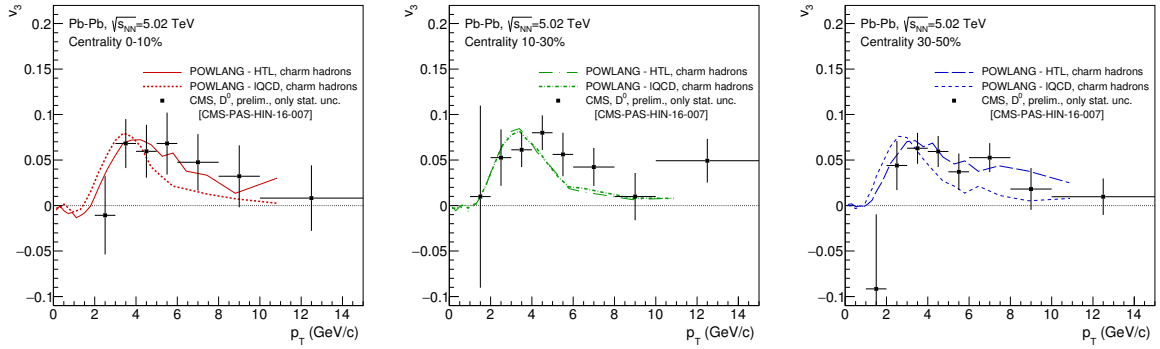

Figure 4: POWLANG predictions for the triangular flow of D mesons in Pb-Pb collisions at the LHC [11] compared to preliminary CMS data [12].

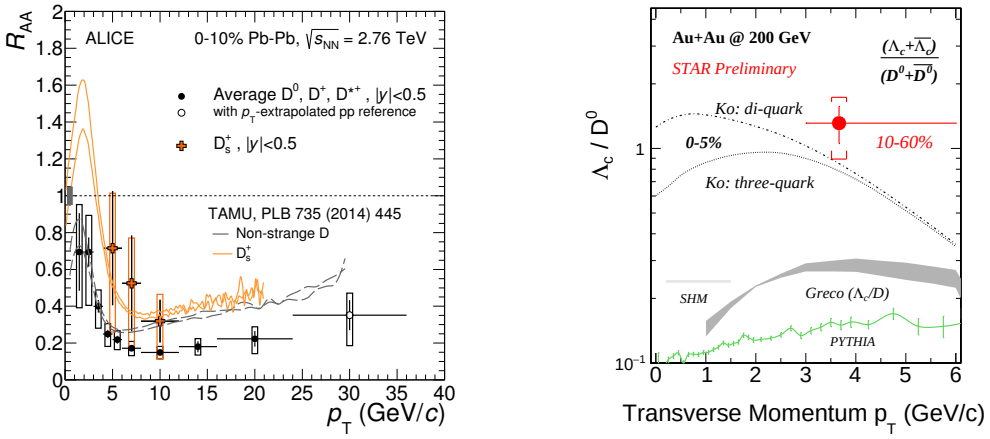

Figure 5: First results for D_s [15] and Λ_c [16] production in nucleus-nucleus collisions compared to transport calculations including in-medium hadronization [17, 18].

Besides modifying the momentum distribution of the final hadrons, recombination can also change the heavy-flavour hadrochemistry, leading for instance to an enhanced production of D_s mesons and Λ_c baryons. Predictions obtained with models based on the formation of resonant states around the phase transition [17] and on the coalescence of quarks and di-quarks [18] are shown in Fig. 5 and compared to ALICE [15] and preliminary STAR data [16].

Finally, although crossing a medium with a lower temperature and hence milder values of the transport coefficients, heavy-flavour particles can suffer rescattering also in the hadronic phase, where the radial and elliptic flow of the fireball is the largest. It is then of interest to evaluate within some effective chiral Lagrangian the transport coefficients of D/B-mesons in a gas of light hadrons [19], whose values – as a function of the temperature – turn out to join quite smoothly the results in the partonic phase (left panel of Fig. 6). One can then include also the possibility of rescattering in the hadronic phase in the transport simulations, however the effect on the final observables is found to be quite small, as shown in the right panel of Fig. 6 which refers to the elliptic flow of electrons from semi-leptonic decays

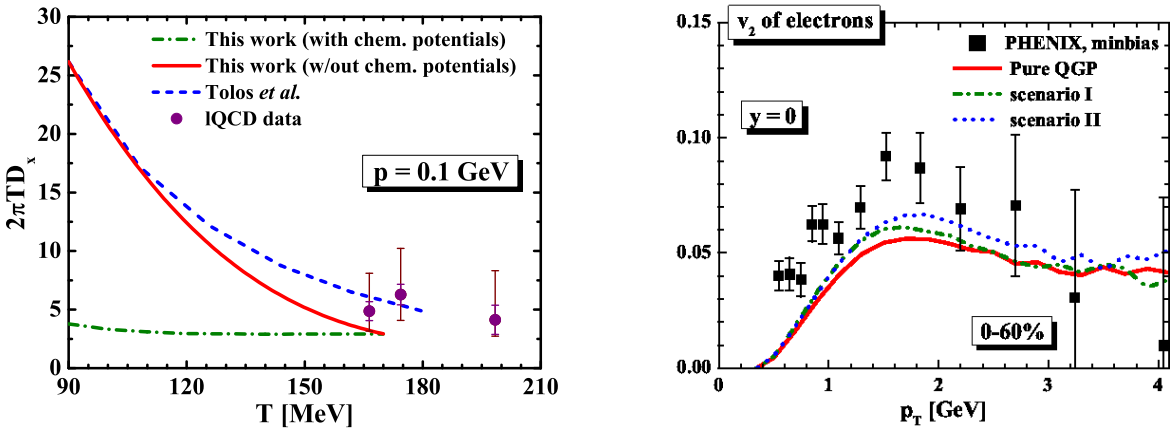

Figure 6: The heavy-quark spatial diffusion coefficient in the hadronic phase (left panel) and its effect on a transport calculation [19] (right panel). Data refer to the heavy-flavour decay electron v_2 measured in [20].

of charm and beauty hadrons [20].

4 Heavy-flavour production in small systems

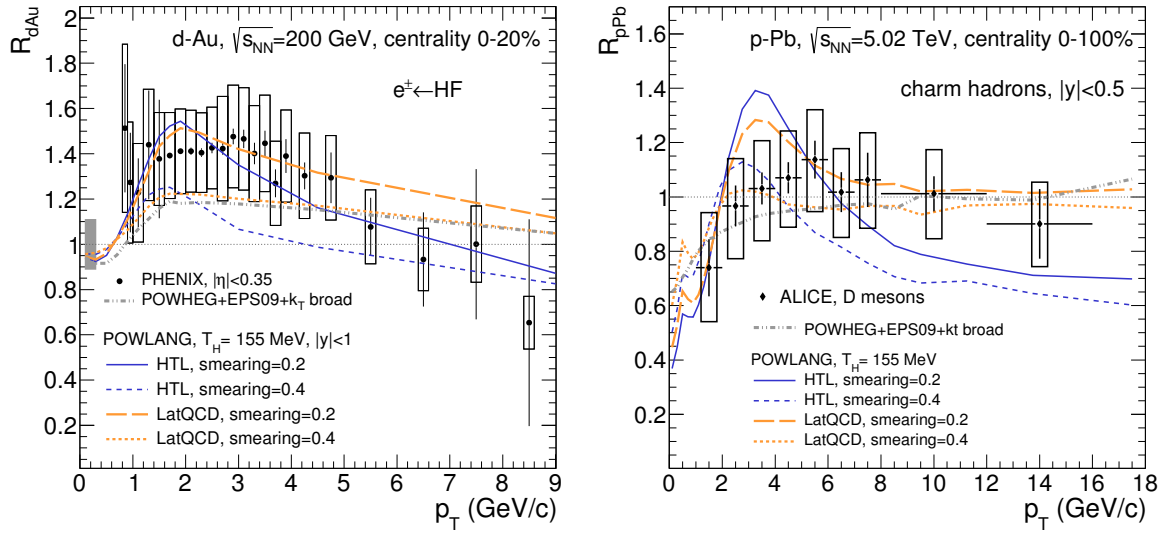

Figure 7: The nuclear modification factor of heavy-flavour decay electrons and D-mesons in d-Au and p-Pb collisions at RHIC and LHC. Transport-model results with different transport coefficients [21] are compared to experimental data [22, 23].

The observation of signatures of collective effects in measurements of particle correlations performed in high-multiplicity proton-nucleus and proton-proton collisions as well as the universal trend of the

integrated particle yields as a function of the final hadron multiplicity led people to wonder about the nature of the possible medium produced in such events. In parallel, no strong evidence of jet-quenching was found in p-p and p-A data: the medium seems to be strongly interacting but not very opaque to highly energetic probes. Hence the interest in studying heavy-flavour production within a transport setup also in the case of small systems. This was done for instance by the POWLANG authors in [21]. Results are shown in Fig. 7, referring to electrons from charm and beauty decays in central d-Au collisions and to charmed hadrons in minimum bias Pb-Pb events. Deviations from unity arise from the interplay of several effects: nuclear PDF's, k_T-broadening in cold nuclear matter, transport in the partonic phase and in-medium hadronization. The large systematic uncertainties of the experimental data [22, 23] do not allow one to draw firm conclusions, but leave room for medium effects.

5 Conclusions and perspectives

The comparison of current transport calculations with experimental data provides strong evidence that charm quarks interact significantly with the medium formed in heavy-ion collision, which affects both their propagation in the plasma and their hadronization. A number of experimental challenges or theoretical questions remain to be answered: charm measurements down to $p_T \to 0$ will provide more solid information on its possible thermalization and production cross-section (of relevance to quantify charmonium suppression!); D_s and Λ_c measurements will shed light on the issue of possible changes in the HF hadrochemistry and, again, on the total charm cross-section; finally, beauty measurements – due to the large heavy-quark mass – will be the golden channel to extract information on the HF transport coefficient from the data.

References

1. S. Caron-Huot and G. D. Moore, *JHEP* **02** (2008) 081.
2. A. Francis *et al.*,, *Phys. Rev.* **D92** (2015) 116003.
3. G. D. Moore and D. Teaney, *Phys. Rev.* **C71** (2005) 064904.
4. W. M. Alberico *et al*, *Eur. Phys. J.* **C71** (2011) 1666.
5. M. He *et al*, *Phys. Rev.* **E88** (2013) 032138.
6. W. M. Alberico *et al*, *Eur. Phys. J.* **C73** (2013) 2481.
7. F. Prino and R. Rapp, *J. Phys.* **G43** (2016) 093002.
8. A. Beraudo *et al*, *Eur. Phys. J.* **C75** (2015) 121.
9. STAR collaboration, L. Adamczyk *et al*, *Phys. Rev. Lett.* **113** (2014) 142301.
10. ALICE collaboration, B. Abelev *et al*, *Phys. Rev. Lett.* **111** (2013) 102301.
11. A. Beraudo *et al*, `1712.00588`.
12. CMS collaboration, Albert M. Sirunyan *et al*, `1708.03497`.
13. V. Greco, C. M. Ko and R. Rapp, *Phys. Lett.* **B595** (2004) 202–208.

14. P. B. Gossiaux, R. Bierkandt and J. Aichelin, *Phys. Rev.* **C79** (2009) 044906.

15. ALICE collaboration, J. Adam *et al.*, *JHEP* **03** (2016) 082.

16. STAR collaboration, L. Zhou, 1704.04364.

17. M. He, R. J. Fries and R. Rapp, *Phys. Lett.* **B735** (2014) 445–450.

18. Y. Oh, C. M. Ko, S. H. Lee and S. Yasui *Phys. Rev.* **C79** (2009) 044905.

19. V. Ozvenchuk *et al.*, *Phys. Rev.* **C90** (2014) 054909.

20. PHENIX collaboration, A. Adare *et al*, *Phys. Rev. Lett.* **98** (2007) 172301.

21. A. Beraudo *et al*, *JHEP* **03** (2016) 123.

22. PHENIX collaboration, A. Adare *et al*, *Phys. Rev. Lett.* **109** (2012) 242301.

23. ALICE collaboration, B. B. Abelev *et al.*, *Phys. Rev. Lett.* **113** (2014) 232301.

Frascati Physics Series Vol. 65 (2017)
LFC17: Old and New Strong Interactions from LHC to Future Colliders
11 - 15 September. 2017

TOP QUARK PHENOMENOLOGY AT THE LHC

Alberto Orso Maria Iorio
Università degli Studi di Napoli Federico II and INFN, Naples Section

Abstract

An outlook on the top quark phenomenology at the LHC is presented. Measurements of inclusive and differential top quark production through strong and electroweak processes are reported, and their impact on the modeling of top quark physics is discussed. Measurements of coupling properties sensitive to physics beyond the standard model appearing in the interaction vertex, like spin correlations and top polarisation, are displayed, and the latest measurements of the top quark width are shown. Finally, the state-of-the-art of the top quark mass measurements is illustrated, including the highest precision measurements and the world-wide combination across the LHC and Tevatron experiments.

1 Introduction

After more than 20 years since the top quark discovery, the study of top quark physics has evolved from the early stages of exploration of the main features of the production towards precision tests of the standard model, aiming at improving the understanding of the modeling of perturbative Quantum Chromo Dynamics to probe the electroweak sector of top quark physics, which could provide for hints of new physics beyond the standard model. At the Large Hadron Collider, several tenths of millions of top quarks have been produced since the beginning of Run-I in proton-proton collision data at 7, 8, and 13 TeV. Two main mechanisms of production at the LHC, top quark pair and single top quark production can be studied by performing inclusive and differential measurements of kinematic and angular variables. The top quark mass is a fundamental parameter of the standard model that can be measured directly with increasingly high precision in top quark events. Given the abundance of top quark production cross section at the LHC, the uncertainty is dominated by systematic effects and modeling effects. At the same time, the high luminosity allows for the exploration of extremely rare SM processes, sensitive

to new physics beyond the standard model. In this article, measurements of inclusive and differential production of top quark pairs and singly-produced top quarks are presented, and precision measurements are reported of top quark mass as well as angular measurements probing the electroweak vertex structure.

2 Strong production

The primary production mechanism for top quark at the LHC is strong production of $q\bar{q}$ pairs, gluon-gluon fusion amounting to approximately 80% of the total. Inclusive and differential $t\bar{t}$ cross sections can provide probes for perturbative and non-perturbative Quantum Chromo Dynamics in top quark physics.

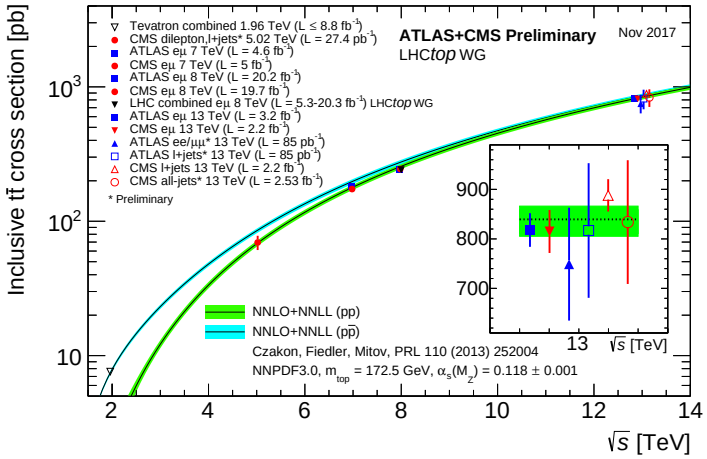

Figure 1: Cross section for $t\bar{t}$ pair production in pp collisions as a function of centre-of-mass energy compared to the NLO+NNLL theoretical predictions.

The measurement of the inclusive $t\bar{t}$ cross-section, $\sigma_{t\bar{t}}$, is sensitive to the strong coupling constant, the gluon parton distribution functions (PDF), and the top quark mass. Furthermore, top production is also one of the main source of backgrounds in many searches for physics beyond the Standard Model(SM), and therefore the study of its production and decay properties forms a core part of the LHC physics program. Inclusive cross-section measurements are of particular importance as theoretical $t\bar{t}$ calculations are nowadays available with a precision of 5−10% [1], a level which is comparable to recent experimental measurements. A variety of decay topologies is used by the ATLAS and CMS collaborations to determine the inclusive production cross-section, where the most precise results are obtained by using events with an opposite-charge isolated electron and muon pair and additional b-tagged jets. Additional information on the gluon parton distribution functions is extracted by CMS by measuring the tt production cross section at a centre-of-mass energy of 5.02 TeV with 27.4 pb^{-1} [2]. The LHCb experiments can provide additional insight to the production in the forward direction, but only the final state with a single muon and a b-tagged jet is statistically accessible in the Run-I data set because of the lower rate of luminosity and smaller fiducial acceptance than the general purpose detectors.

The cross-section for production at $\sqrt{s} = 7, 8$ [3, 4], and 13 TeV [5, 13] is measured by CMS and the ATLAS collaborations using data sets corresponding to an integrated luminosities of 4.6 (5.0), 20.3 (19.7) and 3.2 (2.3) fb^{-1}, respectively for ATLAS and CMS. The cross sections are measured to be:

$$\sigma_{t\bar{t}}^{7\text{TeV}} = 182.9 \pm 3.1(\text{stat.}) \pm 4.2(\text{syst.}) \pm 3.6(\text{lumi.}) \pm 3.3(\text{beam}) \text{ pb},$$
$$\sigma_{t\bar{t}}^{8\text{TeV}} = 242.4 \pm 1.7(\text{stat.}) \pm 5.5(\text{syst.}) \pm 7.5(\text{lumi.}) \pm 4.2(\text{beam}) \text{ pb},$$
$$\sigma_{t\bar{t}}^{13\text{TeV}} = 803 \pm 7(\text{stat.})27(\text{syst.}) \pm 45(\text{lumi.}) \pm 12(\text{beam}) \text{ pb},$$

for ATLAS, and:

$$\sigma_{t\bar{t}}^{7\text{TeV}} = 173.6 \pm 2.1(\text{stat.})^{+4.5}_{-4.0}(\text{syst.}) \pm 3.8(\text{lumi.}) \text{ pb},$$
$$\sigma_{t\bar{t}}^{8\text{TeV}} = 244.9 \pm 1.4(\text{stat.})^{+6.3}_{-5.5}(\text{syst.}) \pm 6.4(\text{lumi.})\text{pb},$$
$$\sigma_{t\bar{t}}^{13\text{TeV}} = 793 \pm 8(\text{stat.}) \pm 38(\text{syst.}) \pm 21(\text{lumi.}) \text{ pb}.$$

for CMS.

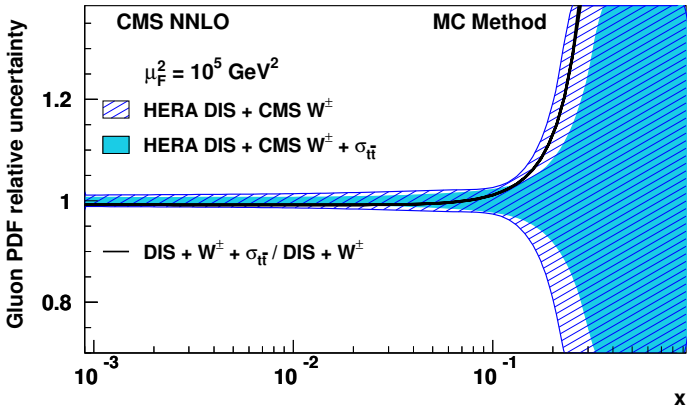

Figure 2: The relative uncertainties in the gluon distribution function of the proton including the HERA DIS and CMS muon charge asymmetry measurements (hatched area), and also including the CMS result $\sigma_{t\bar{t}}$ at $\sqrt{s} = 5.02$ TeV.

The $t\bar{t}$ cross-section evolution with the centre-of-mass energy is presented in Fig. 1. The results are consistent with recent theoretical QCD calculations at NNLO. The impact of the $t\bar{t}$ cross section measurements at 5.02 TeV on gluon parton distribution functions is shown in Fig. 2. The cross-section for top production at $\sqrt{s} = 7$ and 8 TeV [14] is measured by the LHCb collaboration using datasets corresponding to an integrated luminosities of approximately 1 and 2 fb^{-1} . A significance of 5.4σ is obtained, confirming the observation of top quark production in the forward region. The excess is used to calculate the cross-section for top quark production, which includes contributions from both $t\bar{t}$ and single-top-quark production. The cross sections are measured to be:

$$\sigma_{t\bar{t}}^{7\text{TeV}} = 173.6 \pm 3.1(\text{stat.})4.2(\text{syst.}) \pm 3.6(\text{theory}) \text{ fb}$$
$$\sigma_{t\bar{t}}^{8\text{TeV}} = 242.4 \pm 1.7(\text{stat.})5.5(\text{syst.}) \pm 3.6(\text{theory}) \text{ fb}$$

2.1 Differential measurements

The study of the production cross section of top quarks at high energies is a crucial ingredient in testing the standard model and searching for new physics that may alter the production rate. In particular, the differential $t\bar{t}$ cross section as a function of the $t\bar{t}$ kinematic variables is a perfect test of the modeling used in the simulations also sensitive to higher order QCD predictions.

The ATLAS and CMS collaboration has published measurements of the $t\bar{t}$ differential cross sections at 8 TeV, with an integrated luminosity of 20.3 fb^{-1} [8, 9] and 19.7 fb^{-1} [6, 7], respectively.

The results from the two analyses are compatible in all the kinematic dependencies and in both the resolved and boosted regime as shown in Figures 3(a) and 3(c), for CMS, and Figures 3(b) and 3(d), for ATLAS. Both analyses see an overestimation in the MC predictions, especially at high energies. A better agreement is found when using the new NNLO QCD predictions.

A similar trend is observed in the measurements performed at 13 TeV by both experiments, with an integrated luminosity of and 2.3 fb^{-1} (CMS) [11] and 3.2 fb^{-1}(ATLAS) [12], respectively. The results are displayed in Figures 3(c) and 3(d).

Double-differential measurements of the $t\bar{t}$ cross section allow to set stringent constrains on parton distribution functions. Measurements are performed by CMS with 8 TeV data to the tt cross section as function of pairs of kinematic variables [10]. Events with an opposite sign electron-muon pair have been selected, and the effect of the cross section measurement on parton distribution function is evaluated for the different combinations of kinematic variables. Fig. 4(a) shows the cross section as a function of the top quark pair momentum and top quark pair mass, and Fig. 4(b) shows the impact on HERA parton distribution functions.

3 Single top quarks

Top quarks can be singly produced in proton-proton collisions via charged-current electroweak interactions. Three mechanisms contribute to single-top-quark production in the standard model, referred to as the t, s, and W-associated, or tW, channels. In proton-proton collisions at the Large Hadron Collider the t channel mode is by far the most abundant of the three. The study of single-top-quark production provides a unique possibility to investigate many aspects of top-quark physics that cannot be easily probed in $t\bar{t}$ production: one can investigate the tWb vertex structure looking for anomalous couplings [24] and flavor-changing neutral current (FCNC) contributions [25] in the production. Moreover, the cross-sections of all three channels are directly related to the modulus squared of the Cabibbo Kobayashi Maskawa matrix element V_{tb} . A summary of single-top-quark cross-section measurements is found in fig 5(a), while $|V_{\mathrm{tb}}|$ measurements are shown in Fig. 5(b). No deviation from the Standard Model prediction is observed.

3.1 t channel

Single-top-quark production in the t channel yields the highest cross section amongst the three production modes. First measurements of t channel cross section at 13 TeV were performed by ATLAS [26] and CMS [27], already reaching a systematics dominated regime. For both experiments, a selection is applied with two or three jets, one or two of which passing a b-tagging requirement. The main background processes are top pair production, W bosons associated to jets, and QCD multijet production. Multivariate discriminants, shown in Figs. 6(a), 6(b) for ATLAS and CMS respectively, are used to

discriminate the t channel signal from the aforementioned processes. The measured cross sections at 13 TeV result 229 ± 48pb (ATLAS) and 228 ± 33 pb (CMS).

3.2 tW associated production

Top quarks singly produced in association with W bosons, or tW, allow for a complementary route for new physics searches in the single-top-quark sector. This process was observed for the first time in 2014 by CMS [28], and subsequently by ATLAS [29]. Recently, the tW process cross section has been measured at 13 TeV as well by both collaborations CMS and ATLAS, resulting in 94 ± 10 (stat.)$^{+28}_{-22}$ (syst.) $\pm$ 2 (lumi.) pb (ATLAS) [31] and 63.1 ± 1.8 (stat.) ± 6.0 (syst.) ± 2.1 (lumi.) pb (CMS) [30].

3.3 s channel

The most rare of the three production modes for single-top is the s channel. Both ATLAS [32] and CMS [33] have performed searches for this channel at LHC in Run-I, looking for events with 1 lepton and 2 jets stemming from b hadronization in the final state. The ATLAS measurement resulted in the first evidence for the process at LHC, with an observed(expected) significance of 3.2(3.9) standard deviations. The measured cross sections at 8 and 7 TeV are:

$$\sigma^{8\text{TeV}}_{s-\text{channel}} = 4.8 \pm 0.8(\text{stat.})^{+1.6}_{-1.3}(\text{syst.}) \text{ pb, (ATLAS)}$$
$$\sigma^{8\text{TeV}}_{s-\text{channel}} = 13.4 \pm 7.3(\text{stat.} + \text{syst.}) \text{ pb, (CMS)}$$
$$\sigma^{8\text{TeV}}_{s-\text{channel}} = 7.1 \pm 8.1(\text{stat.} + \text{syst.}) \text{ pb (CMS).}$$

3.4 Associated tZq production

Processes involving the associated production of a single top quark and a Z boson are predicted by the standard model to happen at lower cross section with respect to the other modes of production. For this reason, processes involving a tZq vertex in production or in decay are extremely important to probe for potential contributions coming from new physics, which can cause an enhancement of in the way of flavour changing neutral currents in the top sector which are suppressed at tree level in the standard model. Both ATLAS [34] and CMS [35] have now found evidence for the production of tZq with data from Run-II, looking for channels where both the top quark and the Z boson decay leptonically, and building multivariate discriminants to reject the overwhelming backgrounds. The measured cross sections are in agreement with the standard model predictions. Figures 8(a) and 8(b) show the main discriminating variables for ATLAS and CMS. In the former case the output discriminant of a neural network is used, in the latter case two boosted decision tree discriminants are used together with the transverse mass of the W boson reconstructed in regions with 1, 2, and 0 b-jets, respectively.

4 Measurement of angular properties

4.1 Top quark charge asymmetry

In proton-proton collisions at the LHC, the larger average momentum fraction of the valence quarks leads to an excess of top quarks produced in the forward and backward directions, while the antitop quarks are produced more centrally. The asymmetry observable is defined as

$$A_C = \frac{N(\Delta|y| > 0) - N(\Delta|y| > 0)}{N(\Delta|y| > 0) + N(\Delta|y| > 0)}, \quad (1)$$

where $|y| = |y_t - |y_{\bar{t}}|$ and y denotes the rapidity of the top and anti-top quarks. The measurement of this observable is not precise enough to establish the existence of the SM charge asymmetry yet but its high sensitivity to new physics makes this analysis very interesting. Both the ATLAS [16, 17] and CMS [18] collaborations have published results based on the data collected at a centre-of-mass energy of 8 TeV. The analyses are performed in the lepton-plus-jets channel and in both the resolved and boosted kinematic regime. The results are presented both at parton level and in a particle fiducial phase space defined with a selection as close as possible to the reconstruction one. No deviations within two standard deviations from the Standard Model predictions are observed (Figure 9(a)). These measurements, especially the boosted one, provide a constraint on extensions of the SM (Figure 9(b)).

4.2 Top polarisation and CP violation

Top quark polarization can be measured in $t\bar{t}$ as well as single top quark events, and spin correlations are measured by the ATLAS [19] and CMS [20, 21] collaborations at $\sqrt{s} = 8$ TeV. Using the top quark polarization it is possible to estimate on the Wtb coupling element [22, 23]. Different observables are used to obtain unambiguous results. The most common one is the angle θ_{l*} between the lepton and its parent top quark spin axis. In case of $t\bar{t}$ events where two leptons are in the final state, the angle between the two leptons is also used. These are evaluated in the top rest frame and in the laboratory frame respectively. The measured top quark polarization and the spin correlation observables are compared to theoretical predictions in order to search for hypothetical top quark anomalous couplings (Figures 10). No evidence of new physics is observed allowing to place more stringent constrains upon Beyond SM theories. The limit fixed on the Wtb coupling element is also in agreement with the Standard Model prediction.

Sizable CP violating effects in the top quark sector can stem from beyond standard model theories aiming at explaining the matter- antimatter asymmetry in the universe. They can manifest in the top quark electroweak sector, and can therefore be probed in both strong pair production and in single-top-quark production. A measurement to four different observables potentially sensitive to CP violation is performed by by CMS with 8 TeV data [36]. The results are shown in Fig. 11(a). Measurements of top quark polarization in single-topquark processes have been performed in ATLAS [37] , where CP violating phases can affect both the production and decay vertexes. Several asymmetry observables are measured, and shown in Fig. 11(b). No deviation from the standard model expectation has been observed.

4.3 Top quark mass and width measurements

Precise measurements of the top quark mass are of crucial importance as it constitutes one of the fundamental Standard Model parameters. Since top quark decays via weak interaction, it is possible to have access to its decay products in order to define observables sensitive to the top quark mass, making it possible to determine it at the percent level. Measurements from LHC Run-I are leading in terms of precision, as they can profit from the detector calibrations obtained over the course of the years. The most precise single measurements from ATLAS [38] and CMS [39] are based on 8 TeV data, and extract simultaneously the top quark mass together with the jet energy scale from $t\bar{t}$. For CMS, the measurement is performed in the semi-leptonic decay channel, requiring one lepton and at least 4 jets. The hadronically decaying top quark is reconstructed from three jets, which are chosen by performing a kinematic

fit which allows to choose the best permutation of all selected jets. For ATLAS, the 8 TeV measurement is performed in the dileptonic decay channel, requiring two leptons and two b-jets. A template fit is performed on the mass distributions of the pairs of leptons and b-jets, retaining the permutation with the lowest invariant mass possible of the two lepton-b-jet pairs. The resulting measured top quark mass is for the two cases:

$$m_{top} = 172.99 \pm 0.41(\text{stat.}) \pm 0.74(\text{syst.}) \text{ GeV, (ATLAS)}$$
$$m_{top} = 172.35 \pm 0.16(\text{stat.} + \text{jsf}) \pm 0.48(\text{syst.}) \text{ GeV, (CMS)}$$

The variables used in the mass extraction for the two cases are shown in Fig. 12(a), 12(b), respectively for ATLAS and CMS.

The main systematic uncertainty sources for the above methods come from the b hadronization model and the color reconnection model. Several top quark mass measurements are performed by the dierent experiments with dierent techniques. While they lead to an overall lower precision for the single-measurement with respect to the two above mentioned, they allow to gain precision in a combination. The ultimate goal is to combine all measurements across dierent experiments to achieve the best possible precision. A world-wide combination is performed within the LHCTopWG [42]. An overview of the LHC measurements is shown in Fig. 13.

An important feature that can be measured directly in top quark decays is the decay width of the top quark. Models of new physics, predicting anomalous decays of top quarks into new particles, e.g. via additional higgs or Flavor Changing Neutral Currents, can modify the top quark decay width Γ_t. Both CMS [40] and ATLAS [41] have performed direct measurements of the top quark width, via observables sensitive to Γ_t like the reconstructed top quark mass in semi-leptonic events, yielding the following results:

$$\Gamma_t = 1.73 \pm 0.41(\text{stat.})^{+0.74}_{-68}(\text{syst.}) \text{ GeV (ATLAS)},$$
$$0.6 \leq \Gamma_t \leq 2.4 \text{ GeV at 95\% CL., (CMS)}.$$

Figure 14 shows the distribution of the most sensitive variables for the analyses of ATLAS and CMS.

5 Conclusions and outlook

Inclusive and differential measurements of top quark production cross sections have been discussed. Differential and double-differential measurements show high potential to constrain parton distribution functions and provide accurate modeling of QCD parameters, and with the increasing luminosity it will be possible to reach more extreme regions of the kinematic spectra. Single top quarks can provide sensitivity to modification of the standard model due to new physics appearing in the production vertex, and despite being more rare than pair production, they will provide a complementary route to constrain standard modeling parameters as well. While the top quark mass measurements with the Run-II data set are not yet competitive with 7 and 8 Tev, due to the calibrations and systematic uncertainties being more refined, going towards the end of Run-II the additional statistics provided by the increased instantaneous luminosity and cross section at 13 TeV will allow to study in the detail the systematic and modeling

effects affecting the measurement, exploiting data to ultimately reduce uncertainties. Finally, with the increasing statistics it will become possible to probe in the detail rare processes, like associated tZq production, searching for hints of new physics also in differential distributions.

References

1. M. Czakon, P. Fiedler and A. Mitov, Phys. Rev. Lett. 110,252004(2013), doi:10.1103/PhysRevLett.110.252004.
2. V. Khachatryan et al. [CMS Collaboration], [arxiv:1711.03143 [hep-ex]].
3. G. Aad et al. [ATLAS Collaboration], Eur.Phys.J. C 74, no.10,3109(2014), doi:10.1140/epjc/s10052-014-3109-7.
4. V. Khachatryan et al. [CMS Collaboration], [arXiv:1603.02303 [hep-ex]].
5. M. Aaboud et al. [ATLAS Collaboration], [arXiv:1606.02699 [hep-ex]].
6. V. Khachatryan et al. [CMS Collaboration], Eur.Phys.J. C (2015)75,542, doi:10.1140/epjc/s10052-015-3709-x.
7. V. Khachatryan et al. [CMS Collaboration], Phys.Rev. D 94(2016), 072002, doi:10.1103/PhysRevD.94.072002
8. M. Aaboud et al. [ATLAS Collaboration], Eur.Phys.J.C (2016) 76, 538 doi:10.1140/epjc/s10052-016-4366-4
9. M. Aaboud et al. [ATLAS Collaboration], Phys.Rev. D 93 (2016), 032009, doi:.10.1103/PhysRevD.93.032009.
10. V. Khachatryan et al. [CMS Collaboration], Eur.Phys.J. C (2017) 77, 459, doi:10.1140/epjc/s10052-017-4984-5.
11. V. Khachatryan et al. [CMS Collaboration], [arXiv:1708.07638 [hep-ex]].
12. M. Aaboud et al. [ATLAS Collaboration], JHEP 11(2017)191, doi:10.1007/JHEP11(2017)191.
13. V. Khachatryan et al. [CMS Collaboration], CMS-PAS-TOP-16-005.
14. R. Aaij et al. [LHCb Collaboration],Phys.Rev.Lett. 115, no.11, 112001 (2015),doi:10.1103/PhysRevLett.115.112001.
15. R. Aaij et al. [LHCb Collaboration], JINST 10, no.06, P06013 (2015), doi:10.1088/1748-0221/10/06/P06013.
16. G. Aad et al. [ATLAS Collaboration], Eur.Phys.J. C 76(2016) no.2, 87, doi:10.1140/epjc/s10052-016-3910-6.
17. G. Aad et al. [ATLAS Collaboration], Phys.Lett. B 756(2016)52, doi:10.1016/j.physletb.2016.02.055.
18. V. Khachatryan et al. [CMS Collaboration], Phys. Lett. B 757(2016)154, doi:10.1016/j.physletb.2016.03.060.

19. G. Aad et al. [ATLAS Collaboration], Phys.Rev.Lett. 114(2015) no.14, 142001, doi:10.1103/PhysRevLett.114.142001

20. V. Khachatryan et al. [CMS Collaboration], Phys.Rev. D 93(2016) no.5, 052007, doi:10.1103/PhysRevD.93.052007

21. V. Khachatryan et al. [CMS Collaboration], JHEP 1604, 073 (2016) doi:10.1007/JHEP04(2016)073.

22. [ATLAS Collaboration], ATLAS-CONF-2013-032.

23. V. Khachatryan et al. [CMS Collaboration], CMS-PAS-TOP-16-001.

24. Aguilar-Saavedra, J.,Nucl. Phys. B 804 (2008) 160-192

25. Gao, J. et al., Phys. Rev. Lett. 107 (2011) 092002.

26. [ATLAS Collaboration], JHEP 04 (2017) 086.

27. V. Khachatryan et al. [CMS Collaboration], Phys. Lett. B 772 (2017) 752 .

28. V. Khachatryan et al. [CMS Collaboration], PRL 112,231802.

29. G. Aad et al. [ATLAS Collaboration], JHEP 01 (2016) 064, doi:10.1007/JHEP01(2016)064.

30. V. Khachatryan et al. [CMS Collaboration], CMS-PAS-TOP-17-018.

31. G. Aad et al. [ATLAS Collaboration], JHEP01(2018)063, doi:10.1007/JHEP01(2018)063.

32. G. Aad et al. [ATLAS Collaboration], Phys.Lett.B(2016)228-246.

33. V. Khachatryan et al. [CMS Collaboration], JHEP 09 (2016) 027, doi:10.1007/JHEP09(2016)027.

34. G. Aad et al. [ATLAS Collaboration], [arXiv:1710.03659 [hep-ex]].

35. V. Khachatryan et al. [CMS Collaboration], [arXiv:1712.02825 [hep-ex]].

36. V. Khachatryan et al. [CMS Collaboration], JHEP 03 (2017) 101, doi:10.1007/JHEP03(2017)101.

37. G. Aad et al. [ATLAS Collaboration], JHEP 04 (2017) 124, doi:10.1007/JHEP04(2017)124.

38. G. Aad et al. [ATLAS Collaboration], Phys. Lett. B761(2016)350-371 doi:10.1016/j.physletb.2016.08.042.

39. V. Khachatryan et al. [CMS Collaboration], Phys. Rev. D 93 (2016) 072004.

40. V. Khachatryan et al. [CMS Collaboration], CMS-PAS-TOP-16-019

41. G. Aad et al. [ATLAS Collaboration], Eur. Phys. J. C (2018) 78-129, doi:10.1140/epjc/s10052-018-5595-5

42. The ATLAS, CMS, CDF, and D0 Collaborations, arXiv:1403.4427.

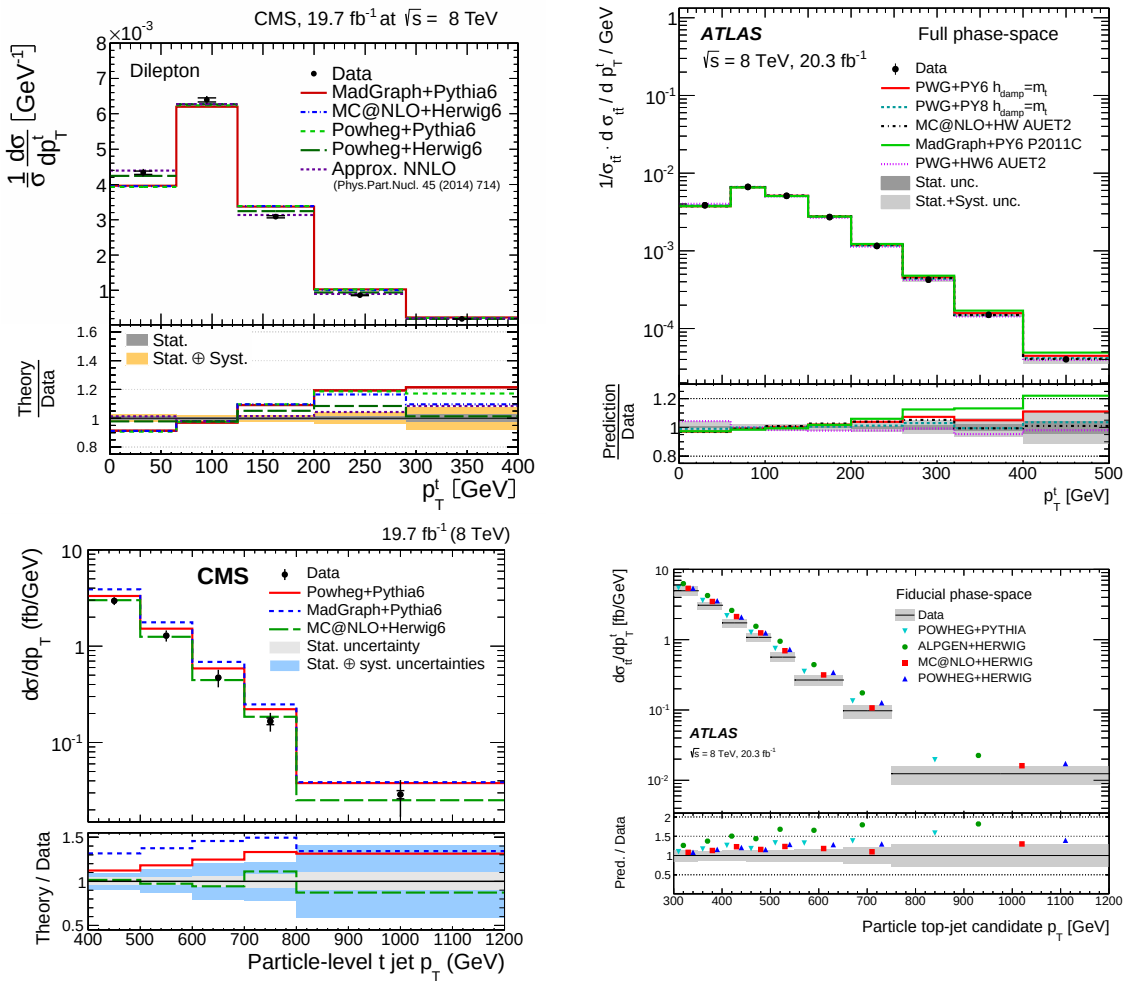

Figure 3: $t\bar{t}$ production cross section as function of top quark pair momentum at 8 TeV: from CMS (a) and ATLAS (b). Same quantity measured in the boosted regime at 8 TeV from CMS (c) and ATLAS (d).

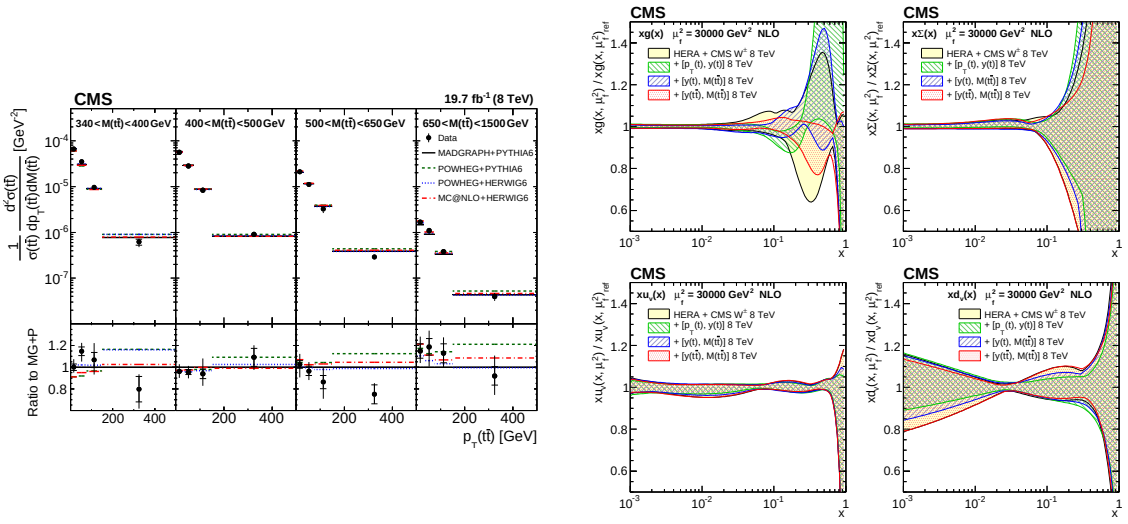

Figure 4: Double-differential $t\bar{t}$ production cross section as a function of the top quark pair transverse momentum $p_T(t\bar{t})$ and top quark pair mass $M(t\bar{t})$ measured with 8 TeV data by CMS (a) at 8 TeV (a). HERAPDF with and without including the double differential measurement (b).

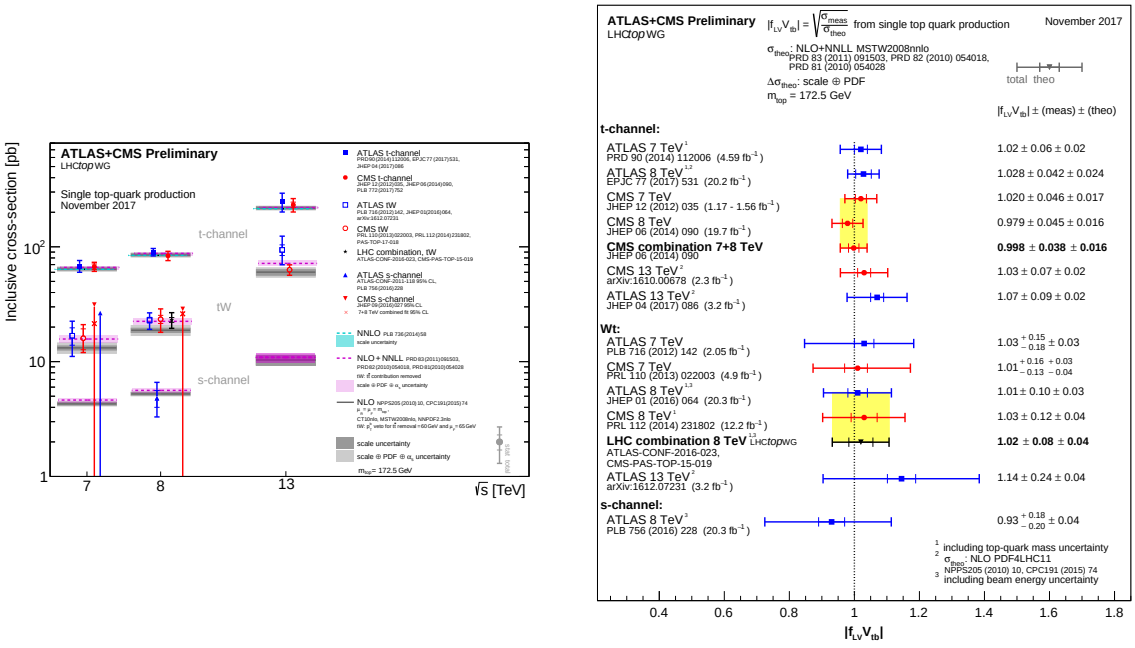

Figure 5: Single-top-quark production cross-section measurements at LHC as a function of the centre-of-mass energy(a) and measurements of $|V_{\mathrm{tb}}|$ from inclusive single-top-quark cross section(b).

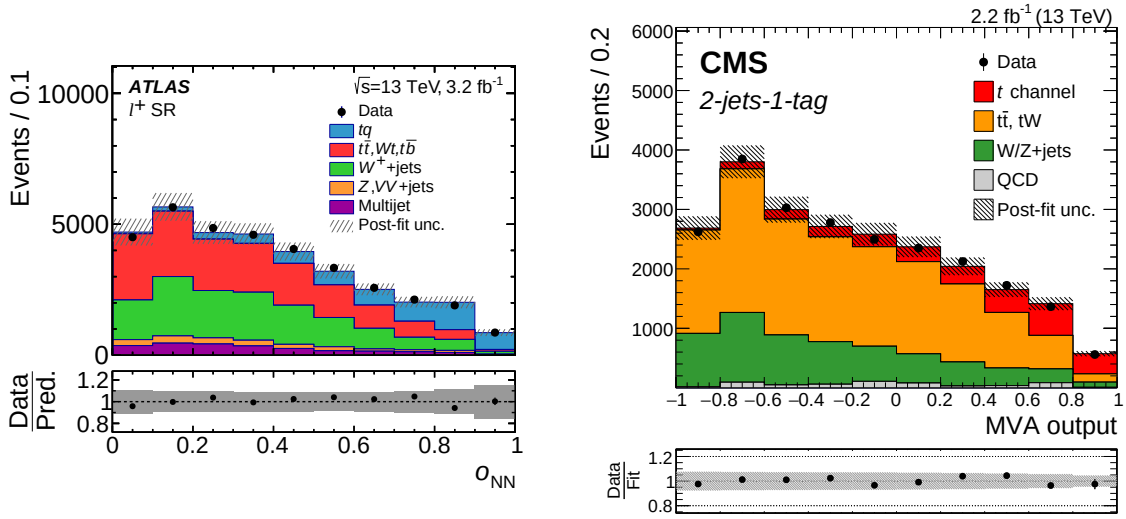

Figure 6: Discriminating observable used for t-channel single-top-quark production cross section extraction for ATLAS(a), the output discriminator of a boosted decision tree Method(a), and for CMS, the output discriminator of a neural network(b), at 13 TeV.

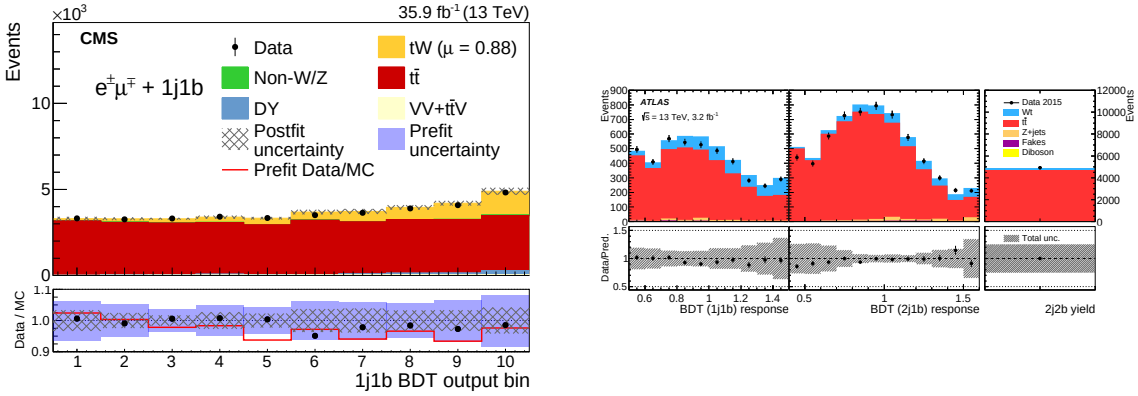

Figure 7: Discriminating variable used for W-associated single-top-quark production cross section extraction for CMS(a) and ATLAS(b) at 8 TeV). In both cases it is the output discriminator of a boosted decision tree.

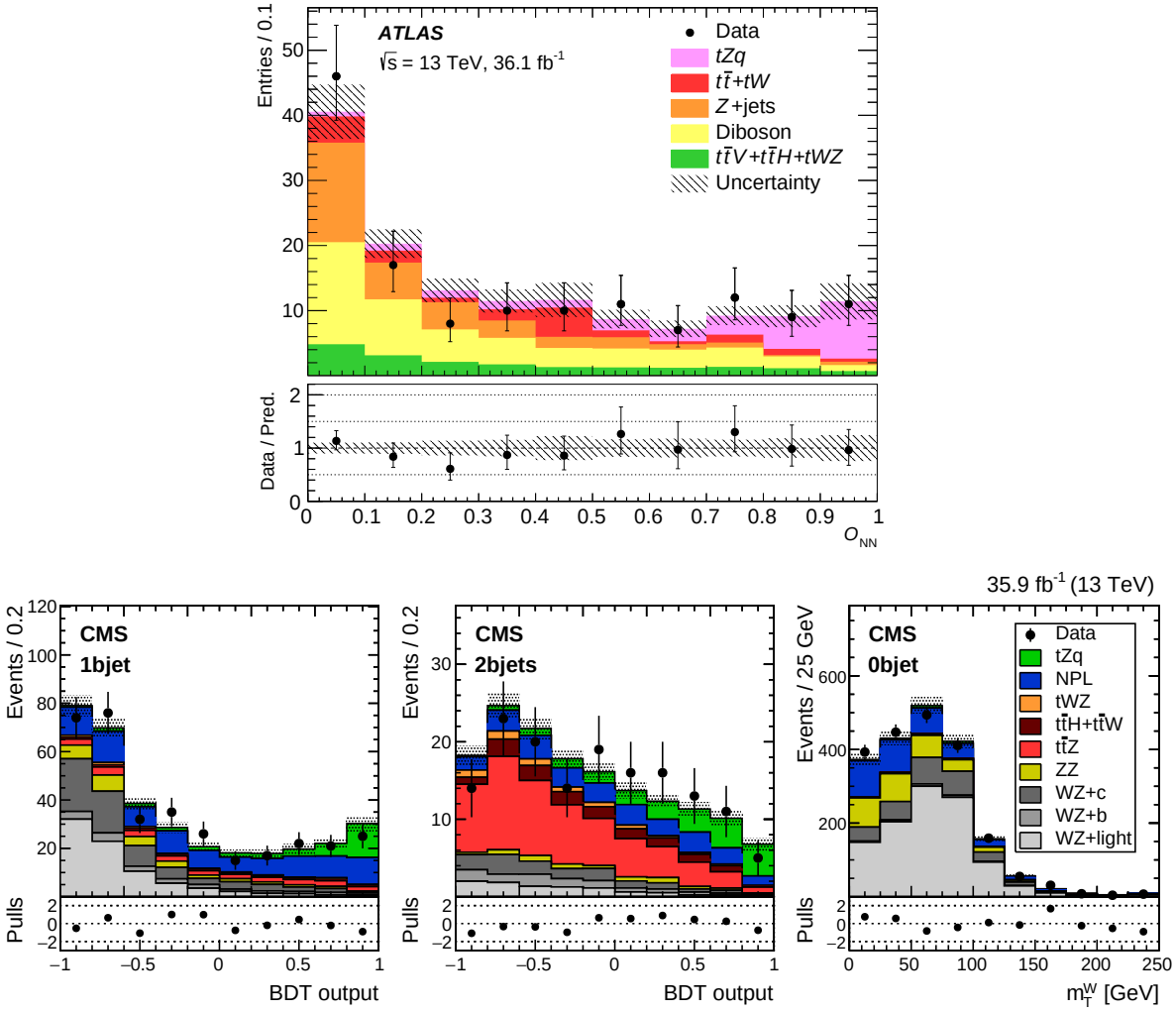

Figure 8: Discriminating variables used for tZq production cross section extraction at 13 TeV for ATLAS (a) and CMS (b). For ATLAS the output of a single neural network discriminant. For CMS two boosted decision tree discriminants are used together with the transverse mass of the W boson reconstructed in regions with 1, 2, and 0 b-jets, respectively.

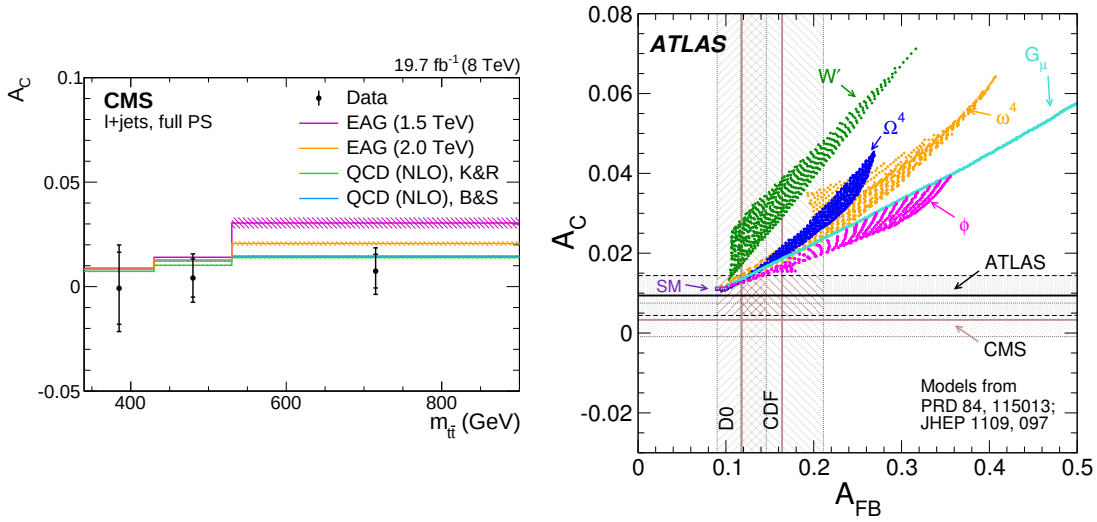

Figure 9: (a)Distribution of the asymmetry observable A_C as a function of the $t\bar{t}$ mass and (b) observed charged asymmetry compared with SM and BSM predictions.

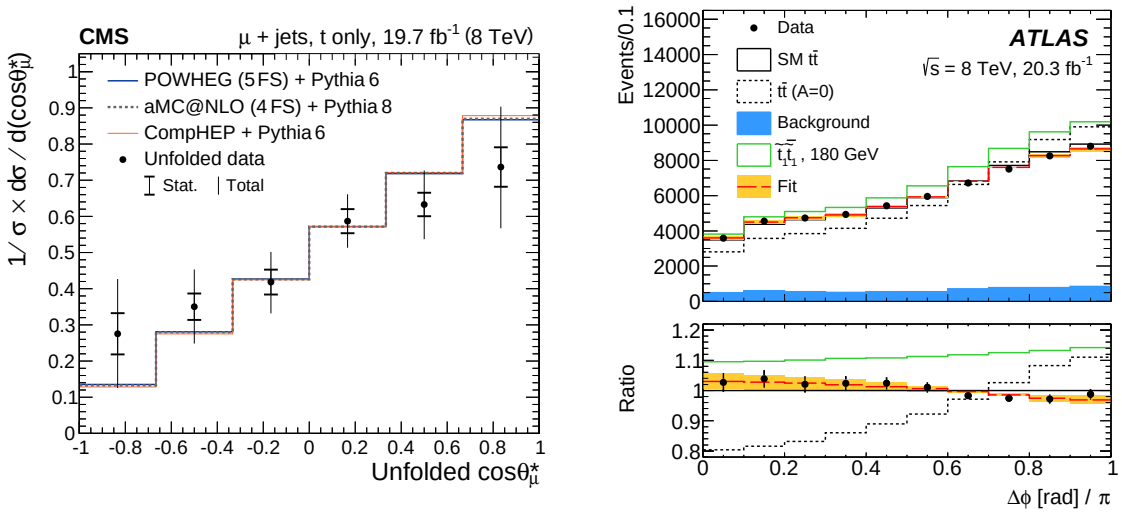

Figure 10: Distributions of the top polarization angles $\cos(\theta_*)$ in single top quark events (a) an ϕ_l in $t\bar{t}$ events (b).

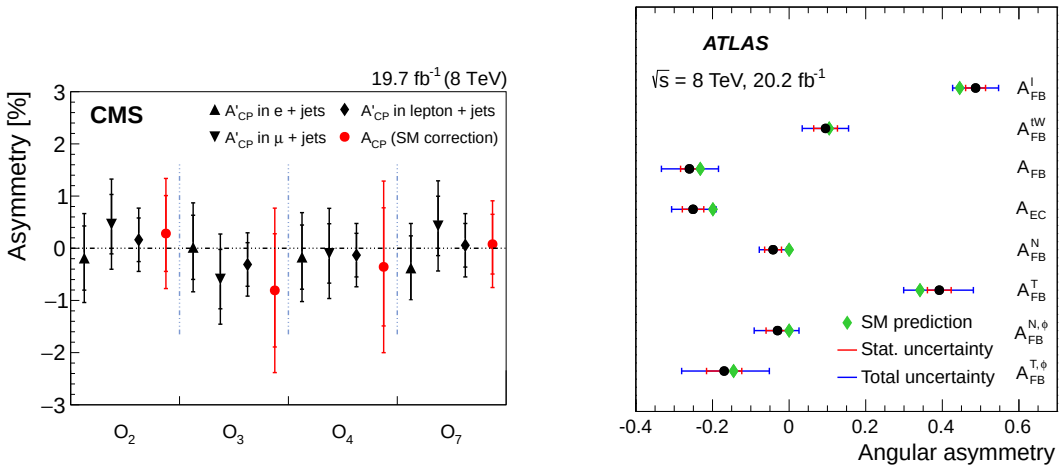

Figure 11: (a)Distribution of the asymmetry observable A_C as a function of the $t\bar{t}$ mass and (b) observed charged asymmetry compared with SM and BSM predictions.

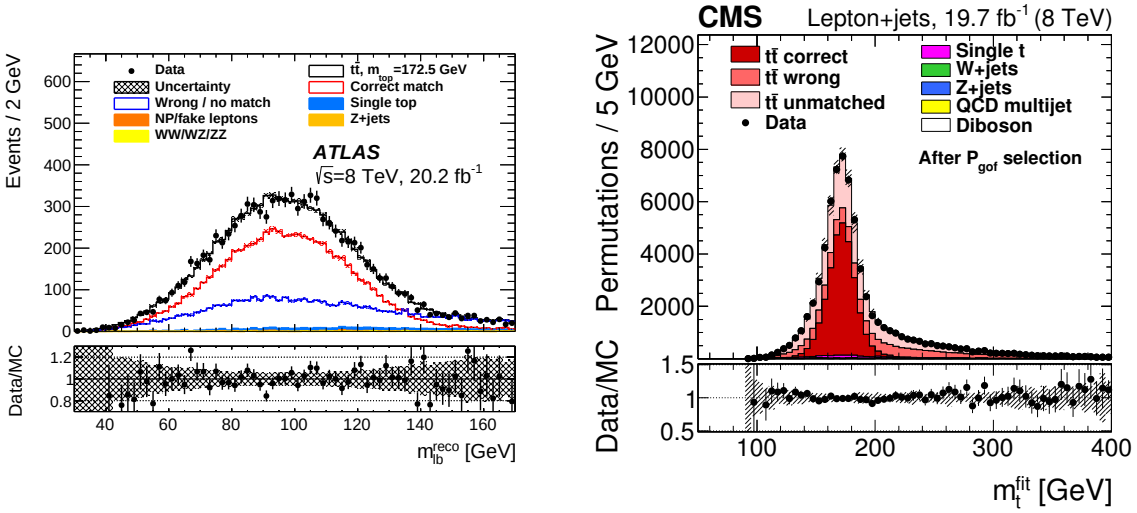

Figure 12: Mass of the lepton-b-jet pair from ATLAS [38], mass of the three jets from the best permutation from CMS [39] .

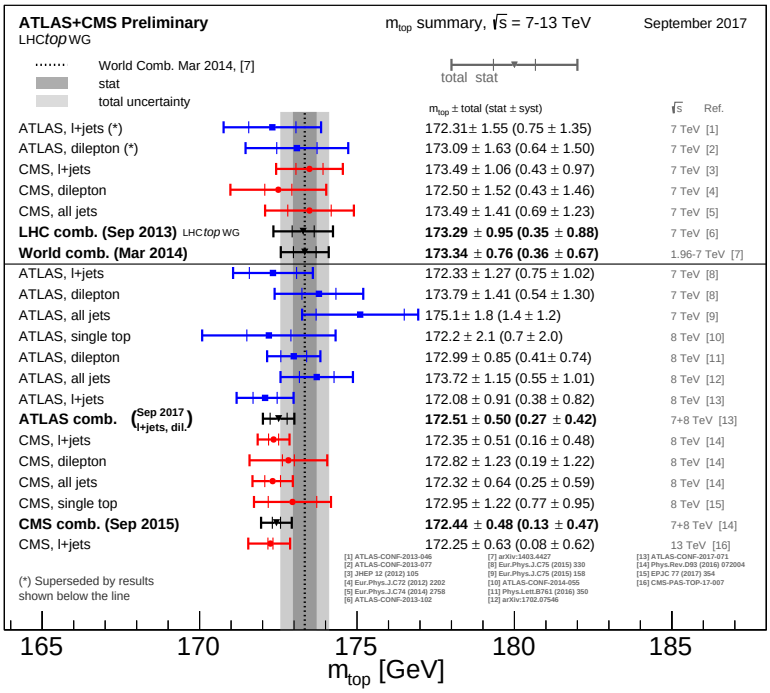

Figure 13: Overview of the most precise single measurements of the top quark mass and top quark mass combinations.

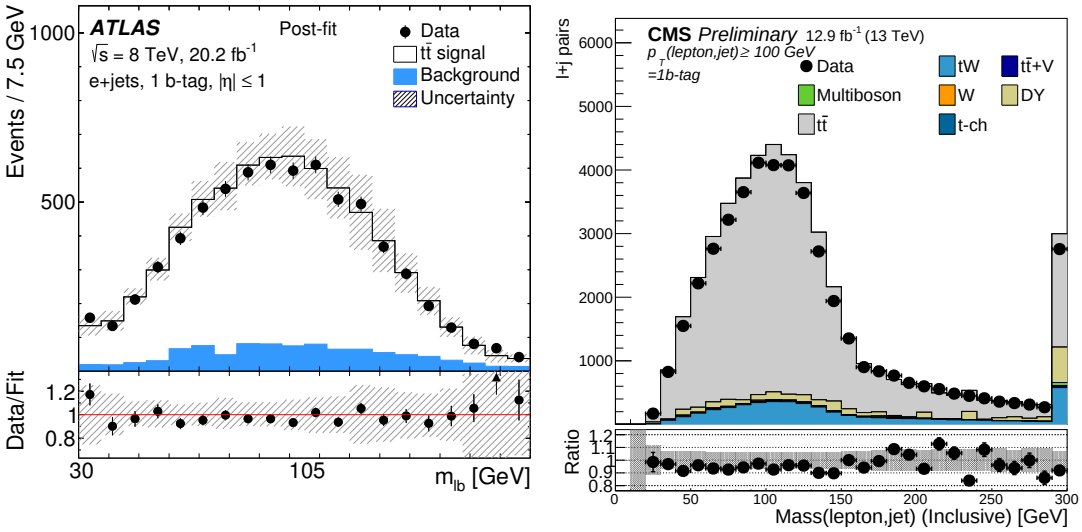

Figure 14: Mass of the invariant mass of the lepton-b-jet pair used in the width measurementfrom ATLAS [41], in the muon+jet channel and one of the 8 categories, and CMS [40], combined for muons and electrons.

Frascati Physics Series Vol. 65 (2017)
LFC17: Old and New Strong Interactions from LHC to Future Colliders
11 - 15 September, 2017

THE TOP QUARK MASS AT THE LHC

Paolo Nason
Theoretical Physics Department, CERN, Geneva, Switzerland
and INFN, Sezione di Milano Bicocca, Milano, ITALY

Abstract

I briefly discuss some theoretical aspects of top mass measurements at the LHC. In particular, I illustrate recent theoretical studies performed using next-to-leading order (NLO) calculations interfaced to shower generators (NLO+PS) of increasing accuracy. I consider three generators: one that has NLO accuracy only at the production stage, and implements spin correlations in an approximate way; one that implements NLO corrections also in decay, and includes exact spin correlations in the narrow-width limit; and one that includes NLO corrections in production and decays, also taking care of finite width, non-resonant contributions and interference of radiation in production and decay.

An important goal of the LHC top-physics program is the measurement of its mass. Since the Higgs mass is known with high precision, improvements of both the W and top mass measurements may lead to a refinement of the Electro-Weak precision tests [1, 2]. The current precision of the W mass measurement, of about 15 MeV, would match a precision on the top mass of about 2.4 GeV.

There is some tension at present between the value of the top mass obtained indirectly through electro-weak fits [1], 176.7 ± 2.1 GeV, and the direct determinations, with the value of 173.34 ± 0.76 GeV from the latest combination [3], and with later measurements yielding values smaller by about 1 GeV [4, 5, 6, 7].[1]

The value of the top mass is also relevant for the issue of vacuum stability in the Standard Model [10, 11, 12]. Direct measurements are now well below the instability region, while the central value extracted from electro-weak fits is near its edge. The only conclusion that one can draw from these results is that no indication of new physics scales below the Plank scale arises from the vacuum

[1] For recent reviews of top-mass measurements by the ATLAS and CMS collaborations see Refs. [8] and [9] from these proceedings.

metastability requirement. On the other hand, the very small value of the Higgs quartic coupling near the Planck scale is an intriguing coincidence, even if at the moment we do not know how to interpret it.

The relatively small errors on top mass measurements quoted by the experimental collaborations has been challenged in some theoretical works, that claimed that the mass extracted in direct measurements is not related to a well defined field-theoretical mass parameter. This claim has appeared in different forms, and with different meanings depending upon the authors. In ref. [13] it is argued in essence that the difference between the pole mass and the Monte Carlo mass parameter is due to effects of non-perturbative origin, and to effects of order $\alpha_s\Gamma_t$. Other publications claim that since the Shower Monte Carlos used to extract the top mass have only leading order accuracy, they cannot be possibly sensitive to a well defined field theoretical mass like the $\overline{\rm MS}$ or the pole mass, since they start to differ at next-to-leading order accuracy [14]. Yet in other works it is argued that the use of jets should be avoided in top mass measurements, since those are affected by hadronization errors [15]. Several theoretical proposals of alternative methods to measure the top mass have appeared in the literature, sometimes motivated by the objections listed above [14, 15, 16, 17, 18, 19]. Furthermore, experimental results are often separated into "direct measurements" and "pole mass measurements", where the latter are obtained by comparing experimental measurements with calculations performed at least at the next-to-leading order level, and no qualification is given to what kind of mass parameter is measured in direct measurements.

It has also been argued that the pole mass is not a viable mass parameter for top mass measurements, because of the mass renormalon problem [13]. Recent studies, however, have shown that the renormalon ambiguity is safely below the current experimental errors, being equal to 110 MeV according to ref. [20], and to 250 MeV according to ref. [21] (for a critical discussion of the larger uncertainty obtained there, see ref. [22]).

In ref. [22] I have argued that direct measurement should be considered pole mass measurements. In short, it is easy to argue that this is the case as far as perturbation theory is concerned, and non-perturbative effects can be estimated in the usual way using Monte Carlo hadronization models, with special attention to their aspects that are particularly worrisome in top mass measurements (as for the case of colour reconnection [23, 24]). Furthermore, there are recent implementation of NLO calculations interfaced to parton shower generators [25, 26] that are particularly relevant for studying whether subtle perturbative effects can have important consequences in top mass measurements, and are typically implemented in the (complex) pole mass scheme.

In ref. [27] we have performed a study using recent generators for top production, aimed at estimating theoretical errors in top mass measurements. We have considered three generators of increasing accuracy: the *hvq* generator [28], that implements NLO corrections only in production, and is widely used by the experimental collaborations in top-mass analyses; the *ttdec* [25] generator, that also implements NLO corrections in top decay and exact spin correlations in the narrow width approximation, and the $b\bar{b}4\ell$ [26] generator, that also implements finite width and non-resonant contributions, including interference effects of radiation in production and decay.

We have focused our study on a simplified observable, the mass of a "particle level top" defined as the system made up of the hardest lepton, the hardest neutrino, and the jet containing the hardest B meson, all with the appropriate flavour to match a top or an anti-top. The peak of this mass distribution, that we call $m^{\rm max}_{Wb_j}$, is of course strongly correlated with the input top mass, that corresponds to the pole mass scheme, since this is the scheme adopted in the NLO calculations of the three generators. Our aim was then to examine the dependence of $m^{\rm max}_{Wb_j}$ on the generator being used (and also on parameters settings, like the factorization and renormalization scale in each generator) for the same input top mass.

Since a differences in $m_{Wb_j}^{\max}$ would result in a difference in the value of the extracted top mass of nearly the same magnitude and opposite sign when examining the same data set, we are in a position to determine intrinsic errors due to parameter settings, and errors due to the use of the less accurate generators.

The result of the comparison of the three generators interfaced to `Pythia8.2` is reported in table 1. Besides reporting the "bare" $m_{Wb_j}^{\max}$ value, we also report the $m_{Wb_j}^{\max}$ value obtained after the application

	PS only		full	
	No smearing	smearing	No smearing	smearing
$b\bar{b}4\ell$	172.522 GeV	171.403 GeV	172.793 GeV	172.717 GeV
$t\bar{t}dec - b\bar{b}4\ell$	-18 ± 2 MeV	$+191 \pm 2$ MeV	$+21 \pm 6$ MeV	$+140 \pm 2$ MeV
$hvq - b\bar{b}4\ell$	-24 ± 2 MeV	-89 ± 2 MeV	$+10 \pm 6$ MeV	-147 ± 2 MeV

Table 1: Differences in the $m_{Wb_j}^{\max}$ for m_t=172.5 GeV for $t\bar{t}dec$ and hvq with respect to $b\bar{b}4\ell$, showered with `Pythia8.2`, at the NLO+PS level and at the full hadron level. Results obtained after smearing the m_{Wb_j} distribution with a Gaussian function with a 15 GeV width are also shown in order to mimic effects due to experimental uncertainties.

of a Gaussian smearing to the m_{Wb_j} distribution, with a Gaussian width equal to 15 GeV (which is the typical experimental resolution of the reconstructed top mass) in order to mimic detector resolution effects. From the table we see that the shift in the peak position is very small for the bare distribution, while it is of the order of 100 MeV in the smeared case.

The very good agreement among the three generators may seem strange at first sight, since the hvq generator does not implement NLO correction to radiation in top decay, and this radiation may influence the peak position, since it controls how much energy is capture in the jet cone. It is however understandable if we remember that `Pythia` implements Matrix Element Corrections (MEC) in top decay, and in our case these are equivalent to NLO accuracy. If MEC are switched off we see a variation of -61 MeV in the bare $m_{Wb_j}^{\max}$ for the hvq generator, while the variation becomes close to -1 GeV for the smeared distribution. This is understood as being due to the fact that the peak position is dominated by events where most radiation in decay is captured by the jet, while when smearing is performed, events that fall on the left side of $m_{Wb_j}^{\max}$, associated to large angle radiation in decay, also contribute.

In ref. [27] several other sources of errors are considered, but none of them is disturbing, leading to the conclusion that the improvement brought by the new generators, and in particular the inclusion of off-shell, non-resonant contribution and the interference of radiation in production and decay, do not displace the peak of the reconstructed mass by more than about 150 MeV.

A very disturbing result is instead found if `Herwig7` is used, as can be seen in table 2. In this case the hvq generator differs substantially from $b\bar{b}4\ell$ and $t\bar{t}dec$ even for the bare m_{Wb_j} distribution, where it exceeds $b\bar{b}4\ell$ by more than 300 MeV, and even more for the smeared one, where the excess raises to almost 700 MeV. Furthermore, the difference between `Pythia8` and `Herwig7` for the smeared distribution when using the $b\bar{b}4\ell$ and $t\bar{t}dec$ generators is larger than 1 GeV. In the hvq case the difference is of the order of 250 MeV and of opposite sign in the bare and smeared case. This signals that the relatively small 250 MeV difference in the smeared case is the accidental consequence of cancellation effects due to the very different description of the reconstructed mass peak in the two Monte Carlos.

In ref. [27] we also examined other observables, namely the peak of the b-jet energy [17] and the set of leptonic observables considered in ref. [18]. Also in these cases we found large differences among

	No smearing		15 GeV smearing	
	He7.1	Py8.2 − He7.1	He7.1	Py8.2 − He7.1
$b\bar{b}4\ell$	172.727 GeV	$+66 \pm 7$ MeV	171.626 GeV	$+1091 \pm 2$ MeV
$t\bar{t}dec$	172.775 GeV	$+39 \pm 5$ MeV	171.678 GeV	$+1179 \pm 2$ MeV
hvq	173.038 GeV	-235 ± 5 MeV	172.319 GeV	$+251 \pm 2$ MeV

Table 2: m_{Wb_j} peak position for m_t=172.5 GeV obtained with the three different generators, showered with Herwig7.1 (He7.1). The differences with Pythia8.2 (Py8.2) are also shown.

the Pythia and Herwig results. In the case of the leptonic observables, this finding contrasts with the naive expectation that leptonic observables should be insensitive to shower and hadronization effects.

It is unlikely that the 1 GeV difference found between Pythia and Herwig may translate directly into a corresponding top mass uncertainty in realistic analysis.[2] It is, however, an important issue to be understood, since Pythia and Herwig differ considerably in the shower model (that is a dipole shower in the former, and an angular ordered parton shower in the latter). Assuming that no specific problems are found either in the two Monte Carlos or in their NLO+PS interfaces, and that both models may be tuned to fit fairly observables that are relevant for top mass measurements, we would be forced to consider remaining differences among the two Monte Carlos as sources of theoretical errors to be accounted for.

References

1. Particle Data Group collaboration, C. Patrignani et al., *Electroweak model and constraints on new physics, Review of Particle Physics*, *Chin. Phys.* **C40** (2016) 100001.

2. Gfitter Group collaboration, M. Baak, J. Cth, J. Haller, A. Hoecker, R. Kogler, K. Mnig et al., *The global electroweak fit at NNLO and prospects for the LHC and ILC*, *Eur. Phys. J.* **C74** (2014) 3046, [1407.3792].

3. ATLAS, CDF, CMS, D0 collaboration, *First combination of Tevatron and LHC measurements of the top-quark mass*, arXiv:1403.4427.

4. ATLAS collaboration, M. Aaboud et al., *Measurement of the top quark mass in the $t\bar{t} \to$ dilepton channel from $\sqrt{s} = 8$ TeV ATLAS data*, *Phys. Lett.* **B761** (2016) 350–371, [1606.02179].

5. CMS collaboration, V. Khachatryan et al., *Measurement of the top quark mass using proton-proton data at $\sqrt{s} = 7$ and 8 TeV*, *Phys. Rev.* **D93** (2016) 072004, [1509.04044].

6. CMS collaboration, *Measurement of the top quark mass with lepton+jets final states in pp collisions at $\sqrt{s} = 13$* TeV, Tech. Rep. CMS-PAS-TOP-17-007, CERN, Geneva, 2017.

7. ATLAS collaboration, *Measurement of the top quark mass in the $t\bar{t} \to$ lepton+jets channel from $\sqrt{s}$=8 TeV ATLAS data*, Tech. Rep. ATLAS-CONF-2017-071, CERN, Geneva, Sep, 2017.

8. B. Pearson, *Top quark mass in ATLAS*, in *10th International Workshop on Top Quark Physics (TOP2017) Braga, Portugal, September 17-22, 2017*, 2017. 1711.09763.

[2] In [27] it is also found that the dependence of $m_{Wb_j}^{\max}$ as a function of the jet radius is different in the two Monte Carlos, and thus it is unlikely that both of them may represent the data fairly.

9. CMS collaboration, A. Castro, *Recent Top Quark Mass Measurements from CMS*, in *10th International Workshop on Top Quark Physics (TOP2017) Braga, Portugal, September 17-22, 2017*, 2017. 1712.01027.

10. G. Degrassi, S. Di Vita, J. Elias-Miro, J. R. Espinosa, G. F. Giudice, G. Isidori et al., *Higgs mass and vacuum stability in the Standard Model at NNLO*, *JHEP* **08** (2012) 098, [1205.6497].

11. D. Buttazzo, G. Degrassi, P. P. Giardino, G. F. Giudice, F. Sala, A. Salvio et al., *Investigating the near-criticality of the Higgs boson*, *JHEP* **12** (2013) 089, [1307.3536].

12. A. Andreassen, W. Frost and M. D. Schwartz, *Scale Invariant Instantons and the Complete Lifetime of the Standard Model*, 1707.08124.

13. A. H. Hoang and I. W. Stewart, *Top Mass Measurements from Jets and the Tevatron Top-Quark Mass*, *Nucl. Phys. Proc. Suppl.* **185** (2008) 220–226, [0808.0222].

14. S. Alioli, P. Fernandez, J. Fuster, A. Irles, S.-O. Moch, P. Uwer et al., *A new observable to measure the top-quark mass at hadron colliders*, *Eur. Phys. J.* **C73** (2013) 2438, [1303.6415].

15. S. Kawabata, Y. Shimizu, Y. Sumino and H. Yokoya, *Weight function method for precise determination of top quark mass at Large Hadron Collider*, *Phys. Lett.* **B741** (2015) 232–238, [1405.2395].

16. A. H. Hoang, S. Mantry, A. Pathak and I. W. Stewart, *Extracting a Short Distance Top Mass with Light Grooming*, 1708.02586.

17. K. Agashe, R. Franceschini, D. Kim and M. Schulze, *Top quark mass determination from the energy peaks of b-jets and B-hadrons at NLO QCD*, *Eur. Phys. J.* **C76** (2016) 636, [1603.03445].

18. S. Frixione and A. Mitov, *Determination of the top quark mass from leptonic observables*, *JHEP* **09** (2014) 012, [1407.2763].

19. S. Kawabata and H. Yokoya, *Top-quark mass from the diphoton mass spectrum*, *Eur. Phys. J.* **C77** (2017) 323, [1607.00990].

20. M. Beneke, P. Marquard, P. Nason and M. Steinhauser, *On the ultimate uncertainty of the top quark pole mass*, *Phys. Lett.* **B775** (2017) 63–70, [1605.03609].

21. A. H. Hoang, C. Lepenik and M. Preisser, *On the Light Massive Flavor Dependence of the Large Order Asymptotic Behavior and the Ambiguity of the Pole Mass*, *JHEP* **09** (2017) 099, [1706.08526].

22. P. Nason, *The Top Mass in Hadronic Collisions*, 1712.02796.

23. D. Wicke and P. Z. Skands, *Non-perturbative QCD Effects and the Top Mass at the Tevatron*, *Nuovo Cim.* **B123** (2008) S1, [0807.3248].

24. T. Sjstrand, *Colour reconnection and its effects on precise measurements at the LHC*, 2013. 1310.8073.

25. J. M. Campbell, R. K. Ellis, P. Nason and E. Re, *Top-pair production and decay at NLO matched with parton showers*, *JHEP* **04** (2015) 114, [1412.1828].

26. T. Ježo, J. M. Lindert, P. Nason, C. Oleari and S. Pozzorini, *An NLO+PS generator for $t\bar{t}$ and Wt production and decay including non-resonant and interference effects*, *Eur. Phys. J.* **C76** (2016) 691, [1607.04538].

27. S. F. Ravasio, T. Jezo, P. Nason and C. Oleari, *A Theoretical Study of Top-Mass Measurements at the LHC Using NLO+PS Generators of Increasing Accuracy*, 1801.03944.

28. S. Frixione, P. Nason and G. Ridolfi, *A Positive-weight next-to-leading-order Monte Carlo for heavy flavour hadroproduction*, *JHEP* **09** (2007) 126, [0707.3088].

29. T. Sjstrand, S. Ask, J. R. Christiansen, R. Corke, N. Desai, P. Ilten et al., *An Introduction to PYTHIA 8.2*, *Comput. Phys. Commun.* **191** (2015) 159–177, [1410.3012].

30. M. Bahr et al., *Herwig++ Physics and Manual*, *Eur. Phys. J.* **C58** (2008) 639–707, [0803.0883].

31. J. Bellm et al., *Herwig 7.0/Herwig++ 3.0 release note*, *Eur. Phys. J.* **C76** (2016) 196, [1512.01178].

Frascati Physics Series Vol. 65 (2017)
LFC17: Old and New Strong Interactions from LHC to Future Colliders
11 - 15 September, 2017

TOP PHYSICS AT FUTURE COLLIDERS

Marcel Vos
IFIC (UVEG/CSIC), Apartado de Correos 22085, E-46071 Valencia, Spain

Abstract

This contribution summarizes a discussion of top quark physics beyond the LHC at the ECT* workshop "Old and new strong interactions from the LHC to future colliders" in Trento in September 2017. The text aims to present a brief review of the top quark physics potential of future lepton and hadron colliders. For five key measurements in top quark physics results of detailed studies into the prospects of hadron and lepton collider projects are reviewed. This summary identifies strengths and weaknesses of lepton and hadron colliders, and finds a clear complementarity between both types of machines.

1 Introduction

Forty-four years after the postulation of a third generation of quarks and twenty-two years after the experimental confirmation of the existence of the top quark, the field of top quark physics is dominated by a single installation. The LHC is producing millions of top quark each year. ATLAS and CMS, and even LHCb, produce a constant stream of results [1], surpassing the precision and sensitivity achieved at the Tevatron in many analyses.

At the same time several new colliders are being planned. A new high-energy hadron or lepton collider should come online by the time the LHC and its luminosity upgrade shut down. What top physics will be left for these machines to explore? And where can they make a real difference? In this contribution I will try to formulate a brief (and therefore necessarily somewhat sketchy) answer to these questions.

A more extensive write-up on top physics beyond the LHC, with some overlap with the current contribution, is found in Ref. [2].

2 Future colliders

In 2017 the field of particle physics is dominated by a single installation. And this will remain true for nearly two more decades. In the next years the LHC is envisaged to continue operation close to its design energy, gradually increasing the integrated luminosity available for analyses to approximately 300 fb^{-1}. After an upgrade of the accelerator complex, the high-luminosity phase (HL-LHC), will continue to collect data, increasing the sample to 3 ab^{-1} by the year 2037.

Possible large-scale particle-physics facilities beyond the LHC can be classified in two main types. A new high-energy hadron collider in the LEP/LHC tunnel can increase the center-of-mass energy achievable in proton-proton to 25-30 TeV (HE-LHC). A new ring with a circumference of up to 100 km is envisaged by the FCC project at CERN [3, 4, 5, 6] and in SPPC in China [7]. The main strengths of high-energy hadron colliders lie are the energy reach and production rate. An integrated luminosity of 10 ab^{-1} at 100 TeV yields approximately 10^{12} top quark pairs. Rare and unconfirmed associated production processes become accessible at such machines. Previously unexplored corner of phase space are unlocked, enhancing the sensitivity to massive new states.

The second category, that of e^+e^- colliders at the energy frontier, operates at lower center-of-mass energy. A circular e^+e^- collider with a circumference of 100 km can reach the top quark pair production threshold at $\sqrt{s} = 2m_t$. This possibility is under study in China (CEPC [7]) and in Europe (FCCee [8]). Linear colliders can explore higher energy, from 250 GeV to 1 TeV with the ILC [9]) or 350 GeV to 3 TeV with CLIC [10]). Both projects have developed a detailed staging scheme [11, 12, 13]. The strength of lepton colliders lies in precision measurements. Thanks to the benign environment, controlled initial state and the calculability of e^+e^- processes, a comparison of sub-% cross section measurement with Standard Model prediction of similar precision is possible at lepton colliders. Such measurements provide sensitivity to new physics at scales that are significantly beyond the direct reach of the machine. Moreover, as the top quark escaped scrutiny at previous lepton colliders, the main production process $e^+e^- \to t\bar{t}$ directly probes the $t\bar{t}Z$ and $t\bar{t}\gamma$ vertices, that are not easily accessible at hadron colliders.

3 Top quark mass

Direct measurements of the top quark mass at the Tevatron and LHC reach an experimental precision of approximately 500 MeV, which may improve to 200-300 MeV with 3 ab^{-1} [14]. The interpretation and theory uncertainty of these measurements are subject of considerable debate [15, 16, 17], also at this workshop [18]. A better understanding of the interpretation and modelling uncertainties in parton shower and hadronization is required to take advantage of the improved experimental precision. The precision of extractions of the top quark pole mass from the (differential) top quark production cross section, which offer a more straightforward interpretation and theory uncertainty estimate, is expected to improve to the level of 1 GeVCMS-PAS-FTR-16-006,Alioli:2013mxa. To achieve sub-GeV precision theory development and improved experimental techniques are required. The ultimate potential of high-energy hadron colliders therefore remains hard to predict [6].

Lepton colliders offer the possiblity of scanning the center-of-mass energy through the top quark pair production threshold. An extraction of the top quark mass from the line shape [19] can offer excellent experimental [20, 21, 22] and theoretical precision [23, 24]. Provided a precise value of the strong coupling constant α_s is available, the total uncertainty can stay within 50 MeV [25].

4 Top quark interactions with SM gauge bosons

Hadron colliders primarily probe the strong interactions of the top quark. Future hig-energy hadron colliders can access a new kinematical regime of several TeV to several tens of TeV. Measurements of rates and asymmetries in highly boosted top quark production are sensitive to new massive mediators and yields stringent limits on the anomalous chromo-magnetic and chromo-electric dipole moments of the top quark [26] and the corresponding dimension-6 operators in an effective-field-theory extension of the SM [27, 28]. Exploitation of these data requires the development of new top-tagging techniques [29, 30].

The vertices of the top quark with electro-weak gauge bosons are probed at hadron colliders by measurements of top quark decay, single top quark production and associated $t\bar{t}V$ production [31] (with $V = \gamma, Z, W$). The HL-LHC and future higher-energy proton-proton colliders are expected to significantly improve the currently statistics-dominated measurements [32, 33, 34]. The ultimate potential depends on a strict control of theory and experimental systematic uncertainties [6].

Lepton colliders provide a complementary view: the $e^+e^- \to t\bar{t}$ process offers exquisite sensitivity to neutral EW gauge bosons [35, 36, 37, 38], while the strong interactions of the top quark can be tested with final-state gluon radiation [39]. The precision on the electric and weak dipole moments of the top quark that can be achieved in a relatively low-energy collider ($\sqrt{s}$ = 350-500 GeV) exceeds that of the HL-LHC by more than an order of magnitude and even exceeds the potential of the SPPC and FCChh projects. Adding data from operation at high energy ($\sqrt{s}$ = 1-3 TeV) helps to constrain four-fermion operators in a global fit [40].

5 Top-quark FCNC interactions

The discovery of flavour-changing neutral-current interactions of the top quark, highly suppressed in the SM, would be clear evidence of physics beyond the SM. Current limits on the branching ratios $t \to uX$ and $t \to cX$ are at the 10^{-3} level [41] are dominated by LHC searches for rare top decays. The HL-LHC is expected the $10^{-4} - 10^{-5}$ level [42]. FCChh and SPPC may access branching ratios as low as 10^{-7} [6], provided systematic limitation can be avoided.

Lepton colliders, with relatively small top quark smalles, clearly offer less potential for rare top quark decay searches, but may offer complementary information in a global analysis [43] and can offer competitive limits on FCNC interactions involving photons and Z-bosons. Searches for $e^+e^- \to tq$ production [44, 45] are possible at $\sqrt{s} < 350$ GeV. Operation above the $t\bar{t}$ threshold can provide limits on the $t \to cH$ and $t \to c\gamma$ branching ratios well below 10^{-4} [46, 47].

6 The top quark and the Higgs boson

Observation of associated $t\bar{t}H$ production provides a direct probe of the interactions between the two heaviest particles of the Standard Model. At the HL-LHC the direct measurement of the top quark Yukawa coupling is expected to reach a precision of 7-10% [48]. Therefore, a direct and precise determination of the top quark Yukawa coupling remains an excellent target for future colliders.

A 100 TeV pp collider can reach 1 % precision according to Ref. [49] by constructing cross-section ratios for very similar processes (i.e. $t\bar{t}H$ and $t\bar{t}Z$) and the use of techniques for boosted top quark production. At linear e^+e^- colliders the precision of the Yukawa coupling measurement reaches approximately 3-4 % [11, 50, 51] for center-of-mass energies in the range $\sqrt{s}$ = 0.55-1.5 TeV.

7 Summary and Outlook

The potential of future installations for five key areas of top quark physics is summarized in Table 1, taken from Ref. [2]. This summary lumps together a variety of studies, with different degrees of sophistication. Question marks indicate areas where no reliable estimates exist.

Table 1 demonstrates that the views on the top quark offered by lepton and hadron colliders are quite complementary: hadron colliders provide stringent limits on the strong interactions of the top quark at very high energy and FCNC interactions, while lepton colliders provide a precise characterization of the $t\bar{t}Z$ and $t\bar{t}\gamma$ vertices and a superior top quark mass measurement. Both types of colliders offer excellent prospects to measure the top Yukawa coupling directly in $t\bar{t}H$ production, arguably the most interesting measurement among those discussed in this contribution.

Table 1: Summary table of top quark physics prospects from Ref. [2]. The current precision of several key measurement in top physics is compared to the projected evolution at the HL-LHC and two categories of future facilities. The HL-LHC prospects and the expected precision at future facilities are based on a highly non-uniform collection of studies, that include extrapolations, parton-level studies and full simulation studies. A more detailed description and references are given in the text.

project	today LEP/Tev/ LHC8	2037 HL-LHC	e^+e^- collider ILC/CLIC/ FCCee/CEPC	new pp collider FCChh/SPPC
$\sqrt{s}$	8 TeV	14 TeV	0.25-3 TeV	100 TeV
$\int \mathcal{L}$	20 fb^{-1}	3 ab^{-1}	0.5-4 ab^{-1}	20-30 ab^{-1}
m_t, exp. $\oplus$ theo. [MeV]	500 $\oplus$ 1000	200 $\oplus$?	20 $\oplus$ 50	?
top QCD $\lvert d_V\rvert$,$\lvert d_A\rvert$	< 0.02, < 0.09	< 0.01, < 0.02	?	< 0.003
top Yukawa (direct)	O (100%)	7-10 %	~ 4 %	1 %
FCNC $BR(t \to qX)$	$\sim 10^{-3}$	$10^{-5} - 10^{-4}$	$\sim 10^{-4}$	$\sim 10^{-7}$?
$t\bar{t}Z$ form factors	-	0.03-0.3	0.002-0.005	0.01-0.07

A precise characterization of top quark production in high-energy electron-positron or proton-proton collisions provides a stringent consistency check of the Standard Model and offers excellent sensitivity to high-scale new physics.

8 Acknowledgements

The author thanks the organizers of the ECT* event, and in particular Gennaro Corcella, for an interesting workshop in a wonderful environment.

References

1. A. O. M. Iorio, *Overview of top phenomenology, these proceedings* .

2. M. Vos, *Review of top and EW physics at future colliders*, *PoS* **EPS-HEP2017** (2017) 471.

3. N. Arkani-Hamed, T. Han, M. Mangano and L.-T. Wang, *Physics Opportunities of a 100 TeV Proton-Proton Collider*, *Phys. Rept.* **652** (2016) 1 [1511.06495].

4. T. Golling et al., *Physics at a 100 TeV pp collider: beyond the Standard Model phenomena*, *Submitted to: Phys. Rept.* (2016) [1606.00947].

5. R. Contino et al., *Physics at a 100 TeV pp collider: Higgs and EW symmetry breaking studies*, 1606.09408.

6. M. L. Mangano et al., *Physics at a 100 TeV pp collider: Standard Model processes*, 1607.01831.

7. CEPC-SPPC Study Group, *CEPC-SPPC Preliminary Conceptual Design Report. 1. Physics and Detector, IHEP-CEPC-DR-2015-01 (2015)*, .

8. M. Bicer, H. Duran Yildiz, I. Yildiz, G. Coignet, M. Delmastro et al., *First Look at the Physics Case of TLEP*, 1308.6176.

9. H. Baer, T. Barklow, K. Fujii, Y. Gao, A. Hoang et al., *The International Linear Collider Technical Design Report - Volume 2: Physics*, 1306.6352.

10. M. Aicheler, P. Burrows, M. Draper, T. Garvey, P. Lebrun, K. Peach et al., *A Multi-TeV Linear Collider Based on CLIC Technology*, .

11. K. Fujii et al., *Physics Case for the International Linear Collider*, 1506.05992.

12. T. Barklow, J. Brau, K. Fujii, J. Gao, J. List, N. Walker et al., *ILC Operating Scenarios*, 1506.07830.

13. CLICdp, CLIC collaboration, M. J. Boland et al., *Updated baseline for a staged Compact Linear Collider*, 1608.07537.

14. CMS Collaboration collaboration, *ECFA 2016: Prospects for selected standard model measurements with the CMS experiment at the High-Luminosity LHC*, Tech. Rep. CMS-PAS-FTR-16-006, CERN, Geneva, 2017.

15. G. Corcella, *Top-quark mass determination at the LHC: a theory overview*, in *Proceedings, 2017 European Physical Society Conference on High Energy Physics (EPS-HEP 2017): Venice, Italy, July 5-12, 2017*, 2017, 1711.09264, DOI.

16. M. Butenschoen, B. Dehnadi, A. H. Hoang, V. Mateu, M. Preisser and I. W. Stewart, *Top Quark Mass Calibration for Monte Carlo Event Generators*, 1608.01318.

17. A. Juste, S. Mantry, A. Mitov, A. Penin, P. Skands, E. Varnes et al., *Determination of the top quark mass circa 2013: methods, subtleties, perspectives*, *Eur. Phys. J.* **C74** (2014) 3119 [1310.0799].

18. P. Nason, *The Top Quark Mass at the LHC*, *these proceedings* .

19. S. Gusken, J. H. Kuhn and P. M. Zerwas, *Threshold Behavior of Top Production in e^+e^- Annihilation*, *Phys. Lett.* **B155** (1985) 185.

20. K. Seidel, F. Simon, M. Tesar and S. Poss, *Top quark mass measurements at and above threshold at CLIC*, *Eur. Phys. J.* **C73** (2013) 2530 [1303.3758].

21. T. Horiguchi, A. Ishikawa, T. Suehara, K. Fujii, Y. Sumino, Y. Kiyo et al., *Study of top quark pair production near threshold at the ILC*, 1310.0563.

22. M. Martinez and R. Miquel, *Multiparameter fits to the t anti-t threshold observables at a future e+ e- linear collider*, *Eur. Phys. J.* **C27** (2003) 49 [hep-ph/0207315].

23. M. Beneke, Y. Kiyo, P. Marquard, A. Penin, J. Piclum and M. Steinhauser, *Next-to-Next-to-Next-to-Leading Order QCD Prediction for the Top Antitop S-Wave Pair Production Cross Section Near Threshold in e^+e^- Annihilation*, *Phys. Rev. Lett.* **115** (2015) 192001 [1506.06864].

24. F. Simon, *Impact of Theory Uncertainties on the Precision of the Top Quark Mass in a Threshold Scan at Future e+e- Colliders*, *PoS* **ICHEP2016** (2017) 872 [1611.03399].

25. M. Vos et al., *Top physics at high-energy lepton colliders*, 1604.08122.

26. J. A. Aguilar-Saavedra, B. Fuks and M. L. Mangano, *Pinning down top dipole moments with ultra-boosted tops*, *Phys. Rev.* **D91** (2015) 094021 [1412.6654].

27. M. Perello Rosello and M. Vos, *Constraints on four-fermion interactions from the $t\bar{t}$ charge asymmetry at hadron colliders*, *Eur. Phys. J.* **C76** (2016) 200 [1512.07542].

28. C. Englert, K. Nordstrom, L. Moore and M. Russell, *Giving top quark effective operators a boost*, *Phys. Lett.* **B763** (2016) 9 [1607.04304].

29. A. J. Larkoski, F. Maltoni and M. Selvaggi, *Tracking down hyper-boosted top quarks*, *JHEP* **06** (2015) 032 [1503.03347].

30. L. Asquith et al., *Jet Substructure at the Large Hadron Collider : Experimental Review*, 1803.06991.

31. A. Buckley, C. Englert, J. Ferrando, D. J. Miller, L. Moore, M. Russell et al., *Constraining top quark effective theory in the LHC Run II era*, 1512.03360.

32. U. Baur, A. Juste, L. H. Orr and D. Rainwater, *Probing electroweak top quark couplings at hadron colliders*, *Phys. Rev.* **D71** (2005) 054013 [hep-ph/0412021].

33. R. Roentsch and M. Schulze, *Probing top-Z dipole moments at the LHC and ILC*, *JHEP* **08** (2015) 044 [1501.05939].

34. M. Schulze and Y. Soreq, *Pinning down electroweak dipole operators of the top quark*, *Eur. Phys. J.* **C76** (2016) 466 [1603.08911].

35. M. S. Amjad, M. Boronat, T. Frisson, I. Garcia, R. Poschl, E. Ros et al., *A precise determination of top quark electro-weak couplings at the ILC operating at $\sqrt{s} = 500$ GeV*, 1307.8102.

36. P. H. Khiem, E. Kou, Y. Kurihara and F. L. Diberder, *Probing New Physics using top quark polarization in the $e^+e^- \to t\bar{t}$ process at future Linear Colliders*, 2015, 1503.04247, http://inspirehep.net/record/1352820/files/arXiv:1503.04247.pdf.

37. P. Janot, *Top-quark electroweak couplings at the FCC-ee*, *JHEP* **04** (2015) 182 [1503.01325].

38. M. S. Amjad et al., *A precise characterisation of the top quark electro-weak vertices at the ILC*, *Eur. Phys. J.* **C75** (2015) 512 [1505.06020].

39. T. G. Rizzo, *Probing anomalous chromomagnetic top quark couplings at the NLC*, *Phys. Rev.* **D50** (1994) 4478 [hep-ph/9405391].

40. J. A. Aguilar-Saavedra, M. C. N. Fiolhais and A. Onofre, *Top Effective Operators at the ILC*, *JHEP* **07** (2012) 180 [1206.1033].

41. LHC top working group, *Summary plots*, .

42. K. Agashe et al., *Working Group Report: Top Quark*, 2013, 1311.2028.

43. G. Durieux, F. Maltoni and C. Zhang, *Global approach to top-quark flavor-changing interactions*, *Phys. Rev.* **D91** (2015) 074017 [1412.7166].

44. J. A. Aguilar-Saavedra and T. Riemann, *Probing top flavor changing neutral couplings at TESLA*, 2001, hep-ph/0102197, http://www-library.desy.de/cgi-bin/showprep.pl?LC-TH-2001-067.

45. H. Khanpour, S. Khatibi, M. Khatiri Yanehsari and M. Mohammadi Najafabadi, *Single top quark production as a probe of anomalous tqγ and tqZ couplings at the FCC-ee*, 1408.2090.

46. CLICdp, ILC Physics Study collaboration, N. van der Kolk, *Toward Precision Top Quark Measurements in e+e- Collisions at Linear Colliders*, *PoS* **EPS-HEP2017** (2017) 470.

47. A. F. Zarnecki, *Top physics at CLIC and ILC*, *PoS* **ICHEP2016** (2016) 666 [1611.04492].

48. S. Dawson et al., *Working Group Report: Higgs Boson*, 2013, 1310.8361.

49. M. L. Mangano, T. Plehn, P. Reimitz, T. Schell and H.-S. Shao, *Measuring the Top Yukawa Coupling at 100 TeV*, *J. Phys.* **G43** (2016) 035001 [1507.08169].

50. T. Price, P. Roloff, J. Strube and T. Tanabe, *Full simulation study of the top Yukawa coupling at the ILC at $\sqrt{s} = 1$ TeV*, *Eur. Phys. J.* **C75** (2015) 309 [1409.7157].

51. H. Abramowicz et al., *Higgs physics at the CLIC electron-positron linear collider*, *Eur. Phys. J.* **C77** (2017) 475 [1608.07538].

Frascati Physics Series Vol. 65 (2017)
LFC17: Old and New Strong Interactions from LHC to Future Colliders
11 - 15 September, 2017

PAST AND FUTURE OF THE MUON G-2 EXPERIMENTS

Anna Driutti for the Muon $g-2$ collaboration
INFN Trieste Gruppo Collegato di Udine, Udine, Italy

Abstract

The most recent high precision measurement of the anomalous magnetic moment of the muon, $a_\mu = (g_\mu - 2)/2$ was performed at the Brookhaven National Laboratory (BNL) by the experiment E-821 and deviates from the Standard model of particle physics calculation by approximately three standard deviations. Since this disagreement could be evidence for new physics, two new Muon $g-2$ experiments are underway to measure a_μ with improved precision. Experiment E-989, located at the Fermi National Accelerator Laboratory (FNAL), will measure a_μ by injecting a beam of polarized positive muons at the "magic momentum" inside the same magnetic storage ring used at BNL. The experiment is currently in commissioning phase and aims to start taking data in 2018. Experiment E-34, planned to be located at the Japan Proton Accelerator Research Complex (J-PARC), will use a novel approach based on an ultra-cold muon beam. After a brief review of the status of the theoretical calculation and the E-821 result, this contribution discusses the status of the new Muon $g-2$ experiments.

1 Introduction

The magnetic moment of the muon is a property of the particle that quantifies the strength of its interaction with the magnetic field, and is given by:

$$\vec{\mu} = g_\mu \frac{e}{2m}\vec{s} \tag{1}$$

where e is the electron charge, m and s are the mass and the spin of the muon. The proportionality factor g_μ is predicted to be exactly two in the Dirac theory. In the framework of the standard model of particle physics (SM) contributions from quantum electrodynamics (QED), electroweak (EW) and quantum chromodynamics (QCD) effects are such that:

$$a_\mu^{\text{theo.}} = \frac{1}{2}(g_\mu^{\text{SM}} - 2_{\text{Dirac}}) = \mathcal{O}(10^{-3})_{\text{QED}} + \mathcal{O}(10^{-9})_{\text{EW}} + \mathcal{O}(10^{-7})_{\text{QCD}}, \tag{2}$$

Table 1: *Current theoretical values of a_μ with all the Standard Model contributions detailed (from [1]). Leading-order and higher-orders are indicated with (lo) and (ho) respectively. For HVP (lo) are quoted the values of two recent evaluations. A new reevaluation is reported in [7].*

Contribution		$a_\mu^{\text{theo.}}(\times 10^{-11})$			
QED		116584718.95	$\pm$	0.08	
EW		154	$\pm$	1	
QCD	HVP (lo)	6923	$\pm$	42	[4]
QCD	HVP (lo)	6949	$\pm$	43	[5]
QCD	HVP (ho)	-98.4	$\pm$	0.7	[5]
QCD	HLbL	105	$\pm$	26	
Total SM		116591802	$\pm$	49	[4]
Total SM		116591828	$\pm$	50	[5]

where a_μ is called muon anomaly. The value of each term for the current prediction of $a_\mu^{\text{theo.}}$ are summarized in Table 1. The QED [2] and EW [3] terms are very well known, while the QCD terms (the hadronic vacuum polarization, HVP [4] [5], and the hadronic light-by-light, HLbL [6]) are the dominant contribution on the overall theoretical uncertainty. The relative precision for the current theoretical value of the anomalous magnetic moment of the muon is about 0.42 ppm [1].

Experimentally, a_μ was measured several times at CERN and more recently at BNL (experiment E-821). The current best experimental measurement was published in 2006 by the E-821 collaboration and is $a_\mu^{E821} = 116592089$
$\pm\ 63 \times 10^{-11}$ [8]. This value is larger that the expected SM prediction by about 3 standard deviations (3σ) and it has a relative precision of 0.54 ppm. Since this discrepancy might be a signal of new physics, it is necessary to confirm it. The new $g-2$ experiments are aiming to achieve a level of precision four times higher than the one of E-821, approximately 0.14 ppm. If the discrepancy remains the same, this precision will provide 5 standard deviations, and with improvements on the theoretical uncertainties could reach 8σ of significance [1].

2 The experimental measurement method

The muon anomaly is measured by injecting polarized muons into a magnetic storage ring. In the presence of both magnetic ($\vec{B}$) and electric ($\vec{E}$) fields the muon anomaly introduces an anomalous precession frequency that could be written as:

$$\vec{\omega}_a = -\frac{e}{m}\left[a_\mu \vec{B} - \left(a_\mu - \frac{1}{\gamma^2 - 1}\right)\frac{\vec{\beta}\times\vec{E}}{c}\right], \tag{3}$$

where e is the electron charge, m is the mass of the muon, γ is the Lorentz factor and $\vec{\beta}$ is the particle velocity in units of speed of light c. If the electric field term of Equation (3) cancels out, a_μ can be determinated by precise measurements of ω_a and ω_p (*i.e.*, the magnetic field B in units of proton Larmor frequency) as follows:

$$a_\mu = \frac{g_e}{2}\frac{m_\mu}{m_e}\frac{\mu_p}{\mu_e}\frac{\omega_a}{\omega_p}. \tag{4}$$

In Equation (4) the electron-to-proton magnetic moment ratio $\mu_e/\mu_p = -658.2109866(20)$, the muon-to-electron mass ratio $m_\mu/m_e = 206.7682826(46)$ and the gyromagnetic moment of the electron $g_e/2 =$

$-2.00231930436182(52)$ are obtained from other experiments with relative precision of 3.0 ppb, 22 ppb and 0.00026 ppb, respectively [9].

Two different approaches are used to eliminate the term that depends on the electric field term. The first approach, which was used by the CERN-III, the BNL E-821 experiments and will be used by the FNAL E-989 experiment, consists of injecting muons with $\gamma = 29.3$ (*i.e.*, muons at the so-called magic momentum of 3.09 GeV/c). The second approach will be implemented by the J-PARC E-34 experiment, and consist of employing an ultra-cold muon beam for which the focusing electric field is not necessary.

3 The E-989 Experiment

The Muon $g-2$ experiment at Fermilab (E-989) is an improved version of the BNL E-821 experiment. The main limitation of the BNL experiment was statistical. The FNAL accelerator complex will provide a muon beam with higher rate and reduced contamination than the BNL beam, resulting in a projection of a factor of 20 increase in muon statistics. The muon beam will be produced by collecting the 3.1 GeV/c polarized and positively-charged muons which decay from pions. The pions are generated by colliding a 8 GeV proton beam with an Inconel target. The muon beam will be injected by means of an inflector magnet, which locally cancels the magnetic field, into the 15-ton and 14-m diameter cryostat ring that was transported from Brookhaven (New York) to Fermilab (near Chicago) in the summer 2013. The ring consists of rectangular vacuum chambers surrounded by a cryo-system and a C-shaped dipole magnets which provide a vertical magnetic field of 1.4 T. The magnetic field inside the storage ring is as uniform as possible (this was obtained by a careful shimming procedure), and it is kept mechanically and thermally stable. The injected muons are moved on the center of the storage ring's orbit by kicker magnets and are vertically contained by the electrostatic quadrupoles plates. The ring is also instrumented with collimators to remove the off-momentum muons and a beam monitoring system.

The measurement of the magnetic field (ω_p), is performed using approximately 400 fixed NMR probes located in the vacuum chambers outside the muon storage ring. Periodically, a trolley travels inside the ring orbit and measures the magnetic field in the muon storage ring. By combining the two measurements it is possible to obtain a precise map of the magnetic field experienced by the stored muons around the ring.

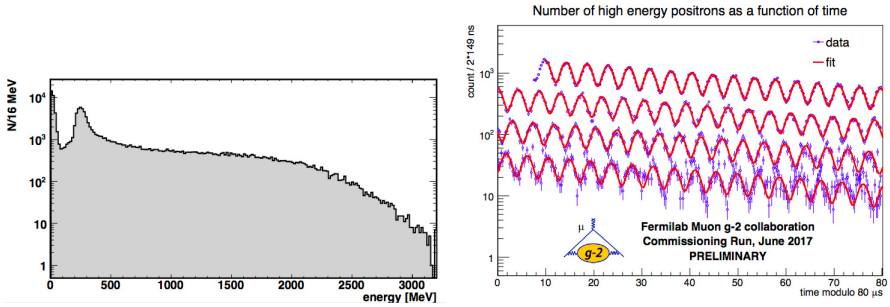

Figure 1: *a) Energy distribution from Summer 2017 data recorded in the calorimeters. The low energy peaks are from proton and lost muons. b) Time distribution of the positrons from muon decay from two weeks of data accumulated during the Summer 2017 run.*

To measure ω_a, the positrons from the decay of the stored muon are detected by 24 highly segmented lead-fluoride electromagnetic calorimeters and 3 straw tracker chambers positioned around the inside of

the storage ring. The detectors will record the energy and the arrival time of these decay positrons. These informations are then used to build the so-called wiggle plot, in which the number of positrons with an energy above a threshold are collected as a function of the time from the injection into the ring. Since the high energy positrons are preferentially emitted with momentum aligned with the muon spin, it is possible to extract ω_a from the wiggle plot. Figure 1a) shows the energy distribution measured by the calorimeters, while figure 1b) the wiggle plot with a preliminary analysis fit. These data were acquired during a 5 week commissioning run performed in summer 2017 to test the experiment. Despite that during this run the rate of muons delivered by the accelerator complex was lower than the one planned for physics runs, the wiggle plot contains approximately 700,000 positrons collected during 2 weeks of the run, and corresponds to about the same statistics of the $g-2$ CERN-II experiment result [10].

4 The E-34 Experiment

The new $g-2$ experiment at J-PARC (E-34) proposes to measure a_μ by injecting an ultra-cold beam of positive muons inside a storage ring. The ultra-cold muon beam will be produced by colliding a 3 GeV/c^2 proton beam into a 20 mm graphite target to produce pions. These positive pions will be stopped on the surface of the target and they will decay into muons. The low-momentum polarized positive muons (called surface muons) will be collected and stopped into a second target to form muonium (μ^+-electron) atoms. At room-temperature, some of these muonium atoms diffuse into the target material and reach its surface where they will be ionized using laser pulses. The resulting ultra-cold muons are then accelerated to 300 MeV/c by a LINAC and injected into the storage ring. The transverse dispersion of the beam is expected to be 10^{-5} thanks to the cold-muon source, then there is no need of a focusing electric field inside the storage ring. Moreover, because of the low momentum (300 MeV/c) of the muons, the storage ring will be a compact 66-cm diameter solenoid with 3.0 T of magnetic field. The positrons produced by the muon decay will be detected with a silicon strip tracker located in the center of the solenoid. The E-34 experiment is at present developing all the components and it is expecting to start data-taking in 2020 [11].

5 Conclusions

The 3 standard deviations between the current theoretical calculation and the most recent experimental measurement of the muon's anomalous magnetic moment may be a hint of new physics. Two new $g-2$ experiments, the E-989 experiment at Fermilab and the E-34 experiment at J-PARC, are aiming to improve the experimental precision to 0.14 ppm. The E-989 experiment successfully completed a commissioning run in Summer 2017 and plans on starting to collect physics data in 2018. The E-34 will provide a measurement of a_μ using a new experimental method, which will be an independent cross-check of the previous measurements. These new direct measurements and a new improved SM prediction will have the potential to definitively confirm (or constrain) new physics effects.

6 Acknowledgements

I would like to thank to the organizers of the LFC17 workshop at the ETC* in Villazzano, Trento for the invitation to this informative and stimulating workshop.

References

1. J. Grange, *et al.* [Muon $g-2$ Collaboration] arXiv:1501.06858 [physics.ins-det] (2015).
2. T. Aoyama, M. Hayakawa, T. Kinoshita and M. Nio, Phys. Rev. Lett. **109**, (11) 111807 (2012).
3. C. Gnendiger, D. Stockinger and H. Stockinger-Kim, Phys. Rev. **D88**, 053005 (2013).
4. M. Davier, A. Hoecker, B. Malaescu and Z. Zhang, Eur. Phys. J. **C71**, 1515 (2011), Erratum: Eur. Phys. J. **C72** ,1874 (2012).
5. K. Hagiwara, R. Liao, A.D. Martin, D. Nomura and T. Teubner, J. Phys. **G38** 085003 (2011).
6. J. Prades, E. De Rafael and A. Vainshtein, Adv. Ser. Direct. High Energy Phys. **20**, 303-317 (2009).
7. M. Davier, A. Hoecker, B. Malaescu, *et al.* Eur. Phys. J. **C77**, 827 (2017).
8. G. W. Bennett, *et al.* Phys. Rev. **D73**, 072003 (2006).
9. P. J. Mohr, D. B. Newell, and B. N. Taylor, Rev. Mod. Phys. **88**, 035009 (2016).
10. F. Farley and E. Picasso *"The CERN (g-2) measurements"*, Quantum Electrodynamics ED. Kinoshita T. (World Scientific) p. 479.
11. O. Masashi, JPS Conf. Proc. **8**, 025008 (2015).

Frascati Physics Series Vol. 65 (2017)
LFC17: Old and New Strong Interactions from LHC to Future Colliders
11 - 15 September, 2017

EXOTIC QUARKS FROM COMPOSITE MODELS

Roberto Leonardi
INFN Perugia, Via A. Pascoli, I-06123, Perugia, Italy
Orlando Panella
INFN Perugia, Via A. Pascoli, I-06123, Perugia, Italy
Giulia Pancheri
Laboratori Nazionali di Frascati, INFN, Frascati, Italy
Yogendra N. Srivastava
Dipartimento di Fsica e Geologia, Università degli studi di Perugia, Via A. Pascoli, I-06123, Perugia, Italy
Meenakshi Narain
Physics Department, Brown University, Providence, USA
Ulrich Heintz
Physics Department, Brown University, Providence, USA

Abstract

We investigate the phenomenology at the CERN LHC of the exotic quarks appearing in composite models considering weak isospin multiplets $I_W = 1$ and $I_W = 3/2$. We focus on $pp \to Qj \to W^+jj \to \ell^+ \not{p}_T jj$ process and then perform a fast simulation of the detector reconstruction based on DELPHES. We study the statistical significance and we estimate a bound on the excited quark mass by recasting an experimental search.

1 Introduction

The composite models represent one of the possible theories beyond the standard model. In this scenario quarks and leptons are assumed not to be elementary particles, but to be bound states of some as yet unknown entities. One consequence of this scenario is that excited quarks and leptons are expected [1, 2, 3, 4, 5]. In general the following parameters are introduced: m_*, the mass of the excited states, and Λ, the energy scale at which the internal substructure becomes manifest (compositeness scale). In our study we will use the parametrization $m_* = \Lambda$. In particular we will take in consideration the extended weak-isospin model [6].

2 Extended weak-isospin model

This model tries to find some properties of excited fermions through the weak isospin spectroscopy without reference to a particular internal structure. This approach is in analogy with the strong isospin symmetry, that allowed to discover baryon and meson resonances before the observation of quarks and gluons.

The standard model fermions have $I_W = 0, 1/2$ and the electroweak bosons have $I_W = 0, 1$, so we can consider fermionic excited states with $I_W \leq 3/2$. The multiplets with $I_W = 1$ (triplet) and $I_W = 3/2$ (quadruplet) of the hadronic sector include ordinary charged excited quarks, U and D, and exotically charged excited quarks, U^+ of charge 5/3 and D^- of charge -4/3:

$$U = \begin{pmatrix} U^+ \\ U \\ D \end{pmatrix}, \quad D = \begin{pmatrix} U \\ D \\ D^- \end{pmatrix}, \quad \Psi = \begin{pmatrix} U^+ \\ U \\ D \\ D^- \end{pmatrix}$$

These multiplets contribute solely to the iso-vector current and do not contribute to the hypercharge current. The exotically charged excited quarks interact with the standard model fermions only via W^+ and W^- gauge bosons, while the ordinary charged excited quarks via W^+, W^-, Z and γ. Because all gauge fields carry no hypercharge Y, a given multiplet couples through the gauge field to light multiplet with the same Y. In order to conserve the $SU(2)$ currents, the couplings between excited and ordinary fermions are magnetic moment type transition couplings. The lagrangians describing these couplings are

$$\mathcal{L}^{(I_W=3/2)} = \frac{g f_{3/2}}{\Lambda} \sum_{M,m,m'} C(\frac{3}{2}, M|1, m; \frac{1}{2}, m') \times (\bar{\Psi}_M \sigma_{\mu\nu} q_{Lm'}) \partial^\nu (W^m)^\mu + h.c. \quad (1)$$

$$\mathcal{L}^{(I_W=1)} = \frac{g f_1}{\Lambda} \sum_{m=-1,0,1} \left[(\bar{U}_m \sigma_{\mu\nu} u_R) + (\bar{D}_m \sigma_{\mu\nu} d_R) \right] \partial^\nu (W^m)^\mu + h.c. \quad (2)$$

where g is the $SU(2)$ coupling, F_1 and $f_3/2$ are dimensionless couplings assumed to be equal to 1, C are the Clebsch-Gordan coefficients and we consider $m_* = \Lambda$.

3 Production and decay of excited quarks

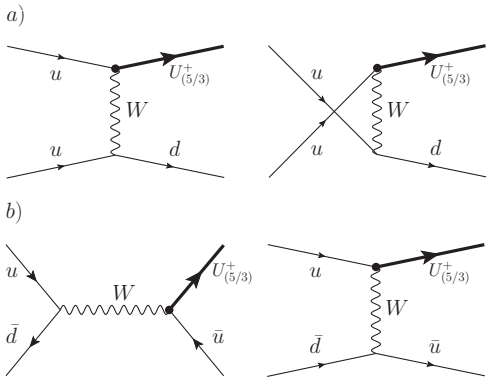

Figure 1: *Feynman diagrams of U^+ resonant production in pp collisions.*

The U^+ quark can be produced through the Feynman diagrams shown in fig.1. The partonic sub-processes cross sections for $I_W = 1$ are characterized by the absence of interference between the kinematical channels and they are

$$\left(\frac{d\hat{\sigma}}{d\hat{t}}\right)^{I_W=1}_{uu\to U^+ d} = \frac{1}{4\hat{s}^2 m_*^2} \frac{g^4 f_1^2}{16\pi} \frac{\hat{t}}{(\hat{t} - M_W^2)^2} \left[m_*^2(\hat{t} - m_*^2) + 2\hat{s}\hat{u} + m_*^2(\hat{s} - \hat{u}) \right]$$
$$+ \frac{1}{4\hat{s}^2 m_*^2} \frac{g^4 f_1^2}{16\pi} \frac{u}{(\hat{u} - M_W^2)^2} \left[m_*^2(\hat{s} - m_*^2) + 2\hat{t}\hat{u} + m_*^2(\hat{t} - \hat{u}) \right]$$

$$\left(\frac{d\hat{\sigma}}{d\hat{t}}\right)^{I_W=1}_{u\bar{d}\to U^+\bar{u}} = \frac{1}{4\hat{s}^2 m_*^2}\frac{g^4 f_1^2}{16\pi}\frac{\hat{s}}{(\hat{s}-M_W^2)^2}\left[m_*^2(\hat{s}-m_*^2)+2\hat{t}\hat{u}+m_*^2(\hat{t}-\hat{u})\right] + \frac{1}{4\hat{s}^2 m_*^2}\frac{g^4 f_1^2}{16\pi}\frac{\hat{t}}{(\hat{t}-M_W^2)^2}\left[m_*^2(\hat{t}-m_*^2)+2\hat{s}\hat{u}+m_*^2(\hat{s}-\hat{u})\right]$$

The ones for $I_W = 3/2$ have nonzero interference and they are

$$\left(\frac{d\hat{\sigma}}{d\hat{t}}\right)^{I_W=3/2}_{uu\to U^+ d} = \frac{1}{4\hat{s}^2 m_*^2}\frac{g^4 f_{3/2}^2}{16\pi}\frac{\hat{t}}{(\hat{t}-M_W^2)^2}\left[m_*^2(\hat{t}-m_*^2)+2\hat{s}\hat{u}-m_*^2(\hat{s}-\hat{u})\right] + \frac{1}{4\hat{s}^2 m_*^2}\frac{g^4 f_{3/2}^2}{16\pi}\frac{\hat{u}}{(\hat{u}-M_W^2)^2}\left[m_*^2(\hat{u}-m_*^2)+2\hat{s}\hat{t}-m_*^2(\hat{s}-\hat{t})\right] + \frac{1}{4\hat{s}^2 m_*^2}\frac{g^4 f_{3/2}^2}{16\pi}\frac{1}{(\hat{u}-M_W^2)}\frac{1}{(\hat{t}-M_W^2)}\left(\hat{s}\hat{t}\hat{u}+\frac{3}{8}\hat{u}\hat{t}m_*^2\right)$$

$$\left(\frac{d\hat{\sigma}}{d\hat{t}}\right)^{I_W=3/2}_{u\bar{d}\to U^+\bar{u}} = \frac{1}{4\hat{s}^2 m_*^2}\frac{g^4 f_{3/2}^2}{16\pi}\frac{\hat{s}}{(\hat{s}-M_W^2)^2}\left[m_*^2(\hat{s}-m_*^2)+2\hat{t}\hat{u}-m_*^2(\hat{t}-\hat{u})\right] + \frac{1}{4\hat{s}^2 m_*^2}\frac{g^4 f_{3/2}^2}{16\pi}\frac{\hat{t}}{(\hat{t}-M_W^2)^2}\left[m_*^2(\hat{t}-m_*^2)+2\hat{s}\hat{u}-m_*^2(\hat{s}-\hat{u})\right] + \frac{1}{4\hat{s}^2 m_*^2}\frac{g^4 f_{3/2}^2}{16\pi}\frac{1}{(\hat{s}-M_W^2)}\frac{1}{(\hat{t}-M_W^2)}\left(\hat{s}\hat{t}\hat{u}+\frac{3}{8}\hat{s}\hat{t}m_*^2\right)$$

For the production of D^- quark we have a similar situation, while for the production of U and D quarks we have analogous diagrams, but involving all the gauge bosons.

For the U^+ and D^- quarks the only decay channel is Wq, while the U and D quarks can decay to all the gauge bosons. In our study we consider the production and decay chain $pp \to Qj \to W^+jj \to \ell^+\not{p}_T jj$, where Q can be U^+, $\bar{D}^-$, U or $\bar{D}$, with all the excited quarks considered to be mass degenerate.

4 Signal and background

The main standard model backround for our signature is the process $pp \to Wjj \to \ell^+\not{p}_T jj$. From the study of the kinematical distribution of signal and background we found that the background can be drastically reduced by applying the cuts

$$p_T(j1) \geq 180 \text{ GeV}, \quad p_T(j2) \geq 100 \text{ GeV}$$

We note that we cannot exactly reconstruct the excited quark mass, because one of its decay product is a neutrino, for which it is not possible to reconstruct the longitudinal momentum. However we can reconstruct the transverse mass defined as

$$M_T^2 = \left(\sqrt{p_{TW}^2 + M_W^2} + p_{Tj1}\right)^2 - (p_{TW} + p_{Tj1})^2 \tag{3}$$

This distribution shows a peak with a relatively sharp end-point at $M_T \approx m_*$ (fig.2, left).

Actually we can still reconstruct the excited quark invariant mass to some degree of accuracy starting from the four-momentum conservation: $M_W^2 = (p_\ell + p_\nu)^2$. From it we obtain a second order equation for the longitudinal momentum of the neutrino and, among the two solutions, we select the one that gives the more central W. Now we have all the quantities to reconstruct the invariant mass $M_{\ell\nu j1}$. This distribution has a clear peak in correspondence of the excited quark mass (fig.2, right).

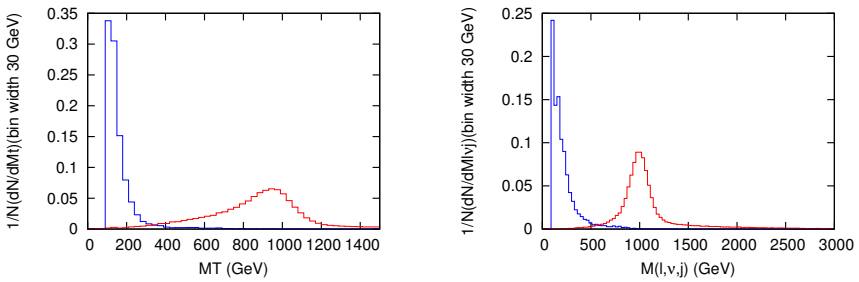

Figure 2: *Transverse mass (left) and invariant mass (right) distribution obtained for an excited quark mass of 1000 GeV. The red line is the signal and the blue line is the background.*

5 Fast detector simulation and reconstructed objects

In order to take into account the detector effects, we have interfaced the LHE output of CalcHEP with the software DELPHES, that simulates the response of a generic detector; we used a CMS-like parametrization. From these simulations we have evaluated the reconstruction efficiencies for signal and background (ϵ_s, ϵ_b); once we have them, it is possible to evaluate the statistical significance as:

$$S = \frac{N_s}{\sqrt{N_s + N_b}}, \quad \text{with} \quad N_s = L\sigma_s\epsilon_s, \quad N_b = L\sigma_b\epsilon_b$$

Finally we can evaluate the luminosity needed to have a given S:

$$L = \frac{S^2}{\sigma_s\epsilon_s}\left[1 + \frac{\sigma_b\epsilon_b}{\sigma_s\epsilon_s}\right]$$

The luminosity curves as function of the excited quark for $S = 3$ and $S = 5$ are reported in fig.3. We

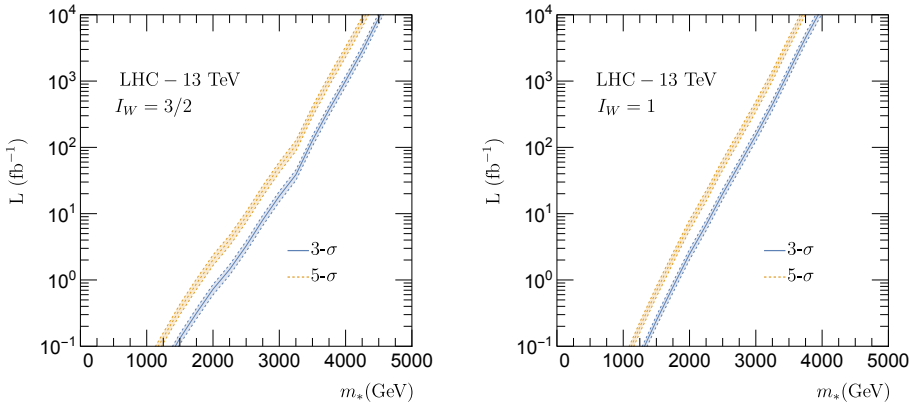

Figure 3: *Luminosity curves at 3-σ (solid) and 5-σ (dashed) level for $\sqrt{s} = 13$ TeV as a function of the excited quark mass, for $I_W = 1$ (left) and $I_W = 3/2$ (right). The shaded bands represent the statistical uncertainties.*

give an estimate of the bound on the excited quark mass by recasting a CMS analysis that search for exotic light flavour quark partner performed at $\sqrt{s} = 8$ TeV [7]. We compare the observed limit on $\sigma(pp \to Dq) \times \mathcal{B}(D \to Zq)$ with the prediction of our model. The results are shown in fig.4.

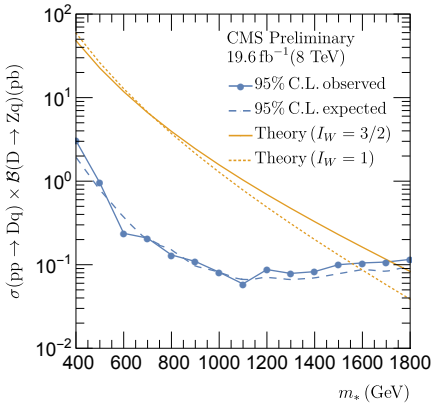

Figure 4: *95% Confidence level limits observed (solid line with disk markers) and expected (dashed line) as reported by a CMS search* [7] *for light flavour quark partners in the Zqq channel are compared with the prediction of our model for* $I_W = 3/2$ *(solid line) and* $I_W = 1$ *(dotted line)*

6 Discussions and conclusions

We have presented the first study of the production at the CERN LHC of exotic quark states which appear in composite models when considering higher isospin multiplets $I_W = 1$ and $I_W = 3/2$. The results obtained are quite interesting and, in our opinion, warrant more detailed studies. For instance the two dimensional parameter space could be fully explored and the effect of the expected contact interaction should be taken into account.

References

1. H. Terazawa, K. Akama and Y. Chikashige, Phys. Rev. D **15**, 480 (1977).
2. H. Terazawa, Phys. Rev. D **22**, 184 (1980).
3. E. Eichten, K.D. Lane and M.E. Peskin, Phys. Rev. Lett. **50**, 811 (1983).
4. N. Cabibbo, L. Maiani and Y. Srivastava, Phys. Lett. B **139**, 459 (1984).
5. U. Baur, M. Spira and P. Zerwas, Phys. Rev. D **42**, 815 (1990).
6. G. Pancheri and Y. Srivastava, Phys. Lett. B **146**, 87 (1984).
7. CMS Collaboration, Tech. Rep. CMS-PAS-B2G-12-016 (CERN, Geneva, 2016)

Frascati Physics Series Vol. 65 (2017)
LFC17: Old and New Strong Interactions from LHC to Future Colliders
11 - 15 September, 2017

THE HADRONIC VACUUM POLARISATION CONTRIBUTIONS TO THE MUON $g-2$

Alexander Keshavarzi
Department of Mathematical Sciences, University of Liverpool, Liverpool L69 3BX, UK
Daisuke Nomura
KEK Theory Center, Tsukuba, Ibaraki 305-0801, Japan
Yukawa Institute for Theoretical Physics, Kyoto University, Kyoto 606-8502, Japan
Thomas Teubner
Department of Mathematical Sciences, University of Liverpool, Liverpool L69 3BX, UK

Abstract

The hadronic vacuum polarisation contributions to the anomalous magnetic moment of the muon, $a_\mu^{\rm had,VP}$, have been re-evaluated from the combination of $e^+e^- \to$ hadrons cross section data. Focus has been placed on the development of a new data combination method, which fully incorporates all correlated statistical and systematic uncertainties in a bias free approach. Using these combined data has resulted in estimates of the hadronic vacuum polarisation contributions to $g-2$ of the muon of $a_\mu^{\rm had,\,LO\,VP} = (693.27 \pm 2.46) \times 10^{-10}$ and $a_\mu^{\rm had,\,NLO\,VP} = (-9.82 \pm 0.04) \times 10^{-10}$. The new estimate for the Standard Model prediction is found to be $a_\mu^{\rm SM} = (11\ 659\ 182.05 \pm 3.56) \times 10^{-10}$, which is 3.7σ below the current experimental measurement. In addition, the prediction for the hadronic contribution to the QED coupling at the Z boson mass has been calculated to be $\Delta\alpha^{(5)}_{\rm had}(M_Z^2) = (276.11 \pm 1.11) \times 10^{-4}$, resulting in $\alpha^{-1}(M_Z^2) = 128.946 \pm 0.015$.

1 Introduction

The anomalous magnetic moment of the muon, $a_\mu = (g-2)_\mu/2$, stands as an enduring test of the Standard Model (SM), where the $\sim 3.5\sigma$ (or higher) discrepancy between the experimental measurement $a_\mu^{\rm exp} = 11\ 659\ 209.1\ (5.4)\ (3.3) \times 10^{-10}$ [1, 2] and the SM prediction $a_\mu^{\rm SM}$ could be an indication of the existence of new physics beyond the SM. Efforts to improve the experimental estimate at Fermilab (FNAL) [3] and at J-PARC [4] aim to reduce the experimental uncertainty by a factor of four compared to the BNL measurement. It is therefore imperative that the SM prediction is also improved to determine whether the $g-2$ discrepancy is well established.

The uncertainty of $a_\mu^{\rm SM}$ is completely dominated by the hadronic contributions, where the hadronic vacuum polarisation contributions can be separated into the leading-order (LO) and higher-order contributions. These are calculated utilising dispersion integrals and the experimentally measured cross

section $\sigma^0_{\mathrm{had},\gamma}(s) \equiv \sigma^0(e^+e^- \to \gamma^* \to \mathrm{hadrons}+\gamma)$, where the superscript 0 denotes the bare cross section (undressed of all vacuum polarisation (VP) effects) and the subscript γ indicates the inclusion of effects from final state photon radiation (FSR). At LO, the dispersion relation reads

$$a_\mu^{\mathrm{had,\,LO\,VP}} = \frac{\alpha^2}{3\pi^2}\int_{m_\pi^2}^{\infty}\frac{\mathrm{d}s}{s}R(s)K(s) \quad ; \quad R(s) = \frac{\sigma^0_{\mathrm{had},\gamma}(s)}{\sigma_{\mathrm{pt}}(s)} \equiv \frac{\sigma^0_{\mathrm{had},\gamma}(s)}{4\pi\alpha^2/3s}\,, \tag{1}$$

where $K(s)$ is a well known kernel function. In addition to calculating $a_\mu^{\mathrm{had,\,VP}}$, the combination of hadronic cross section data is also used to calculate the effective QED coupling at the Z boson mass, $\alpha(M_Z^2)$, which is the least precisely known of the three fundamental electro-weak (EW) parameters of the SM (the Fermi constant G_μ, M_Z and $\alpha(M_Z^2)$) and hinders the accuracy of EW precision fits.

2 Radiative corrections and data combination

Equation (1) requires the experimental cross section to be undressed of all VP effects. However, recent data are more commonly undressed in the experimental analyses already, removing the need to apply a correction to these data sets and, hence, reducing the impact of the extra radiative correction uncertainty which is applied to each channel. Concerning FSR, detailed studies have been performed for the important $\pi^+\pi^-$ and K^+K^- channels. The K^+K^- final state is dominated by the ϕ peak, where the phase space for real radiation is severely restricted and the possibility for any hard real radiation is strongly suppressed. Therefore, no correction or additional error estimate due to FSR is now applied in the K^+K^- channel (or the $K^0_SK^0_L$ channel). For the two pion channel, in principle larger contributions from real radiation can arise. Therefore, the fully inclusive scalar QED correction [5] is applied where necessary. It should be noted, however, that recent sets from radiative return (where accounting for FSR effects is an integral part of the analysis) have now become dominant in the $\pi^+\pi^-$ data combination, reducing the impact of the fully inclusive FSR correction from older data. For the sub-leading, multi-hadron channels, there are, at present, no equivalent FSR calculations. Therefore, possible effects are accounted for by applying a conservative additional uncertainty.

Within each hadronic channel, data points from different experiments are re-binned into *clusters* [6]. A covariance matrix is then constructed for the combination which contains the uncertainty and correlation information of all data points. Using the covariance matrix as defined by the data alone could result in bias (see [7, 8]). To avoid this, the covariance matrix is redefined at each step of an iterative linear χ^2-minimisation [9, 10] using the fitted values for the cluster centres, R_m (see [6]). Convergence of the iteration is observed in this work to occur after only a few steps. Performing the minimisation yields the cluster centres R_m and the covariance matrix $V\big(m,n\big)$, which is inflated according to the local $\chi^2_{\mathrm{min}}/\mathrm{d.o.f.}$ for each cluster if $\chi^2_{\mathrm{min}}/\mathrm{d.o.f.} > 1$. This is done in order to account for any tensions between the data. The use of the full covariance matrix allows for the inclusion of any-and-all uncertainties and correlations that may exist between the measurements. Hence, the appropriate influence of the correlations is incorporated into the determination of the cluster centres, R_m, with the correct propagation of all experimental errors to the uncertainty. The data are then integrated in order to obtain $a_\mu^{\mathrm{had,VP}}$ and the five flavour contribution to the running α, $\Delta\alpha^{(5)}_{\mathrm{had}}(M_Z^2)$.

3 Determining $a_\mu^{\mathrm{had,VP}}$ and $\Delta\alpha^{(5)}_{\mathrm{had}}(M_Z^2)$

In the $\pi^+\pi^-$ channel, two recent radiative return measurements from the KLOE collaboration [11,12] and the BESIII collaboration [13] in the ρ region have improved the estimate of this final state. As indicated

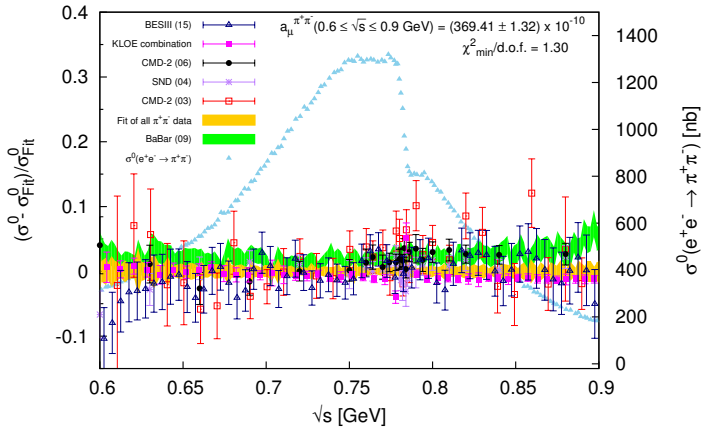

Figure 1: The relative difference of the radiative return and most relevant direct scan data sets contributing to $a_\mu^{\pi^+\pi^-}$ and the combination of all data, plotted in the ρ region. The width of the coloured bands represents the propagation of the statistical and systematic uncertainties added in quadrature.

Channel	**Energy range (GeV)**	$a_\mu^{\text{had, LO VP}} \times 10^{10}$	$\Delta\alpha^{(5)}_{\text{had}}(M_Z^2) \times 10^4$
$\pi^+\pi^-$	$0.305 \leq \sqrt{s} \leq 1.937$	502.97 ± 1.97	34.26 ± 0.12
$\pi^+\pi^-\pi^0$	$0.660 \leq \sqrt{s} \leq 1.937$	47.79 ± 0.89	4.77 ± 0.08
$\pi^+\pi^-\pi^+\pi^-$	$0.613 \leq \sqrt{s} \leq 1.937$	14.87 ± 0.20	4.02 ± 0.05
$\pi^+\pi^-\pi^0\pi^0$	$0.850 \leq \sqrt{s} \leq 1.937$	19.39 ± 0.78	5.00 ± 0.20
K^+K^-	$0.988 \leq \sqrt{s} \leq 1.937$	23.03 ± 0.22	3.37 ± 0.03
$K^0_S K^0_L$	$1.004 \leq \sqrt{s} \leq 1.937$	13.04 ± 0.19	1.77 ± 0.03
$KK\pi$	$1.260 \leq \sqrt{s} \leq 1.937$	2.71 ± 0.12	0.89 ± 0.04
$KK2\pi$	$1.350 \leq \sqrt{s} \leq 1.937$	1.93 ± 0.08	0.75 ± 0.03
Inclusive channel	$1.937 \leq \sqrt{s} \leq 11.200$	43.67 ± 0.67	82.82 ± 1.05

Table 1: Contributions to $a_\mu^{\text{had, LO VP}}$ and $\Delta\alpha^{(5)}_{\text{had}}(M_Z^2)$ [6]. The first column indicates the hadronic final state or individual contribution, the second column gives the respective energy range of the contribution, the third column gives the determined value of $a_\mu^{\text{had, LO VP}}$ and the last column states the value of $\Delta\alpha^{(5)}_{\text{had}}(M_Z^2)$.

in Figure 1, tension exists between the BaBar data [14] and all other contributing data. Although BaBar still influences the combination with an increase, the agreement between the other radiative return measurements and the direct scan data largely compensates for this effect. However, the tension between data is reflected in the local χ^2_{min}/d.o.f. error inflation, which results in an $\sim 15\%$ increase in the uncertainty of $a_\mu^{\pi^+\pi^-}$. The full combination of all $\pi^+\pi^-$ data results in the contributions to $a_\mu^{\text{had, LO VP}}$ and $\Delta\alpha^{(5)}_{\text{had}}(M_Z^2)$ as given in Table 1. The cross section in the ρ region is displayed in plot (a) of Figure 2.

The results and cross sections from other major sub-leading channels are also given in Table 1 and Figure 2, respectively. In all cases, these channels include new data sets which, coupled with the new data combination routine, have improved the estimates of $a_\mu^{\text{had, LO VP}}$ and $\Delta\alpha^{(5)}_{\text{had}}(M_Z^2)$ from these final states. In particular, a new measurement of the $\pi^+\pi^-\pi^0\pi^0$ channel by BaBar [15] has provided the only new data in this channel since 2003. The uncertainty contribution from $\pi^+\pi^-\pi^0\pi^0$ is, however, still relatively large in comparison with its contribution to $a_\mu^{\text{had, LO VP}}$ and requires better new data. Notably, the K^+K^- channel now includes a precise and finely binned measurement by the BaBar collaboration, supplemented with full statistical and systematic covariance matrices [16], being the first and only example to date of the

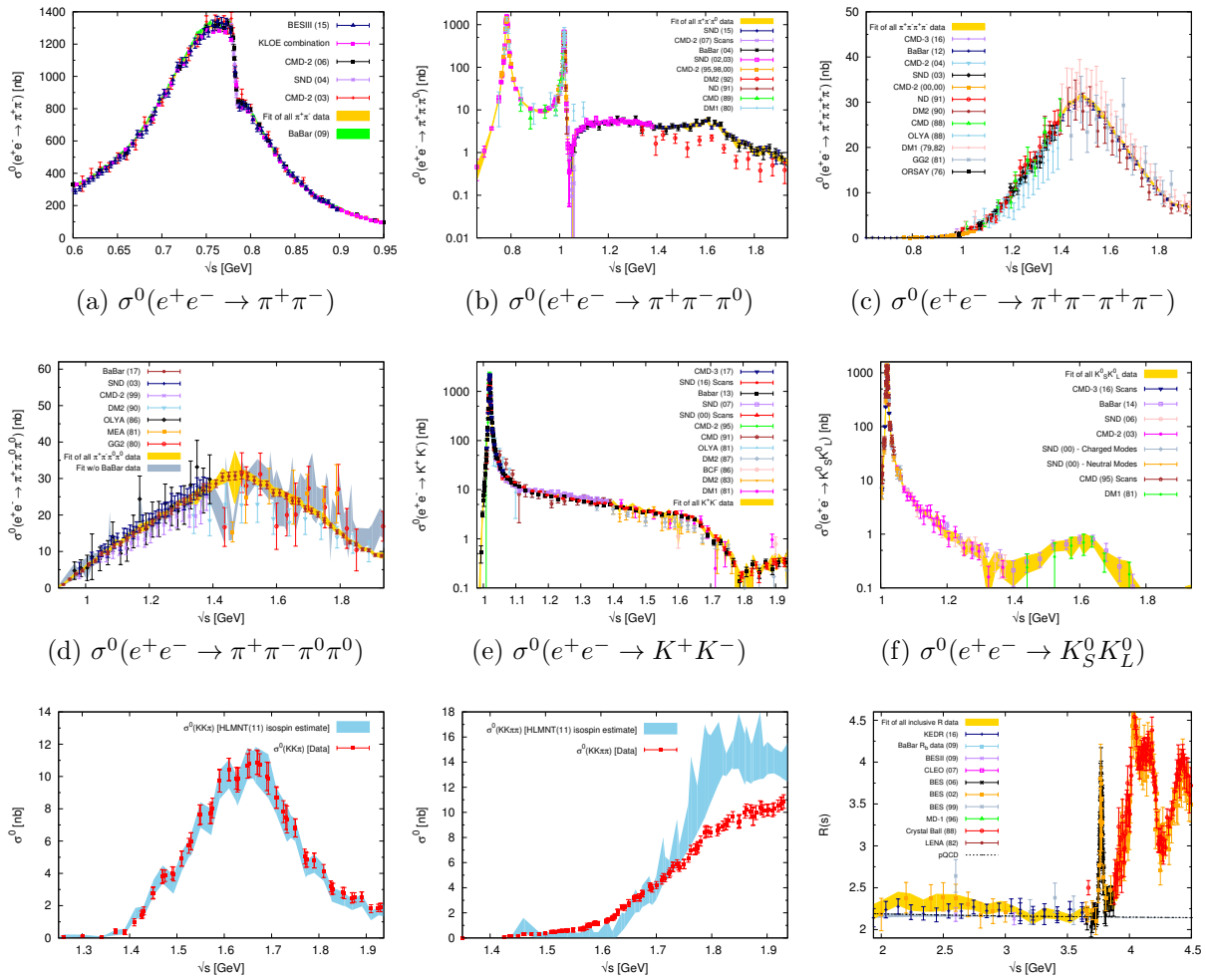

(a) $\sigma^0(e^+e^- \to \pi^+\pi^-)$ (b) $\sigma^0(e^+e^- \to \pi^+\pi^-\pi^0)$ (c) $\sigma^0(e^+e^- \to \pi^+\pi^-\pi^+\pi^-)$

(d) $\sigma^0(e^+e^- \to \pi^+\pi^-\pi^0\pi^0)$ (e) $\sigma^0(e^+e^- \to K^+K^-)$ (f) $\sigma^0(e^+e^- \to K^0_S K^0_L)$

(g) $\sigma^0(e^+e^- \to KK\pi)$ (h) $\sigma^0(e^+e^- \to KK\pi\pi)$ (i) Inclusive data

Figure 2: The resulting cross sections of the leading and major sub-leading hadronic final states.

release of energy dependent, correlated uncertainties outside of the $\pi^+\pi^-$ channel. The neutral final state $K^0_S K^0_L \pi^0$ has been measured by SND [17] and BaBar [19], completing all modes that contribute to the $KK\pi$ final state. Plot (g) of Figure 2 demonstrates good agreement between the previously used isospin estimate [18] and the data-based approach in this analysis. In addition, BaBar have also completed all modes that contribute to the $KK\pi\pi$ channel [19]. Examining plot (h) of Figure 2, it is evident that the isospin relations provided a poor estimate of this final state. The inclusive hadronic R-ratio now includes precise measurements by the KEDR collaboration [20]. The fit of the inclusive data in the range $1.937 \leq \sqrt{s} \leq 3.80$ GeV is shown in plot (i) of Figure 2, which demonstrates that the inclusive data combination is much improved. With the new KEDR data, the differences between the inclusive data and pQCD are not as large as previously and, hence, the contributions in the entire inclusive data region are now estimated using the inclusive data alone.

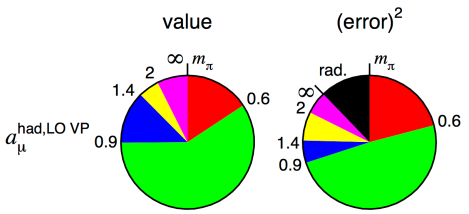

(a) Fractional contributions to $a_\mu^{\text{had, LO VP}}$

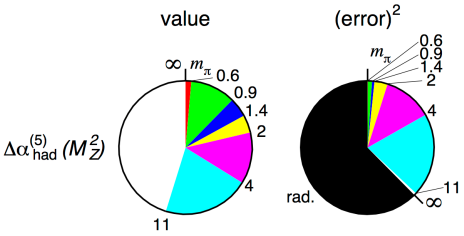

(b) Fractional contributions to $\Delta\alpha^{(5)}_{\text{had}}(M_Z^2)$

Figure 3: Pie charts showing the fractional contributions to the total mean value and (error)^2 of both $a_\mu^{\text{had, LO VP}}$ and $\Delta\alpha^{(5)}_{\text{had}}(M_Z^2)$ from various energy intervals.

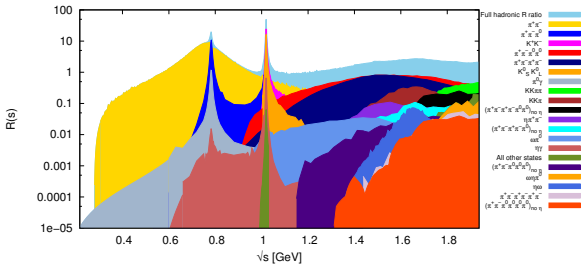

(a) The hadronic R ratio

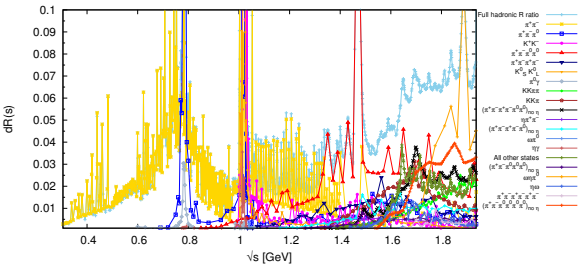

(b) The uncertainty of the hadronic R ratio

Figure 4: Contributions to the total hadronic R ratio from the different final states (left panel) and their uncertainties (right panel) below 1.937 GeV. The full R ratio and its uncertainty is shown in light blue in each plot, respectively. Each final state is included as a new layer on top in decreasing order of the size of its contribution to $a_\mu^{\text{had, LO VP}}$.

3.1 Total contribution of $a_\mu^{\text{had, LO VP}}$ and $\Delta\alpha^{(5)}_{\text{had}}$

From the sum of all hadronic contributions, the estimate for $a_\mu^{\text{had, LO VP}}$ from this analysis is [6]

$$a_\mu^{\text{had, LO VP}} = (693.27 \pm 1.19_{\text{stat}} \pm 2.01_{\text{sys}} \pm 0.22_{\text{vp}} \pm 0.71_{\text{fsr}}) \times 10^{-10} = (693.27 \pm 2.46_{\text{tot}}) \times 10^{-10} \ , \quad (2)$$

where the uncertainties include all available correlations and local χ^2_{min}/d.o.f. inflation. Using the same data compilation as for the calculation of $a_\mu^{\text{had, LO VP}}$, the next-to-leading order (NLO) contribution to $a_\mu^{\text{had,VP}}$ is determined here to be $a_\mu^{\text{had,NLOVP}} = (-9.82 \pm 0.04) \times 10^{-10}$. The corresponding result for $\Delta\alpha^{(5)}_{\text{had}}(M_Z^2)$ is [6]

$$\Delta\alpha^{(5)}_{\text{had}}(M_Z^2) = (276.11 \pm 0.26_{\text{stat}} \pm 0.68_{\text{sys}} \pm 0.14_{\text{vp}} \pm 0.82_{\text{fsr}}) \times 10^{-4} = (276.11 \pm 1.11_{\text{tot}}) \times 10^{-4} \ , \quad (3)$$

where the superscript (5) indicates the contributions from all quark flavours except the top quark. The fractional contributions to the total mean value and uncertainty of both $a_\mu^{\text{had, LO VP}}$ and $\Delta\alpha^{(5)}_{\text{had}}(M_Z^2)$ from various energy intervals is shown in Figure 3. Figure 4 shows the contributions from all hadronic final states to the hadronic R ratio and its uncertainty below 1.937 GeV.

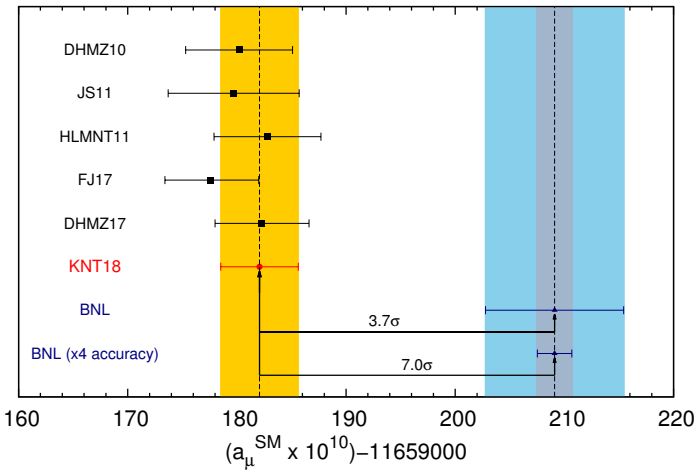

Figure 5: A comparison of recent and previous evaluations of $a_\mu^{\rm SM}$. The analyses listed in chronological order are: DHMZ10 [21], JS11 [22], HLMNT11 [18], FJ17 [23] and DHMZ17 [24]. The prediction from this work is listed as KNT18 [6], which defines the uncertainty band that other analyses are compared to. The current uncertainty on the experimental measurement [1, 2] is given by the light blue band. The light grey band represents the hypothetical situation of the new experimental measurement at Fermilab yielding the same mean value for $a_\mu^{\rm exp}$ as the BNL measurement, but achieving the projected four-fold improvement in its uncertainty [3].

3.2 SM prediction of $g-2$ of the muon and $\alpha(M_Z^2)$

Combining the results for $a_\mu^{\rm had,\,LO\,VP}$ and $a_\mu^{\rm had,\,NLO\,VP}$ with the contributions from QED: $a_\mu^{\rm QED} = (11\,658\,471.8971 \pm 0.007) \times 10^{-10}$ [25], the electro-weak sector: $a_\mu^{\rm EW} = (15.36 \pm 0.10) \times 10^{-10}$ [26], the hadronic vacuum polarisation at NNLO: $a_\mu^{\rm had,\,NNLO\,VP} = (1.24 \pm 0.01) \times 10^{-10}$ [27], the hadronic light-by-light (LbL) at LO: $a_\mu^{\rm had,\,LbL} = (9.8 \pm 2.6) \times 10^{-10}$ [28] and the hadronic LbL at NLO: $a_\mu^{\rm had,\,NLO\,LbL} = (0.3 \pm 0.2) \times 10^{-10}$ [29], the SM prediction of the anomalous magnetic moment of the muon is found to be

$$a_\mu^{\rm SM} = (11\,659\,182.05 \pm 3.56) \times 10^{-10}\,. \tag{4}$$

Comparing this with the current experimental measurement results in a deviation of $\Delta a_\mu = (27.05 \pm 7.26) \times 10^{-10}$, corresponding to a 3.7σ discrepancy. This result is compared with other determinations of $a_\mu^{\rm SM}$ in Figure 5. The total value of the QED coupling at the Z boson mass is found in this work to be

$$\alpha^{-1}(M_Z^2) = \Big(1 - \Delta\alpha_{\rm lep}(M_Z^2) - \Delta\alpha_{\rm had}^{(5)}(M_Z^2) - \Delta\alpha_{\rm top}(M_Z^2)\Big)\alpha^{-1} = 128.946 \pm 0.015\,. \tag{5}$$

4 Conclusions

This analysis, KNT18 [6], has completed a full re-evaluation of the hadronic vacuum polarisation contributions to the anomalous magnetic moment of the muon, $a_\mu^{\rm had,\,VP}$ and the hadronic contribution to the effective QED coupling at Z boson mass, $\Delta\alpha_{\rm had}(M_Z^2)$. Combining all available $e^+e^- \to$ hadrons cross section data, this analysis found $a_\mu^{\rm had,\,LO\,VP} = (693.27 \pm 2.46) \times 10^{-10}$ and $a_\mu^{\rm had,\,NLO\,VP} = (-9.82 \pm 0.04) \times 10^{-10}$. This has resulted in a new estimate for the Standard Model prediction of $a_\mu^{\rm SM} = (11\,659\,182.05 \pm 3.56) \times 10^{-10}$, which deviates from the current experimental measurement by 3.7σ.

Acknowledgements

We would like to thank the organisers of *LFC17: Old and New Strong Interactions from LHC to Future Colliders* for a very productive and enjoyable workshop.

References

1. G. W. Bennett *et al.* [Muon g-2 Collaboration], Phys. Rev. Lett. **89** (2002) 101804 [Erratum: Phys. Rev. Lett. **89** (2002) 129903]; Phys. Rev. Lett. **92** (2004) 161802; Phys. Rev. D **73** (2006) 072003.
2. C. Patrignani et al. (Particle Data Group), Chin. Phys. C **40**, 100001 (2016) and 2017 update.
3. J. Grange *et al.* [Muon g-2 Collaboration], arXiv:1501.06858.
4. T. Mibe [J-PARC g-2 Collaboration], Chin. Phys. C **34** (2010) 745.
5. A. Hoefer, J. Gluza and F. Jegerlehner, Eur. Phys. J. C **24** (2002) 51; J. Gluza, A. Hoefer, S. Jadach and F. Jegerlehner, Eur. Phys. J. C **28** (2003) 261.
6. A. Keshavarzi, D. Nomura and T. Teubner, arXiv:1802.02995 [hep-ph].
7. G. D'Agostini, Nucl. Instrum. Meth. A **346** (1994) 306.
8. V. Blobel, eConf C **030908** (2003) MOET002.
9. R. D. Ball *et al.* [NNPDF Collaboration], JHEP **1005** (2010) 075.
10. M. Benayoun, P. David, L. DelBuono and F. Jegerlehner, Eur. Phys. J. C **75** (2015) 613.
11. D. Babusci *et al.* [KLOE Collaboration], Phys. Lett. B **720** (2013) 336.
12. A. Anastasi *et al.* [KLOE-2 Collaboration], arXiv:1711.03085 [hep-ex].
13. M. Ablikim *et al.* [BESIII Collaboration], Phys. Lett. B **753** (2016) 629.
14. B. Aubert *et al.* [BaBar Collaboration], Phys. Rev. Lett. **103** (2009) 231801.
15. J. P. Lees *et al.* [BaBar Collaboration], Phys. Rev. D **96** (2017) 092009.
16. J. P. Lees *et al.* [BaBar Collaboration], Phys. Rev. D **88** (2013) 032013.
17. M. N. Achasov *et al.*, arXiv:1711.07143 [hep-ex].
18. K. Hagiwara, R. Liao, A. D. Martin, D. Nomura and T. Teubner, J. Phys. G **38** (2011) 085003.
19. J. P. Lees *et al.* [BaBar Collaboration], Phys. Rev. D **95** (2017), 052001; Phys. Rev. D **89** (2014, 092002; Phys. Rev. D **95** (2017) 092005.
20. V. V. Anashin *et al.*, Phys. Lett. B **770** (2017) 174; Phys. Lett. B **753** (2016) 533.
21. M. Davier, A. Hoecker, B. Malaescu and Z. Zhang, Eur. Phys. J. C **71** (2011) 1515 [Erratum: Eur. Phys. J. C **72** (2012) 1874].
22. F. Jegerlehner and R. Szafron, Eur. Phys. J. C **71** (2011) 1632.
23. F. Jegerlehner, arXiv:1705.00263 [hep-ph].
24. M. Davier, A. Hoecker, B. Malaescu and Z. Zhang, Eur. Phys. J. C **77** (2017) 827.
25. T. Aoyama, M. Hayakawa, T. Kinoshita and M. Nio, Phys. Rev. Lett. **109** (2012) 111808, arXiv:1712.06060 [hep-ph].
26. C. Gnendiger, D. Stöckinger and H. Stöckinger-Kim, Phys. Rev. D **88** (2013) 053005.

27. A. Kurz, T. Liu, P. Marquard and M. Steinhauser, Phys. Lett. B **734** (2014) 144.

28. A. Nyffeler, Phys. Rev. D **94** (2016) 053006.

29. G. Colangelo, M. Hoferichter, A. Nyffeler, M. Passera and P. Stoffer, Phys. Lett. B **735** (2014) 90.

Frascati Physics Series Vol. 65 (2017)
LFC17: Old and New Strong Interactions from LHC to Future Colliders
11 - 15 September, 2017

LATTICE FIELD THEORY RESULTS ON NEW STRONG DYNAMICS

Enrico Rinaldi
RIKEN BNL Research Center, Brookhaven National Laboratory, Upton, NY 11973, USA

Abstract

Lattice gauge theory is a robust framework to study non-perturbative physics and it is amenable to numerical simulations. It has been succesfully used to study the low-energy regime of QCD. Modern-day lattice simulation codes are actually flexible enough that users can change the theory being simulated: we can study different number of colors N_c, number of quarks N_f and quarks in different representations N_r, in addition to the usual parameters, gauge coupling β and quark masses m_f.

These new theories, although interesting in their own rights as well-defined gauge theories, can be used as templates to study physics beyond the Standard Model (BSM). I will report on a particular SU(3) gauge theory with 8 fermions in the fundamental representation. In particular I will highlight how lattice simulations of the flavor-singlet scalar and pseudoscalar spectrum compare to QCD.

1 Introduction

We perform lattice field theory simulations of QCD with different numbers of light (massless) fermions to study the spectrum of bound states in the scalar and pseudoscalar channel, in particular focusing on particles that have no flavor charge (flavor singlets). The flavor-singlet scalar channel has the same symmetries as the QCD vacuum and it is related to the trace anomaly, while the flavor-singlet pseudoscalar channel is related to the chiral anomaly. These anomalies dictate the low-energy behavior of QCD and are instrumentals in the construction of effective models, hence a direct study of these flavor-singlet states is of paramount importance for the understanding of strong dynamics.

While experiments provide direct access to this spectrum in the case of QCD with $N_f = 2$–where only the up and down flavors are light– we can only use approximate models with somewhat large theoretical uncertainties to understand the spectrum for $N_f > 2$. Our lattice simulations aim at filling this gap and at providing data with which phenomenological models could be benchmarked.

This is not only relevant for the understanding of strongly interacting theories like QCD, but also for physics Beyond the Standard Model (BSM)—in particular extensions of the Standard Model based on strong dynamics. For example, composite Higgs models regard the SM Higgs sector as a low-energy description of new strong dynamics where the Higgs boson is a flavor-singlet scalar bound state. Therefore, the study of this channel with first-principle calculations becomes important to determine which UV completion has the correct properties to behave like the SM Higgs sector at low energies.

Composite Higgs models based on the idea of *walking technicolor* require that the strongly interacting theory has near-conformal dynamics and these have been studied on the lattice in recent years [1, 2].

Interestingly, it is still not clear what would the signs of near-conformal dynamics be at the full non-perturbative level even though there are qualitative expectations from approaches like SD ladder equations which capture some features of the non-perturbative dynamics. These are only supposed to be used as guidelines for the lattice investigation. In order to shed light on signals of near-conformal dynamics we compare the flavor-singlet spectrum from lattice simulations of QCD with $N_f = 4$, 8 and 12, focusing on $N_f = 8$ as a promising candidate.

Previous lattice numerical simulations indicate that these 3 different values of N_f correspond to rather different type of dynamics: while $N_f = 4$ is expected to show the same features as QCD with $N_f = 2$, namely confinement and spontaneous chiral symmetry breaking, the theory with $N_f = 12$ is expected to have conformal dynamics, with ratios of mass scales that stay constant toward the massless limit. This points to QCD with $N_f = 8$ as a candidate for near-conformal dynamics, with several lattice studies confirming the presence of a flavor-singlet scalar state much lighter than the vector state, in contrast with QCD with smaller number of flavors[1].

In the following we will highlight the differences, or the similarities, between QCD theories with different numbers of light (or massless) flavors, in a quantitative way. We leave the interpretation of the results in terms of composite Higgs models, or walking technicolor theories, to future and more thorough investigations[2].

2 The flavor-singlet scalar state

Extracting the mass of the flavor-singlet scalar state with $J^{PC} = 0^{++}$ is difficult because of the need to calculate expensive disconnected contributions and to tame the statistical noise from gauge fluctuations. Even from the experimental point of view it is hard to study the lightest 0^{++} properties because this state appears only as a broad resonance, identified as the $f_0(500)$ or σ particle with mass $\sim 400-500$ MeV [4]. In that case the σ decays to two pions. This is an additional complication for lattice calculations—even for the real-world case of QCD with $N_f = 2$ light fermions, results have appeared only in the last year [5]. The lattice results support the nature of the σ as a broad resonance if the quark mass is not too heavy. However, if the pion in QCD with $N_f = 2$ becomes heavier, the σ does not decay and it becomes a bound state with a mass $M_\sigma \approx 0.9 M_\rho$ when $M_\rho/M_\pi \approx 2.2$ [5], or even heavier than the ρ meson, at larger fermion masses [6].

In this section we would like to highlight the difference between the $N_f = 2$ theory and the large-N_f theories. For example, our most precise and extensive results in QCD with $N_f = 8$ show that the lightest 0^{++} particle is degenerate with the pion in the whole fermion mass range explored. This of course

[1] So far we have used the term QCD to refer to a generic SU(3) gauge theory with N_f light quarks in the fundamental irreducible representation of the gauge group, and we continue to do so in the following.

[2] We also remind the readers that some of the unpublished results reported in the following sections should be considered as preliminary and might change (albeit slightly) in the future.

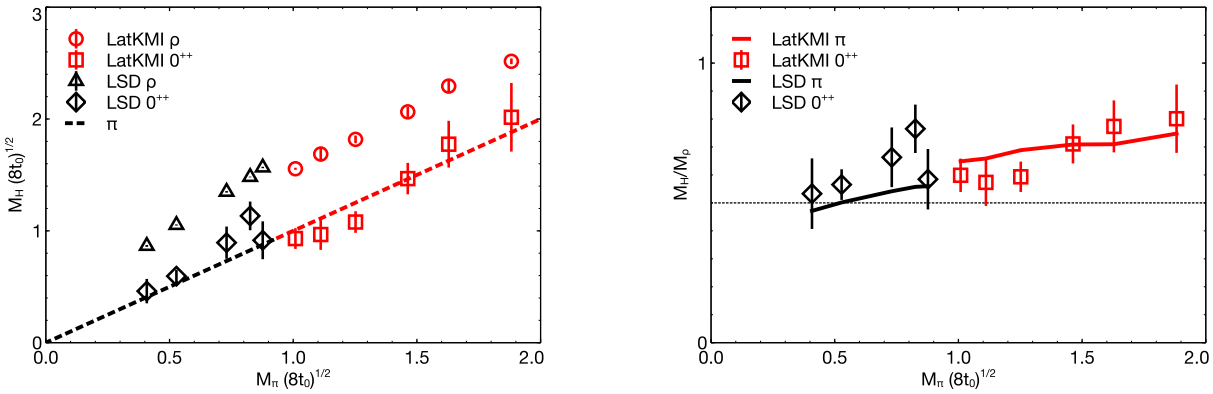

Figure 1: Combining LatKMI and LSD results for the flavor-singlet scalar state, a clear trend can be seen towards the masslesss fermion limit. The 0^{++} state remains degenerate with the pion (left) and much lighter than the vector meson (right), all the way to the lightest fermions studied by the LSD collaboration [3].

simplifies the numerical analysis with respect to the real-world scenario because the states propagating in the two-point function are stable. Moreover, not only the lightest 0^{++} state is degenerate with π, but it is also much lighter than the ρ meson [7].

The LSD collaboration has performed the same measurements, with a more sophisticated analysis technique, for QCD with $N_f = 8$ using a different discretization. While the hadron masses in units of the lattice spacing are different, using the Wilson flow scale $\sqrt{8t_0}$ [8] measured on every ensemble[3] to rescale all results allows us to combine the two datasets and draw suggestive comments. In Fig. 1 the LatKMI results [7] and the LSD results [9, 3] are combined. The left panel shows the flavor-singlet scalar state following the pion from heavier (LatKMI) to lighter (LSD) fermion masses. In the fermion mass region explored there is no sign of the 0^{++} state "peeling" off from the pion, which would happen at very light fermion masses due to the pseudo-Nambu-Goldstone nature of the pions. The right panel instead shows a direct comparison between the flavor-singlet scalar state and the ρ meson. There is a clear trend towards the massless fermion limit, indicating that the mass hierarchy between the two states increases. As a comparison, the lattice results for QCD with $N_f = 2$ for a pion to vector mass ratio corresponding to the lightest point in the figure yield $M_\sigma \approx 0.9 M_\rho$ [5].

We can contrast the $N_f = 8$ flavor-singlet scalar result with the $N_f = 12$ case, which was the first discovered example of a many-flavor theory showing a light scalar state [10]. For QCD with $N_f = 12$ we have found a flavor-singlet state even lighter than the pion. Moreover, its mass interestingly follows a hyperscaling relation dictated by the mass anomalous dimension γ (extracted from scaling relations for the rest of the spectrum, which has much smaller statistical uncertainties).

We also mention that we have extracted the mass of the flavor-singlet scalar state in QCD with $N_f = 4$ and its mass on our lightest point is heavier than the pion mass but lighter than the vector mass [11]. This result is shown in panel (a) of Fig. 3.

The qualitative conclusion we draw from the wealth of our results is that the flavor-singlet scalar state gets lighter with respect to the ρ and π states as the number of light degenerate flavors increases

[3]For LatKMI ensembles, the Wilson flow scale is reported in Ref. [7], while for LSD ensembles we use results that have been shared in private communications and used in Ref. [9].

(eventually becoming the lightest state in the spectrum when the theory enters the conformal window).

3 The flavor-singlet pseudoscalar state

While the results presented for the flavor-singlet scalar had been previously presented in conference talks or in published papers, the flavor-singlet pseudoscalar results were presented for the first time at this conference for three values of $N_f = 4$, 8 and 12. Preliminary results for $N_f = 8$ have been reported in Ref. [12].

The flavor-singlet pseudoscalar state has quantum numbers $J^{PC} = 0^{-+}$ and corresponds to the so-called η' particle in QCD with $N_f = 2$. Witten [13] and Veneziano [14] showed that the η' mass is directly related to the contribution of the axial anomaly and the topological structure of the QCD vacuum. In fact, in the limit of a SU(N_c) gauge theory with $N_c \to \infty$, the η' becomes massless, behaving as a Nambu-Goldstone boson. This mechanism for $N_c = 3$, therefore for QCD, is not applicable and the axial anomaly makes this state very heavy, measured experimentally to be ~ 958 MeV [4].

It is notoriously difficult to compute the mass of the flavor-singlet pseudoscalar, because the pion contribution is statistically challenging to remove. In our calculations we adopt a gluonic operator, which does not suffer from the aforementioned problem, since it does not couple directly to π states. The same method has been adopted in QCD with $N_f = 2 + 1$ and has led to results in agreement with experiments [15].

In practice, the interpolating operator used is the topological charge density defined through the clover-plaquette strength-energy field tensor $F^{\mu\nu}(x)$:

$$q(x) \;=\; \frac{1}{32\pi}\epsilon_{\mu\nu\rho\sigma}\mathrm{Tr}\, F^{\mu\nu}(x)F^{\rho\sigma}(x) \quad , \tag{1}$$

The two-point function $\langle q(x)q(y)\rangle$ is computed for all pairs of points (x,y) in the four-dimensional volume $L^3 \times T$ efficiently using FFT. Moreover, because of translation invariance, the two-point correlator only depends on the distance $r = |x-y|$ and we average all contributions at fixed distance to increase statistics. For a particle freely propagating in four dimensions, the correlator takes the form

$$C(r) = \frac{A}{r^{1.5}}\left(1 + \frac{3}{8r}\right) e^{-M_{\eta'} r} \tag{2}$$

at large distances $r \to \infty$. We fit the data of $C(r)$ to this form, in a specific window of distances $r \in [r_{\mathrm{min}}, r_{\mathrm{max}}]$, to extract the two parameters A and $M_{\eta'}$.

Additionally, we utilize the Wilson flow [8] as a smearing technique to remove ultraviolet fluctuations and obtain interpolating operators with *physical size* — having enhanced overlap to the ground state. Using the operator in Eq. (1), where $F^{\mu\nu}(x)$ is computed for several Wilson flow times t_w, we obtain a large number of correlators $C_{t_w}(r) = -\langle q_{t_w}(x)q_{t_w}(y)\rangle$. The statistical fluctuations are dramatically reduced by the Wilson flow smearing, such that correlators at larger t_w can be easily fitted to the exponential form in Eq. (2). However, the smearing introduces systematic corrections that have to be addressed [16]. In fact, it turns out that the dominant source of uncertainty in extracting $M_{\eta'}$ is coming from systematic effects of the fitting procedure. There are two competing effects:

- Eq. (2) can only be assumed to be valid in a specific region of large r, where only the ground state dominates, such that the extracted mass does not depend on the value of r_{min}.
- The correlator at large distances suffers from larger statistical fluctuations and can be extracted only at large values of smearing t_w, where smearing artifacts [16] are larger.

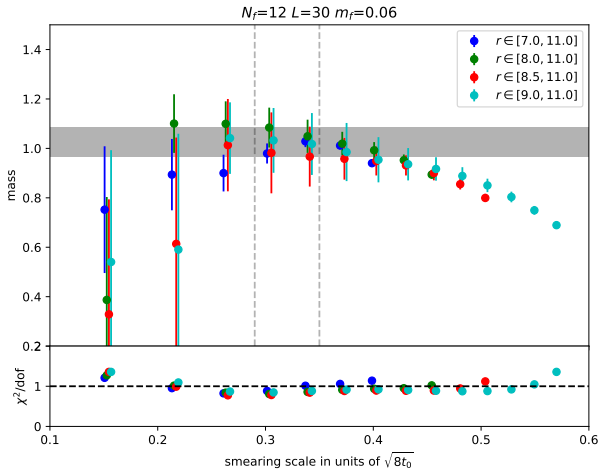

Figure 2: The η' mass fitted for different distance regions and smearings, for a specific ensemble of QCD with $N_f = 12$. The main features are described in the text.

We estimate the systematic uncertainty on $M_{\eta'}$ by looking for a plateaux in the fitting range $[r_{\rm min}, r_{\rm max}]$, and for a plateaux in the smearing range $\sqrt{8t_w}$. This is exemplified in the panels of Fig. 2 for a representative ensemble of QCD with $N_f = 12$. The smearing range $\sqrt{8t_w}$ is considered in units of the characteristic radius given by the Wilson flow scale $\sqrt{8t_0}$, and we find a common region for all the ensembles at fixed N_f—we see that it does not depend on the fermion mass or the volume. This indicates that such a smearing corresponds to some physical scale for the operator with the best coupling to the ground state. In the identified region, we take the difference between the largest and the smallest fitted mass as an estimate of the systematic error. The statistical errors of the individual points are usually smaller than this systematic uncertainty.

We can now compare the flavor-singlet pseudoscalar state with the rest of the low-lying spectrum as we change the number of flavors. The compilation of results for QCD with $N_f = 4$, 8 and 12 is reported in Fig. 3. We identify a notable increase in the gap between the flavor-singlet pseudoscalar and the vector meson. In QCD with $N_f = 4$ the mass ratio $M_{\eta'}/M_\rho$ is close to one, while it grows to $\sim 3-4$ for $N_f = 8$ and 12.

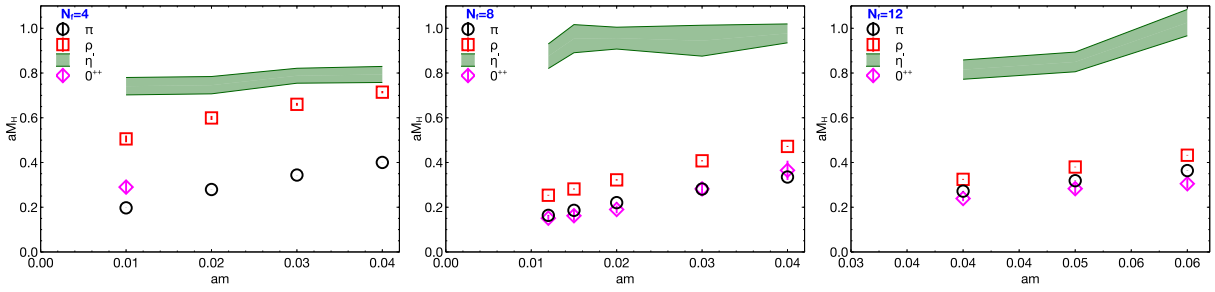

Figure 3: Flavor-singlet scalar and pseudoscalar spectrum compared to flavor-non-singlet pseudoscalar and vector spectrum for $N_f = 4$, 8 and 12. The η' mass is shown with error bands that reflect a large systematic uncertainty. Only statistical errors are shown for the other states.

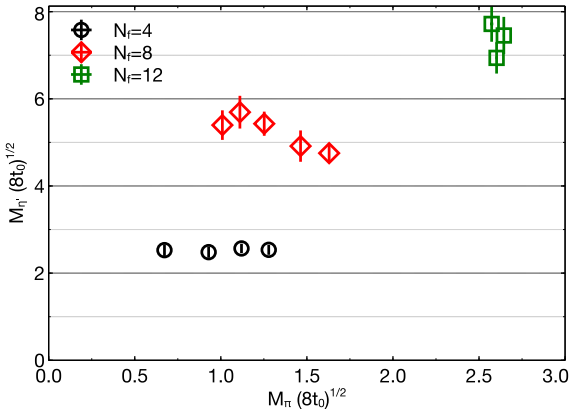

Figure 4: Comparison of the flavor-singlet pseudoscalar mass for $N_f = 4$, 8 and 12 as a function of the pion mass. The hadronic masses are in units of the Wilson flow scale $\sqrt{8t_0}$ to partially remove discretization effects due to different gauge couplings for the various N_f theories. Different quark mass regions are explored for different N_f values.

4 Summary

There are theoretical expectations [17] suggesting that the flavor-singlet scalar state becomes light near the conformal window as N_f is increased, while the flavor-singlet pseudoscalar becomes heavier. In particular, the flavor-singlet pseudoscalar is expected to scale with N_f in QCD, as a consequence of a *anti*-Veneziano limit where $N_f/N_c \gg 1$ is fixed as $N_c \to \infty$. This is confirmed by comparing QCD with $N_f = 4$, 8 and 12 in Fig. 4 after rescaling all the masses with the Wilson flow scale $\sqrt{8t_0}$.

Moreover, a low-energy description of many-flavor QCD [18], based on the linear sigma model, is able to incorporate our numerical results for the flavor-singlet scalar and pseudoscalar states in a consistent framework. This effective description points out a potentially simple way to use our data in order to discriminate if a particular many-flavor QCD theory is inside or outside the conformal window. Another effective discription based on the linear sigma model [19] was benchmarked against the spectrum of QCD with $N_f = 8$, along the lines of the work in Ref. [20] which used a different effective description including the effects of a dilaton.

In conclusion, understanding the flavor-singlet spectrum of QCD for varying number of flavors from first principles is challenging but it is of paramount importance to obtain a quantitative low-energy description of strong dynamics in different regimes, from spontaneous chiral symmetry breaking to conformality.

5 Acknowledgements

I would like to thank the LatKMI collaboration and the Lattice Strong Dynamics Collaboration for sharing their result. I also want to thank the organizers of the LFC17 workshop. I am supported by a Special Postdoctoral Researcher fellowship from RIKEN, Japan.

References

1. B. Svetitsky, Looking behind the Standard Model with lattice gauge theory, in *Proceedings of 35th International Symposium on Lattice Field Theory (Lattice2017): Granada, Spain*, to appear in EPJ

Web Conf.

2. Claudio Pica, Beyond the Standard Model: Charting Fundamental Interactions via Lattice Simulations, *PoS* LATTICE2016 (2016) 015.

3. G. Fleming, Near-conformal dynamics in SU(3) $N_f = 8$ gauge theory. in *Proceedings of 35th International Symposium on Lattice Field Theory (Lattice2017): Granada, Spain*, to appear in EPJ Web Conf.

4. C. Patrignani et al, Review of Particle Physics, *Chin. Phys.* C40 (2016) 100001.

5. Raul A. Briceno, Jozef J. Dudek, Robert G. Edwards and David J. Wilson, Isoscalar $\pi\pi$ scattering and the σ meson resonance from QCD, *Phys. Rev. Lett.* 118 (2017) 022002.

6. Teiji Kunihiro, Shin Muroya, Atsushi Nakamura, Chiho Nonaka, Motoo Sekiguchi and Hiroaki Wada, Scalar mesons in lattice QCD, *Phys. Rev.* D70 (2004) 034504.

7. Yasumichi Aoki, Tatsumi Aoyama, Ed Bennett, Masafumi Kurachi, Toshihide Maskawa, Miura Kohtaroh, Kei-ichi Nagai, Hiroshi Ohki, Enrico Rinaldi, Akihiro Shibata, Koichi Yamawaki and Takeshi Yamazaki, Light flavor-singlet scalars and walking signals in $N_f = 8$ QCD on the lattice, *Phys. Rev.* D96 (2017) 2017.

8. Martin Lscher. Properties and uses of the Wilson flow in lattice QCD, *JHEP* 08 (2010) 071 [Erratum: *JHEP* 03 (2014) 092].

9. Thomas Appelquist, R. C. Brower, G. T. Fleming, Anna Hasenfratz, X. Y. Jin, Joe Kiskis, E. T. Neil, J. C. Osborn, Claudio Rebbi, Enrico Rinaldi, David Schaich, Pavlos Vranas, Evan Weinberg and Oliver Witzel, Strongly interacting dynamics and the search for new physics at the LHC, *Phys. Rev.* D93 (2016) 114514.

10. Yasumichi Aoki, Tatsumi Aoyama, Masafumi Kurachi, Toshihide Maskawa, Kei-ichi Nagai, Hiroshi Ohki, Enrico Rinaldi, Akihiro Shibata, Koichi Yamawaki and Takeshi Yamazaki, Light composite scalar in twelve-flavor QCD on the lattice, *Phys. Rev. Lett.* 111 (2013) 2013.

11. Yasumichi Aoki, Tatsumi Aoyama, Ed Bennett, Masafumi Kurachi, Toshihide Maskawa, Miura Kohtaroh, Kei-ichi Nagai, Hiroshi Ohki, Enrico Rinaldi, Akihiro Shibata, Koichi Yamawaki and Takeshi Yamazaki, SU(3) gauge theory with four degenerate fundamental fermions on the lattice, *PoS* LATTICE2015 (2016) 215.

12. Yasumichi Aoki, Tatsumi Aoyama, Ed Bennett, Masafumi Kurachi, Toshihide Maskawa, Miura Kohtaroh, Kei-ichi Nagai, Hiroshi Ohki, Enrico Rinaldi, Akihiro Shibata, Koichi Yamawaki and Takeshi Yamazaki, Walking and conformal dynamics in many-flavor QCD. *PoS* LATTICE2015 (2016) 213.

13. Edward Witten, Current Algebra Theorems for the U(1) Goldstone Boson, *Nucl. Phys.* B156 (1979) 269.

14. G. Veneziano, Goldstone Mechanism From Gluon Dynamics, *Phys. Lett.* 95B (1980) 90.

15. H. Fukaya, S. Aoki, G. Cossu, S. Hashimoto, T. Kaneko and J. Noaki, η' meson mass from topological charge density correlator in QCD. *Phys. Rev.* D92 (2015) 111501.

16. Mattia Bruno, Stefan Schaefer and Rainer Sommer, Topological susceptibility and the sampling of field space in $N_f = 2$ lattice QCD simulations, *JHEP*, 08 (2014) 150.

17. Shinya Matsuzaki and Koichi Yamawaki, Walking on the ladder: 125 GeV technidilaton, or Conformal Higgs, *JHEP* 12 (2015) 053. [Erratum: *JHEP* 11 (2016) 158(2016)].

18. Y. Meurice, A linear sigma model for multiflavor gauge theories, arXiv:1006.4518 [hep-lat].

19. A. Gasbarro, Can a Linear Sigma Model Describe Walking Gauge Theories at Low Energies?, in *Proceedings of 35th International Symposium on Lattice Field Theory (Lattice2017): Granada, Spain*, to appear in EPJ Web Conf.

20. Thomas Appelquist, James Ingoldby and Maurizio Piai, Dilaton EFT Framework For Lattice Data, *JHEP* 07 (2017) 035.

Frascati Physics Series Vol. 65 (2017)
LFC17: Old and New Strong Interactions from LHC to Future Colliders
11 - 15 September, 2017

STRONG DYNAMICS AT THE TEV SCALE FOR THE HIERARCHY PROBLEM

Alex Pomarol
Dept. de Física, IFAE and BIST, Universitat Autònoma de Barcelona, 08193 Bellaterra, Barcelona

Abstract

I present an holographic approach to strongly-coupled theories close to the conformal transition, trying to understand the presence of light scalars as recent lattice simulations seem to suggest. This can have important implications for solutions to the hierarchy problem via TeV strong-dynamics and their searches at the LHC.

1 Introduction

Understanding strongly-coupled systems is indispensable either from a phenomenological as well as a theoretical point of view. On one side, we already know that Nature makes use of a fundamental theory in the strongly-coupled regime, quantum chromodynamics. Furthermore, there is also the possibility that the SM Higgs could emerge as a composite state from a strongly-coupled theory at the TeV. On the other hand, theoretically, it is also necessary to understand strongly-coupled systems in order to provide a complete mapping of quantum field theories and their predictions.

We are interested here in strongly-coupled theories close to the conformal transition. This is the transition from a theory in the conformal regime to a non-conformal one. For example, in QCD, when the number of fermions is enlarged, we expect the theory to become a conformal field theory (CFT) at the IR. It is unclear where this exactly happens, but lattice simulations suggest that this could be around $N_F \sim 10$. There are several motivations to study strongly-coupled theories close to the conformal

transition. First, recent lattice simulations suggest that, contrary to ordinary QCD, theories close to the conformal transition have as the lightest resonance a 0^{++} scalar (apart, of course, from the goldstone bosons, the pions) [1, 2]. It is unclear the origin of the lightness of this state. Some arguments suggest that this could be a dilaton, the goldstone associated to the breaking of scale invariance. For physics beyond the SM (BSM), theories close to the conformal transition are also of utmost interests. These theories allow to generate a large hierarchy of scales that could be useful to explain, for example, the difference between the electroweak scale and the Planck scale, or the differences in the SM fermion mass spectrum. Furthermore, if a light scalar is present in these theories, one could speculate whether this can be the Higgs, or whether this could be the most feasible resonance to search for at the LHC.

It has been suggested in Ref. [3] that the conformal transition is characterized by the merging of an IR fixed point with a UV fixed point. This is expected to occur when the dimensionality of a scalar operator of the theory, e.g. $q\bar{q}$ in a QCD-like theory, approaches two. In this case, conformality is lost when this operator gets a complex dimension. Holography, based on the correspondence (or duality) between strongly-coupled CFTs and weakly-coupled five-dimensional Anti-de-Sitter theories (AdS_5) [4], allows to study this transition. As we will discuss below, in the AdS_5 theory the scale symmetry is lost when a scalar Φ, that plays the role of the $q\bar{q}$ operator, gets a mass below the BF-bound $M_\Phi^2 = -4/L^2$ [3]. When this happens, the scalar becomes tachyonic and gets a non-zero profile. Working with the weakly-coupled AdS_5 theory it will be possible to calculate the spectrum of resonances of the theory and see whether it contains a light scalar or not [5].

2 A five-dimensional model for the conformal transition

We will work within the simplest possible holographic five-dimensional model that embody the properties of strongly-coupled theories that we want to study. This is a deformed CFT with a scalar operator, $q_L^i \bar{q}_R^j$ $(i, j = 1, ..., N_F)$ for concreteness, whose dimension becomes imaginary. This means that the scalar $q_L^i \bar{q}_R^j$ gets a vacuum expectation value (VEV), signaling the lost of conformality. The global symmetry of this theory is $U(N_F)_L \otimes U(N_F)_R$ that is also broken by the VEV of the scalar $\langle q_L^i \bar{q}_R^j \rangle \propto \mathbb{1}$ down to the diagonal subgroup $U(N_F)_L \otimes U(N_F)_R \to U(N_F)_V$. This holographic model will consists in a $U(N_F)_L \otimes U(N_F)_R$ gauge theory in 5D with a complex scalar Φ transforming as a $(\mathbf{N_F}, \overline{\mathbf{N}}_\mathbf{F})$. [1] This scalar plays the role of the $q\bar{q}$ operator whose VEV is responsible for the breaking of the conformal and gauge symmetry, and therefore its mass will be related to the dimension of the $q\bar{q}$ operator through the AdS/CFT dictionary entree [4]:

$$\mathrm{Dim}[q\bar{q}] = 2 + \sqrt{4 + M_\Phi^2}\,. \tag{1}$$

We also impose parity, defined as the interchange $L \leftrightarrow R$. The Lagrangian is given by

$$\frac{1}{M_5}\mathcal{L}_5 = -\frac{1}{4}\,\mathrm{Tr}\left[L_{MN}L^{MN} + R_{MN}R^{MN}\right] - \frac{\alpha}{4}\left(\mathrm{Tr}\left[L_{MN} + R_{MN}\right]\right)^2 + \frac{1}{2}\,\mathrm{Tr}\,|D_M\Phi|^2 - V(\Phi)\,, \tag{2}$$

with the indices running over the five dimensions, $M = \{\mu, 5\}$. We parametrize the fields as $\Phi = \Phi_s + T_a\Phi_a$, with $\mathrm{Tr}[T_aT_b] = \delta_{ab}$ (and similarly for L_M and R_M). The fields Φ_s and Φ_a will respectively transform as a singlet and adjoint under the $U(N_F)_V$. The covariant derivative and the potential are given by

$$D_M\Phi = \partial_M\Phi + iL_M\Phi - i\Phi R_M\ , \quad V(\Phi) = \frac{1}{2}M_\Phi^2\,\mathrm{Tr}\,|\Phi|^2 + \frac{1}{4}\lambda_1\,\mathrm{Tr}\,|\Phi|^4 + \frac{1}{4}\lambda_2(\mathrm{Tr}\,|\Phi|^2)^2\,. \tag{3}$$

[1] We could incorporate the anomaly of the $\mathrm{U}(1)_A$ by adding a CS-term to the 5D theory.

The 5D metric in conformal coordinates is defined as $ds^2 = a^2(z)\big(\eta_{\mu\nu}dx^\mu dx^\nu - dz^2\big)$ where $a(z)$ is the warp factor. We will work within AdS_5: $a(z) = L/z$, where L is the AdS curvature radius. As explained above, our important assumption here is to consider that the conformal breaking arise from the RG-evolution of $\mathrm{Dim}[q\bar{q}]$ down to 2 where it becomes imaginary. On the AdS side, this corresponds from Eq. (1) to a 5D mass of Φ below the BF bound, making the AdS tachyon to turn on. For this purpose, we will take

$$M_\Phi^2 = -(4+\epsilon)/L^2\,, \tag{4}$$

and work in the limit $\epsilon \to 0$. As the mass of Φ is slightly below the BF bound, the profile of Φ turns on in the 5D bulk, breaking the conformal and chiral symmetry $U(N_F)_L \otimes U(N_F)_R \to U(N_F)_V$. Φ will grow as $\sim z^2$, as expected from a dimension-two perturbation. When the energy momentum tensor induced by the nonzero Φ profile gets of order the inverse of the 5D Newton constant, $1/G_N$, the backreaction on the metric will be important, starting to depart then from AdS, and signaling the breaking of the conformal symmetry. Instead of considering the change in the metric, that will complicate and then obscure our results, we will take the simplified assumption that the growth of the 5D tachyon is regularized by an IR-brane at some point in the AdS throat $z = z_{\rm IR}$. This will be determined dynamically by minimizing with respect $1/z_{\rm IR}$, as this corresponds to the VEV of a dynamical field, the radion, or the corresponding dilaton in the dual theory (see section 2.3). We consider that the IR-boundary will capture in a simple way the effect of the metric feedback that will be generically parametrized by the boundary terms. In particular, this means that Φ might also have a potential on the IR-boundary. For this reason, we will consider the presence of a mass term on the IR-boundary: $\mathcal{L}_{\rm IR} = a^4 m_b^2\,\mathrm{Tr}\,|\Phi|^2/2\big|_{z_{\rm IR}}$, and study its impact on the properties of the model. As it is usual in AdS/CFT, we will be regularizing the UV-divergencies by placing a UV-boundary at $z = z_{\rm UV}$ and taking the limit $z_{\rm UV} \to 0$ at the end of the calculation of physical quantities.

By the AdS/CFT correspondence, the mass-parameter M_5, that corresponds to the inverse of the 5D gauge coupling squared, is related to the large-N_c expansion parameter of the dual strongly-coupled CFT: $1/(M_5 L) \sim 16\pi^2/N_c$. In this correspondence 5D double-trace operators are suppressed with respect to single-trace ones, i.e.,

$$\alpha \sim \lambda_2/\lambda_1 \sim 1/N_c\,. \tag{5}$$

For this reason these terms were neglected in previous holographic approaches to QCD [6, 7]. Nevertheless, the parameters α and λ_2 are accompanied by a factor N_F and then their effects are not suppressed for large values of N_F. Therefore it is important to keep double-trace operators in Eq. (2) when comparing our results to strongly-coupled theories in the large N_c and N_F limit. In particular, λ_2 will be responsible to generate a mass splitting in the scalar sector between the singlet (Φ_s) and the adjoint states (Φ_a), as it is observed in lattice results with large N_F [1, 2].

It is important to remark that we cannot consider the strict limit $N_F \sim N_c$ in our 5D model. In this limit loops of vector or scalar resonances contribute as $\frac{N_F}{M_5 L}\frac{1}{16\pi^2} \sim N_F/N_c \sim 1$, meaning that we cannot perform a perturbative expansion since the 5D theory is strongly-coupled. Therefore the 5D theory will be only reliable if we approach the large-N_F and large-N_c limit ($M_5 L \to \infty$) keeping $N_F \ll 16\pi^2 M_5 L$. Basically, the only difference here with respect to previous models for holographic QCD is the non-negligible presence of α and λ_2.

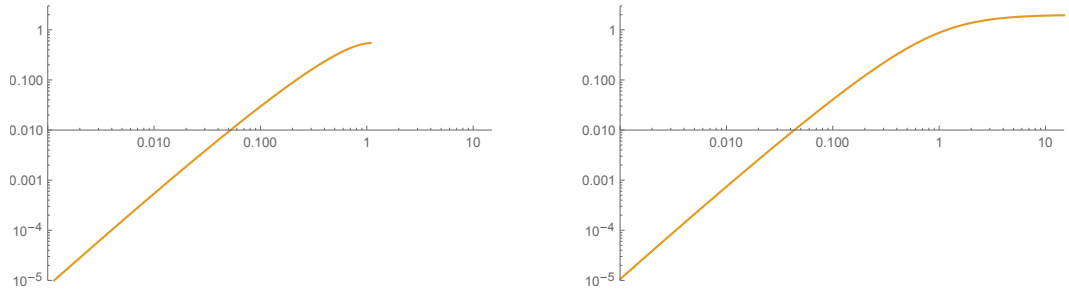

Figure 1: *5D tachyon solutions for case (I) with* $z_{\rm IR} = 1.2\, z^c_{\rm IR}$ *(left), and case (II) with* $z_{\rm IR} = 20\, z^c_{\rm IR}$ *(right). We have taken* $\lambda = 1$ *and* $m_b = 0$.

2.1 The tachyon solution

The non-zero profile for Φ will be taken to be along the $\phi = |\Phi_s|$ direction. Since we will be interested in the solution close to the conformal transition, we will take the limit $\epsilon \to 0$. Therefore the solution for ϕ only depends on $z_{\rm IR}$, λ and m_b. At the UV-boundary we will impose $\phi = 0$, otherwise we would be breaking the chiral symmetry from UV-physics (as adding an explicit mass term to the quarks in the dual theory). On the other hand, at the IR-boundary, we must impose the boundary condition determined by the model above: $z_{\rm IR}\partial_5\phi|_{z_{\rm IR}} = -m_b^2\phi|_{z_{\rm IR}}$. This boundary condition however cannot be satisfied for all values of $z_{\rm IR}$ (unless $\phi = 0$), meaning that the tachyon can only turn on if the IR-boundary is beyond some critical value, $z_{\rm IR} > z^c_{\rm IR}$. It is easy to find this value $z^c_{\rm IR}$, just by looking for the place where the IR-boundary must be placed in order to have a 4D massless mode. For this to happen, the wave-function of this massless mode must satisfy the linearized bulk EOM with $p^2 = 0$. We obtain

$$\phi(z) = A\, z^2 \sin\left(\sqrt{\epsilon}\ln\frac{z}{z_{\rm UV}}\right)\,, \tag{6}$$

where A is a normalization constant, and where the IR-boundary condition at $z_{\rm IR} = z^c_{\rm IR}$ leads to

$$\sqrt{\epsilon}\ln\frac{z^c_{\rm IR}}{z_{\rm UV}} = n\pi\ ,\quad n = 1, 2, \dots\,, \tag{7}$$

after taking the formal limit $\epsilon \to 0$ (and $z_{\rm UV} \to 0$). The presence of n solutions is a well-known feature of this configurations, and it is associated to the existence of Efimov states. We will be considering $n = 1$, that will give us the global minimum, being the other possibilities just local minima.

For $z_{\rm IR} > z^c_{\rm IR}$, the above massless mode will have a negative mass, becoming a tachyon, and then getting a nonzero profile and triggering the breaking of conformal and chiral symmetry breaking. We can distinguish two limits:

I) For $z_{\rm IR} \gtrsim z^c_{\rm IR}$, the tachyon profile is very close to Eq. (6).

II) For $z_{\rm IR} \gg z^c_{\rm IR}$, the tachyon profile grows till reaching a maximum value determined by the minimum of the 5D potential $V(\Phi)$, i.e., $\phi_{\rm max} = \sqrt{M^2_\Phi/\lambda}$.

Both types of configurations are shown in Fig. 1. In the figure in the left we have taken $z_{\rm IR} \approx z^c_{\rm IR}$, while the one in the right $z^c_{\rm IR} \gg z_{\rm IR}$. The model can provide both configurations, as $z_{\rm IR}$ can be dynamically settled,

depending on m_b, either relatively close to $z_{\rm IR}^c$ or to much larger values. The scale $1/z_{\rm IR}^c$ corresponds to the scale of chiral symmetry breaking, while $1/z_{\rm IR}$ is the scale of confinemet. Therefore, while in case (I) both scales are similar, in case (II) the scale of chiral breaking is much larger than the scale of confinement. Indeed, in case (II) the theory below $1/z_{\rm IR}^c$ enters into another CFT where the (gauge) symmetry is just $SU(N_F)_V$ with Φ_s and Φ_a respectively in the singlet and Adjoint representation. Their squared masses are given by $\sim 8/L^2$ and $8(1-2\lambda_2/(3\lambda))/L^2$ respectively. This corresponds in the dual theory to $q\bar{q}$ operators of very high dimension (becoming irrelevant). In this new CFT, scale invariance is broken at $1/z_{\rm IR}$.

2.2 Excitations around the 5D tachyon

We will start studying the spectrum for a fixed value of the IR-boundary, $z_{\rm IR}$, to discuss later the properties of the dilaton, whose mass will be determined by minimizing the energy with respect to $z_{\rm IR}$. The purpose is to show the properties of the spectrum as we increase $z_{\rm IR}$ and move from scenario (I) to (II). The results are presented in the left plot of Fig. 2 as a function of $z_{\rm IR}/z_{\rm IR}^c$ and for $\lambda = 1$, $\lambda_2 = -3\lambda$ and $m_b = 0$ (solid line) and $m_b = -1$ (dashed line). Following the notation used in QCD, we refer by f_0, a_0, ρ and a_1 respectively the singlet-scalar, adjoint-scalar, vector and axial-vector resonances. Since F_π is the only quantity that depends on M_5 (N_c in the dual theory), we have fixed its value following [7]. We have normalized the spectrum to m_ρ. From the left figure of Fig. 2 we see that for $z_{\rm IR} \sim z_{\rm IR}^c$ we are in the scenario (I) where the chiral breaking scale is smaller or of order the confinement scale. This is reflected in the $\rho - a_1$ mass splitting that is always small. As we increase $z_{\rm IR}/z_{\rm IR}^c$, we move towards scenario (II) where the breaking of the chiral symmetry is larger, as can be appreciated by the growth of F_π and the $\rho - a_1$ splitting. For $z_{\rm IR} \gg z_{\rm IR}^c$ the theory is close to a different CFT, the one discussed before, where the global group is $U(N_F)$ and the scalars and axial-vector have masses larger than $1/z_{\rm IR}$.

Another important prediction of the proposed 5D model is that only the scalar sector presents a mass splitting between the singlet (f_0) and the adjoint (a_0). This splitting is generated by λ_2. In the gauge sector the only physical difference between the singlet and adjoint arises from α in Eq. (2). This however does not produce any mass splitting in the vector sector V_M between the the singlet resonances (the ω in QCD) and the adjoint resonances (ρ), as these do not depend on α but only on the boundary conditions on the IR-boundary that are the same for all gauge fields. For the axial-vector A_M a mass splitting could arise from their coupling to Φ that, for $\alpha \neq 0$, is different for the singlet and adjoint. Nevertheless, when fitting the model to the UV, as we do here, one obtains $\alpha = 0$ [7]. Therefore the proposed 5D model predict that the only mass splitting between the singlet and adjoint resonances (the Kaluza-Klein states) can only be possible in the scalar sector. Of course, these mass splittings could be generated at the loop level or from higher-dimensional operators in Eq. (2), but this are suppressed by the 5D cutoff (scale at which the 5D theory becomes strongly coupled) $\Lambda_5 \lesssim 24\pi^3 M_5$.

It is more instructive, also to compare later our results with lattice simulations, to analyze the spectrum at equal F_π. For this purpose, we adjust λ to fulfill, for the different values of $z_{\rm IR}/z_{\rm IR}^c$, the relation $F_\pi \sim m_\rho/8$ as in QCD. This can always be achieved as F_π roughly scale as $1/\sqrt{\lambda}$. The results are given in the right plot of Fig. 2. For $z_{\rm IR} \gg z_{\rm IR}^c$, however, we must increase λ to a too large values, putting in danger the perturbative approach. We find the for $m_b = 0$ ($m_b = -1$), in order to stay with $\lambda \leq 4$, we must have $z_{\rm IR}/z_{\rm IR}^c \lesssim 2.6$ ($z_{\rm IR}/z_{\rm IR}^c \lesssim 4.1$). Keeping in this region, we find that the scalar f_0 is the lightest resonance. A reason for the relative lightness of the scalar excitation is the following. As

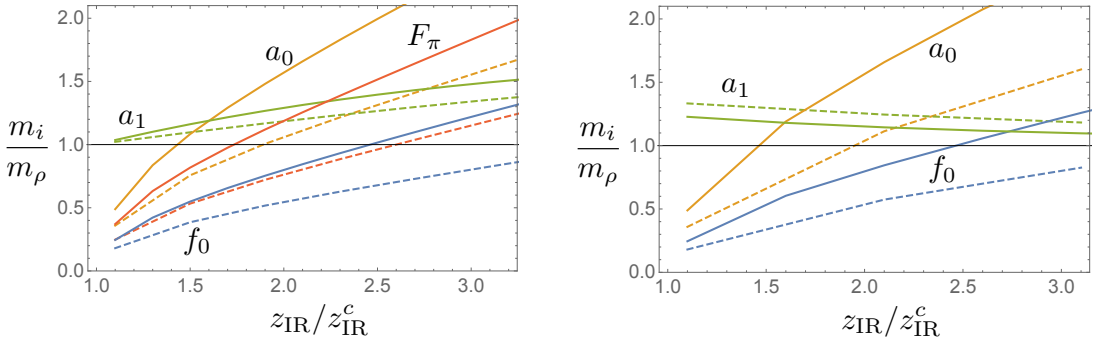

Figure 2: *Resonance mass spectrum as a function of the position of the IR-boundary, either for constant λ (left) or constant F_π (right), for two values of the boundary mass: $m_b = 0$ (solid line) and $m_b = -1$ (dashed line).*

we approach the conformal edge, the corresponding dimension of the scalar operator becomes close to 2. This is the lowest value before being imaginary. As it is well-known, the dimension of a scalar operator has a minimal value determined by its unitarity bound, in this case $\mathrm{Dim}[q\bar{q}] = 1$, a limit in which the scalar decouple from the CFT. Therefore it is expected that, as the scalar approach this limit, the mass of the lightest resonance becomes smaller.

2.3 Dilaton mass

Since $1/z_{\rm IR}$ is a dynamical field, the radion, that in the dual 4D CFT corresponds to the dilaton, its value must be determined by its EOM. Interestingly, the 5D tachyon provide a minimum for $z_{\rm IR}$ due to its logarithmic dependence (see Eq. (6)). The minimization condition can be read from the junction condition following Ref. [8]. From there we can get the mass of the dilaton: $m_D^2 \propto L(m_b^2 L^2 + 2)^3/\sqrt{\lambda} \times \partial_{z_{\rm IR}}\phi(z_{\rm IR})/z_{\rm IR}$. From this equation, it is clear that only when the value of the tachyon on the IR-boundary mildly depends on the IR-boundary position, we can expect a light dilaton. From Fig. 1, this only happens for large $z_{\rm IR}/z^c_{\rm IR}$, but in this case the chiral breaking is large. Lattice simulations do not seem to see a large breaking of the chiral symmetry when approaching the conformal transition, therefore we can conclude that the light 0^{++} state is not expected to be the dilaton.

3 Lattice QCD in the large N_F

Lattice results for QCD with $N_F = 8$ have been reported in Ref. [1, 2]. At such large value of N_F, it is believed that QCD is close to the conformal transition, expected to occur around $N_F \sim 10$. It was found [1, 2]

$$F_\pi \simeq 0.14\, m_\rho\ , \quad m_{f_0} \simeq 0.5\, m_\rho\ , \quad m_{a_0} \simeq m_\rho\ , \quad m_{a_1} \simeq 1.4\, m_\rho\, . \tag{8}$$

As compare to real QCD these values show a lighter f_0 scalar and a smaller mass splitting between the vector and axial-vector resonance. Surprisingly, the ratio of F_π/m_ρ is quite similar to real QCD, showing that this quantity is quite independent of N_F. Let us compare our results to the values of Eq. (8). From the right plot of Fig. 2, where we fixed $F_\pi = m_\rho/8$ and used the matching to the two-point vector-vector correlator in the UV following [7], we see that for values of $z_{\rm IR}/z^c_{\rm IR} \lesssim 2$ our predictions on the spectrum

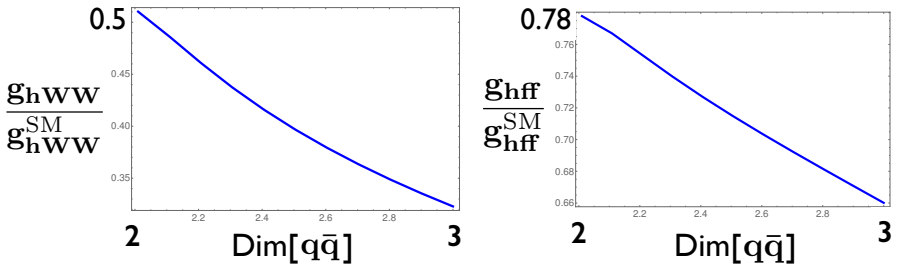

Figure 3: *Couplings of the f_0 resonance to SM gauge bosons and fermions as a function of the dimension of the associated operator in the dual theory using Eq. (1).*

of resonances follows quite close to the pattern given in Eq. (8). This suggests that the light scalar found in lattice simulations could mostly be a meson scalar $q\bar{q}$, with its lightness arising from the fact that Dim$[q\bar{q}]\sim 2$. Another prediction from the holographic model is the small mass splitting between adjoint and singlet in the vector and axial-vector sector. It would be interesting to check this prediction from lattice simulations.

4 Implications for BSM

The model described here open new possibilities for physics beyond the SM. First, it can solve the big hierarchy problem, since by choosing small values of ϵ, we can generate a small IR scale from a large UV scale. Indeed, from Eq. (7) we have

$$\frac{1}{z_{\rm IR}} \sim \frac{1}{z^c_{\rm IR}} = e^{-\pi/\sqrt{\epsilon}} \frac{1}{z_{\rm UV}} \ll \frac{1}{z_{\rm UV}} \,. \tag{9}$$

Furthermore, the presence of a light scalar f_0 in the spectrum raises the old question of whether this resonance could be identified with the Higgs h. In the holographic model we can calculate the couplings of f_0 to the SM fields. The result is shown in Fig. 3. As expected, the couplings tend to the SM values as we decrease the dimension of $q\bar{q}$ and approach the decoupling limit where f_0 becomes closer to an elementary field. Nevertheless, for Dim$[q\bar{q}]\sim 2$ the departures from the SM are still too large to properly fit the present experimental values.

For models in which the Higgs arises as a composite pseudo-goldstone boson, that have been extensively searched for at the LHC, the presence of a light scalar f_0 has also important implications. Being f_0 the lightest resonance, it implies that other resonances will mostly decay to f_0, that sequentially will decay to tops or W_L, Z_L, h. As a consequence LHC search strategies must be changed. For example, searches for top partners T must look for three SM particles in the final states instead of two, as we could have, for example, $T \to t f_0 \to t\bar{t}t$. Finally, the fact that the Higgs operator $q\bar{q}$ has dimension close to 2 allows to alleviate the flavor limits on this type of models, similarly as in walking technicolor. In particular, flavor models as the one proposed in Ref. [9] can satisfy all flavor and CP-violating constraints for an IR scale of few TeV.

5 Conclusions

Strongly-coupled theories provide a motivation for physics at the TeV. Using holography, we have studied the implications of these theories close to the conformal transition following the approach of Ref. [3]. We have seen that the theory predicts a scalar 0^{++} as the lightest resonance. Nevertheless, this scalar is not the dilaton but a scalar whose interpolating operator $q\bar{q}$ gets the lowest possible dimension. Furthermore, the mass of this scalar cannot be parametrically much smaller than the mass gap of the theory. This could be checked by lattice simulations. Being the scalar the lightest resonance have important implications for the LHC, as other resonances (vectorial of fermionic) will decay to it with BR of order one. Therefore LHC search strategies must be optimized differently from present ones.

Acknowledgements

I would like to thank my collaborators L. Salas and O. Pujolas that contributed to the work reported here. This work was supported by the Catalan ICREA Academia Program and FPA2014-55613-P, 2014-SGR-1450 and SO-2012-0234.

References

1. Y. Aoki *et al.* [LatKMI Collaboration], Phys. Rev. D **96** (2017) no.1, 014508; Phys. Rev. D **89** (2014) 111502.
2. R. C. Brower, A. Hasenfratz, C. Rebbi, E. Weinberg and O. Witzel, Phys. Rev. D **93** (2016) no.7, 075028.
3. D. B. Kaplan, J. W. Lee, D. T. Son and M. A. Stephanov, Phys. Rev. D **80** (2009) 125005.
4. J. M. Maldacena, Adv. Theor. Math. Phys. **2** (1998) 231; S. S. Gubser, I. R. Klebanov and A. M. Polyakov, Phys. Lett. B **428** (1998) 105; E. Witten, Adv. Theor. Math. Phys. **2** (1998) 253.
5. L. Salas, A. Pomarol and O. Pujolas in preparation.
6. J. Erlich, E. Katz, D. T. Son and M. A. Stephanov, Phys. Rev. Lett. **95** (2005) 261602.
7. L. Da Rold and A. Pomarol, Nucl. Phys. B **721** (2005) 79; JHEP **0601** (2006) 157.
8. C. Csaki, M. L. Graesser and G. D. Kribs, Phys. Rev. D **63** (2001) 065002.
9. G. Panico and A. Pomarol, JHEP **1607** (2016) 097.

Frascati Physics Series Vol. 65 (2017)
LFC17: Old and New Strong Interactions from LHC to Future Colliders
11 - 15 September, 2017

COMPOSITE DARK MATTER AND THE HIGGS

Giacomo Cacciapaglia
Université de Lyon, Université Lyon 1, CNRS/IN2P3, IPNL, 69622 Villeurbanne, France

Abstract

The Higgs boson and a scalar Dark Matter candidate may both arise from the same composite sector responsible for the breaking of the electroweak sector. This scenario is natural in models featuring a simple underlying gauge-fermion description, where large pNGB sectors are common. The preferred value of the Dark Matter mass lies in the natural ballpark for a composite Higgs, and will be probed in future experiments.

1 Introduction

The discovery of a Higgs boson has crowned the physics program at the Large Hadron Collider (LHC) at CERN. The measurements of its properties, which will keep improving with increasing accumulated data, so far confirm the predictions from the Standard Model (SM), where the Higgs is the relic of a scalar field transforming as a doublet of the electroweak SU(2) symmetry. Furthermore, the searches for New Physics effects have given negative results.

This situation that emerged at the LHC nicely fits with the expectations for a composite Higgs boson. In fact, among the many theories that aim at addressing the hierarchy problem associated to the mass of the Higgs field, compositeness does not necessarily require very light new degrees of freedom. The Higgs boson is replaced at high energies by more elementary fermions, of which the Higgs boson is a bound state. Thus, it is the absence of fundamental scalars that naturally screens the Higgs mass, and the electroweak (EW) scale, from higher energy scales. This idea has been applied to the electroweak sector shortly after the establishment of the SM itself [1, 2]. The lightness of the Higgs can be explained by associating it to a pseudo-Nambu-Goldstone boson (pNGB) [3], whose mass is parametrically lighter than the other resonances of the theory. The price to pay is a tuning between the electroweak scale

$v = 246$ GeV and the scale of compositeness f, such that all the corrections to the properties of the composite Higgs with respect to the SM predictions scale with powers of v^2/f^2. This is similar to the decoupling limit achievable, for instance, in supersymmetric theories. Other non-pNGB composite states are expected to be heavier than f, and their mass is usually parametrised as $m_\rho = g_\rho f$, where $1 < g_\rho \leq 4\pi$ is a (large) coupling generated by the strong dynamics. Thus, is we assume $f \sim 1$ TeV, the corrections to the Higgs properties reach the percent level, thus difficult to test at the LHC, while new heavy states lie above a few TeV, thus difficult to produce.

Another holy grail of particle physics is Dark Matter (DM): from Cosmological observations and from Astrophysics at various scales, we know that the matter budget of the Universe is largely dominated by a component that cannot be associated to baryonic particles. The most intriguing possibility is that Dark Matter is constituted by a new neutral particle, stable on Cosmological time-scales, that has weak interactions to the SM. Once the DM particle drops from thermal equilibrium from the bath of SM particles, its relic density will be preserved. The possibility that the DM particle is composite is very appealing for various reasons: on the one hand, the interactions among pNGBs are determined by global symmetries of the underlying theory, thus it is not uncommon that they are prevented from decaying, on the other hand there may exist unbroken global symmetries, analogous to baryon number in QCD, under which some of the composite states are charged [4]. One reason for the composite sector being dark can simply be the fact that none of the underlying components are charged under SM quantum numbers, giving rise to hidden-valley scenarios [5].

In this contribution, however, we will be interested in a more ambitious scenario in which both the Higgs and a Dark Matter particle arise from the same strong dynamics. The challenge is easily spotted: the interactions with the SM that are responsible for misaligning the condensate in a direction that breaks the EW symmetry may also decays for the DM candidate. If both DM and Higgs are pNGBs, the global symmetry should be large enough to accommodate for enough pNGBs in the coset of the symmetry breaking patterns. Below we list the main features that a model of composite pNGB Higgs and DM needs:

- The pNGBs need to be at least 5, with 4 of them transforming like the Higgs doublet under the electroweak symmetry.

- The gauging of the electroweak interactions in the strong sector, required in order to obtain a Higgs, need to preserve the symmetry stabilising the DM candidate inside the coset.

- Topological terms, that typically violate parities in the pNGB sector, need to preserve the stability of the DM candidate. In particular, decays into two gauge bosons may be generated, and they are associated to anomalies of the global symmetries in composite theories of fermions. Thus, in models that address the hierarchy problem, these terms are inevitable.

- Interactions with the fermions (and top quark, in particular) are needed to misalign the condensate towards breaking the electroweak gauge symmetry. They need to preserve the DM parity while allowing for the proper misalignment.

It if clear form this list that the nature of the underlying theory, defined in terms of confining interactions and underlying fermions that compose the Higgs (and DM) is essential: it determines both the form and presence of topological terms, and the form of the couplings of the (top) quarks to the strong sector. A simple example is provided by the most minimal case, based on the symmetry breaking pattern SU(4)/Sp(4), which has a single additional pNGB, singlet under the SM interactions [6]: in a theory

Table 1: *List of minimal models and transformation properties of the underlying fermions ψ and of the pNGBs under the custodial SU(2)$_L\times$ SU(2)$_R$. The column "Dark pNGB" lists the odd pNGBs, the lightest of which is the DM candidate.*

	$N_{\rm pNGB}$	ψ	pNGBs	Dark pNGBs
SU(4)/Sp(4)	5	$(2,1)\oplus(1,2)$	$(2,2)\oplus(1,1)$	
SU(5)/SO(5)	14	$(2,2)\oplus(1,1)$	$(2,2)\oplus(3,3)\oplus(1,1)$	
SU(4)×SU(4)/SU(4)	15	$(2,1)\oplus(1,2)$	$(2,2)\oplus(1,1)$	$(2,2)\oplus(3,1)\oplus(1,3)$
SU(6)/Sp(6)	14	$(2,1)\oplus(1,2)\oplus 2\times(1,1)$	$(2,2)\oplus 2\times(1,1)$	$2\times(2,1)\oplus 2\times(1,2)$
SU(6)/SO(6)	20	$(2,2)\oplus(1,1)\oplus(1,1)$	$(2,2)\oplus(3,3)\oplus(1,1)\oplus(1,1)$	$(2,2)\oplus(1,1)$

based on underlying fermions, topological terms induce prompt decays of the would-be DM candidate into SM gauge bosons [7]. Another important advantage of defining an underlying theory is that it can be studied on the lattice to extract the spectrum and couplings in a non-perturbative way.

The underlying theories we focus on are defined following the principle of minimality: one confining gauge symmetry $G_{\rm HC}$ and a set of fermions charged under $G_{\rm HC}$ and the SM gauge interactions. This principle strongly limits the possible symmetry breaking patterns, and thus the properties of the pNGBs. As we will see, simple and minimal gauge-fermion models will lead to a large number of pNGBs (including dark ones) [8, 9]. Models based on cosets that minimise the number of pNGBs have also been studied in the literature [10, 11]. The new minimal, however, is non minimal pNGB sectors.

2 Fundamental composite dynamics: one ring to rule them all

Once the confining gauge group $G_{\rm HC}$ and the representation (*irrep*) of the fermions composing the Higgs and DM are defined, the symmetry breaking patterns can be determined [12, 13]:

$$\begin{array}{lcl} \psi\in\text{real } \textit{irrep} & \Rightarrow & \mathrm{SU}(N)/\mathrm{SO}(N)\,, \\ \psi\in\text{pseudo-real } \textit{irrep} & \Rightarrow & \mathrm{SU}(2N)/\mathrm{Sp}(2N)\,, \\ \psi\in\text{complex } \textit{irrep} & \Rightarrow & \mathrm{SU}(N)\times\mathrm{SU}(N)/\mathrm{SU}(N)\,, \end{array} \tag{1}$$

where N counts Weyl spinors for real *irreps* and Dirac for the other two cases. The embedding of the EW symmetry inside the global symmetry also depends on the symmetry breaking patters. For complex (pseudo-real) *irreps*, the minimal possibility is that the underlying fermions transform as a doublet of SU(2)$_L$ and a doublet of SU(2)$_R$[1], so that the minimal number of flavours is 4 Dirac (4 Weyl, i.e. 2 Dirac). The EW symmetry is thus embedded in a SU(2)×SU(2) subgroup of the unbroken SU(N) (Sp($2N$)). For real *irreps*, the EW symmetry needs to be embedded into a SO(4) subgroup of the unbroken SO(N), so that the underlying fermions must contain one bi-doublet of the custodial symmetry. The minimal number of flavours is therefore $N = 5$ (where the additional singlet allows for the formation of the composite Higgs doublet).

The minimal case in terms of number of pNGBs is SU(4)/Sp(4), which has a gauge singlet in addition to the Higgs doublet. The singlet has been considered as a possible candidate for composite DM [6], however this model is ruled our once topological interactions are included. Similarly, the case SU(5)/SO(5), which contains 14 pNGBs, is ruled out by topological terms that allow the decays of all the non-Higgs pNGBs into EW gauge bosons [14]. Thus, the minimal models that may contain a DM

[1]We implicitly require that the EW breaking sector of the model preserves the custodial symmetry of the SM, i.e. it breaks SU(2)$_L\times$ SU(2)$_R\to$ SU(2)$_C$, where the hypercharge is associated to the diagonal generator of the partly-gauged SU(2)$_R$.

candidate are: SU(4)× SU(4)/SU(4), SU(6)/Sp(6) and SU(6)/SO(6). The properties of the pNGBs are summarised in Table 1.

The SU(4)× SU(4)/SU(4) coset, which can be obtained in a very simple QCD-like underlying theory based on $G_{\rm HC} = {\rm SU}(N_c)$ with 4 fermions in the fundamental, has been studied in detail [8, 9]: a DM candidate is allowed if a parity is preserved by the top interactions. The SU(6)/Sp(6) model has been studied in the framework of Little Higgs models [15]. For DM and Higgs, the SU(6)-based models are special as they allow for a DM protected by an unbroken global U(1) symmetry, and the study of their DM phenomenology of the DM candidate is under way. We remark that all the minimal Higgs + DM models feature very non-minimal pNGB sectors, and a "dark" second doublet is always present.

2.1 Composite Higgs: a myth-buster's approach

Before presenting results for the composite DM model, it is useful to recap the main features of a composite Higgs boson. However, a comprehensive review is not possible in limited space: here we will focus on some widely accepted properties of composite Higgs models, but keeping a critical perspective. The most important issue for a successful composite Higgs model is related to generating a potential for the pNGBs: this will fix the hierarchy between v and the compositeness scale f as well as the mass of the Higgs candidate. This issue can only be analysed in an effective field theory approach, following the standard chiral expansion used for pNGBs.

The choice of vacuum

The most common procedure in the literature is to define a vacuum condensate (of order f) which is aligned along a direction that preserves the EW symmetry, and then use the potential to induce a vacuum expectation value for the Higgs. This procedure allows to clearly follow the EW properties of all the pNGBs, however it is dangerous because v explicitly violates the symmetries on which the chiral expansion is based and, thus, it can be trusted only for $v \ll f$. A more correct procedure would be to rotate the vacuum in the direction of the generator of the Higgs boson until all vacuum expectation values of the pNGBs vanish: v is thus replaced by a misalignment angle $\sin\theta = v/f$, which is fixed by the pNGB potential. In this way, no couplings proportional to v will violate the shift symmetry of the pNGBs. As a consequence, all couplings between one Higgs boson and two DM candidates $h \to \eta_{\rm DM}\eta_{\rm DM}$ need to be proportional to couplings that explicitly break the global symmetries, i.e. $\lambda v\, h\eta_{\rm DM}^2$. Couplings with derivative, therefore, are naturally higher order and suppressed by a factor f^2/Λ^2, $\Lambda \sim 4\pi f$ being the cut-off of the effective theory. Observables sensitive to the energy dependence of the coupling, like the annihilation of DM via s-channel Higgs, will therefore differ in the two approaches. The choice of the EW preserving vacuum is also critical: it depends on the structure of the symmetry breaking couplings and an improper choice may lead to vacuum expectation values for EW singlets which are not physical. An example of the latter is the apparent spontaneous CP violation due to the vacuum expectation value of a singlet pseudo-scalar in the SU(4)/Sp(4) model [16].

The role of top partners (and partial compositeness)

Top partners, i.e. composite fermions that mix linearly to the SM quarks (the top in particular), have been introduced in order to address the flavour problem in strongly interacting models [17]. After holographic descriptions of a composite Higgs were proposed [18], top partners also started playing the role of regulators of the top loop contributions to the Higgs mass. This is due to the fact that holography offers calculable and weakly-coupled descriptions in extra dimensions. The enhanced calculability has thus been extended to more general composite Higgs models [19]. However, this prescription does not

necessarily apply to all compositeness scenarios. We remark here that the role of light top partners to achieve the correct misalignment and Higgs mass value is solely based on this assumption. If their role is limited to flavour, then they may be heavy and thus phenomenologically irrelevant. Underlying models of partial compositeness based on gauge-fermion theories have been proposed [20], and preliminary lattice results so far point towards heavy top partners in the few TeV range [21]. This mass on its own would violate the requirements for enhanced calculability as they are too heavy to be treated within the chiral perturbative expansion.

Vacuum misalignment
The vacuum misalignment towards small $\sin\theta \sim v/f$ always requires some cancellations between the contribution of top couplings, which tend to misalign the vacuum towards $\theta = \pi/2$, and some other contributions. In models with enhanced calculability, this is achieved by means of cancellations between loops containing top and top partners, in the same way as in Little Higgs models with elementary fermionic partners. In general, cancellations between various operators generated by the top couplings are also possible [16]. Another logical possibility is the presence of additional breaking terms: in models with underlying fermions, as long as an EW preserving vacuum can be defined, a mass term for the fermions is also allowed by all gauge symmetries. The mass can also be effectively used to balance the top contribution in models without or with heavy top partners [7].

3 A minimal Higgs-DM model: SU(4)×SU(4)/SU(4)

The symmetry breaking pattern SU(4)× SU(4)/SU(4) can originate from a simple theory based on a confining $G_{\rm HC} = {\rm SU}(N_c)$ underlying model, with 4 Dirac fermions in the fundamental *irrep*. The minimal number of colours, $N_c = 3$, gives a QCD-like theory, whose spectrum has been already studied on the Lattice: the non-pNGB resonances of this theory, therefore, tend to be heavy and thus will not play a significant role for the phenomenology of the Higgs and DM. We will thus focus on the physics of the light pNGBs [8, 9].

Following the notation of Ref. [8], the pNGBs can be described by a 4×4 matrix

$$U = e^{i\Pi/f}\,, \qquad \text{with} \quad \Pi = \frac{1}{2}\begin{pmatrix} \sigma^i\Delta_i + \frac{1}{\sqrt{2}}s & -i\ \Phi_H \\ i\ \Phi_H^\dagger & \sigma^i N_i - \frac{1}{\sqrt{2}}s \end{pmatrix}, \tag{2}$$

where the 2×2 matrix $\Phi_H = \left(i\sigma^2(H_1^* + iH_2^*), H_1 + iH_2\right)$ contains the two doublets $H_{1,2}$, and Δ_i and N_i are the two triplets of $\mathrm{SU}(2)_L$ and $\mathrm{SU}(2)_R$ respectively. The lowest-order chiral Lagrangian can be written as

$$\mathcal{L}_{\chi pT} = f^2\ {\rm Tr}\left[(D_\mu U)^\dagger D^\mu U\right]\,, \tag{3}$$

where the covariant derivatives contain the EW gauge symmetry. The misalignment can be introduced via a matrix that rotates the vacuum (and the pNGB matrix with it) without touching the SM gauging. With the normalisation chosen above, $2\sqrt{2}f\sin\theta = v$ by matching the value of the W and Z masses.

We find that there is a unique parity that is respected by the gauging of the SM, including topological terms, and it is defined in term of a charge-conjugation operation times a global SU(4) rotation, under which:

$$U \to P_B \cdot U^T \cdot P_B^\dagger\,, \quad A_\mu \to -P_B \cdot A_\mu^T \cdot P_B^\dagger = A_\mu\,, \quad \text{with} \quad P_B = \begin{pmatrix} \sigma^2 & 0 \\ 0 & -\sigma^2 \end{pmatrix}, \tag{4}$$

where A_μ are the EW gauge bosons embedded in SU(4), which are left invariant by the transformation. We find that it is the two triplets Δ and N, plus the second doublet H_2, that are odd under this

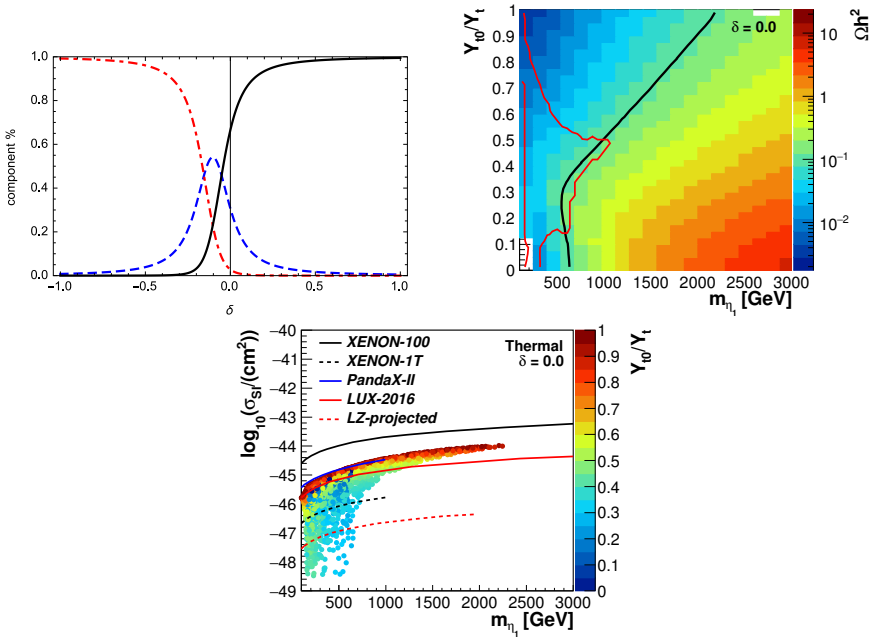

Figure 1: *a) Components of the DM candidate as a function of δ relative to the singlet (black line), second doublet (dashed blue) and triplet (dotted red); b) Relic DM abundance Ωh^2 as a function of the DM mass m_{η_1} and the ratio of Yukawas* [9]*. The black line indicates the preferred value by PLANCK, while the region encircled in red is allowed by Direct Detection experiments. c) Spin-independent cross section as a function of the DM mass for points with relic abundance below the PLANCK value, compared to Direct Detection bounds* [9]*.*

parity (in fact, only the singlet s decays via the topological terms). In the fermion sector, we consider a model without top partners, where the fermion masses are generated by 4-fermion interactions bilinear in the elementary SM fields [2]: in general, 4 independent Yukawas can be written down, corresponding to different four-fermion couplings. Intuitively, they corresponds to the two doublets contained in U, and another two in $U^\dagger$. Imposing the DM parity defined above requires that two combination of Yukawas vanish, and we are left with two independent ones. The first, Y_f, determines the mass of the SM fermion and its couplings to the Higgs, the second independent Yukawa Y_{f0} appears in higher order couplings to fermions and in the masses of the pNGBs. The stabilisation of the vacuum misalignment is guaranteed by the presence of a mass term for the underlying fermions. Once all the SM parameters and the vacuum alignment θ are fixed, the model contains only two free parameters: the second Yukawa Y_{t0} (we neglect the effect of the light fermions) and an underlying fermion mass parameter related to the mass difference δ between the two doublets (C.f. Table 1).

The masses of the pNGBs, as well as their couplings, only depend on these two parameters. The lightest mode is always a neutral scalar, which is a superposition of the triplet Δ_0, the singlet N_0 (that belongs to an $SU(2)_R$ triplet) and the inert Higgs doublet h_2. The relative composition in terms of the three gauge eigenstates mainly depends on the value of δ, as illustrated in Fig. 1a for $Y_{t0}/Y_t = 0.5$. We thus see that for $\delta > 0$, the DM is mostly made of the singlet N_0, nevertheless couplings to two

[2]The cases with top partners are under study.

gauge bosons and to two tops are generated by higher-order terms in the pNGB matrix expansion. The main annihilation processes are in two tops (dominating for large and small Y_{t0}/Y_t) and in W's. The results from a numerical scan of the parameter space is shown in Fig. 1b, where the black line shows the preferred value of the relic abundance Ωh^2. The region on the right-side of the black line is excluded because of excessive relic abundance. In Fig. 1c we compare the points that do not exceed the measured relic abundance to Direct Detection experiments, showing that only the region with intermediate values of the Yukawa coupling $Y_{t0}/Y_t \sim 0.15 \div 0.5$ are still allowed. This is also shown in Fig. 1b by the red line that encircles the allowed region.

It is noteworthy that the preferred mass range for DM is between 500 and 1000 GeV. This range can be converted in a range of values for the misalignment angle θ by observing that $m_{\eta_1} \sim m_h/\sin\theta$, giving an approximate range $0.1 \leq \sin\theta \leq 0.25$. These values roughly correspond to modification of the Higgs couplings between 1 to 6% that will be tested at the High-Luminosity upgrade of the LHC and at future Higgs-factory colliders.

4 Conclusions

Models where both the Higgs boson and a Dark Matter candidate arise as composite pNGBs from an underlying fermion-gauge theory are easy to achieve. The main reason behind is that minimal models in terms of the underlying symmetries contain non-minimal sets of pNGBs. A first example is a QCD-like model with four flavours, giving the symmetry breaking pattern SU(4)×SU(4)/SU(4). The dark pNGB sector will thus contain a second inert Higgs doublet, a triplet and singlets (forming a $\mathrm{SU}(2)_R$ custodial triplet). The DM candidate is thus a mixture of the 3 neutral component scalars. We find that the correct relic abundance can be achieved for masses between 500 GeV to 1 TeV, which are natural with respect to the compositeness scale expected from the Higgs sector. Direct Detection experiments severely constrain the model, however leaving open a region for intermediate Yukawa values. Future precision measurements of the Higgs couplings will be able to probe this class of models, thanks to the upper bound on the compositeness scale coming from Cosmology.

5 Acknowledgements

I would like to thank my collaborators Ma Teng and Wu Yongcheng, without which the results discussed here would not have been possible. The author acknowledges partial support from the Labex-LIO (Lyon Institute of Origins) under grant ANR-10-LABX-66 and FRAMA (FR3127, Fédération de Recherche "André Marie Ampère"). This project has also received support from the LIA French-China Particle Physics Laboratory (FCPPL).

References

1. S. Weinberg, Phys. Rev. D **13** (1976) 974 Addendum: [Phys. Rev. D **19** (1979) 1277].
2. S. Dimopoulos and L. Susskind, Nucl. Phys. B **155** (1979) 237.
3. D. B. Kaplan and H. Georgi, Phys. Lett. **136B** (1984) 183.
4. S. Nussinov, Phys. Lett. **165B** (1985) 55.
5. M. J. Strassler and K. M. Zurek, Phys. Lett. B **651** (2007) 374 [hep-ph/0604261].

6. M. Frigerio, A. Pomarol, F. Riva and A. Urbano, JHEP **1207** (2012) 015 [arXiv:1204.2808 [hep-ph]].

7. G. Cacciapaglia and F. Sannino, JHEP **1404** (2014) 111 [arXiv:1402.0233 [hep-ph]].

8. T. Ma and G. Cacciapaglia, JHEP **1603** (2016) 211 [arXiv:1508.07014 [hep-ph]].

9. Y. Wu, T. Ma, B. Zhang and G. Cacciapaglia, JHEP **1711** (2017) 058 [arXiv:1703.06903 [hep-ph]].

10. G. Ballesteros, A. Carmona and M. Chala, Eur. Phys. J. C **77** (2017) no.7, 468 [arXiv:1704.07388 [hep-ph]].

11. R. Balkin, M. Ruhdorfer, E. Salvioni and A. Weiler, JHEP **1711** (2017) 094 [arXiv:1707.07685 [hep-ph]].

12. C. Vafa and E. Witten, Nucl. Phys. B **234** (1984) 173.

13. D. A. Kosower, Phys. Lett. **144B** (1984) 215.

14. M. J. Dugan, H. Georgi and D. B. Kaplan, Nucl. Phys. B **254** (1985) 299.

15. I. Low, W. Skiba and D. Tucker-Smith, Phys. Rev. D **66** (2002) 072001 [hep-ph/0207243].

16. T. Alanne, N. Bizot, G. Cacciapaglia and F. Sannino, arXiv:1801.05444 [hep-ph].

17. D. B. Kaplan, Nucl. Phys. B **365** (1991) 259.

18. R. Contino, Y. Nomura and A. Pomarol, Nucl. Phys. B **671** (2003) 148 [hep-ph/0306259].

19. D. Marzocca, M. Serone and J. Shu, JHEP **1208** (2012) 013 [arXiv:1205.0770 [hep-ph]].

20. G. Ferretti and D. Karateev, JHEP **1403** (2014) 077 [arXiv:1312.5330 [hep-ph]].

21. V. Ayyar, T. DeGrand, D. C. Hackett, W. I. Jay, E. T. Neil, Y. Shamir and B. Svetitsky, arXiv:1801.05809 [hep-ph].

Frascati Physics Series Vol. 65 (2017)
LFC17: Old and New Strong Interactions from LHC to Future Colliders
11 - 15 September, 2017

MEASURING QUARK POLARIZATIONS AT ATLAS AND CMS

Yevgeny Kats
Department of Physics, Ben-Gurion University, Beer-Sheva 8410501, Israel

Abstract

Being able to measure the polarization of quarks produced in various processes at the LHC would be of fundamental significance. Measuring the polarizations of quarks produced in new physics processes, once discovered, can provide crucial information about the new physics Lagrangian. In a series of recent papers, we have investigated how quark polarization measurements can be done in practice. The polarizations of heavy quarks (b and c) are expected to be largely preserved in the lightest baryons they hadronize into, the Λ_b and Λ_c, respectively. Furthermore, it is known experimentally that s-quark polarization is preserved as well, in Λ baryons. We study how ATLAS and CMS can measure polarizations of b, c and s quarks using certain decays of these baryons. We propose to use the Standard Model $t\bar{t}$ and Wc samples to calibrate these measurements. We estimate that the Run 2 dataset will suffice for measuring the quark polarizations in these Standard Model samples with precisions of order 10%. We also propose various additional measurements for the near and far future that would help characterize the polarization transfer from the quarks to the baryons.

1 Introduction

ATLAS and CMS already measure the polarization of top quarks. In single top production, the tops are found to be highly polarized, [1, 2] as expected from the parity-violating electroweak nature of the process, while tops from pair production are found to be unpolarized, [3, 4] as one indeed expects from production via QCD. Similarly, if top quarks from new physics processes are discovered, measuring their polarization will teach us about their production mechanism.

The question we have asked in three recent papers [5, 6, 7] was whether analogous polarization measurements could be done for quarks other than the top. The answer is, of course, not straightforward because these quarks are observed only as jets of hadrons. We have shown that it is nevertheless possible for ATLAS and CMS to measure the quark polarizations, as will be summarized in this note.

2 Quark polarization retention in baryons

2.1 Bottom and charm quarks

For heavy quarks, $m_q \gg \Lambda_{\rm QCD}$ (like the b and c), the quark usually ends up in a very energetic heavy-flavored hadron [8, 9] that is easy to tell apart from the other hadrons in the jet. When this hadron is a baryon, an $\mathcal{O}(1)$ fraction of the quark polarization is expected to be retained in the hadron. [10, 11, 12] Indeed, since the b-quark chromomagnetic moment $\mu_b \propto 1/m_b$, and $m_b \gg \Lambda_{\rm QCD}$, the b spin should be approximately preserved during hadronization. If the light degrees of freedom of the baryon are in a spin-0 state, the b spin is preserved also during the hadron's lifetime, τ, despite the fact that $\tau \gg 1/\Lambda_{\rm QCD}$. Such a spin-1/2 baryon, with the valence light quarks being the u and d (which is the most common case), is called the Λ_b. The light degrees of freedom may also be in a spin-1 state. This gives rise to the Σ_b and Σ_b^* baryons, which have spins 1/2 and 3/2, respectively. In this case the b spin oscillates during the baryon's lifetime. This is important to take into account because the Λ_b sample has a significant contribution from $\Sigma_b^{(*)} \to \Lambda_b \pi$ (where the soft pion is difficult to identify, especially when it is neutral). The total fragmentation fraction $f(b \to \text{baryons}) \approx 8\%$, and the baryons are almost entirely Λ_b, produced either directly or via $\Sigma_b^{(*)}$.

For the c quark, one also has $m_c \gg \Lambda_{\rm QCD}$, although only as a rough approximation, and the same story holds. The analogs of the Σ_b and Σ_b^* baryons are often called the $\Sigma_c(2455)$ and $\Sigma_c(2520)$, respectively, but for the purpose of our discussion we will be referring to them as the Σ_c and Σ_c^*. The fragmentation fraction to baryons in this case is $f(c \to \text{baryons}) \approx 6\%$.

The dominant b-quark polarization loss effect in the Λ_b baryons sample is expected to be due to the $\Sigma_b^{(*)} \to \Lambda_b \pi$ decays. [12] The quantity of interest, the polarization retention fraction

$$r \equiv \frac{\mathcal{P}(\Lambda_b)}{\mathcal{P}(b)} \,, \tag{1}$$

can be expressed in terms of two parameters, A and w_1, [12] which can be determined independently from other measurements, as described in the following. These parameters describe the probabilities for the heavy quark to hadronize in various ways. The parameter A is the ratio of the Σ_b and Σ_b^* vs. direct Λ_b production rates, which depends on the probability for the b quark to hadronize with the spin-0 vs. spin-1 states of the light degrees of freedom. The parameter w_1 describes the probability for the spin-1 state of the light degrees of freedom to have polarization ± 1 (as opposed to 0) along the fragmentation axis. If one neglects the interference between the Σ_b and Σ_b^* states, the polarization loss effect is simply due to the fact that the process starts with the *b quark* having a definite spin, while when the hadron decays the wavefunction needs to collapse on a state of a definite *hadron* spin (because the Σ_b and Σ_b^* decays can in principle be distinguished due to their different masses). Using the appropriate Clebsch-Gordan coefficients, one then obtains the polarization retention fractions

$$r_L \simeq \frac{1 + (1 + 4w_1)A/9}{1 + A} \,, \qquad r_T \simeq \frac{1 + (5 - 2w_1)A/9}{1 + A} \tag{2}$$

for the cases in which the quark is polarized longitudinally and transversely, respectively, relative to the fragmentation axis. In practice, the Σ_b and Σ_b^* widths are not completely negligible relative to the mass splitting between them. With a more accurate calculation approach, which takes this into account, [5] one gets

$$r_L \approx \frac{1 + (0.23 + 0.38w_1)A}{1 + A} \,, \qquad r_T \approx \frac{1 + (0.62 - 0.19w_1)A}{1 + A} \tag{3}$$

for the b-quark system. The analogous results for the c-quark system are

$$r_L \approx \frac{1+(0.07+0.46w_1)A}{1+A} \ , \qquad r_T \approx \frac{1+(0.54-0.23w_1)A}{1+A} \ . \tag{4}$$

As we discuss in more detail in Ref. [5], at the moment it is still difficult to extract precise and reliable values of A and w_1 (for either the bottom or the charm system) from the various existing measurements or theoretical models. One can conclude from them, however, that $A \sim \mathcal{O}(1)$, while the value of w_1, for which the physically meaningful range is $0 \leq w_1 \leq 1$, is uncertain. This is sufficient for concluding from Eqs. (3) and (4) that the polarization retention fractions are $\mathcal{O}(1)$.

Notably, the ALEPH, DELPHI and OPAL experiments at LEP have attempted to measure the polarization transfer from quarks to baryons by analyzing the Λ_b baryons in $Z \to b\bar{b}$ events, and have indeed found $\mathcal{O}(1)$ retention of the longitudinal polarization, although the statistical uncertainties were too large to extract a precise value of r_L. [13, 14, 15]

2.2 Light quarks

Moving to the strange quark, one cannot argue for polarization retention based on the heavy-quark picture. At the same time, one cannot argue for polarization loss either. And in fact Λ polarization studies have been done in Z decays at LEP, and found $\mathcal{O}(1)$ polarization retention for Λ baryons that carry a significant fraction of the original quark's momentum. [16, 17, 18] The dependence of the polarization transfer on the momentum fraction is described by the polarized (or spin-dependent) fragmentation functions, [19] which are universal functions, up to renormalization-group evolution, similar to the parton distribution functions.

Similarly to the strange quark, up and down quarks hadronizing to baryons are also expected to retain a fraction of their polarization. This will be difficult to measure, however, because the baryons most frequently produced in the u and d hadronization, the protons and neutrons, do not decay within the detector. One may still imagine using the Λ, for example, although that will require significantly more statistics.

3 Opportunities at the LHC

Nice Standard Model samples of highly-polarized quarks are available in $pp \to t\bar{t}$ events: [5, 6]

- The decays $t \to W^+b$ produce polarized b quarks, and the subsequent decays $W^+ \to c\bar{s}, u\bar{d}$ produce polarized c, s, u, d quarks.
- It is easy to select a clean $t\bar{t}$ sample (e.g., in the lepton+jets channel).
- Kinematic reconstruction of the event, along with charm tagging, enable obtaining separate samples of jets dominated by b, c, or s jets.
- Already by the end of Run 2, the statistics of polarized quarks from $t\bar{t}$ events will be as high as of those produced in the Z decays at LEP.

Another potentially useful source of polarized charm quarks in the Standard Model is available in $pp \to Wc$ events (with $W \to \ell\nu$). [7] The statistics here are even higher than in $t\bar{t}$ (by an order of magnitude), but the backgrounds are higher too.

The simplest measurement to do is probably in s jets (which can be selected as jets that accompany the charm-tagged jets in $t\bar{t}$ events), since one can use the low-background (thanks to the large displacement) and fully reconstructible decay

$$\Lambda \to p\,\pi^- \,. \tag{5}$$

The Λ polarization can be extracted from the angular distribution of the decay products, which is given by

$$\frac{1}{\Gamma}\frac{d\Gamma}{d\cos\theta} = \frac{1}{2}\left(1 + \alpha\mathcal{P}(\Lambda)\cos\theta\right) \,, \tag{6}$$

where $\alpha = 0.642 \pm 0.013$ [20] and θ is the angle (in the Λ rest frame) between the proton momentum and the Λ polarization. We estimate [6] that statistical precision of roughly 16% is possible in ATLAS/CMS $t\bar{t}$ samples with 100 fb^{-1} of data.

The next simplest measurement is probably in c jets, where one has the fully reconstructible, although not background-free, decay

$$\Lambda_c^+ \to pK^-\pi^+ \,, \tag{7}$$

where the angular distribution is again sensitive to the polarization (see Ref. [7] for more details). We find that in $t\bar{t}$ samples, 100 fb^{-1} of data will allow achieving statistical precision of order 10%. [5] The reach of such a measurement in W+c samples may be better or worse than in $t\bar{t}$, depending on the details. [7] It is interesting to note that the measurement we propose in the W+c samples is quite similar to the existing measurements of the W+c production cross section in ATLAS [21] and CMS [22], which in particular rely on reconstructing the decay $D^+ \to K^-\pi^+\pi^+$, which is somewhat similar to our decay of interest. LHCb has analyzed the W+c production process as well, [23] and may also be able to measure the charm polarization.

In b jets, the measurement is somewhat more complicated because the best decays to use seem to be the semileptonic decays (with a muon)

$$\Lambda_b \to X_c\,\mu^-\bar{\nu} \,, \tag{8}$$

where X_c stands for a charmed hadron (a typical example is the Λ_c) and any accompanying particles (e.g., pions). [5] The Λ_b has several much cleaner decay channels, such as $\Lambda_b \to (J/\psi \to \mu^+\mu^-)\,(\Lambda \to p\pi^-)$, however their branching fractions are very small. Having a sizable branching fraction is an important consideration in our context because the most interesting potential application—new physics samples—will likely involve limited statistics. Additionally, the spin analyzing properties of the inclusive semileptonic decay in Eq. (8) are known accurately from theory. [24, 25, 26]

Because of the invisible neutrino, and due to the difficulty in distinguishing between light neutral hadrons that are part of the X_c and those coming from the primary vertex, the reconstruction of the Λ_b here involves certain approximations. Additionally, there is a large intrinsic background due to the semileptonic decays of B mesons. Even though the B-meson decay products are distributed isotropically in the meson rest frame, they contribute to the angular distribution measurements via statistical fluctuations. We have analyzed three different approaches for dealing with the B-meson background. In the first, *exclusive* approach, we demand a fully-reconstructible Λ_c decay candidate to be present in the jet. In the second, *semi-inclusive* approach, we only require a reconstructed $\Lambda \to p\,\pi^-$ decay candidate to be present. In the third, *inclusive* approach, no attempt is made to reduce the B-meson background, so the signal efficiency is maximal. We find that all the three approaches happen to offer similar levels of sensitivity, giving statistical precision of order 10% for 100 fb^{-1} of $t\bar{t}$ data.

It is also interesting to consider the dominant production mechanism of b quarks at the LHC, namely the inclusive QCD production, $pp \to b\bar{b} + X$. Despite the enormous cross section of this process, it is not the most promising avenue for polarization measurements because these quarks are produced unpolarized at the leading order. However, a small transverse polarization is predicted at the next-to-leading order. [27, 28] This, in principle, provides an opportunity to measure the transverse polarization transfer, namely the parameter r_T.[1] It is not a simple measurement because the transverse polarization is suppressed at high momenta, $\mathcal{P}(b) \sim \alpha_s m_b/p_b$, and has a strong dependence on the kinematics of the parton-level process. There already exist analyses in LHCb [31] and CMS [32] (and a related analysis in ATLAS [33]) that have attempted to detect the Λ_b transverse polarization (using the very rare but clean decay channel $\Lambda_b \to J/\psi\,\Lambda$), although they are subobtimal due to their inclusiveness over the kinematics. More detailed studies will be possible with higher statistics.

Finally, we note that the parameters A and w_1 that enter the expressions for r_L and r_T in Eqs. (3) and (4) can be measured independently, as has been pointed out already in Ref. [12], even in samples of unpolarized b or c quarks, such as the inclusive QCD samples available to the LHC experiments. The measurements can be done in any experiment that can reconstruct the $\Sigma_b^{(*)} \to \Lambda_b\pi$ or $\Sigma_c^{(*)} \to \Lambda_c\pi$ decays, and involve measuring the production rates of these baryons (for determining A) and the angular distribution of the pion (for determining w_1). In fact, it might have been possible to do such measurements even at the Tevatron. [34] Measurements of the $\Sigma_c^{(*)}$ can be done also at B factories, as demonstrated by the recently released analysis from Belle, [35] from which one may infer $A \approx 0.5$ for the charm system.

4 Conclusions

Our work [5, 6, 7] motivates a number of experimental analyses:

1. In $t\bar{t}$ samples in ATLAS and CMS:

   - Longitudinal Λ_b polarization measurement in b jets from top decays. This will allow determining r_L for the bottom.
   - Longitudinal Λ_c polarization measurement in c jets from W decays. This will allow determining r_L for the charm.
   - Longitudinal Λ polarization measurement in s jets from W decays. This will provide information about the longitudinally-polarized $s \to \Lambda$ fragmentation function.
   - In the far future: longitudinal Λ polarization measurement in u and d jets from W decays. This will provide information about the longitudinally-polarized $u \to \Lambda$ and $d \to \Lambda$ fragmentation functions.

2. In $W(\to \ell\nu) + c$ samples in ATLAS, CMS, and perhaps LHCb:

   - Longitudinal Λ_c polarization measurement in the c jets. This will allow determining r_L for the charm.
   - LHCb in particular may attempt separating out the $\Sigma_c^{(*)} \to \Lambda_c\pi$ contributions.

[1] One should be careful with the interpretation though, since transverse polarization in baryons is not protected from being generated by soft QCD effects independent of the polarization of the original quark. [29, 30]

3. In QCD production of hard quarks in ATLAS, CMS, and LHCb:

   - Transverse Λ_b (maybe also Λ_c) polarization measurement, properly binned in the event kinematics. This may allow determining r_T for the bottom (charm).

4. In any (even unpolarized) samples of hard quarks in LHCb, ATLAS and CMS:

   - Measurement of the $\Sigma_b^{(*)}$ production yields (relative to direct Λ_b production), and the pion angular distribution in the Σ_b^* decays. This will allow determining the parameters A and w_1, respectively, for the bottom quark.
   - Measurement of the $\Sigma_c^{(*)}$ production yields (relative to direct Λ_c production), and the pion angular distribution in the Σ_c^* decays. This will allow determining the parameters A and w_1, respectively, for the charm quark.

5. In new-physics samples, once discovered by ATLAS and/or CMS:

   - Measurements of the final-state quark polarizations. The results will provide important information about the structure of the new-physics interactions.

     We note however, that given that no new physics has been discovered so far, and considering the price one needs to pay in fragmentation and branching fractions to measure quark polarizations, statistics will likely be a serious limitation for such measurements.

6. In $t\bar{t}$ and Wc production, in the long term, in ATLAS, CMS, and LHCb:

   - Measurements of the full polarized fragmentation functions for the various quark flavors. It will be possible to confront the results with models based on the heavy-quark effective theory for the b and c quarks, and more phenomenological models of QCD for the light quarks. Additionally, knowing the full fragmentation functions will allow computing the scale dependence (due to the renormalization group evolution) [36] of the polarization retention fractions.

5 Acknowledgements

I would like to thank the organizers of the LFC17 workshop at ECT* for their invitation to present these ideas and for a stimulating workshop. I am also grateful to Mario Galanti, Andrea Giammanco, Yuval Grossman, Emmanuel Stamou and Jure Zupan for the collaboration on the work that started this research program.

References

1. V. Khachatryan *et al.* [CMS Collaboration], JHEP **1604** (2016) 073 [arXiv:1511.02138 [hep-ex]].
2. M. Aaboud *et al.* [ATLAS Collaboration], JHEP **1704** (2017) 124 [arXiv:1702.08309 [hep-ex]].
3. S. Chatrchyan *et al.* [CMS Collaboration], Phys. Rev. Lett. **112** (2014) 182001 [arXiv:1311.3924 [hep-ex]].
4. M. Aaboud *et al.* [ATLAS Collaboration], JHEP **1703** (2017) 113 [arXiv:1612.07004 [hep-ex]].

5. M. Galanti, A. Giammanco, Y. Grossman, Y. Kats, E. Stamou and J. Zupan, JHEP **1511** (2015) 067 [arXiv:1505.02771 [hep-ph]].

6. Y. Kats, Phys. Rev. D **92** (2015) 071503 [arXiv:1505.06731 [hep-ph]].

7. Y. Kats, JHEP **1611** (2016) 011 [arXiv:1512.00438 [hep-ph]].

8. G. Abbiendi *et al.* [OPAL Collaboration], Eur. Phys. J. C **29** (2003) 463 [hep-ex/0210031].

9. M. Cacciari, G. Corcella and A. D. Mitov, JHEP **0212** (2002) 015 [hep-ph/0209204].

10. T. Mannel and G. A. Schuler, Phys. Lett. B **279** (1992) 194.

11. A. H. Ball *et al.*, J. Phys. G **18** (1992) 1703.

12. A. F. Falk and M. E. Peskin, Phys. Rev. D **49** (1994) 3320 [hep-ph/9308241].

13. D. Buskulic *et al.* [ALEPH Collaboration], Phys. Lett. B **365** (1996) 437.

14. P. Abreu *et al.* [DELPHI Collaboration], Phys. Lett. B **474** (2000) 205.

15. G. Abbiendi *et al.* [OPAL Collaboration], Phys. Lett. B **444** (1998) 539 [hep-ex/9808006].

16. D. Buskulic *et al.* [ALEPH Collaboration], Phys. Lett. B **374** (1996) 319.

17. ALEPH Collaboration, CERN-OPEN-99-328.

18. K. Ackerstaff *et al.* [OPAL Collaboration], Eur. Phys. J. C **2** (1998) 49 [hep-ex/9708027].

19. D. de Florian, M. Stratmann and W. Vogelsang, Phys. Rev. D **57** (1998) 5811 [hep-ph/9711387].

20. C. Patrignani *et al.* [Particle Data Group], Chin. Phys. C **40** (2016) 100001; and 2017 update.

21. G. Aad *et al.* [ATLAS Collaboration], JHEP **1405** (2014) 068 [arXiv:1402.6263 [hep-ex]].

22. S. Chatrchyan *et al.* [CMS Collaboration], JHEP **1402** (2014) 013 [arXiv:1310.1138 [hep-ex]].

23. R. Aaij *et al.* [LHCb Collaboration], Phys. Rev. D **92** (2015) 052001 [arXiv:1505.04051 [hep-ex]].

24. A. V. Manohar and M. B. Wise, Phys. Rev. D **49** (1994) 1310 [hep-ph/9308246].

25. A. Czarnecki, M. Jezabek, J. G. Korner and J. H. Kuhn, Phys. Rev. Lett. **73** (1994) 384 [hep-ph/9312249].

26. A. Czarnecki and M. Jezabek, Nucl. Phys. B **427** (1994) 3 [hep-ph/9402326].

27. W. G. D. Dharmaratna and G. R. Goldstein, Phys. Rev. D **53** (1996) 1073.

28. W. Bernreuther, A. Brandenburg and P. Uwer, Phys. Lett. B **368** (1996) 153 [hep-ph/9510300].

29. P. J. Mulders and R. D. Tangerman, Nucl. Phys. B **461** (1996) 197; erratum *ibid.* **484** (1997) 538 [hep-ph/9510301].

30. M. Anselmino, D. Boer, U. D'Alesio and F. Murgia, Phys. Rev. D **63** (2001) 054029 [hep-ph/0008186].

31. R. Aaij *et al.* [LHCb Collaboration], Phys. Lett. B **724** (2013) 27 [arXiv:1302.5578 [hep-ex]].

32. A. M. Sirunyan *et al.* [CMS Collaboration], arXiv:1802.04867 [hep-ex].

33. G. Aad *et al.* [ATLAS Collaboration], Phys. Rev. D **89** (2014) 092009 [arXiv:1404.1071 [hep-ex]].

34. T. Aaltonen *et al.* [CDF Collaboration], Phys. Rev. D **85** (2012) 092011 [arXiv:1112.2808 [hep-ex]].

35. M. Niiyama *et al.* [Belle Collaboration], arXiv:1706.06791 [hep-ex].

36. M. Stratmann and W. Vogelsang, Nucl. Phys. B **496** (1997) 41 [hep-ph/9612250].

Frascati Physics Series Vol. 65 (2017)
LFC17: Old and New Strong Interactions from LHC to Future Colliders
11 - 15 September, 2017

LHC SEARCHES FOR MOMENTUM DEPENDENT DARK MATTER INTERACTIONS

Daniele Barducci
SISSA and INFN Sezione di Trieste, via Bonomea 265, 34136 Trieste, Italy

Abstract

We discuss the properties of dark matter scenarios featuring momentum-dependent couplings between the dark sector and the Standard Model. These frameworks are both motivated by composite pseudo-Goldstone dark matter models and interesting since they weaken direct detection constraints. We derive bounds from existing LHC searches in the monojet channel, estimate the future LHC sensitivity for higher integrated luminosities, and compare our results with models exhibiting conventional momentum independent-interactions with the dark sector.

1 INTRODUCTION

The prince channel for the search for invisible particles at the LHC is the one featuring a hard jet recoiling against an imbalanced missing transverse momentum. Commonly know as monojet channel, it has been exploited by both the ATLAS and CMS collaborations to probe massive neutral particles that are stable on detector or even cosmological scales [1)]. In the latter case these states could contribute to the Dark Matter (DM) energy density of the Universe and monojet searches could offer invaluable information about their existence. Despite being a rather general signature of models predicting a stable neutral particle, it is well know that the jet transverse momentum distribution is one of the key observable that could unravel the nature of the DM coupling to the Standard Model (SM) states.

Motivated by the fact that derivative couplings are well motivated by new physics setup featuring pseudo Nambu-Goldstone bonsons (pNGB) such as Composite Higgs models [2)], we show in this proceeding [1] the effects of derivative and non-derivative couplings between the SM and the new physics

[1]Based on the original work [3)].

sector on the monojet kinematics. In particular, by relying on an simplified effective model inspired by the pNGB setup, we derive current constraints stemming from monojet analyses, assessing the effects of momentum-dependent and momentum-independent DM couplings on monojet distributions and deriving the corresponding bounds on the model parameter space for both cases. We further discuss the dependence of the DM relic abundance and direct detection rate on the two types of interactions, complementing these astrophysical bounds with the collider probes and discussing how the latter can be used to discriminate amongst the two hypotheses should an excess in monojet events be seen at the LHC.

2 THEORETICAL FRAMEWORK

In order to study the impact of derivative and non-derivative couplings between the DM particle and the mediator with the visible sector we extend the SM by two gauge-singlet real scalar fields, η and s. We impose a $\mathcal{Z}_2$ symmetry under which η is odd while s and the SM fields are even, thus making η stable. We also impose that the scalar potential does not spontaneously break the $\mathcal{Z}_2$ symmetry, or equivalently that η does not acquire a non-vanishing vacuum expectation value (vev). We further demand, without any loss of generality, that the vev of the s field vanishes as the latter could always be absorbed in a redefinition of the couplings. Under these assumptions the relevant Lagrangian is given by

$$\begin{aligned}\mathcal{L}_{\eta,s} = \mathcal{L}_{\rm SM} &+ \frac{1}{2}\partial_\mu\eta\partial^\mu\eta - \frac{1}{2}m_\eta^2\eta\eta + \frac{1}{2}\partial_\mu s\partial^\mu s - \frac{1}{2}m_s^2 ss \\ &+ \frac{c_{s\eta}f}{2}s\eta\eta + \frac{c_{\partial s\eta}}{f}(\partial_\mu s)(\partial^\mu\eta)\eta + \frac{\alpha_s}{16\pi}\frac{c_{sg}}{f}sG^a_{\mu\nu}G^{a\mu\nu}\ ,\end{aligned} \tag{1}$$

where we include an effective coupling between s and gluon fields. Consequently, the mediator can be produced at the LHC via gluon fusion and can give rise to a monojet signal via the mechanism $gg \to gs \to g\eta\eta$. In our numerical analysis we will focus on the configuration where $m_S < 2m_\eta$, since in the opposite (on-shell) regime the momentum-dependence of the coupling reduces to a constant, thus making momentum-dependent and momentum-independent interactions indistinguishable.

3 CONSTRAINTS ON THE MODEL

Constraints on the model parameter space arise from both collider as well as astrophysical and underground experiments, since we assume η to be (part of) the measured DM relic abundance of the Universe. In particular we find that the strongest constraints arise from dijet measurements at Tevatron and $Sp\bar{p}S$, relic abundance measurements from Planck, direct detection experiments from LUX and monojet measurements at the LHC. We will discuss these constraints separately in the following, assuming only the momentum-dependent or the momentum-independent coupling to be present at one time and restricting to the range $m_s < 1$ TeV.

3.1 Constraints from dijet measurements

A singly-produced mediator via gluon fusion can decay back into a pair of jets ($gg \to s \to gg$). From the Lagrangian of Eq. (1) the partial decay widths of the s particle into a gluon and η pairs is computed to be

$$\Gamma(s \to gg) = \frac{\alpha_s^2 c_{sg}^2 m_s^3}{128\pi^3 f^2}\ , \tag{2}$$

$$\Gamma(s \to \eta\eta) = \frac{f^2}{32\pi m_s}\left(c_{\partial s\eta}\frac{m_s^2}{f^2} + c_{s\eta}\right)^2\sqrt{1-\frac{4m_\eta^2}{m_s^2}}\ \theta(m_s^2 - 4m_\eta^2)\ , \tag{3}$$

while, in the narrow width approximation, the dijet cross section can be expressed as

$$\sigma(pp \to s \to gg) = \int_0^1 \mathrm{d}x_1 \int_0^1 \mathrm{d}x_2 \; f_g(x_1, m_s) f_g(x_2, m_s) \frac{\alpha_s^2 c_{sg}^2 m_s^2}{1024\pi f^2} \; \delta(\hat{s} - m_s^2) \mathrm{BR}\Big(s \to gg\Big) \; , \qquad (4)$$

where $\sqrt{\hat{s}}$ denotes the partonic center-of-mass energy and $f_g(x, \mu)$ the universal gluon density that depends on the longitudinal momentum fraction x of the gluon in the proton and the factorization scale μ. For the values of m_s considered in this proceeding, the most stringent dijet constraints arise from Sp$\bar{\text{p}}$S [4] and Tevatron [5] data. They provide upper limits on the new physics cross section for mediator masses between 140–300 GeV and 200–1400 GeV respectively. Assuming a value of $f = 1000$ GeV, we find that c_{sg} values up to about 100 are allowed independently of the other parameters, and we adopt this upper limit henceforth.

3.2 Relic abundance measurements

Assuming that η is stable on cosmological scales, the model should yield a relic density in agreement with the Planck measured value $\Omega h^2 \leq 0.1188 \pm 0.0010$ [6]. Restricting the calculation to the leading S-wave contribution and ignoring all possible special kinematic configurations (such as intermediate resonances), the thermally-averaged cross section associated with η annihilation into a pair of gluons is given by

$$\langle \sigma v \rangle_{gg} \simeq \frac{\alpha_s^2 c_{sg}^2 m_\eta^2 \left(c_{s\eta} f^2 + 4 c_{\partial s\eta} m_\eta^2\right)^2}{16\pi^3 f^4 \left(m_s^2 - 4m_\eta^2\right)^2} \; . \qquad (5)$$

In the case where $m_\eta > m_s$, an additional $2 \to 2$ annihilation channel contributes, $\eta\eta \to ss$, whose leading S-wave contribution reads

$$\langle \sigma v \rangle_{ss} \simeq \frac{\sqrt{1 - \frac{m_s^2}{m_\eta^2}} \left(c_{\partial s\eta} m_s^2 + c_{s\eta} f^2\right)^4}{16\pi f^4 m_\eta^2 \left(m_s^2 - 2m_\eta^2\right)^2} \; . \qquad (6)$$

Assuming a standard thermal freeze-out mechanism, and again ignoring singular parameter space regions such as resonances, the DM relic density does not depend strongly on whether $m_\eta > m_s/2$ or $< m_s/2$. This condition is, however, crucial for the LHC: monojet searches can typically only reach couplings that correspond to thermal self-annihilation cross sections once the mediator can be produced and decay on-shell. Instead, in the off-shell regime, the LHC tends to probe parameter space regions where the dark matter abundance lies below $\Omega h^2|_{\text{exp}}$ [7].

3.3 Direct detection constraints

Underground experiments searching for DM particles recoiling against heavy nuclei, *i.e.* direct detection DM experiments, yield additional constraints on the model parameter space. However, these measurements do not constrain the strength of the momentum-dependent interaction, as the corresponding scattering cross section is proportional to the dark matter-nucleus momentum transfer which is very small compared to the mediator mass. On the other hand, the momentum-independent couplings in Eq. (1) lead to an effective interaction between η particles and gluons,

$$\mathcal{L}_{\eta g} = f_G \; \eta^2 \; G_{\mu\nu} G^{\mu\nu} \qquad \text{with} \qquad f_G = \frac{\alpha_s c_{sg} c_{s\eta}}{32\pi} \frac{1}{m_s^2} \; . \qquad (7)$$

The spin-independent dark matter scattering cross section σ_{SI} is then found to take the form [8]

$$\sigma_{\text{SI}} = \frac{1}{\pi} \left(\frac{m_\eta m_p}{m_\eta + m_p}\right)^2 \left| \frac{8\pi}{9\alpha_s} \frac{m_p}{m_\eta} f_G f_{TG} \right|^2 \; , \qquad (8)$$

where the term inside the brackets corresponds to the DM-nucleon reduced mass, and the squared matrix element depends on the gluon form factor $f_{TG} = 1 - \sum_{q=u,d,s} f_{Tq}$ for which we take the values $f_{Tu} = 0.0153$, $f_{Td} = 0.0191$ and $f_{Ts} = 0.0447$ [9]. In presenting our final results we will compare our predictions for $\sigma_{\rm SI}$ to the limits extracted from LUX data [10] [2].

3.4 Monojet constraints

In order to evaluate the LHC sensitivity to our model that arise from monojet searches, we compare our theoretical predictions to official ATLAS results based on early 13 TeV data at an integrated luminosity of 3.2 fb^{-1} [12]. This analysis selects event containing a high p_T jet recoiling against a large amount of missing transverse energy ($E_T^{\rm miss}$), vetoing on the presence leptons with a transverse momentum greater than 10 GeV. More precisely the analysis selection requires $p_T^j > 250$ GeV and various inclusive and exclusive signal regions are defined in terms of $E_T^{\rm miss}$ thresholds. We have also evaluated the LHC sensitivity to our model for a luminosity of 300 fb^{-1}, extrapolating the predictions for the expected SM background and the associated uncertainties. We refer to the original publication [3] for details of the extrapolation procedure.

For the discrete choices of the mediator mass $m_s = 50$ and 250 GeV, we scan over various ranges of the DM mass with $2m_\eta > m_s$. The mediator coupling to the gluon field strength tensor is fixed to $c_{sg} = 100$, as allowed by the dijet bounds discussed.

As a first illustration of the differences between scenarios featuring momentum-independent and momentum-dependent interactions, we show the leading jet p_T distributions obtained for the representative mass combinations $(m_s, m_\eta) = (50, 100/300)$ GeV in the left panel of Figure 1. From the shape of the distributions it is evident that momentum-dependent interactions induce a harder jet p_T spectrum. One thus expect that a larger fraction of events would pass a monojet selection when momentum-dependent interactions are present. This in turns imply that monojet searches are potentially sensitive to smaller cross section in the case of a derivative coupling. This is well illustrated in the right panel of Fig. 1 where we show the upper limits on the monojet cross section at the LHC arising from both from existing data as well as for projections for a higher integrated luminosity. As it can be noticed, the cross sections excluded at the 95% CL are significantly smaller in the momentum-dependent setup than in the moment-independent one, so that the former is more efficiently constrained than the latter. We additionally observe that the exclusion bounds become stronger with increasing m_η. As long as enough phase space is available, larger η masses imply a larger amount of missing energy so that the signal regions of the monojet analysis are more populated and stronger limits can be derived, as shown in the figure.

4 RESULTS

In order to estimate the regions of the model parameter space that are viable with respect to all current data, we show in this Section the interplay between the various measurements described in Sec. 3. Assuming momentum-independent dark matter interactions, the LUX results exclude the spin-independent direct detection cross section predicted by Eq. (8) in the entire parameter space region accessible with the 13 TeV LHC monojet results. Therefore, in the momentum-independent case, an observable monojet

[2] While the work on which this proceeding is based was being completed, the LUX collaboration has updated their results on the basis of 332 live days of exposure [11]. We do not include the latest limits in our analysis. Although more constraining, the new LUX results do not imply significant differences in the allowed region of the parameter space.

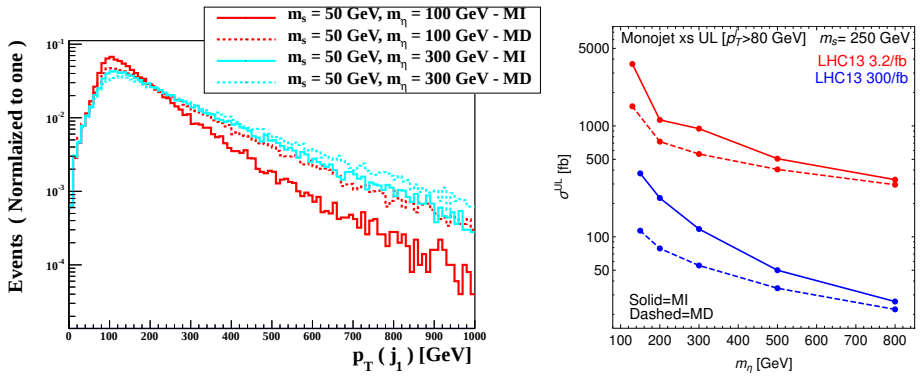

Figure 1: *Left:* Normalized distributions in the transverse momentum of the leading jet assuming $m_s =$ 50 GeV and $m_\eta = 100,\ 300$ GeV. The solid lines reflect scenarios featuring momentum-independent interactions while the dashed lines correspond to scenarios featuring momentum-dependent interactions. *Right:* 95% CL UL on the monojet production fiducial cross section for 3.2 fb^{-1} and 300 fb^{-1} (red and blue respectively) for $m_s = 250$ GeV as a function of m_η. The solid lines correspond to the momentum-independent case, whereas the dashed lines correspond to the momentum-dependent case.

signal could be explained only by missing energy unrelated to DM. Thus, in the following, we show the constraint from the DM relic density only for the momentum-dependent case.

In Fig. 2 we superimpose constraints arising from the 13 TeV LHC current and projected monojet searches on those obtained by imposing the relic density bound. In the shaded regions, $\eta\eta$ annihilation is not efficient enough, so that the Universe is overclosed. Along the borders of these regions, the relic density limit is exactly reproduced. In the un-shaded region, the predicted abundance is smaller than the observed Planck value.

Our findings show that existing monojet constraints are not yet strong enough to probe regions of parameter space where η can account for the entire DM energy density of the Universe. We therefore recover the fairly well-known result that in the "off-shell" regime of DM models, the LHC tends to be sensitive to dark matter candidates for which the relic density is underabundant [13]. That is, collider searches probe large values of the $s\eta\eta$ coupling while the Planck results instead constrain small values, where the Universe tends to be overclosed. In this sense, there is an interesting complementarity between collider and cosmological measurements. Besides, we observe that for an integrated luminosity of 300 fb^{-1}, the LHC will be able to access a part of the low-mass region of our model where the observed DM abundance can be exactly reproduced, for DM masses up to about 140 GeV for $m_s = 50$ GeV. It is important to stress that our results are valid regardless of the stability of the η states at cosmological timescales, hence our analysis holds for metastable η particles as well, as long as they do not decay within the LHC detectors.

5 CONCLUSIONS

In this proceeding we have discussed the properties of DM models where the coupling between the dark and the visible sector features a momentum-dependent interaction. Derivative interactions are common in broad classes of ultraviolet complete DM models, in particular whenever the DM particle is an approximate Goldstone boson of the underlying theory. On the phenomenological side, scenarios involving momentum-dependent couplings can reproduce the observed DM abundance in the Universe,

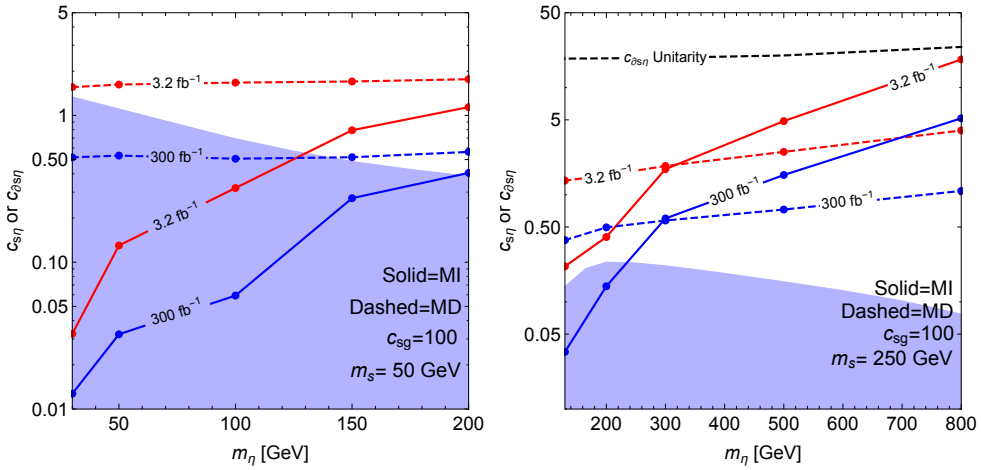

Figure 2: Constraints on the c_i couplings of Eq. (1) from monojet searches. The red lines depict constraints from existing 3.2 fb^{-1} of data whereas blue ones correspond to predictions for an integrated luminosity of 300 fb^{-1}. We fix $f = 1$ TeV, $m_s = 50$ GeV (left) and 250 GeV (right) and the results are represented as functions of m_η for $c_{sg} = 100$. The shaded regions correspond to momentum-dependent coupling values for which the Universe is overclosed. The solid and dashed lines correspond to the momentum-independent and dependent cases respectively.

while evading the stringent bounds from direct detection experiments.

We have reviewed the impact that current experimental measurements, both from collider as well as from astrophysical and underground experiments, have on the parameter space of such models. In particular we have shown that being the high-energy tail of the monojet differential distribution harder in the momentum-dependent case, the associated cross-section is expected to be more efficiently constrained by current LHC data with respect to the momentum-independent case. This difference in sensitivity however appears only when the mediator is produced off-shell. Moreover, in the momentum-dependent case, that is free from direct detection constraints, we compared the monojet upper bounds on the DM couplings with the requirement of not exceeding the observed dark matter abundance in the Universe. Our study indicates that, in the near future, the LHC can cover the most significant portion of the parameter space in the case of a light, off-shell mediator to the dark sector. Indeed, one can progressively close the gap between the collider upper limits on the DM couplings, and their values preferred by cosmological observations. Were a monojet signal observed, the differences in the monojet p_T distribution between the momentum-dependent and the momentum-independent couplings could provide handles on the nature of the DM interactions with the SM. In this case a discrimination among the two scenarios appears feasible, once the statistics become sufficient to analyse the shape of the distributions.

References

1. M. Aaboud *et al.* [ATLAS Collaboration], arXiv:1711.03301 [hep-ex].

2. M. Frigerio, A. Pomarol, F. Riva and A. Urbano, JHEP **1207** (2012) 015 doi:10.1007/JHEP07(2012)015 [arXiv:1204.2808 [hep-ph]].

3. D. Barducci *et al.*, JHEP **1701** (2017) 078 doi:10.1007/JHEP01(2017)078 [arXiv:1609.07490 [hep-

ph]].

4. J. Alitti *et al.* [UA2 Collaboration], Nucl. Phys. B **400** (1993) 3. doi:10.1016/0550-3213(93)90395-6

5. T. Aaltonen *et al.* [CDF Collaboration], Phys. Rev. D **79** (2009) 112002 doi:10.1103/PhysRevD.79.112002 [arXiv:0812.4036 [hep-ex]].

6. P. A. R. Ade *et al.* [Planck Collaboration], Astron. Astrophys. **594** (2016) A13 doi:10.1051/0004-6361/201525830 [arXiv:1502.01589 [astro-ph.CO]].

7. J. L. Feng, S. Su and F. Takayama, Phys. Rev. Lett. **96** (2006) 151802 doi:10.1103/PhysRevLett.96.151802 [hep-ph/0503117].

8. J. Hisano, K. Ishiwata and N. Nagata, Phys. Rev. D **82** (2010) 115007 doi:10.1103/PhysRevD.82.115007 [arXiv:1007.2601 [hep-ph]].

9. G. Blanger, F. Boudjema, A. Pukhov and A. Semenov, Comput. Phys. Commun. **192** (2015) 322 doi:10.1016/j.cpc.2015.03.003 [arXiv:1407.6129 [hep-ph]].

10. D. S. Akerib *et al.* [LUX Collaboration], Phys. Rev. Lett. **116** (2016) no.16, 161301 doi:10.1103/PhysRevLett.116.161301 [arXiv:1512.03506 [astro-ph.CO]].

11. D. S. Akerib *et al.* [LUX Collaboration], Phys. Rev. Lett. **118** (2017) no.2, 021303 doi:10.1103/PhysRevLett.118.021303 [arXiv:1608.07648 [astro-ph.CO]].

12. M. Aaboud *et al.* [ATLAS Collaboration], Phys. Rev. D **94** (2016) no.3, 032005 doi:10.1103/PhysRevD.94.032005 [arXiv:1604.07773 [hep-ex]].

13. D. Abercrombie *et al.*, arXiv:1507.00966 [hep-ex].

Frascati Physics Series Vol. 65 (2017)
LFC17: Old and New Strong Interactions from LHC to Future Colliders
11 - 15 September, 2017

SEARCH FOR NEW MASSIVE PARTNERS OF THE THIRD GENERATION OF QUARKS

Meenakshi Narain
Brown Univesrity, Providence, RI, USA
(On behalf of the CMS Collaboration)

Abstract

In this note, we present a review of the searches for new massive partners of the third generation quarks in the framework of Vector-like quarks. These searches have been recently primarily carried out by the LHC experiments, ATLAS and CMS. A brief review of the searches carried out at the s=8 and 13 TeV run of the LHC is presented, with the examples drawn from the CMS experiment.

1 Introduction

Vector-like quarks (VLQ) appear in several non-supersymmetric models: extra dimensions, composite Higgs, Little Higgs, or their holographic versions. They help improve the theory fit to electroweak observables. VLQs are the simplest type of colored fermions which are still allowed by experiment. VLQs at the TeV scale are strongly motivated by two theoretical ideas: they can explain the observed lightness of the Higgs and they emerge as fermion resonances in the partial-compositeness theory of flavor. Due to the large Yukawa coupling of the top quark, both mechanisms give rise to a sizable mixing of the VLQs with third gen quarks and hence commonly referred to as heavy "top and b partners". The VLQ are colored, charged, and spin 1/2 particles, but have no difference between chiralities, i.e. they couple to left- and right- handed charged currents (in the same way) [1]. Vector-like quarks can have mass terms without violating gauge invariance.

Vector-like quarks with charge 2/3 and $-1/3$ are referred to as T and B quark respectively. In addition, the VLQs with charges 5/3, and $-4/3$ are called X and Y quarks respectively. Vector-like quarks may exist in various SU(2) representations: singlets (T, and B), doublets [(X, T),(T, B),(B, Y)], or triplets [(X, T, B), (T, B, Y)]. VLQs are pair produced through QCD via gluon-gluon fusion or can produced singly in association with a t or a b quark by via electroweak interactions. At high masses, the

rate for single production may dominate over that of pair production, but it depends on the couplings. The VLQs decay to a third generation quark and a SM boson and the decay branching ratios depend on multiplet. In the presence of VLQs, flavor changing neutral current decays are possible (though constrained by rare top decays, D meson mixing and EW precision). Also there is potential for decays to quark and a dark matter candidate. In the searches presented here, T quarks decay to bW, tZ, or tH and B quarks decay to tW, bZ, or bH. In the bench mark scenario, the weak isospin singlets decay to the three final states with branching fractions (BR) of 50%, 25%, 25%, respectively, while the weak isospin doublets decay to tZ and tH [2)] with equal branching ratios. The Y quark decays to bW and X quark decays to tW. The final results are also interpreted for many allowed branching fraction combinations. In general, the pair production searches set limits on $\sigma\times$ BR depending on the VLQ partner mass, where σ is the production cross section. The single production cross section depends on model parameters such as mass, width and coupling to SM quarks and hence allows to set limits in a 2-dimensional coupling vs. mass plane. The coupling coefficients of the T quark to SM particles are denoted C(bW) for the T(b) process, and C(tZ) for the T(t) process. The VLQs can have both left-handed (LH) and right-handed (RH) couplings to SM particles. In the case of a singlet (doublet) VLQ, the RH (LH) chirality is suppressed by a factor proportional to the ratio of the masses of the SM quark and the VLQ [1)].

At higher energies, heavier new particles produce decay products with large Lorentz boost, and their subsequent decay products can merge into a single jet. Thus we employ jet substructure techniques to identify SM bosons and top quarks. The angular separation ΔR of the decay products in a jet due to a particle with mass M depends on its transverse momentum p_T and is approximately proportional to $\frac{2M}{p_T}$. Thus the cone size ΔR to catch all decay products in a boosted W, Z or Higgs Boson jet with $p_T > 200$ GeV is 0.8 and is 1.5 for a jet originating from a boosted top quark. An algorithm called "n-subjettiness" [3)] creates jet shape variables that quantify the consistency of a jet with having n or fewer subjets (1, 2, 3, etc). Mass grooming techniques are used to remove soft jet constituents so that the mass of the hard constituents can be measured more clearly. The "pruning" [4)] technique is used to remove soft jet constituents so that the mass of the hard constituents can be measured more clearly. For example, a jet with $p_T > 200$ GeV, and a pruned mass between 65 and 105 GeV, with the ratio of n-subjettiness variables $\tau_2/\tau_1 < 0.6$ is called a boosted W jet. In addition to boosted boson and top quark identification, efficient lepton (electron and muon), jet, missing E_T, and b jet reconstruction and identification is required for selection of VLQ events in various final state signature.

2 Searches for weakly produced single VLQ signatures

Searches for single production of VLQs have been carried out for the following processes: $T \to bW$ using single leptons and jets (ATLAS, CMS), $T \to tH$ using all hadronic final states and single leptons plus jets (CMS), and $T \to tZ$ with Z decaying to two leptons in the final state (CMS).

2.1 Search for Single $T/Y \to bW$

This analysis is based on requiring a single isolated lepton with $p_T > 30$ GeV from the W and the presence of a central b jet with high p_T (> 200 GeV) in the final state which is separated in azimuth from the lepton with $\Delta\phi(\ell, b) > 2$. The missing E_T in the event is required to be 50 GeV. A extra forward jet with $p_T > 30$ GeV, a particular characteristic of single production of VLQs, is also requested. The search proceeds by reconstructing the VLQ T/Y mass from the b jet and leptonic W decay. The modeling of the dominant backgrounds is checked in control regions dominated by top pair and and W+jets events. For Y quarks with coupling of 0.5 and B($Y \to bW$) = 100%, the observed (expected) lower mass limits

are 1.40 (1.0) TeV [6]. The limits on the $\sigma\times$ BR on the single production of the Y vector-like quark as function of the Y mass from a dataset corresponding to 2.3 fb^{-1} is shown in Fig. 1.

2.2 Search for Single $T \to tH$

A search is performed by CMS for single electroweak production of a T quark decaying to a top quark and a Higgs boson.

The search [7] in the final in fully hadronic final states focuses on T quark with mass above 1 TeV. At these high masses, the decay products of the T quark, the top quark and Higgs boson are highly Lorentz-boosted, and can each appear as single hadronic jet. Jet substructure and b tagging techniques are employed to identify the high p_T boosted hadronic top quark and Higgs boson jets. The merged Higgs boson jets (H tag) with $p_T > 300$ GeV are required to have at least 2 subjets identified as b jets, while the hadronic top jet (t tag) with $p_T > 400$ GeV is required to have one b subjet. Boosted jets with both subjets failing the b tagging criteria but otherwise satisfying the H tagging criteria are labeled as anti-H-tagged jet. The highest p_T H-tagged and t-tagged jets are combined to form the T quark candidate, and the mass of the T quark M(T) is taken to be the invariant mass of the dijet system. The events in the signal region are also required to have H_T, the scalar sum of the jet p_T to be larger than 1.1 TeV.

The main backgrounds for this signal are from $t\bar{t}$+jets, multijets, and, W+jets. The contributions from $t\bar{t}$+jets, and, W+jets are estimated using simulations. The multijet background is estimated from the data by using the $ABCD$ method, which defines four regions A, B, C, and D based on object tags. Events in region A, have at least one anti-H-tagged jet and no H-tagged or t-tagged jets; in region B have at least one anti-H-tagged jet and at least one t-tagged jet, and zero H-tagged jets; in region C have at least one H-tagged jet and no t-tagged jets; in region D, the the signal region, contains events with at least one H-tagged and one t-tagged jet. Since H and t tagging are uncorrelated,the number of background events in the signal region D is given by: $N_D = N_B\, N_C/N_A$. The $ABCD$ method is also used to obtain the background M(T) distribution for the signal region.

The T quark candidate mass distribution M(T) shows no excess and is found to be consistent with the expected backgrounds. The 95% CL upper limits on the product of the single T quark production cross sections and the branching fraction $T \to tH$, vary between 0.31 and 0.93 pb for large T quark masses in the range 1000–1800 GeV.

A search in the lepton+jets final state for $T \to tH$ is performed by CMS [5]. The top quark decay includes an electron or a muon while the Higgs boson decays into a pair of b quarks. For T with large masses in the TeV range, both the Higgs boson and the top quark have large Lorentz boosts. This leads to both the b jets from the Higgs decays merged into a single jet. In the top quark decays, the lepton from the W boson is nonisolated and in close proximity with the b jet. Jet substructure techniques together with b jet tagging is employed to identify boosted decays of the Higgs boson into b quark pairs. To select these events we also utilize the forward light-flavored jet produced in association with the T quark. The event selection requires the p_T of the lepton to be at least 50 GeV, at least two jets with the high p_T jet above 250 (100) GeV for electron (muon) events. The scalar sum of the p_T of all the objects are required to be at least 400 GeV. The dominant backgrounds are due to top quark pair production, W+jets and multijet processes. The background shape is determined from signal depleted region using data with no forward jet, and only one subjet b tag. The variable used for discrimination between signal and background is M(T) reconstructed from the H tagged jet and the top quark four-momentum reconstructed from the lepton, b jet and missing ET.

No significant excess over expected background is observed in the M(T) distribution. The 95% exclusion limits on the product of the production cross section and the branching fraction, $\sigma \times \mathcal{B}$, are derived in the T quark mass range 700 to 1800 GeV. For a mass of 1000 GeV, values of $\sigma \times \mathcal{B}$ greater than 0.8 (0.7) pb are excluded for left- (right-) handed coupling of the T quark to standard model particles.

2.3 Search for Single $T \to tZ$

The CMS search for single production of a T decaying to a Z boson and a top quark, proceeds by identifying the Z boson decaying two leptons and the hadronic decay signature of the top quark [8]. Several T quark widths (10%, 20%, 40%) are considered for different benchmark masses between 0.8 1.6 TeV. Depending on the mass of the T quark, the hadronic top quark jet maybe boosted (with fully merged W jet and b jet), semi-boosted (with partially merged products where the W is boosted with its decays products merged into a single jet, but separated from the bjet), or resolved (with all three particles in the final state are unmerged). Thus, the analysis relies heavily on identification of b jets and use of jet substructure to identify merged top jets, and W jets. As is the case of other single T searches, the forward jet tag is also a powerful selection criterion. A set of very sophisticated categorization using the number of leptons, bjets, forward tagged jet, and boosted and resolved top quarks is performed to obtain the best sensitivity to the T signal. Among the resulting ten categories, the most sensitive categories are found to be those with at least one jet in the forward region. The reconstruction and identification hadronic top quark jets allows the direct reconstruction of the T mass. The mass of the T, M(T), is computed using the leptons from the Z boson decays and the boosted jets. The mass of the T quark is used as a discriminating variable between signal and background. The signal is searched for as an excess in the mass spectrum of reconstructed T quark candidates. The background yield in the signal region is evaluated by using alpha ratio method from a control region where loosely identified b-jets are vetoed: $N_{bkg}(M_{tZ}) = N_{CR}(M_{tZ})\,\alpha(M_{tZ})$ where $N_{CR}(M_{tZ})$ is the number of events in the data in the control region as a function of M_{tZ}, and $\alpha(M_{tZ})$ is the binned ratio between the shapes of M_{tZ} in the signal region to that in the sideband control region.

No significant deviations from the expected background are observed in the M(T) distributions. The observed and expected limits upper limits on the $\sigma \times \mathcal{B}$ for $T \to tZ$ is shown in Fig. 1 (center), for the singlet LH T(b) production modes. For the model in Ref. [9] a singlet LH T quark with C(bW) = 0.5 is excluded at 95% CL for masses below 1.2 TeV. In Fig. 1(right), the observed and expected upper limits at 95% CL are shown as a function of the T quark width and T quark mass in the ranges from 10 to 30% and 0.8 to 1.6 TeV, respectively. A sensitivity similar to that for a narrow-width T quark is observed. A singlet LH (RH) T quark produced in association with a b quark, is excluded for masses below the range 1.34 (0.82) and 1.42 (0.94) TeV depending on the width.

3 Searches for strong pair produced VLQ signatures

3.1 Search for T or Y Pair production with decay $T \to bW$

A search for T/Y pair production with the signature $T\overline{T} \to bW^+bW^-$ is performed by CMS [13] using events with leptons and jets in the final state. The events are selected with a single isolated electron or muon, large missing transverse momentum, and at least four jets with large transverse momenta. For large VLQ masses, the quark pair from the hadronically decaying W boson becomes increasingly collimated, producing overlapping hadronic showers that cannot be resolved as separate jets. Thus this analysis has to incorporate strategies to include both low p_T resolved and high p_T boosted jets while

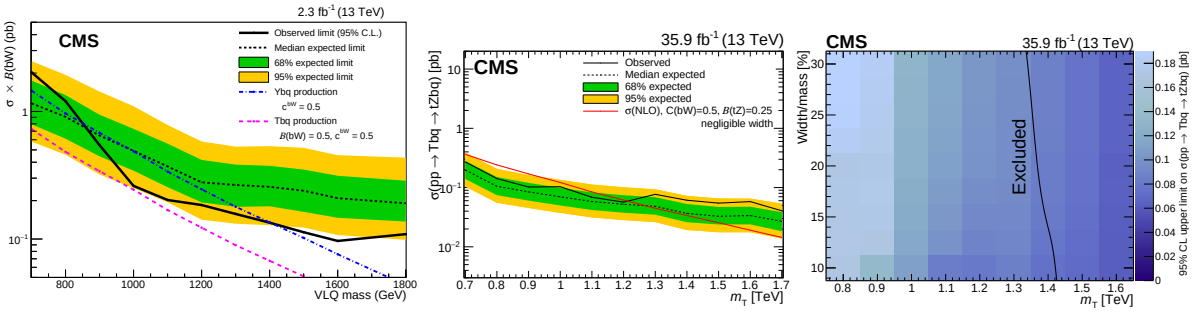

Figure 1: **Left:** *Expected and observed limits on the single VLQ production (Ybq and Tbq) cross section together with the one and two standard deviation uncertainty band. For* $T \to tZ$, **Center:***observed and expected limits at 95% CL on* $\sigma \times \mathcal{B}$ *for the singlet LH* T *quark produced in association with a b quark and* **Right:** *observed limits as a function of the* T *quark width from 10% to 30% of its mass. In the right plot, the solid black lines indicate theoretical cross sections* [10, 11, 12] *and the excluded region lies to the left of the line*

computing the mass of the vector-like T/Y quarks. Selected events are required to contain exactly one charged isolated lepton (muon or electron) with $p_T > 55$ GeV. Events with at least four jets (with a cone radius $\Delta R = 0.4$) with $p_T > 30$ GeV or at least 3 jets with radius 0.4 and one large radius jet ($\Delta R = 0.8$) with $p_T > 200$ GeV. The missing transverse momentum is required to at least 30 GeV. In addition, the two highest-p_T jets must satisfy $p_T > 100$ and 70 GeV.

To compute the mass of the T/Y quark, a constrained kinematic fit on each selected event for the signal decay process $T\overline{T} \to bW^+bW^-$. This requires reconstruction of full kinematic quantities of the final state from which the invariant mass of the T quark, M_{reco} is obtained. For the cases when W bosons decaying hadronically at high Lorentz boosts are reconstructed as single jets, performing constrained kinematic fits that use jets as proxies for the final-state quarks in the signal decay process is challenging. A strategy based on resolving the merged W jets into two subjets by jet substructure techniques [14] is utilized. The resolved subjets contribute separately in the kinematic fit.

The kinematic reconstruction of the final state observables is performed to compute M_{reco}. The distribution of M_{reco} is expected to show a signal with a resolution of 7% and is displayed in Fig. 2(left). The observed number of events is found to be consistent with the standard model prediction. Assuming strong pair production of the VLQs and a 100% branching fraction to bW, a lower limit of 1295 GeV at 95% CL is set on the T and Y quark masses.

3.2 Search for T or Y Pair production with decays $T \to bW, tZ, and tH$

A search for pair production of massive vector-like T and B quarks has been performed in leptonic final states by CMS [15, 16]. The T and B quarks are assumed to decay through three possible channels into a heavy boson (either a W, Z or Higgs boson) and a third generation quark. Vector-like T quarks are predicted to decay to bW, tZ, and tH and likewise, vector-like B quarks are predicted to decay to tW, bZ, and bH. This search is performed in three channels corresponding to final states with a single lepton, two leptons with the same electric charge sign, and at least three leptons. Due to the large mass of the T and B quarks, the single lepton search exploits jet substructure techniques to identify W or Higgs bosons decaying hadronically with large transverse momenta. An electroweak isospin singlet T quark is expected

to have a branching fraction of approximately 50% for $T \to bW$, and 25% for each of $T \to tZ$, and tH, and is used as a benchmark.

The single-lepton channel includes events with exactly one charged lepton and is highly sensitive to $T \to bW$ and $T \to tH$ decays, as well as $B \to tW$ and $B \to bH$ decays. Boosted hadronic decay products of W and Higgs bosons are identied and used to categorize events. The techniques showcased in this analysis for understanding highly-boosted final states are important as the sensitivity to new particles is extended to higher masses. The minimum mass computed using lepton and b jet pairs min[(Mℓ, b)] and S_T, the scalar sum of the p_T of leptons, jets and the event missing E_T, are used to discriminate between signal and backgrounds. The single-lepton channel analysis is optimized to gain sensitivity by using 16 different categories based on lepton avor and the presence of H tagged, W tagged, and b-tagged jets. The same-sign (SS) dilepton channel attempts to draw out a unique feature of VLQ signals, the presence of prompt SS dilepton pairs. In TT production SS lepton pairs are most common in events with $T \to tH$ decay, with the Higgs boson decaying to a pair of W bosons, yielding 3 W bosons in the nal state. In BB production SS lepton pairs are more frequent, arising from $B \to tW$ decays. The trilepton nal state is highly sensitive to $T \to tZ$ and $B \to bZ$ or tW decays. These VLQ decays can produce three or more leptons in the nal state, a signature which is rare in the SM processes. The S_T variable is used to provide discrimination between signal and backgrounds.

The combination of single-lepton, SS dilepton, and trilepton channels improves sensitivity across the various decay modes of the TT and BB processes. No excess over the predicted standard model background is observed. Limits are calculated in a simultaneous t to binned marginal likelihoods from min[M(ℓ, b)] and S_T distributions for the 16 single-lepton signal-region categories, H_T distributions for the 6 single-lepton aggregate control regions, event yields for the SS dilepton channel, and S_T distributions for the 4 trilepton categories.

This study excludes T (B) quarks at 95% condence level with masses below 1200 (1170) GeV in the singlet branching fraction scenario and 1280 (940) GeV in the doublet branching fraction scenario. For other branching fraction combinations this search excludes T quark masses in the range of 11401300 GeV and B quark masses in the range of 9101240 GeV. This represents improvements in sensitivity compared to previous CMS results of 200600 GeV for most T and B quark branching combinations. These results are the strongest exclusion limits to date for T quarks with $\mathcal{B}(bW) < 0.6$ and B quarks with $\mathcal{B}(tW) < 0.6$. The results are shown in Fig. 2(center) and (right).

Search for X Pair production with decays $X^{\frac{5}{3}} \to tW$

Searches for exotic charge 5/3 vector-like X quark is perfomred using single-lepton and SS dilepton signatures [17]. Currently X quarks with masses below ≈1.2 TeV have been ruled out.

4 Outlook

The analyses of 2016 and 2017 datasets accumulated by the experiments are still ongoing. The current focus is on new algorithms to charaterize and developing techniques to identify efficiently boosted object signatures. An additional challenge is to develop control regions for background which are similar to the phase space of the heavy particles, as much of systematic uncertainty arises from the understanding of the background dominated control regions. Many VLQ search results, both in the single and double production modes will be completed in the near future. These have the potential to probe VLQ masses upto about 1-1.2 TeV. With the full sample of data collected during Run2 (100 fb^{-1}), reach maybe extended somewhat. With Run3 (300 fb^{-1}), and augmented search techniques, we expect to probe around 1.5 TeV with both single production (depending on couplings) and pair production searches.

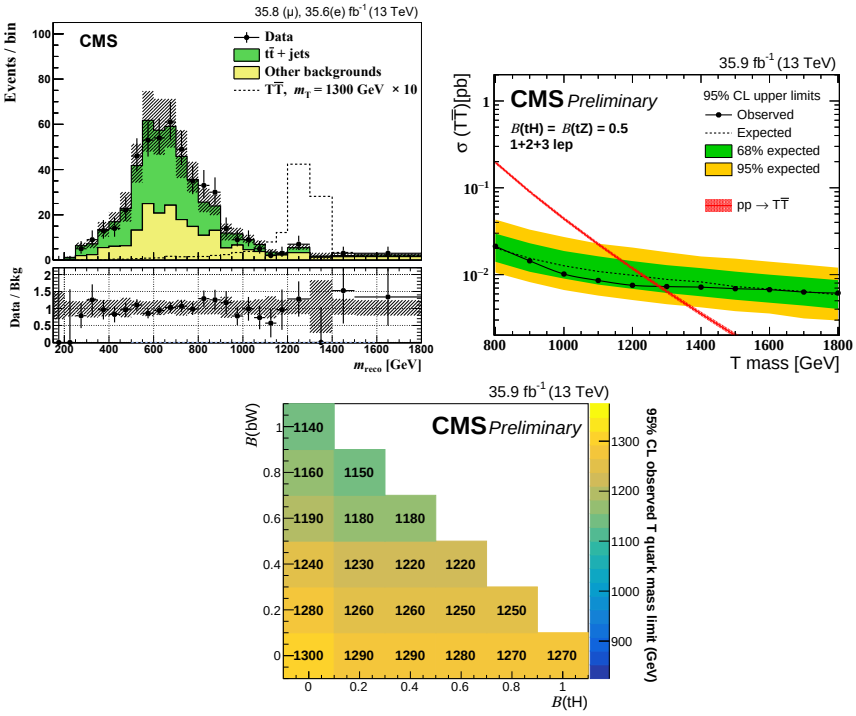

Figure 2: **Left:** *The post-fit distribution of the reconstructed T quark mass.The shaded band on the histogram and on the ratio plot shows the quadrature sum of the statistical and systematic uncertainties. The MC prediction for heavy quark production with a mass of 1300 GeV is shown by a dashed line, enhanced by a factor of 10.* **Center:** *The 95% CL expected upper limits (Bayesian) on the cross section of TT production after combining all channels for the doublet branching fraction scenarios.* **Right:** *The 95% CL observed lower limits (Bayesian) on the T quark mass after combining all channels for various branching fraction combinations.*

Acknowledgements: Narain would like to extend her thanks to Dr. Corcella and Dr. Pancheri for their invitation and the generous hospitality during the workshop.

References

1. G. Cacciapaglia et al., "Heavy vector-like top partners at the LHC and flavour constraints", *JHEP* **03** (2012) 070, arXiv:1108.6329 [hep-ph].

2. F. del Aguila, L. Ametller, G.L. Kane, J. Vidal, "Vector-like fermion and standard Higgs production at hadron colliders", Nucl. Phys. **B334**, 1 (1990)

3. J. Thaler and K. Van Tilburg, JHEP **1202**, 093 (2012) doi:10.1007/JHEP02(2012)093 [arXiv:1108.2701 [hep-ph]].

4. S. D. Ellis, C. K. Vermilion and J. R. Walsh, Phys. Rev. D **80**, 051501 (2009) doi:10.1103/PhysRevD.80.051501 [arXiv:0903.5081 [hep-ph]].

5. V. Khachatryan *et al.* [CMS Collaboration], Phys. Lett. B **771**, 80 (2017) doi:10.1016/j.physletb.2017.05.019 [arXiv:1612.00999 [hep-ex]].

6. A. M. Sirunyan *et al.* [CMS Collaboration], Phys. Lett. B **772**, 634 (2017) doi:10.1016/j.physletb.2017.07.022 [arXiv:1701.08328 [hep-ex]].

7. A. M. Sirunyan *et al.* [CMS Collaboration], JHEP **1704**, 136 (2017) doi:10.1007/JHEP04(2017)136 [arXiv:1612.05336 [hep-ex]].

8. A. M. Sirunyan *et al.* [CMS Collaboration], arXiv:1708.01062 [hep-ex].

9. O. Matsedonskyi, G. Panico, and A. Wulzer, "On the interpretation of top partners searches", *JHEP* **12** (2014) 097, arXiv:1409.0100 [hep-ph]

10. M. Buchkremer, G. Cacciapaglia, A. Deandrea, and L. Panizzi, "Model independent framework for searches of top partners", *Nucl. Phys. B* **876** (2013) 376, arXiv:1305.4172 [hep-ph].

11. B. Fuks and H.-S. Shao, "QCD next-to-leading-order predictions matched to parton showers for vector-like quark models", *Eur. Phys. J. C* **77** (2017) 135, arXiv:1610.04622 [hep-ph].

12. A. Oliveira, "Gravity particles from warped extra dimensions, predictions for LHC", (2014). arXiv:1404.0102 [hep-ph].

13. A. M. Sirunyan *et al.* [CMS Collaboration], Phys. Lett. B **779**, 82 (2018) doi:10.1016/j.physletb.2018.01.077 [arXiv:1710.01539 [hep-ex]].

14. A. J. Larkoski, S. Marzani, G. Soyez, and J. Thaler, "Soft drop", *JHEP* **05** (2014) 146, arXiv:1402.2657 [hep-ph].

15. A. M. Sirunyan *et al.* [CMS Collaboration], JHEP **1711**, 085 (2017) doi:10.1007/JHEP11(2017)085 [arXiv:1706.03408 [hep-ex]].

16. A. M. Sirunyan *et al.* [CMS Collaboration], CMS-PAS-B2G-17-011, "https://cds.cern.ch/record/2308309".

17. A. M. Sirunyan *et al.* [CMS Collaboration], CMS-PAS-B2G-16-019, "https://cds.cern.ch/record/2256747".

    Search for heavy vector-like quarks decaying to same-sign dileptons

Frascati Physics Series Vol. 65 (2017)
LFC17: Old and New Strong Interactions from LHC to Future Colliders
11 - 15 September, 2017

B DECAY ANOMALIES AND DARK MATTER FROM STRONG DYNAMICS

James M. Cline
Niels Bohr International Academy, Copenhagen, Denmark,
and
McGill University, Physics Department, Montréal, Canada

Abstract

Indications of lepton flavor universality violation in semileptonic B decays to K or K^* and muons or electrons can be explained by leptoquark exchange. I present a model in which the leptoquark is a bound state of constituents charged under a new confining $\mathrm{SU}(N_{\mathrm{HC}})$ hypercolor interaction. The lightest neutral bound state in the theory is an asymmetric dark matter candidate, assuming some mechanism in the early universe generates its asymmetry.

1 Introduction

Strong dynamics has been a useful idea for going beyond the standard model (SM) in the context of several tentative experimental anomalies from the past, such as the 750 GeV diphoton excess at LHC and the 130 GeV gamma ray excess at the Fermi telescope. It has also proved useful for building models of composite dark matter arising from a possibly rich hidden sector. One motivation for such models is the hint of strong dark matter self-interactions from cosmological N-body simulations versus observations of galactic structure.

Recently the LHCb experiment at CERN has found tentative evidence for violation of lepton flavor universality in the decays of $B \to K$ or K^* and e^+e^- or $\mu^+\mu^-$ [1, 2]. Popular theoretical explanations involve tree-level exchange of new heavy states—gauge bosons or leptoquarks, or exchange of new particles in a loop. Here I will focus on the leptoquark option. One might consider the leptoquark as a rather odd beast in the beyond-the-standard-model zoo, not being required by any new principles such as supersymmetry. However in the context of strong dynamics the existence of leptoquarks can be natural, since all that is required is that new hypercolored fields interacting with quarks or leptons respectively become bound to each other in a meson-like state. If there also exist new fields that are neutral under

	SU(3)	$\mathrm{SU(2)}_L$	$\mathrm{U(1)}_y$	$\mathrm{U(1)}_{\mathrm{em}}$	$\mathrm{SU(N)}_{HC}$	Z_2
Ψ	3	1	2/3	2/3	N	-1
S	1	1	0	0	N	-1
ϕ	1	2	$-1/2$	$(0,-1)$	$\bar{N}$	-1

Table 1: New particles and their quantum numbers

the standard model symmetries but charged under hypercolor, then a composite dark matter candidate comes at no extra cost, beyond considerations of its stability.

Model-independent fits, for example ref. [3], show that the new physics can be well-described by the addition of a single operator

$$\mathcal{O}_{b_L\mu_L} = \frac{c}{\Lambda^2}(\bar{s}_L\gamma_\alpha b_L)(\bar{\mu}_L\gamma^\alpha\mu_L) \tag{1}$$

in the effective Hamiltonian, with

$$\frac{c}{\Lambda^2} = \frac{1.0\times10^{-3}}{\mathrm{TeV}^2}\,. \tag{2}$$

By a Fierz transformation, the operator (1) can be put into the form more suggestive of leptoquark exchange, $(\bar{s}_L\gamma_\alpha\mu_L)(\bar{\mu}_L\gamma^\alpha s_L)$.

2 Model

Our model [4] introduces three new particles: a vectorlike quark partner Ψ and right-handed neutrino partner S, and an inert Higgs doublet ϕ, all charged under $\mathrm{SU(N)}_{HC}$ and an accidental Z_2, which are listed in table 1. The allowed couplings to standard model left-handed quarks and leptons are

$$\mathcal{L} = \tilde{\lambda}_f\,\bar{Q}_{f,a}\,\phi^a_A\Psi^A + \lambda_f\,\bar{S}_A\tilde{\phi}^A_a\,L^a_f \tag{3}$$

with f being the generation index. We work in a basis where the mass matrices of the charged leptons and down-like quarks are presumed to be diagonal, hence CKM mixing comes exclusively from diagonalization of the up-like quark mass matrix. After going to the mass basis, the couplings to down-like quarks remain λ_f, but those to up-like quarks are rotated, $\tilde{\lambda}_i\bar{Q}_i \to \tilde{\lambda}_j\left(\ \bar{u}_{L,i}V_{ij},\ \bar{d}_{L,j}\ \right) \equiv \left(\ \tilde{\lambda}'_i\bar{u}_i,\ \tilde{\lambda}_i\bar{d}_i\ \right)$.

Because of confinement by the hypercolor interaction, there are various meson-like bound states $\bar{S}S$, $\bar{\Psi}\Psi$ and $\bar{\Psi}S$, the last of which has leptoquark quantum numbers. All of these states can have either spin 0 or spin 1. The spin-0 (pseudoscalar) leptoquark Π couples to SM fermions through a derivative interaction since the matrix element $\langle0|(\bar{S}\gamma_\mu\gamma_5\Psi)|\Pi\rangle = f_\Pi\,p^\mu_\Pi$ is analogous to that of the pion in QCD. When p^μ_Π is contracted with the $\bar{q}\gamma_\mu\ell$ current of the SM fermions, it leads to the small masses m_q and m_ℓ following from the Dirac equation, which suppresses the matrix element. For this reason the vector leptoquark Φ_μ interacts more strongly with the SM fermions. Its matrix element is $\langle0|(\bar{S}\gamma_\mu\Psi)|\Phi_\lambda\rangle = f_\Phi\,m_\Phi\epsilon^\mu_\lambda$ for a state with polarization labeled by λ.

To determine the effective coupling g^{fg}_Φ of Φ_μ to the SM fermions, we can compare the decay rate computed in the effective theory, $\Gamma(\Phi_\mu\to L_g\bar{Q}_f) = \frac{|g^{fg}_\Phi|^2}{24\pi}m_\Phi$, to its prediction in terms of the constituents in the bound state [5],

$$\Gamma(\Phi_\mu\to L_g\bar{Q}_f) = \sigma v_{\mathrm{rel}}(S\bar{\Psi}\to L_g\bar{Q}_f)|\psi(0)|^2 \tag{4}$$

where $\psi(0)$ is the wave function of the bound state evaluated at the origin, and σ is the perturbative cross section for the indicated scattering. This gives

$$g^{fg}_\Phi = \left(\frac{N_{HC}}{4m_\Phi}\right)^{1/2}\frac{\tilde{\lambda}_f\lambda_g\,(m_S+m_\Psi)\,\psi(0)}{(m^2_\phi+m_sm_\Psi)} \tag{5}$$

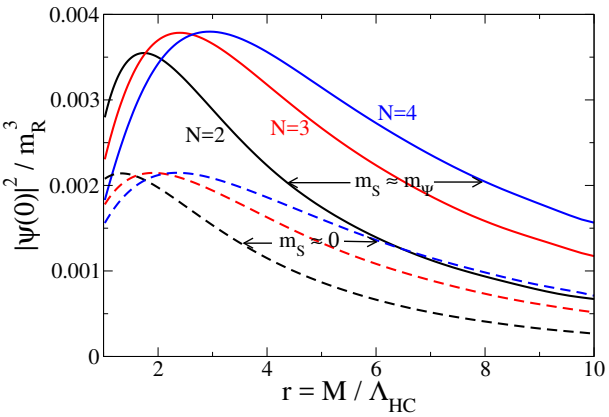

Figure 1: The function $\zeta = |\psi(0)|^2/m_\Phi^3$ (eq. (7)) Solid curves correspond to both constituents (and the inert doublet ϕ) having the same mass M, while dashed ones show the case of $m_S \ll M$.

We still need to determine $\psi(0)$. We will be interested in heavy constituent masses, of order the confinement scale Λ_{HC}, for which a nonrelativistic potential model should give reasonable estimates. We take a Cornell potential

$$V_c = -\frac{\alpha_{HC}}{2r}\left(N_{HC} - \frac{1}{N_{HC}}\right) + 2(N_{HC}-1)\Lambda_{HC}^2\, r \tag{6}$$

between fundamental and anti-fundamental states, and a hydrogen-like variational ansatz for the wave function, $\psi \sim e^{-\mu_* r/2}$. The scale μ_* and the mass of the bound state are then found by minimizing the total energy. This allows us to make predictions for the Wilson coefficient of (1) in terms of the fundamental parameters of the theory. All of the nonperturbative physics is encoded in the dimensionless ratio

$$\zeta \equiv \frac{|\psi(0)|^2}{m_\Phi^3}\,, \tag{7}$$

It depends only on Λ_{HC}/M, where M is the common mass scale for the new particles that we have assumed for simplicity. As shown in fig. 1, ζ is always small and is maximized near $\zeta \cong 0.004$ for $M \sim 2.5\Lambda_{HC}$. As benchmark values we will adopt

$$M = 1\,\text{TeV}, \quad \Lambda_{HC} = 400\,\text{GeV} \tag{8}$$

3 Flavor Physics

We can fit the anomalies in $B \to K\ell\bar{\ell}$ decays by imposing

$$|\lambda_2^2\,\tilde{\lambda}_2\,\tilde{\lambda}_3| \cong 0.3\left(\frac{M}{\text{TeV}}\right)^2\left(\frac{3}{N_{HC}}\right)\,. \tag{9}$$

hence the relevant couplings can be reasonably small. However it is not trivial to find value that satisfy other flavor constraints. This is because analogous exchanges of $\bar{\Psi}\Psi$ bound states give rise to meson-antimeson mixing, as illustrated in fig. 2(c). Especially for B_s mixing, the same combination of quark couplings $\tilde{\lambda}_2\tilde{\lambda}_3$ as in (9) is relevant. To keep them sufficiently small, we must take λ_2 in (9) to be sizable.

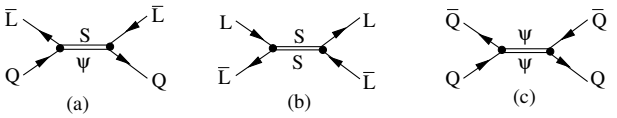

Figure 2: Flavor changing neutral currents mediated by the three different kinds of bound states.

An example of values that can satisfy all constraints is

$$\begin{aligned} \tilde{\lambda}_1 &= -0.01, \quad \tilde{\lambda}_2 = 0.1, \quad \tilde{\lambda}_3 = 0.66, \quad \lambda_2 = 2.1 \\ (\tilde{\lambda}'_1 &= 0.014, \quad \tilde{\lambda}'_2 = 0.13, \quad \tilde{\lambda}'_3 = 0.66)\,. \end{aligned} \tag{10}$$

The predicted values of products of couplings relevant to mixing of the neutral mesons is shown in table 2. We choose to saturate the B_s mixing constraint [6].

In addition to meson mixing, there are radiative FCNCs like $b \to s\gamma$, coming from transition magnetic moments between heavy bound state quark partners $\Psi\phi$ and the SM quarks. Because there is mass mixing induced by the interaction (3) between these states, in the mass basis the transition moment between heavy quark partners and SM quarks induces transition moments between different flavors of SM quarks, notably b and s. However the amplitude turns out to be well below the current limit.

The previous processes have counterparts involving leptons, from fig. 2(b). They can be avoided by assuming $\lambda_1 = \lambda_3 = 0$ (the couplings to first and third generation leptons), which is radiatively stable since to generate them from λ_2 at one loop requires a neutrino mass insertion. But in general one finds upper bounds on λ_1 and λ_3 from $\mu \to 3e$, $\tau \to 3\mu$, and radiative transitions. The most stringent constraint arises from $\mu \to e\gamma$ and $\tau \to \mu\gamma$,

$$|\lambda_1| \lesssim 7.5 \times 10^{-4}, \quad |\lambda_3| \lesssim 0.56\,, \tag{11}$$

The new contribution to $(g-2)_\mu$ is much smaller (by a factor of 300) than needed to explain the outstanding discrepancy.

4 Composite dark matter

The new S particle is neutral under SM interactions, and stable by virtue of the accidental Z_2 symmetry, if it is the lightest of the new particles. The baryon-like bound state $\Sigma = S^{N_{HC}}$ is therefore a stable dark matter (DM) candidate. The nonrelativistic potential model predicts its mass to be several TeV, given (8). Previous studies of composite baryon-like DM in this mass and coupling range show that its thermal relic density is highly suppressed by annihilations to hypergluons at temperature above the confinement scale [7, 8]. We must therefore assume there exists some mechanism for generating an asymmetry in its

meson	quantity	upper limit (units M/TeV)	fiducial value (units M/TeV)
K^0	$\lvert\tilde{\lambda}_1\tilde{\lambda}_2\rvert$	1.3×10^{-3}	1×10^{-3}
D^0	$\lvert\tilde{\lambda}'_1\tilde{\lambda}'_2\rvert$	2×10^{-3}	7×10^{-4}
B^0	$\lvert\tilde{\lambda}_1\tilde{\lambda}_3\rvert$	0.026	0.0066
B^0_s	$\lvert\tilde{\lambda}_2\tilde{\lambda}_3\rvert$	0.066	0.066

Table 2: Predicted and limiting values of products of couplings determining neutral meson mixing, assuming eq. (10).

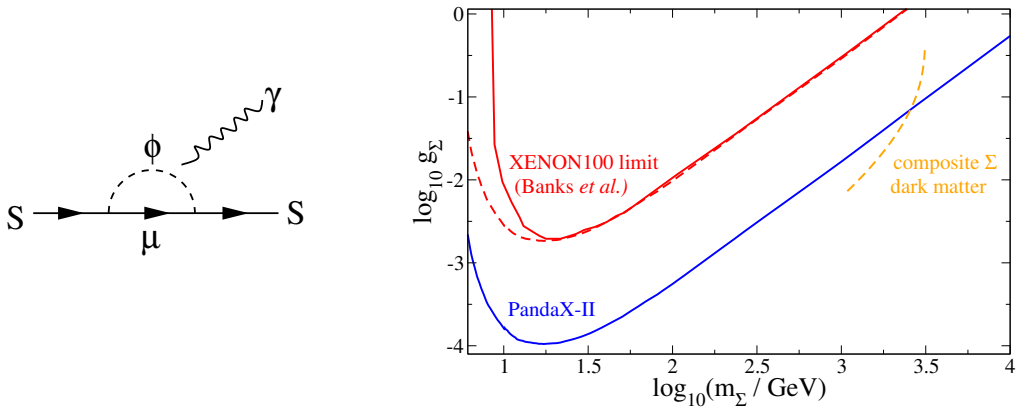

Figure 3: Left: diagram generating a magnetic moment for the S fermion. Right: direct detectioon constraint on the dark matter $S^{N_{HC}}$ gyromagnetic ratio.

number density, which is conserved in our model (hyperbaryon number can be consistently assigned to all the new particles).

The model is strongly constrained by direct searches for the dark matter, if N_{HC} is odd. The S fermion gets a magnetic moment at one loop from the diagram in fig. 3(a),

$$\mu_S = \frac{e|\lambda_2|^2 m_S}{32\pi^2\, m_\phi^2} f(R)\,, \tag{12}$$

where $R \equiv m_S^2/m_\phi^2$ and the loop function $f(R) \sim 1$. If N_{HC} is odd, Σ is fermionic and inherits a magnetic moment from its constituents of order $N_{HC}\mu_S$. Updating older constraints on dark matter with a magnetic moment [9], we obtain fig. 3(b) where the predicted curve (dashed line) is parametrized by m_S. Since m_Σ varies rather weakly with m_S, due to the large contribution to its mass from the hypergluons, the curve is steep as a function of m_Σ. It is only below current limits for $m_S \lesssim 800$ GeV.

5 LHC constraints

Bound states can be produced resonantly at a hadron collider through the processes shown in fig. 4(left). The parton level cross sections can be computed in analogy to those for producing QCD bound states like J/Ψ at an electron collider. For example the cross section to produce the vector meson $\rho_\Psi = \bar\Psi\Psi$ from $q\bar q$ is

$$\sigma(q\bar q \to \rho_\Psi) = N_{HC}\frac{64\pi^3\alpha_s^2|\psi(0)|^2}{3\, m_{\rho_\Psi}^3}\,\delta(s - m_B^2) \tag{13}$$

whose nonperturbative component resides in the same ratio ζ as in (7), given that we have approximated all the bound state masses and wave functions as being approximately the same. Thus we can predict the cross sections for these processes at LHC with no extra freedom from adjusting parameters.

The processes in fig. 4(left) produce dileptons, dijets or diphotons. ATLAS and CMS dijet constraints turn out to give the most stringent limits on the model [10, 11], shown in fig. 5(left). The ρ_Ψ vector meson mass must exceed 2.8 TeV, which does not yet rule out our fiducial model where all the resonances have mass $\cong 3.6$ TeV. The other resonant states give rise to weaker limits.

It is also possible to pair-produce the bound states by open production of the hyperquarks, followed by hadronization in the SU(N_{HC}) sector, as shown in fig. 4(right). This requires more energy and leads

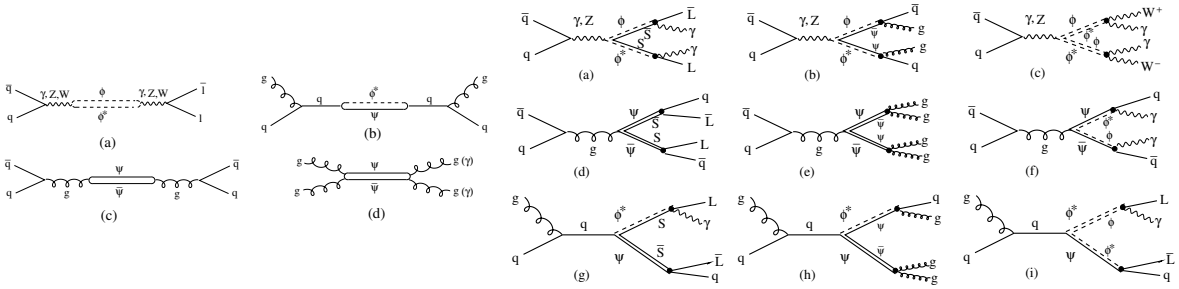

Figure 4: Left: Resonant production of HC bound states leading to dileptons, dijets or diphotons; right: pair production of bound states.

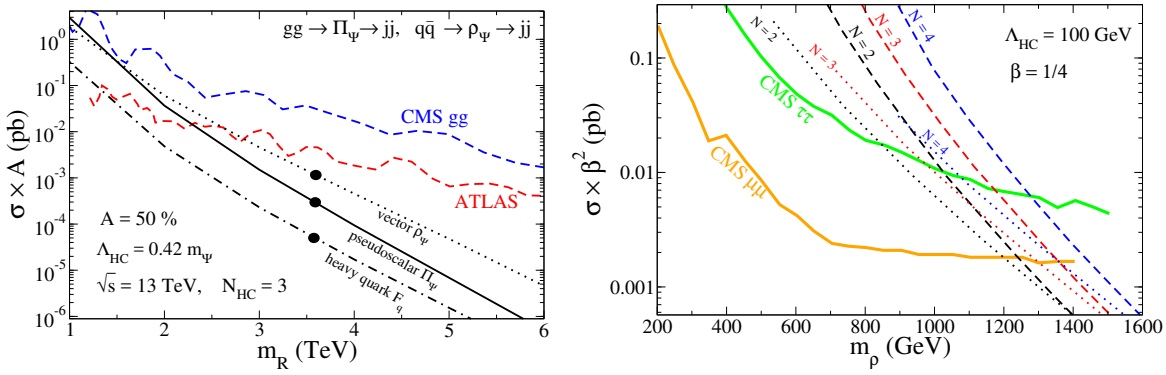

Figure 5: Left: LHC dijet limits; right: leptoquark search limits

to large phase-space suppression of the cross sections. If $m_S \ll \Lambda_h c$ then this effect is mitigated for the states containing S, including the leptoquarks. Then leptoquark searches can be used to constrain the model, where final states with two leptons and two jets are scrutinized [12, 13]. The limits, shown in fig. 5(right) along with our model predictions for $m_S = 0$, are less constraining than those from the resonant production searches.

6 Conclusions

Ours is not the first model of composite leptoquarks that has been proposed to account for the $B \to K\ell\bar{\ell}$ decay anomalies, but we believe it is considerably simpler than others [14, 15, 16, 17]. It is tightly constrained by FCNC processes, namely meson mixing, and LHC searches for resonant production of bound states of the heavy quark-like constituents. It has the virtue of providing a composite dark matter candidate Σ, that is also challenged by current direct searches if Σ contains an odd number of constituents (hence is fermionic). More accurate predictions of the model could be obtained by a lattice study of the SU(N_{HC}) bound state properties, that we have estimated in a rough manner.

References

1. R. Aaij *et al.* [LHCb Collaboration], "Test of lepton universality using $B^+ \to K^+\ell^+\ell^-$ decays," Phys. Rev. Lett. **113**, 151601 (2014) doi:10.1103/PhysRevLett.113.151601 [arXiv:1406.6482 [hep-ex]].

2. R. Aaij *et al.* [LHCb Collaboration], "Test of lepton universality with $B^0 \to K^{*0}\ell^+\ell^-$ decays," JHEP **1708**, 055 (2017) doi:10.1007/JHEP08(2017)055 [arXiv:1705.05802 [hep-ex]].

3. G. D'Amico, M. Nardecchia, P. Panci, F. Sannino, A. Strumia, R. Torre and A. Urbano, "Flavour anomalies after the R_{K^*} measurement," JHEP **1709**, 010 (2017) doi:10.1007/JHEP09(2017)010 [arXiv:1704.05438 [hep-ph]].

4. J. M. Cline, "B decay anomalies and dark matter from vectorlike confinement," Phys. Rev. D **97**, no. 1, 015013 (2018) doi:10.1103/PhysRevD.97.015013 [arXiv:1710.02140 [hep-ph]].

5. J. Kang and M. A. Luty, "Macroscopic Strings and 'Quirks' at Colliders," JHEP **0911**, 065 (2009) doi:10.1088/1126-6708/2009/11/065 [arXiv:0805.4642 [hep-ph]].

6. P. Arnan, L. Hofer, F. Mescia and A. Crivellin, "Loop effects of heavy new scalars and fermions in $b \to s\mu^+\mu^-$," JHEP **1704**, 043 (2017) doi:10.1007/JHEP04(2017)043 [arXiv:1608.07832 [hep-ph]].

7. A. Mitridate, M. Redi, J. Smirnov and A. Strumia, "Dark Matter as a weakly coupled Dark Baryon," arXiv:1707.05380 [hep-ph].

8. J. M. Cline, W. Huang and G. D. Moore, "Challenges for models with composite states," Phys. Rev. D **94**, no. 5, 055029 (2016) doi:10.1103/PhysRevD.94.055029 [arXiv:1607.07865 [hep-ph]].

9. T. Banks, J. F. Fortin and S. Thomas, "Direct Detection of Dark Matter Electromagnetic Dipole Moments," arXiv:1007.5515 [hep-ph].

10. M. Aaboud *et al.* [ATLAS Collaboration], "Search for new phenomena in dijet events using 37 fb^{-1} of pp collision data collected at $\sqrt{s}$ =13 TeV with the ATLAS detector," arXiv:1703.09127 [hep-ex].

11. CMS Collaboration [CMS Collaboration], "Searches for dijet resonances in pp collisions at $\sqrt{s}$ = 13 TeV using data collected in 2016.," CMS-PAS-EXO-16-056.

12. CMS Collaboration [CMS Collaboration], "Search for pair-production of second-generation scalar leptoquarks in pp collisions at $\sqrt{s} = 13$ TeV with the CMS detector," CMS-PAS-EXO-16-007.

13. A. M. Sirunyan *et al.* [CMS Collaboration], "Search for third-generation scalar leptoquarks and heavy right-handed neutrinos in final states with two tau leptons and two jets in proton-proton collisions at $\sqrt{s} = 13$ TeV," JHEP **1707**, 121 (2017) doi:10.1007/JHEP07(2017)121 [arXiv:1703.03995 [hep-ex]].

14. B. Gripaios, M. Nardecchia and S. A. Renner, "Linear flavour violation and anomalies in B physics," JHEP **1606**, 083 (2016) doi:10.1007/JHEP06(2016)083 [arXiv:1509.05020 [hep-ph]].

15. R. Barbieri, C. W. Murphy and F. Senia, "B-decay Anomalies in a Composite Leptoquark Model," Eur. Phys. J. C **77**, no. 1, 8 (2017) doi:10.1140/epjc/s10052-016-4578-7 [arXiv:1611.04930 [hep-ph]].

16. S. Matsuzaki, K. Nishiwaki and R. Watanabe, "Phenomenology of flavorful composite vector bosons in light of B anomalies," JHEP **1708**, 145 (2017) doi:10.1007/JHEP08(2017)145 [arXiv:1706.01463 [hep-ph]].

17. D. Buttazzo, A. Greljo, G. Isidori and D. Marzocca, "B-physics anomalies: a guide to combined explanations," arXiv:1706.07808 [hep-ph].

Frascati Physics Series Vol. 65 (2017)
LFC17: Old and New Strong Interactions from LHC to Future Colliders
11 - 15 September, 2017

STRONGLY INTERACTING LIGHT DARK MATTER

Alfredo Urbano
Theoretical Physics Department, CERN, Geneva, Switzerland.

Abstract

We discuss a class of Dark Matter (DM) models that, although inherently strongly coupled, appear weakly coupled at small-energy and fulfill the WIMP miracle, generating a sizable relic abundance through the standard freeze-out mechanism. Such models are based on approximate global symmetries that forbid relevant interactions; fundamental principles, like unitarity, restrict these symmetries to a small class, in such a way that the leading interactions between DM and the Standard Model are captured by effective operators up to dimension-8. The underlying strong coupling implies that these interactions become much larger at high-energy and represent an interesting novel target for LHC missing-energy searches.

1 Introduction and motivations

Studies of processes with missing energy at the LHC constitute an important part of the Dark Matter (DM) research program, that aims at unravelling possible non-gravitational interactions between the Standard Model (SM) and the dark sector. Information from the LHC would be particularly useful for light DM, $m_{\rm DM} \lesssim 10$ GeV, below the threshold for direct detection experiments. In this case, the *WIMP miracle* seems to provide a convincing hint that light DM originates from *weakly coupled* dynamics. Indeed, parameterizing the thermally-averaged annihilation cross section as

$$\langle \sigma v_{\rm rel} \rangle \sim \frac{\alpha_{\rm DM}^2}{m_{\rm DM}^2} \tag{1}$$

with $m_{\rm DM}, \alpha_{\rm DM}$ the DM mass and coupling to the Standard Model (SM) fields, we find for the relic density

$$\Omega_{\rm DM} h^2 \approx \frac{10^{-26}\,{\rm cm}^3/{\rm s}}{\langle \sigma v_{\rm rel} \rangle} \approx 0.1 \left(\frac{0.1}{\alpha_{\rm DM}} \right)^2 \left(\frac{m_{\rm DM}}{10\,{\rm GeV}} \right)^2 \ . \tag{2}$$

A weak coupling $\alpha_{\rm DM} \ll 1$ reproduces the observed value $\Omega_{\rm DM}h^2 \approx 0.1$. Note that, for simplicity, we limit the present discussion to s-wave annihilation. Annihilation in p-wave would imply in eq. (1) the presence of the suppression factor $v_{\rm rel}^2$ due to the relative velocity of the two annihilating particles, roughly $v_{\rm rel} \sim 1/3$ at freeze-out temperature. In this contribution we want to explore how solid this indication is and study the viability of light DM associated with a new *strong*, yet perturbative, coupling which we call $g_* \lesssim 4\pi$. The core aspect of our analysis is *approximate symmetries*, which forbid relevant (renormalizable) SM-DM interactions, but allow irrelevant (non-renormalizable) interactions of dimension D. Referring to M as the *physical* scale suppressing the latter, the amplitude for $2 \to 2$ annihilation, would scale as

$$\alpha_{\rm DM} \sim \frac{g_*^2}{4\pi}\left(\frac{E}{M}\right)^{D-4} , \tag{3}$$

where E denotes the collision energy. At low energies $E \ll M$, such as those relevant at freeze-out, the interaction of eq. (3) appears weak, despite their strongly coupled nature at high-energy: this reconciles an underlying strong coupling with the WIMP miracle. For instance, for D=6, considering that in the relevant non-relativistic limit $E \sim m_{\rm DM}$,

$$\Omega_{\rm DM}h^2 \approx 0.1\left(\frac{4\pi}{g_*}\right)^4\left(\frac{5\,{\rm GeV}}{m_{\rm DM}}\right)^2\left(\frac{M}{3\,{\rm TeV}}\right)^4 , \tag{4}$$

showing that even an extremely strongly coupled system $g_* \approx 4\pi$, can reproduce the observed relic abundance, as long as the mediator scale M is in the multi-TeV region. At high-energy $E \lesssim M$, DM interacts strongly with itself and with the SM, eq. (3). This is in fact very appealing for the LHC which, operating at high-energy, has direct access to the strongly coupled regime. Moreover, in this regime, the signal from the strongly coupled sector is expected to be strong, and dominate over the LHC irreducible backgrounds (such as $jZ \to j\nu\nu$). For this reason, because large effects can be obtained even for $E \lesssim M$, DM from a strongly coupled sector provides one of the few examples where the use of a DM Effective Field Theory (EFT) is well motivated even to parametrize LHC DM searches - a topic that has received enormous attention in recent years (see refs. [1, 2, 3] and the literature that followed).

In this contribution we will use symmetry arguments to discuss all structured scenarios where DM is strongly coupled, but fulfills the WIMP miracle. This work in based on [4, 5]. After identifying the relevant symmetries, we use simple power counting rules to build the EFT describing the physics of these scenarios at collider energies, both in the case where DM is a scalar or a fermion. We will see that, in some cases, the EFT for strongly coupled DM differs substantially from the original DM EFT of refs. [1, 2, 3].

2 Analysis and results

So, what symmetries are compatible with irrelevant operators only? For scalars a well-known example is the shift symmetry associated with Nambu–Goldstone bosons (NGBs) from strong dynamics, like QCD pions. In this case the leading interactions appear at D=6 or D=8. For Dirac fermions, on the other hand, chiral symmetry and the absence of gauge interactions are enough to guarantee $D \geq 6$. Alternatively, for Majorana fermions (in analogy with NGBs), non-linearly realized supersymmetry (SUSY) ensures that $D \geq 8$. Indeed the leading interactions of Goldstini from spontaneously broken SUSY only exhibit higher-derivative interactions in the limit where all other SUSY particles are heavy [6]. We will discuss these examples in detail below, but first we want to answer the question of whether, beyond these examples, we can find an infinite set of symmetries such that the low-energy amplitude is suppressed by higher and higher powers of energy, i.e. where $D \geq 10$ constitute the only interactions allowed in the limit of

Table 1: *Building blocks for the effective Lagrangian with different SSB patterns. Dots denote higher order terms in* $1/f$.

G/H	ϕ	d_μ^a	ε_μ^a
$\frac{U(1)}{\mathcal{Z}_2}$	$\phi \in \mathbb{R}$	$\frac{\partial_\mu \phi}{f}$	0
$\frac{SU(2)}{U(1)}$	$\phi \in \mathbb{C}$	$(1 + \frac{\lvert\phi\rvert^2}{f^2} + ...)\frac{\partial_\mu \phi}{f}$	$\frac{\phi^\dagger \overset{\leftrightarrow}{\partial}_\mu \phi}{f^2} + ...$
$\frac{SO(6)}{SO(5)}$	$H^i, \phi \in \mathbb{R}$	$\left(1 + \frac{\lvert\phi\rvert^2}{f^2} + \frac{\lvert H\rvert^2}{f^2} + ...\right)\frac{\partial_\mu \phi}{f}$	$\frac{H^\dagger \overset{\leftrightarrow}{\partial}_\mu H}{f^2} + ...$

exact symmetry. As a matter of fact the answer is negative. Fundamental principles based on analyticity, unitarity and crossing symmetry of the $2 \to 2$ amplitude provide strict positivity constraints for some of the coefficients of D=8 operators [7]. This implies that generally there is no limit in which a symmetry that protects operators with four fields and $D \geq 10$, forbidding $D \leq 8$, can be considered exact. So the complete set of scenarios with a naturally light strongly coupled DM, that however appears weakly coupled at small E (and therefore fulfills the WIMP miracle) is given by the above examples and is captured by operators of $D \leq 8$.

In the following, we shall focus on the case of scalar DM. Naturally light scalars originate as pseudo-NGBs of the spontaneously symmetry breaking (SSB) pattern G/H. If the sector responsible for SSB is strong, NGB interactions become strong at high-E. These scenarios are particularly interesting in association with the hierarchy problem [8, 9, 10, 11, 12, 13, 14], but also independently from it [15, 16]. Qualitatively different cases of interest can be identified, depending on the particular group structure being considered and the interplay with Higgs physics. First, a light scalar DM can be associated with an abelian $U(1) \to \mathcal{Z}_2$ breaking pattern, while a light composite Higgs originates from e.g. $G/H = SO(5)/SO(4)$ [17]. Alternatively, the DM originates from a non-abelian, e.g. $SU(2) \to U(1)$ or larger, symmetry breaking patterns [8, 13, 15, 14]. Finally, both the Higgs and DM can arise together from a non-factorizable group G, such as $SO(6)/SO(5)$ [18, 9, 10, 12]. The very power of EFTs is that, at low-E, large groups of theories fall in the same universality classes: in our case the generic EFTs that we will now build to describe the above-mentioned scenarios can be matched to any model with approximate symmetries. In all these cases, the NGB interactions are described by the CCWZ construction: the light degrees of freedom ϕ^a are contained in the coset representative $U = \exp(i\phi^a t^a/f) \in G/H$ and appear in the Lagrangian only through the building blocks d_μ^a and ε_μ^A in $U^{-1}\partial_\mu U = i d_\mu^a t^a + i\varepsilon_\mu^A T^A$, where $t^a(T^A)$ are the broken (unbroken) generators in G, f is the analog of the pion decay constant and is related to the mass and couplings of resonances from the (strong) sector that induces SSB through the naive dimensional analysis estimate $f = M/g_*$. Table 1 shows some specific examples. Under a transformation $g \in G$, $U \to gUh(\phi, g)^{-1}$, where $h(\phi, g) \in H$. Then $d_\mu \equiv d_\mu^a t^a$ and $\varepsilon \equiv \varepsilon_\mu^A T^A$ transform under G respectively in the fundamental representation of H and shift as a connection, so that $D_\mu^\varepsilon \equiv \partial_\mu + i\varepsilon_\mu$ is the covariant derivative. With these ingredients, the low energy Lagrangian describing the canonically normalized light scalars only, is simply $\mathcal{L}^{eff} = M^2 f^2 \mathcal{L}\left(d_\mu^a/fM, D_\mu^\varepsilon/M\right)$, with the additional requirement of invariance under the unbroken group H: this automatically guarantees also G invariance.

Clearly DM cannot be an exact massless NGB: the global symmetry must be broken explicitly. We keep track of this breaking by weighting interactions that violate the CCWZ construction with m_ϕ^2/M^2; an assumption that reflects to good extent the expectations in explicit models (see for instance [9]). We further assume the most favorable case in which, to the extent possible, the SM itself is part of the strong dynamics, as discussed in ref. [19], so that DM-SM interactions do not introduce further symmetry

breaking effects (we discuss below cases where only some species take part in the new dynamics). This implies in particular that we assume the new dynamics respects the SM (approximate) symmetries: custodial symmetry, CP, flavor symmetry (broken only by the SM Yukawas) and baryon and lepton numbers. Finally we assume the new dynamics can be faithfully described by a single new scale M and coupling g_*. Compatibly with these assumptions, the most general Lagrangian at the leading $D = 6$ order in the $1/M$ expansion is,

$$ {}_6\mathcal{L}_{\rm eff}^{DM_\phi} = c_\psi^V \frac{g_*^2}{M^2}\phi^\dagger \overset{\leftrightarrow}{\partial}_\mu \phi\, \psi^\dagger \bar\sigma^\mu \psi + c_B^{dip}\frac{g_*}{M^2}\partial_\mu\phi^\dagger\partial_\nu\phi\, B^{\mu\nu} + c_H^S \frac{g_*^2}{M^2}|\partial_\mu\phi|^2\,|H|^2 + c_H^{\not S}\frac{g_*^2 m_{\phi,H}^2}{M^2}|\phi|^2\,|H|^2 + c_\psi^{\not S}\frac{g_*^2 y_\psi}{M^2}|\phi|^2\psi\psi H \tag{5} $$

where each operator is weighed by the maximum coefficient that we can expect following the power-counting rules associated with the above mentioned-symmetries. The scaling in powers of the coupling g_* can be unambiguously determined from a bottom-up perspective by restoring $\hbar \neq 1$ in the Lagrangian: the coefficient c_i of an operator $\mathcal{O}_i$ with n fields scales as $c_i \sim (\text{coupling})^{n-2}$. Similarly, at D=8, focussing on operators that contribute to $2 \to 2$ scattering,

$$ {}_8\mathcal{L}_{\rm eff}^{DM} = C_V^{\not S}\frac{g_*^2 m_\phi^2}{M^4}|\phi|^2 V^a_{\mu\nu}V^{a\,\mu\nu} + C_\psi^S\frac{g_*^2 y_\psi}{M^4}|\partial^\mu\phi|^2\psi\psi H + C_V^S\frac{g_*^2}{M^4}|\partial^\mu\phi|^2 V^a_{\nu\rho}V^{a\,\rho\nu} + C_H^S\frac{g_*^2}{M^4}|\partial^\mu\phi|^2|D^\nu H|^2 \tag{6} $$

$$ + C_V^T\frac{g_*^2}{M^4}\partial^\mu\phi^\dagger\partial^\nu\phi V^a_{\mu\rho}V^{a\,\rho}_\nu + C_H^T\frac{g_*^2}{M^4}\partial^\mu\phi^\dagger\partial^\nu\phi D_{\{\mu}H^\dagger D_{\nu\}}H + C_\psi^T\frac{g_*^2}{M^4}\partial^\mu\phi^\dagger\partial^\nu\phi\psi^\dagger\bar\sigma_\mu D_\nu\psi\,, \tag{7} $$

with $V^a_{\mu\nu} = B_{\mu\nu}, W^a_{\mu\nu}, G^a_{\mu\nu}$ for $U(1)_Y \times SU(2)_L \times SU(3)_C$ gauge bosons, and ψ, H the SM fermions and Higgs. We use a notation based on left-handed Weyl fermions, which carry additional internal indices to differentiate left-handed ψ and right-handed $(\psi^c)^\dagger$ components of Dirac fermions; the Wilson coefficients c, C, associated to the $D = 6, 8$ Lagrangians respectively, carry these indices, and are expected to be $O(1)$, unless otherwise stated, see table below.

Of course there are more operators that contribute to $2 \to 2$ scattering, but these can either be eliminated through partial integration, field redefinitions (that eliminate operators proportional to the equations of motion), Bianchi or Fierz identities, or they violate some of the linearly realized symmetries that we assume (CP, custodial). For instance, operators antisymmetric in the Higgs field, such as

$$ c_H^{\not{cust}}\frac{g_*^2}{M^2}\phi^\dagger\overset{\leftrightarrow}{\partial}_\mu\phi\, H^\dagger\overset{\leftrightarrow}{D^\mu}H \tag{8} $$

transform as (**1**,**3**) under custodial symmetry $SU(2)_L \times SU(2)_R$: their coefficient is expected to be generated first at loop level by custodial breaking dynamics, involving for instance g', which satisfies the required transformation rules $c_H^{\not{cust}} \sim g'^2/16\pi^2$. On the other hand at D=8,

$$ \partial^\mu\phi^\dagger\overset{\leftrightarrow}{\partial}_\nu\partial_\mu\phi H^\dagger\overset{\leftrightarrow}{D^\nu}H\,, \qquad \partial^\mu\phi^\dagger\overset{\leftrightarrow}{\partial}_\nu\partial_\mu\phi\psi^\dagger\bar\sigma^\nu\psi\,, \tag{9} $$

share the same symmetries (among the linearly and non-linearly realized ones that we have presented) as operators in ${}_6\mathcal{L}_{\rm eff}^{DM_\phi}$ and contribute to the same observables; for this reason their contribution is expected to be always suppressed by $\sim E^2/M^2 \ll 1$ in the amplitude and we neglect them (a similar logic was followed in ref. [20] to argue that the Peskin-Takeuchi U-parameter can be neglected, since it shares the same symmetries as the T parameter, but is higher-dimension).

Similarly, $m_\phi^2|\phi|^2|H|^4$ and $\partial_\mu\phi^\dagger\partial^\mu\phi|H|^4$ give a subleading (by a factor $g_*^2 v^2/M^2 \lesssim 1$) contribution w.r.t. c_H^S and $c_H^{\not S}$, in processes with 2 longitudinal vectors or Higgses and can only be distinguished in processes with three or more external longitudinal vector bosons/Higgses. Finally, operators of the form $|\phi|^2 \times_6 \mathcal{L}_{\rm eff}^{SM}$, where ${}_6\mathcal{L}_{\rm eff}^{SM}$ is the D=6 SM Lagrangian (see ref. [21]) but also includes total derivatives, are

generally further suppressed by m_ϕ^2/M^2 and count as D=10 effects in our perspective. The important novel aspect that is emphasized by our analysis and summarized in the Lagrangians eqs. (5,7) and table 1, is the following. Both the D=6 and D=8 Lagrangians can be important, as symmetries can suppress the expected leading interactions in favor of higher order ones. Indeed, as table 1 shows, the structures c_ψ^V vanishes for antisymmetry if DM has a single real degree of freedom (such as for the $U(1)/\mathcal{Z}_2$ and $SO(6)/SO(5)$ cosets), so that in this case the leading DM-fermion interaction is given by the D=8 operator C_ψ^T. On the other hand the structures $c_\psi^{\not S}$ and c_H^S are unsuppressed only when the generators associated with ϕ and H do not commute (such as in the $SO(6)/SO(5)$ model [18, 9]), but will be further suppressed by $\sim m_{\phi,H}^2/M^2$ in other cases. In those cases the leading DM-Higgs interactions are the D=8 C_H^S and C_H^T. Finally, an important source of suppression is represented by the degree of compositeness of the SM particles - either fermions or (transverse) gauge bosons. The most favorable situation is when the SM particles are fully composite since in this case they feature an unsuppressed g^* coupling to the strong sector. On the contrary, if SM fermions and gauge bosons are elementary degrees of freedom, we expect a suppression in the corresponding couplings, as shown in the first two rows of table 2. In models where the DM dominantly couples to gluons only, the leading effects at high-energy, not suppressed by any small parameters, are the D=8 C_V^S and C_V^T. We summarize in table 2 these and other such situations, where some of the above operators are suppressed by additional small parameters (such as symmetry breaking effects), and become therefore less interesting from the point of view of collider searches.

Table 2: $\times$ *denotes suppression of a given EFT coefficient, according to specific properties of the microscopic dynamics:* ψ_{elem} *denotes the limit where SM fermions are not composite,* V_{elem} *denotes instead the familiar case where the transverse polarizations of vectors are elementary (as opposed to strong multipolar interactions* [19]*).*

	c_ψ^V	c_B^{dip}	c_H^S	$c_H^{\not S}$	$c_\psi^{\not S}$	$C_V^{S,T}$	C_ψ^T
ψ_{elem}	$\times$				$\times$		$\times$
V_{elem}		$\times$				$\times$	
$U(1)/\mathcal{Z}_2$	$\times$	$\times$	$\times$	$\times$	$\times$		
$SU(2)/U(1)$			$\times$	$\times$	$\times$		
$SO(6)/SO(5)$	$\times$	$\times$					

In Fig. 1 we compare the LHC reach (blue region) in the (g_*, M)-plane with relic density (RD) expectations (green band) for $D = 6$ (e.g. DM as a PNGB of $SU(2)/U(1)$), showing that visible LHC effects are compatible with a non-vanishing RD. Here the LHC constraints have been derived from the data of ref. [22], imposing an additional cut in the centre-of-mass energy $\hat{s} < M^2$. This cut, and the representation in the (g_*, M)-plane, help us establishing consistency of the EFT assumption [23, 24]. Indeed, as M is lowered within the LHC kinematic region, the constraints rapidly deteriorate, since less and less data remains available: this signals the fact that, in that region, our EFT assumptions are not verified.

LHC constraints for the examples discussed above, where D=8 represent the leading effect at high-E, are also shown in Fig. 1 with a dashed (red) curve. Notice that here, while the E-growing cross sections implied by our symmetry structure clearly dominate at LHC energies $M \gtrsim E \gg m_{\rm DM}$, they might be comparable to symmetry breaking $m_{\rm DM}$-suppressed interaction at low-E, relevant at freeze-out. In other words, the complementarity between different DM experiments is partially lost in this setup – we discuss this issue further in [4, 5].

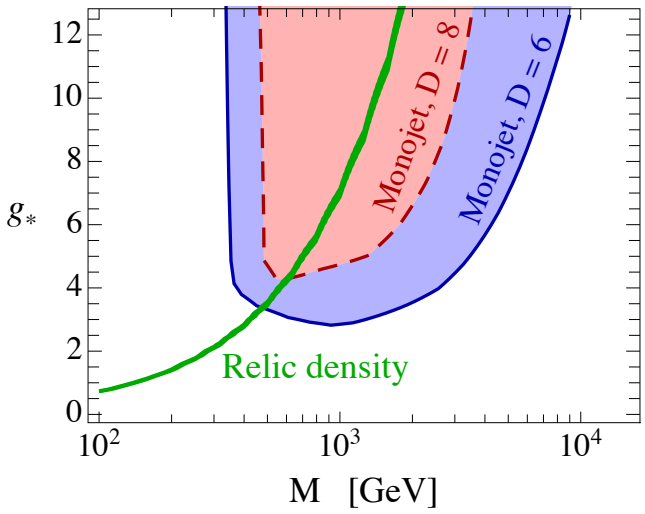

Figure 1: *Constraints on scalar DM with* $m_{\rm DM} = 5$ *GeV. Blue region: excluded by consistent LHC constraints on D=6 operator* c_ψ^V *in eq. (5) (e.g. pseudo-NGB DM from a non-abelian SSB pattern), and comparison with the parameters where the RD is correctly reproduced with the same D=6 operator (solid green). Red region: LHC constraints on D=8,* C_ψ^T *in eq. (7) (e.g. one scalar DM from an abelian SSB).*

3 Outlook

In Summary, we have discussed natural situations in which light DM originates from a strongly-coupled sector but its interactions are small at low-energies because of approximate symmetries, that forbid relevant interactions and allow only irrelevant (higher-derivative) ones. Prime principles dictate that such symmetries are consistent only with D=6 and D=8 operators for $2 \to 2$ scattering. In this article we have identified generic effective Lagrangians at these orders and introduced a power-counting that captures the most well-motivated scenarios that can imply large effects in irrelevant interactions: scalar DM as a PNGB.

These provide a class of models in which the LHC high-E reach plays an important rôle with respect to other types of experiments (such as RD indications and direct detection) and contains genuinely complementary information. Moreover, in these scenarios the DM EFT is not only consistent with LHC analysis (due to the underlying strong coupling, as shown in fig. 1, but also necessary, as the underlying dynamics is uncalculable. Our characterization provides a well-motivated context to model missing transverse-energy distributions at the LHC, in mono-jet, mono-W,Z,γ or mono-Higgs searches, with a handful of relevant parameters and yet a clear and consistent microscopic perspective. To the question of what we have learned from LHC DM searches, these models provide one answer.

4 Acknowledgements

It is my pleasure to thank Sebastian Bruggisser and Francesco Riva for the fruitful collaboration.

References

1. Q. H. Cao, C. R. Chen, C. S. Li and H. Zhang, JHEP **1108** (2011) 018.
2. J. Goodman, M. Ibe, A. Rajaraman, W. Shepherd, T. M. P. Tait and H. B. Yu, Phys. Lett. B **695** (2011) 185.
3. Y. Bai, P. J. Fox and R. Harnik, JHEP **1012** (2010) 048.
4. S. Bruggisser, F. Riva and A. Urbano, SciPost Phys. **3**, no. 3, 017 (2017).
5. S. Bruggisser, F. Riva and A. Urbano, JHEP **1611** (2016) 069.
6. See, e.g., Z. Komargodski and N. Seiberg, JHEP **0909** (2009) 066.
7. A. Adams, N. Arkani-Hamed, S. Dubovsky, A. Nicolis and R. Rattazzi, JHEP **0610** (2006) 014
8. A. Belyaev, M. T. Frandsen, S. Sarkar and F. Sannino, Phys. Rev. D **83** (2011) 015007.
9. M. Frigerio, A. Pomarol, F. Riva and A. Urbano, JHEP **1207** (2012) 015.
10. D. Marzocca and A. Urbano, JHEP **1407** (2014) 107.
11. O. Antipin, M. Redi and A. Strumia, JHEP **1501** (2015) 157.
12. M. Chala, JHEP **1301** (2013) 122.
13. A. Hietanen, R. Lewis, C. Pica and F. Sannino, JHEP **1412** (2014) 130.
14. A. Carmona and M. Chala, JHEP **1506** (2015) 105.
15. S. Bhattacharya, B. Melić and J. Wudka, JHEP **1402** (2014) 115.
16. O. Antipin, M. Redi, A. Strumia and E. Vigiani, JHEP **1507** (2015) 039.
17. R. Contino, Y. Nomura and A. Pomarol, Nucl. Phys. B **671** (2003) 148.
18. B. Gripaios, A. Pomarol, F. Riva and J. Serra, JHEP **0904** (2009) 070.
19. D. Liu, A. Pomarol, R. Rattazzi and F. Riva, JHEP **1611** (2016) 141.
20. R. Barbieri, A. Pomarol, R. Rattazzi and A. Strumia, Nucl. Phys. B **703** (2004) 127.
21. B. Grzadkowski, M. Iskrzynski, M. Misiak and J. Rosiek, JHEP **1010** (2010) 085.
22. G. Aad *et al.* [ATLAS Collaboration], Eur. Phys. J. C **75** (2015) no.7, 299 Erratum: [Eur. Phys. J. C **75** (2015) no.9, 408].
23. D. Racco, A. Wulzer and F. Zwirner, JHEP **1505** (2015) 009.
24. A. Biekötter, A. Knochel, M. Krämer, D. Liu and F. Riva, Phys. Rev. D **91** (2015) 055029.